DEFENCE ACADEMY
OF THE UNITED KINGDOM
Cranfield UNIVERSITY
Defence College of Management and Technology

Michael C. Gibson

Determination of Residual Stress Distributions in Autofrettaged Thick-Walled Cylinders

PhD

Department of Engineering Systems and Management
Defence College of Management and Technology
April 2008

CRANFIELD UNIVERSITY

DEFENCE COLLEGE OF MANAGEMENT AND TECHNOLOGY

ENGINEERING SYSTEMS DEPARTMENT

PhD THESIS

Academic Year 2007-2008

Michael C. Gibson

Determination of Residual Stress Distributions in Autofrettaged Thick-Walled Cylinders

Supervisor: Dr A Hameed

April 2008

Abstract

High pressure vessels such as gun barrels are autofrettaged in order to increase their operating pressure and fatigue life. Autofrettage causes plastic expansion of the inner section of the cylinder – setting up residual compressive stresses at the bore after relaxation. Subsequent application of pressure has to overcome these compressive stresses before tensile stresses can be developed, thereby increasing its fatigue lifetime and safe working pressure.

A series of Finite Element (FE) models of hydraulic autofrettage were created, to establish the correct boundary conditions required and means of developing accurate but computationally efficient models. Close agreement was observed between the solutions obtained from the developed models and those from existing analytical and numerical models. These initial models used a simplistic bi-linear stress-strain material representation; this deficiency was then addressed through the development of two means of creating radial position dependent non-linear material behaviour within FE, crucial for accurate prediction of residual stresses.

The first utilised a method of altering the elastic properties of the material to achieve non-linear stress-strain response. This provided accurate results that compared well with existing methods, but was unable to be used in simulation of swage autofrettage due to its elastic nature. The second method achieved non-linear behaviour through direct manipulation of the stress and plastic strain states of the FE model at a fundamental level. This was hence suitable for arbitrary loading procedures, including swage autofrettage.

A swage-like model that applied deformation via a band of pressure was developed, to investigate the influence of localised loading and shear stresses that result on the residual stress field.

A full model of swage autofrettage was then developed, which was optimised on the basis of accuracy and solution effort. It was then used to investigate the effects of various mandrel and contact parameters on the creation of residual stresses. The model is suitable for use in future optimisation studies of the swage autofrettage procedure.

Acknowledgements

The Acknowledgments is a tricky section to write – they give a much broader insight to the author than the rest of the thesis, but must be kept brief. There are so many to thank and little space to do so in. Having written my thesis, and sat through my viva, I find the writing of acknowledgements by far the most daunting – there are many more aspects than merely the technical that must be recounted. That said, I would like to thank:

My supervisors, Dr Amer Hameed (for having faith in my ability to undertake a PhD) and Prof Tony Parker, for their help and direction throughout these studies, plus Prof John Hetherington for his general guidance and advice.

Those who made it possible for me to achieve my goals: John Reynolds, Helen Iremonger, Mary Tutt, Evelyn Hopwood and Sue Gale, to name but a few.

The Engineering and Physical Sciences Research Council (EPSRC) and Engineering Systems Department (latterly, Department of Engineering Systems and Management) for their financial support of these studies. The members of the XANSYS mailing list, for their insights into ANSYS and how I should achieve objectives.

All those who helped and taught me prior to these studies, at Ferndale School, Longcot and Fernham CofE School, King Alfred's School and 6th Form, the Royal Military College of Science and all those from all walks of life who have inspired me along the way, in all its aspects.

My friends, for making it fun – especially Leon Rosario, Lorna Frewer, Paul Bourke, Senthil Muniyasamy, Stuart Thomson, Darina Fišerová, Satheesh and Suresh Jeyaraman, Susan Servais and many other students from the Heaviside Post Grad Centre and the wider DCMT.

Lastly, I thank my parents, Ros and Cleve, for the examples they set and their love and support that allowed me to achieve my PhD and all earlier stages in my life. Without them, none of this would have been possible.

Table of Contents

List of Figures

List of Tables

PREAMBLE

NOMENCLATURE

Latin Symbols

a	A723 Material-fit constant
A_{1-4}	Material Model Parameters (Huang's Model)
$B_{1,2}$	Material Model Exponents (Huang's Model)
c	A723 Material-fit constant
d	A723 Material-fit constant
$E_{1,2}$	Loading and Unloading Young's Moduli
El_{Ax}	Number of axial elements in mesh
$El_{Ax\text{-}ll}$	Number of axial elements along the parallel section of a mandrel
El_{Rad}	Number of radial elements in mesh
El_{Tan}	Number of tangential elements in mesh
G	Material Shear Modulus
G_P	Pressure gradient (Band of Pressure model, moving band)
$H_{1,2}$	Loading and Unloading reverse Tangent Moduli
k	Material Yield Stress in pure torsion ($\sigma_Y/\sqrt{3}$ using Mises Yield Criterion)
K	Tube Wall Ratio, r_b/r_a
l_{BW}	Length of pressure band (Band of Pressure model, static band)
l_{El}	Length of element edge
l_{ll}	Length of parallel section of mandrel
l_m	Mandrel Length
l_r	Wall Depth, $r_b - r_a$
l_z	Tube Section Length
m	Multiplicative constant (Band of Pressure model, static band)
$N_{El\text{-}Ax}$	Number of element lengths moved by the mandrel as it passes through the tube undergoing swage autofrettage (a distance of $l_z + l_m$)
n_j	Unit vector, normal and outwards to the surface
P_{AF}	Autofrettage pressure
P_{MB}	Mid-band pressure (Band of Pressure model, moving band)
P_{SB}	Static band pressure (Band of Pressure model, static band)
PS	Scaling parameter used to control the number of sub-steps specified during the sensitivity analysis of the value, documented in Chapter 8.
ΔP	Pressure increment between elements (Band of Pressure model, moving band)
p_e	Limiting Elastic Pressure at which yielding initiates (at r_a)
p_i	Interface Pressure (at r_a)
r_a, r_b	Inner and Outer tube radii
r_i	Mandrel-Tube Interface radius
r_M	Mandrel radius (to parallel portion)

r_N	Normalised radial position, given by $(r - r_a)/(r_b - r_a)$
r_p, r_s	Primary and Secondary Yield radii
s_{ij}	Deviatoric stress tensor.
u, v, w	Radial, Hoop and Axial Deflections

Greek Symbols

β	Bauschinger Effect Factor, a ratio of reverse yield strength to initial yield strength.
δ	Mandrel-Tube Interference $(r_m - r_a)$
δ_{ij}	Kronecker delta ($\delta_{ij} = 0$ for $i \neq j$, 1 for $i = j$).
ε_Y	Yield Strain, in simple tension
ε_{ij}	Strain tensor.
θ_{MF}	Angle between axis and forward taper of mandrel
θ_{MR}	Angle between axis and rear taper of mandrel
θ_{Sec}	Angle of section in Hoop Section model
λ	First Lamé Constant
μ	Second Lamé Constant
ν	Poisson's Ratio
σ_E	Elastic stress range between peak plastic strain and onset of reverse yielding.
σ_{ij}	Stress tensor.
σ_{Max}	Maximum stress reached during initial deformation
σ_Y	Yield Stress, in simple tension
σ_{Y0}	Initial Yield Stress, in simple tension
φ	Uni-axial stress-strain function, relating equivalent stress and equivalent plastic strain (Jahed and Dubey method)
Δ	Convergence criterion (Jahed and Dubey method)

Subscript Characters

m, r, t	Mandrel, ram and Tube subscripts
Max	Maximum value (stress or strain) experienced during autofrettage, where plastic strain occurred
N	Subscript indicating a normalised value
$Peak$	Maximum value (stress or strain) experienced during autofrettage, where plastic strain did not occur

Superscripts

L	Loading superscript
UL	Unloading superscript

APDL Variables

`Axi_Div`	Number of axial elements
`Rad_Div`	Number of radial elements
`Tan_Div`	Number of tangential elements

FORTRAN Variables

`absdpleq`	Absolute value of plastic strain increment
`BEF`	Bauschinger effect factor
`MatParms`	Array used to store material-fit parameters
`MaxEqSig`	Maximum equivalent stress reached during loading/autofrettage
`MaxTotStrn`	Maximum total strain reached during loading/autofrettage
`qStrn`	Current equivalent total strain (`_t` suffix denotes the initial iteration value)
`RevElStrn`	Amount of elastic strain in unloading before reverse yielding occurs
`Revpleq`	Reverse plastic equivalent strain
`RevYProx`	Strain value used to indicate proximity to reverse yield
`RevYStrn`	Equivalent strain, after which reverse yielding occurs
`Tensepeq`	Maximum equivalent plastic strain reached during loading/autofrettage
`UnldFact`	Factor used to control tolerance to strain reduction before unloading is triggered
`UnldFlag`	Flag used to indicate unloading state
`UnldParm`	Parameter calculated using initial and incremented strains to determine whether unloading occurs (compared against `UnldFact`)

Acronyms and Abbreviations

AF	Autofrettage
APDL	ANSYS Parametric Design Language
EMPRAP	Elastic Modulus and Poisson's Ratio adjustment procedure
Fortran	A portmanteau of Formula Translator/Translation; a procedural programming language, in which ANSYS UPFs may be written
GB	Gigabyte, a measure of computer storage capacity, 1024^3 bytes.
ID	Inner Diameter
OD	Outer Diameter
UPF	User Programmable Feature, a means of extending/customising various features within ANSYS. Generally written in the Fortran language, then compiled and linked with ANSYS.
USERMAT	A UPF in which a material's stress-strain state may be customised.

GLOSSARY

Elastic Range — The stress range between peak stress in initial deformation (σ_{Max}) and the reverse yield stress ($\beta\ \sigma_{Y0}$).

Loading — The pressurisation phase of the hydraulic autofrettage procedure, during which pressure is increased from zero to the specified autofrettage pressure.

Overstrain — Defined as the proportion of the tube wall that has undergone plastic deformation; often defined as a percentage of the wall thickness.

Unloading — The depressurisation phase of the hydraulic autofrettage procedure, during which pressure is decreased from the specified autofrettage pressure to zero, and residual stresses are developed.

ANSYS PROPERTY NAMES

Symbol	ANSYS Property	Description
σ_r	`S,X`	Radial Stress
σ_θ	`S,Z`	Hoop Stress
σ_z	`S,Y`	Axial Stress
σ_{rz}	`S,XY`	Shear Stress (in the radial direction on the plane perpendicular to the tube axis)
σ_{vM}	`S,EQV`	von Mises Equivalent Stress
ε_r^e	`EPEL,X`	Elastic Radial Strain
ε_θ^e	`EPEL,Z`	Elastic Hoop Strain
ε_z^e	`EPEL,Y`	Elastic Axial Strain
ε_{rz}^e	`EPEL,XY`	Elastic Shear Strain (oriented identically to σ_{rz})
ε_{vM}^e	`EPEL,EQV`	von Mises Equivalent Elastic Strain
ε_r^p	`EPPL,X`	Plastic Radial Strain
ε_θ^p	`EPPL,Z`	Plastic Hoop Strain
ε_z^p	`EPPL,Y`	Plastic Axial Strain
ε_{rz}^p	`EPPL,XY`	Plastic Shear Strain (oriented identically to σ_{rz})
ε_{vM}^p	`EPPL,EQV`	von Mises Equivalent Plastic Strain

NOTES

ANSYS “Classic” v11.0 SP1 was used to generate all results presented in this document, and any references made to the software are specific to this version and its associated documentation. However, the models created and references made are thought to be mostly compatible with earlier (beyond v8.0, the first version used in these studies) and future versions.

Throughout this thesis, the word mandrel is used solely to refer to the physical object that is passed through the inner diameter of a tube, while swaging refers to the process of swage autofrettage.

1. INTRODUCTION

Even today, in the era of guided missiles and smart munitions, guns and other tube weapons are crucial in the defence of national interests. In terms of large bore weapons, artillery and other indirect fire platforms deliver long range and preparatory strikes in support of other forces (indeed, Stalin designated artillery the 'god of war'), and direct fire weapons as found on tanks provide the ability to engage and destroy other such vehicles so that they may take and hold ground.

Guns must be able to contain high pressures, as the amount of work done on the projectile depends on the pressure acting upon its base as it travels along the barrel. This is quantified by (1.1), which applies the principle of conservation of energy to the projectile. Neglecting losses due to friction between the projectile and barrel, and any changes in gravitational potential energy, the amount of kinetic energy gained by the projectile equals the mechanical work done on it by the expanding propellant gases, or:

$$KE = A\int_0^{l_b} P_b(x)dx = \frac{1}{2}mv_m^2 \tag{1.1}$$

Where:

A	=	base area of projectile,
l_b	=	barrel length,
m	=	mass of projectile,
$P_b(x)$	=	shot base pressure (pressure acting upon the base of the projectile),
v_m	=	muzzle velocity of projectile,
x	=	location in barrel.

Kinetic energy may be imparted to either a small payload projectile launched at a high muzzle velocity (allowing for long range and/or a high-velocity impact) or a large payload projectile launched at a lower velocity; maximising the pressure for a given gun geometry allows the highest possible kinetic energy.

In addition, high pressure vessels are used in a number of other applications, namely:

- Food sterilisation, using high pressure to kill large proportions of bacteria present in foods,
- Sintering of components from powders to create near final dimensions and minimise material usage and subsequent machining,
- Hyper-sonic (up to Mach 16) wind tunnels,
- Power generation,
- Water jet cutting.

To contain a high pressure would typically require a very thick tube wall due to the concentration of tensile hoop stresses at the inner diameter (ID), creating a heavy

weapon system. The magnitude of pressure is also limited by the material yield stress, which must not be exceeded in normal use.

Figure 1.1: Turkish Bombard – given the relatively low density stone shot it fired, its thick wall is testament to its poor material utilisation (Public domain photograph taken at Royal Armouries, Fort Nelson, Portsmouth, England)

This may be allowable in large or static domains, where size and mass are relatively unconstrained, but is not feasible for land based mobile weapon systems. Simply selecting a high strength steel, or other metal, is not practical as high ultimate tensile strength (UTS) is rarely accompanied by high fracture toughness. Hence a gun made from a high UTS steel in order to permit high pressure operation will have a shorter fatigue lifetime than its lower-pressure equivalent.

Autofrettage is a means of pre-stressing thick-walled tubes to better distribute the tensile hoop stress throughout the tube wall, so reducing the magnitude of the hoop stresses found at the ID when the tube is re-pressurised subsequent to pre-stressing. This is achieved by overloading the ID of the tube to cause plastic expansion of some or all of the tube wall, such that residual compressive hoop stresses are created in the near-bore region whilst residual tensile hoop stresses are created in the outer portion.

Use of autofrettage allows the wall thickness ($r_b - r_a$) of gun barrels to be reduced considerably, by definition decreasing its wall ratio, K, given by r_b/r_a. This greatly lessens its mass which, for a cylindrical barrel of constant cross-section, is given by:

$$\begin{aligned} m_b &= \rho \cdot l_b \cdot \pi \cdot \left(r_b^2 - r_a^2\right) \\ &= \rho \cdot l_b \cdot \pi \cdot r_a^2 \left(K^2 - 1\right) \end{aligned} \tag{1.2}$$

Where:

K = Wall ratio, r_b/r_a,
m_b = Mass of barrel,
r_a = Inner radius of barrel,
r_b = Outer radius of barrel,
ρ = Density of barrel material.

Hence, for a given calibre of round such that r_a is fixed, the mass is proportional to (K^2 – 1). This reduction in mass may be used to allow greater portability of the weapon, and/or extending the barrel length, l_b, to increase muzzle velocity (by allowing the pressure of the propellant gas to act on the projectile along a longer distance), provided barrel droop (curvature) does not affect accuracy. Such curvature of the barrel causes lateral acceleration of projectiles as they travel along it, the reaction force to which induces lateral vibration of the barrel; such vibration may alter the orientation of the projectile as it leaves the barrel, modifying its trajectory.

However, the amount that the wall thickness may be reduced depends on how well the residual stresses are known; if they are not precisely known the factor of safety must be increased, limiting the amount by which the wall may be thinned.

In addition to reducing barrel mass, autofrettage is used to increase their fatigue life, expressed in terms of the number of full effective firing cycles. This allows for fewer interruptions in service, reduced load on the logistic chain and reduced acquisition cost. Wear life can be increased with barrel liners and coatings so it is essential that fatigue lifetime should equal or exceed wear lifetime. This requires accurate knowledge of residual stresses present and the nature of cyclic loading.

There are two methods of autofrettage: hydraulic and swage. Hydraulic autofrettage involves the application of high pressure to the ID of a tube, until the desired extent of plastic deformation is achieved. Swage autofrettage creates the required deformation by passing an oversized mandrel through the ID of the tube, causing a moving, axially-localised outward radial displacement at the bore of the tube.

Swage autofrettage generally makes the pre-stressing process less complex than hydraulic autofrettage; the latter requires careful pressure sealing arrangements and accurate control of the applied pressure and monitoring of tube expansion, as small changes in the material yield stress may result in large changes in the depth of yielding. Conversely, swage autofrettage applies displacement based loading, which generally creates consistent depths of autofrettage yielding despite normal variations in material yield stress.

Analytical modelling of hydraulic autofrettage of constant cross-section cylindrical tubes, subject to some of the range of end conditions, is possible through the use of simplifying assumptions, such as choice of yield criteria and material compressibility and, critically, material stress-strain behaviour. However, the transient and localised nature of swage autofrettage, and resultant deviation from plane conditions, makes it intractable to analytical solution. In addition, very few numerical studies of swage autofrettage have been published.

Autofrettage causes large plastic strains around the ID of the tube, which noticeably alters the unloading properties of those materials commonly used and causes the early onset of non-linearity; a phenomenon termed the Bauschinger effect. This non-linearity is dependent on prior plastic strain, as well as the material in question, and typically causes significant deviation from those material models that are often

assumed. The effect is most pronounced around the ID, which experiences the greatest initial deformation, where compressive residual stresses are most desired.

This in turn has a significant effect on the residual stresses developed when the autofrettage load is removed, especially as it can cause reverse yielding to occur when it otherwise would not be expected.

To avoid such assumptions, or to model swage autofrettage, requires the utilisation of numerical methods; it was clear that these must be adopted to allow the goals of the research to be achieved. It was decided to use Finite Element Analysis (FEA) to develop firstly a general model of hydraulic autofrettage incorporating a realistic material representation, and then a model of swage autofrettage, for which no analytical solution exists.

The original contributions in this work are:

1. Validation and configuration of an FEA package called ANSYS, to accurately represent a thick-walled tube undergoing hydraulic autofrettage and subsequent unloading allowing its stress-strain state to be assessed at both peak pressure and after removal of such pressure.

2. Implementation of an existing method for simulating non-linear material behaviour through linear-elastic analysis (Elastic Modulus and Poisson's Ratio Adjustment Procedure (EMPRAP)), as an initial method of incorporating non-linear material behaviour in the developed model of hydraulic autofrettage.

3. Development of a custom material model (within the ANSYS package) to represent general non-linear material behaviour in arbitrary geometry and loading configurations, allowing it to be used within models of both hydraulic and swage autofrettage.

4. Assessment of the transient and residual stress-strain and displacement distributions in a swage-like procedure. An initial model of localised transient loading was created, utilising a cylindrical band of pressure moving along the ID in a manner analogous to the passage of a mandrel.

5. Assessment of the transient and residual stress-strain and displacement distributions in a realistic model of swage autofrettage. This more advanced model uses a sliding contact between the deformable mandrel and the ID of the tube; the displacements resulting from this interference cause the requisite plastic strains for autofrettage.

The significance of the work presented in this thesis lies in the newly-developed capability of incorporating a realistic material representation and hence predicting the residual stress fields created during both:

1. Hydraulic autofrettage of a non-uniform cross-section pressure vessel,
2. Swage autofrettage.

This knowledge allows more accurate prediction of fatigue life and safe-working pressures for gun barrels, which can lead to either lighter weight and/or better system performance characteristics. It will also provide a greater degree of confidence in these calculations for real systems. The contents of the thesis chapters are summarised below.

Chapter 2 introduces the topic of thick-walled, high-pressure, vessels, and gives a brief description of their history. A review of literature pertinent to the topic is then presented, including relevant analysis techniques.

Chapter 3 introduces the different material models relevant to this study, and describes an early analytical model of autofrettage. The adaption of this model to include additional stress-strain behaviours, and use in a pseudo-swage interference model, is then detailed. The chapter ends with a summary of the selected models and their usage, for comparison with numerical models to be developed in future chapters.

Chapter 4 documents the development of a set of models of hydraulic autofrettage that were created in an FEA package, called ANSYS. The models use a simplistic, bi-linear kinematic hardening, material model but span the range of four end conditions which are generally assessed when hydraulic autofrettage is considered; the simplistic material model allowed structural constraints to be focussed upon. The chapter ends with a comparison of the FEA results with those from two other models (one analytical, one numerical), which serves to validate ANSYS as a suitable platform for modelling the geometrical aspects of hydraulic autofrettage.

Chapter 5 introduces initial material non-linearity, using a quasi-elastic model, into the set of hydraulic autofrettage models developed in Chapter 4. Results from the combined model are then compared with the same numerical model used in Chapter 4, verifying the ability of ANSYS to include material non-linearity in the context of hydraulic autofrettage.

Chapter 6 describes the development of a more general method for incorporating material non-linearity, which would then be of use in models of swage autofrettage. The material was initially checked via simulation of a uni-axial test which accurately reproduces the original uni-axial stress-strain data. In addition, the material was validated in hydraulic autofrettage through comparison with both the numerical model used in Chapters 4 and 5, and the material model implemented in Chapter 5.

Chapter 7 documents the creation of a swage-like model, in which autofrettage loading is applied to a long section of tube by a band of pressure that travels along its ID. This developed the methodology for modelling a long tube section in ANSYS, and gave a first approximation of stresses that would be developed during swage autofrettage. These results were then available for comparison with those that would be generated by a more accurate swage autofrettage model.

Chapter 8 details the development of an accurate model of swage autofrettage, adding a deformable mandrel to the long tube model described in Chapter 7. Several sensitivity analyses were conducted on the model, to ensure mesh sizing, section length and time

stepping were specified such that representative mid-section properties of a swaged tube could be derived from the model. A systematic analysis was then made of various mandrel geometry parameters, allowing transient and residual stress-strain states to be assessed.

Chapter 9 collates compares and contrasts various aspects of issues raised within individual chapters, and addresses them in a context relevant to the overall thesis.

Chapter 10 then summarises the conclusions drawn throughout the thesis, and assesses the various strands of work collectively.

Chapter 11 compiles the appendices for the thesis, containing information and results felt important, but not appropriate for inclusion within the main body of work

2. LITERATURE REVIEW AND FUNDAMENTAL THEORY

2.1. INTRODUCTION

This chapter introduces the topics relevant to the work described in this thesis and the literature underpinning them. It begins by presenting a brief overview of the history of cannons, the first form of pressure vessel widely adopted, and efforts made to refine them.

The two methods of autofrettage, a means of pre-stressing cylindrical vessels, are then described, followed by a summary of models of hydraulic autofrettage that are pertinent to this study.

Several methods of numerical modelling are then described and subsequently assessed based on their suitability for use in this investigation.

The conclusions drawn within this chapter are then summarised, and followed by a programme of work which was developed based on them to achieve the desired aims.

2.2. HISTORY OF CANNONS

The first pressure vessels of note that were widely utilised were cannons, making their history synonymous with that of pressure vessels. Indeed, the word "cannon" is derived from the Latin *canna*, meaning tube, which reinforces their place in the wider thick-walled pressure vessel field. As has been the case many times throughout history, and particularly during the mid-19th and 20th Centuries, military demands have focussed development efforts, causing rapid progress in specific areas. Such progress is eventually disseminated, resulting in many advances across wide fields of application. This is, and continues to be, true for cannons and pressure vessels even in the age of rockets and airborne munitions. Even today, cannons continue to be developed, with particular focus on reducing mass to allow enhanced air-portability, to satisfy tactical requirements that cannot be fulfilled with rockets (such as rapid target engagement, low minimum range, continuous fire, with the ability to switch targets rapidly).

The first cannon were comparatively low pressure devices, due mainly to the poor seal between the projectile and the tube wall and ineffective gunpowder (serpentine powder). However, combustion pressures soon increased as corned powder was developed (a more consistent gunpowder) and heavier spherical projectiles were introduced. Projectiles were primarily made from stone (such as granite or marble) or iron. By the end of the 1400s, it was realised that high operating pressures led to early fracture of cannons, often causing them to split.

Although some early cannon were assembled from strips of metal and held together with metal hoops (as a wooden barrel might be), since then cannon have almost invariably been cast.

Gun designers during the mid-1800s recognised the poor utilisation of material (uneven stress distribution) within thick-walled guns, applying a practical upper limit on the range of wall ratios that could be used. It was realised that if some inwards force could be applied to a barrel, the effect of poor material utilisation could be mitigated. To this end, barrels were "hooped" to pre-compress the inner surface of the barrel – for example, William Armstrong [1] assembled compound cylinders from wrought iron tubes.

Additionally, it was recognised by Rodman [2] that if the cooling of a cast cannon were controlled, the sequence of crystallisation from liquid could influence the residual stress distribution and hardness of the tube material at the bore.

2.2.1. Early Modelling

The earliest form of modelling that reflected the uneven stress distribution in pressurised thick-walled cylinders, practically addressed via compound barrels by manufacturers such as Armstrong, was that from Lamé's solution [3]. However, a model of a pressurised tube incorporating plasticity would be required to model one method of overcoming the stress concentration. The envisaged method would achieve pre-stressing by causing plastic expansion of the near-bore region, achieving similar pre-stressing to that developed by compound tubes; the barrel could be made to hoop itself.

The term *autofrettage*, or self-hooping, is generally attributed to a French artillery officer, L. Jacob, who appears to have coined the expression in 1907, hence its French origin. In 1909 LB Turner presented a "complete mathematical study" at King's College, Cambridge. Autofrettage was adopted by the French in 1923, and soon after saw widespread use. Macrae, a British artillery officer, produced a "complete solution" [4]. Additional contributions were made by Manning [5], Dirmoser [6] and Faupel [7].

To correctly model the plastic deformation and subsequent residual stress field within a thick-walled cylinder, several physical requirements must be addressed:

1. Equilibrium and Compatibility Equations,
2. Stress-strain profile of the considered material,
3. Equivalence/Yield criterion,
4. End conditions of the tube,
5. Flow Rule and Compressibility.

2.3. PRE-STRESSING OF MODERN CANNONS AND PRESSURE VESSELS

As mentioned above, cannon are cast and/or forged then machined to intermediate dimensions. They are then autofrettaged, and then undergo a final stage of machining to ensure accurate sizing of the finished article. Autofrettage introduces compressive hoop stresses in the region surrounding the ID to reduce the magnitude of the hoop stresses developed there when the tube is pressurised. This may be accomplished in one of two ways, as described in sub-sections 2.3.1 and 2.3.2.

Generally, the greater the amount of residual compressive stress developed around the ID, the more beneficial pre-stressing resulting from autofrettage is. However a phenomenon termed the *Bauschinger effect*, typically observed in steels often used for high-pressure vessels, limits the degree of pre-stressing that may be applied. In particular, it causes the early onset of non-linearity around the ID when compressive stresses are developed following tensile deformation experienced during autofrettage. The Bauschinger effect is described more fully in sub-section 3.2.3.

2.3.1. Hydraulic Autofrettage

Hydraulic autofrettage involves the application of hydrostatic pressure to the ID of the tube, such that equivalent stress at the ID exceeds the material yield stress and plastic deformation begins. Pressure is further increased such that the deformation propagates to the desired depth within the tube wall. Oil is used to pressurise the tube as it is non-corrosive and only slightly compressible; compared to a highly compressible gas, this reduces both the work done when increasing its pressure, and danger if failure should occur. Typically a solid spacer is first inserted into the centre of the tube to be autofrettaged, reducing the volume of fluid that must be pumped into the tube.

The ends of the tube must be sealed to contain the pressurised oil; this is achieved either through use of floating bungs or caps that attach to tube, which in turn carries the applied axial force. The net axial force applied to the tube in the Closed-Ends case will alter the ratio of component stresses (compared to the Open-Ends case) found at peak pressure conditions, potentially altering the residual stresses developed. These two states, or end conditions, are classified as Open- and Closed-Ends, respectively, and the details of their modelling are found in Chapter 4. Hydraulic autofrettage, and the two end conditions described above, are depicted by Figure 2.1.

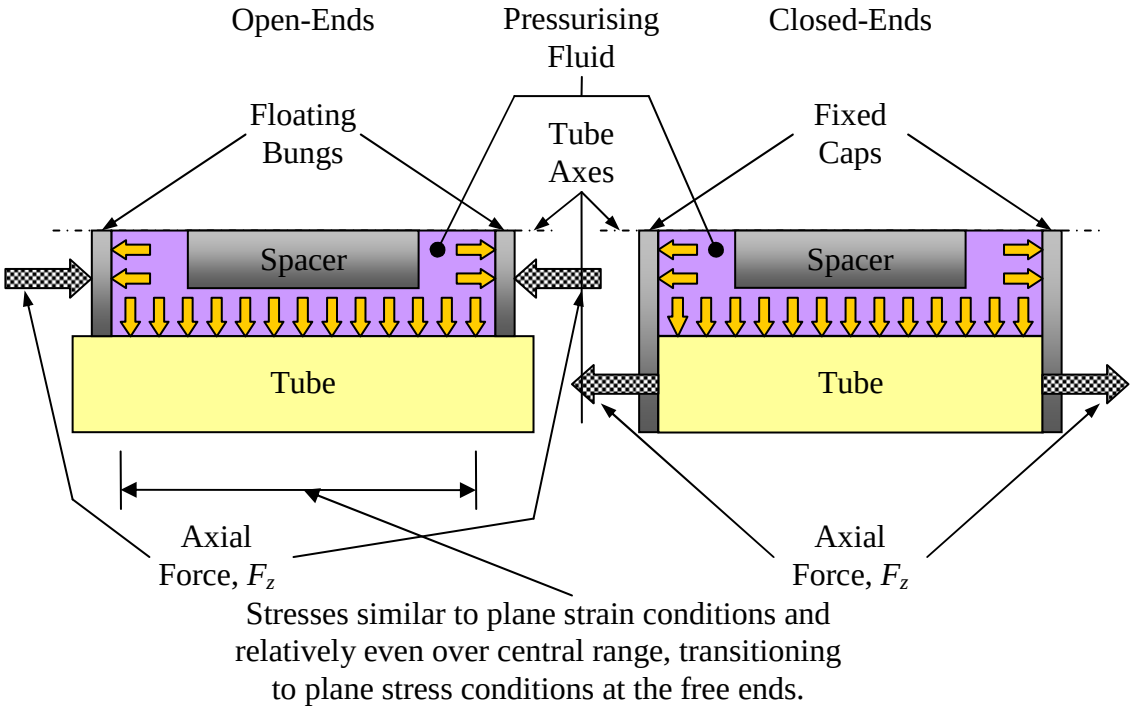

Figure 2.1: Hydraulic Autofrettage Diagram, for Open- and Closed-Ends

Hydraulic autofrettage tends to be time consuming, as the applied pressure must be very carefully controlled to ensure the desired deformation is achieved; for a given pressure, small variations of the material yield stress may cause considerable changes in the depth of overstrain. Also, sealing the ends of the tube is non-trivial because the tube expands as the applied pressure increases.

2.3.2. Swage Autofrettage

Swage autofrettage achieves the required plastic expansion of the inner portions of the subject tube via mechanical interference between an oversized mandrel and the inner surface of the tube; Davidson, Kendall and Rainer conducted an early scientific investigation [8]. The nature of the loading deviates considerably from that encountered during hydraulic autofrettage because of the small, travelling area of contact. Shear stresses are developed due to the localised loading and friction between the mandrel and tube surface. Residual stresses in relatively short tube section were modelled by O'Hara [9], and mandrel driving force was investigated by Iremonger and Kalsi [10]; aside from these studies, few investigations have been reported.

Mandrels typically consist of two conical sections joined by a short length of constant diameter; the forward conical section has a shallower slope than the rear section. The conical sections not only aid alignment of the mandrel, but also help control the initial deformation (forward cone) and subsequent unloading (rear cone) of the tube.

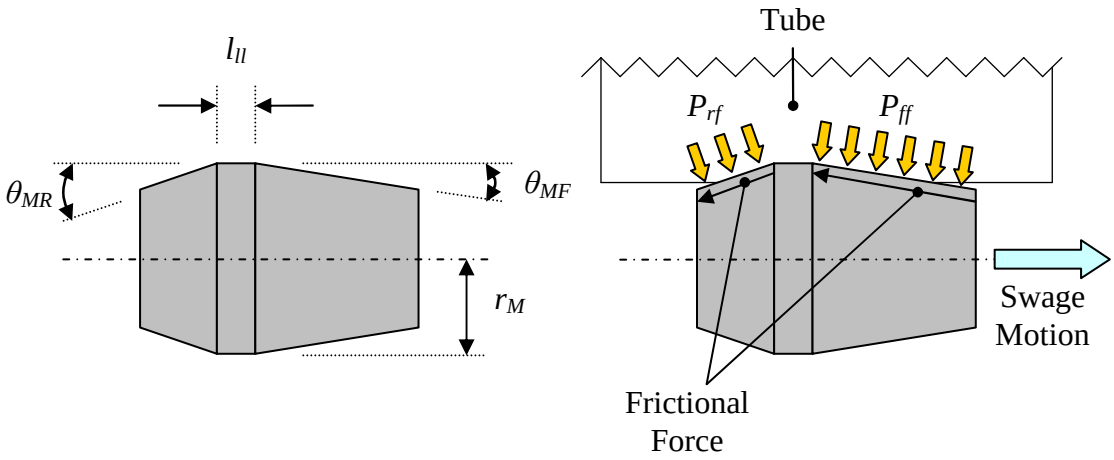

Figure 2.2: Mandrel and Swage Autofrettage Diagram

The contact between the mandrel and the tube is lubricated to reduce the sliding friction, for example with a stearate based lubricant impregnated into a porous phosphorus coating [9].

Despite the use of lubrication, a considerable axial force is applied by the mandrel to the tube, which then must be constrained. The choice of constraint location, either the mandrel entry or exit end, determines whether the deformed length of tube is held is tension (the former case) or the un-deformed length is compressed (the latter). As with the Open- and Closed-Ends cases of hydraulic autofrettage, these axial stresses may influence the precise nature of the residual stress pattern developed. The tube modelled by O'Hara [9] was constrained at its mandrel entry end, around its OD.

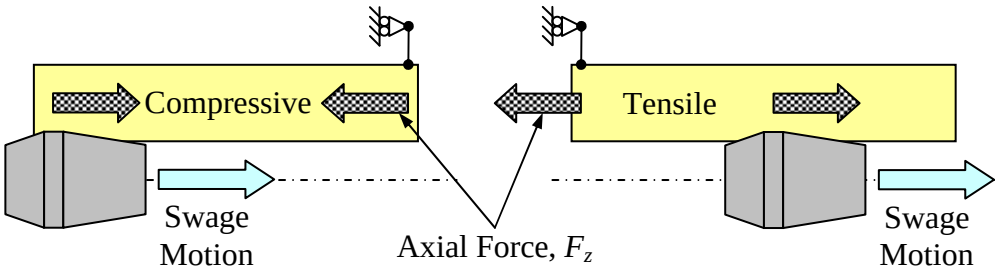

Figure 2.3: Tube Constraint during Swage Autofrettage

2.3.3. Post-Autofrettage Machining

Machining is conducted on the autofrettaged tube (hydraulic or swage) to ensure it possesses the correct final dimensions and that the applied pre-stressing is consistent along the required length. This generally involves the removal of the tube's ends which would have had developed a different initial deformation during autofrettage due to the interruption of axial stresses at the tube ends, and machining of the inner diameter to that desired. This also removes the most highly deformed material and alters the residual stress field.

2.4. MODERN MODELLING

This section introduces the concepts and theories underpinning the analytical modelling of pressurised tubes and describes some of the initial approximate solution methods considered. The assumptions, presented in sub-section 2.4.1, underlie all modelling techniques hence their early placement within this thesis.

2.4.1. Problem Formulation

The typical geometry of a thick-walled high pressure vessel is shown in Figure 2.4. Given the shape of the vessel it is natural to model it in cylindrical polar co-ordinates, r, θ, and z, corresponding, in the case of plane end conditions and hydraulic loading, to the principal stress-strain directions, radial, circumferential and axial.

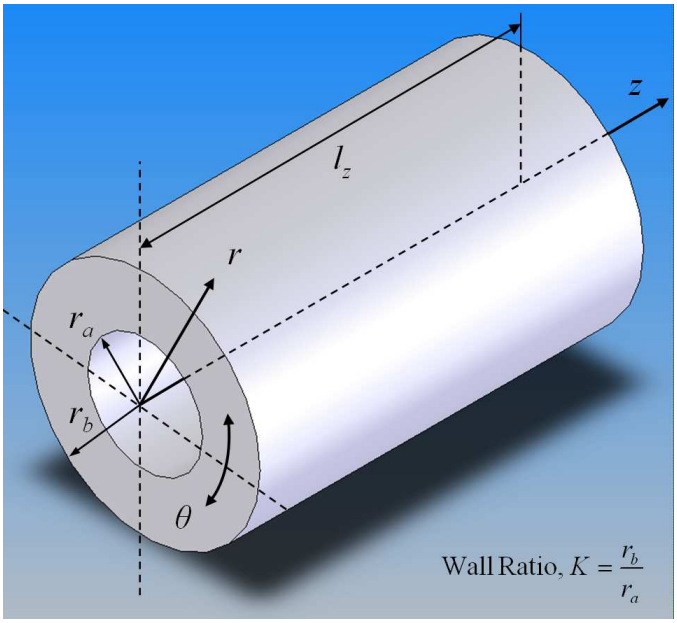

Figure 2.4: Tube Geometry and Dimensions

The dimensions shown on the diagram are:

r_a Inner radius
r_b Outer radius
l_z Tube length

The Wall Ratio, K, is the geometrical value that has the most influence on autofrettage and residual stress fields developed within the tube walls; it is defined as:

$$K = \frac{r_b}{r_a}$$

2.4.1.1. Element Diagram

Figure 2.5 displays the stresses acting upon a small element of a tube, modelled in cylindrical co-ordinates.

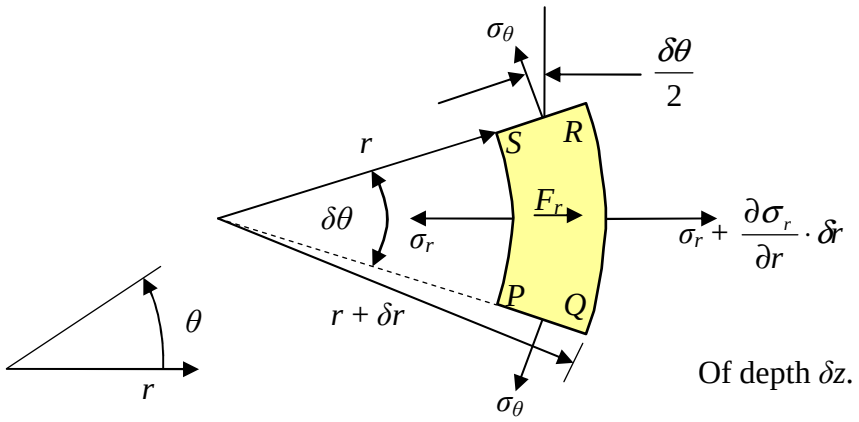

Figure 2.5: Element Diagram (in Plane Conditions)

The standard assumptions for such a system are:

1. Normal Stress in the z-direction (σ_z) is assumed to have no effect on the r,θ plane equilibrium.
2. Due to axial symmetry, there are no variations of in-plane stress with θ.
3. Axial Symmetry implies mirror symmetry i.e. $\tau_{r\theta} = \tau_{\theta r} = 0$.
4. Axial symmetry precludes a body force in the θ direction, but allows one in the radial direction – e.g. a centrifugal effect.
5. Radial body forces, represented as F_r in Figure 2.5, are ignored, as the tube is defined as non-rotational (no centrifugal effects), and gravitational forces are considered negligible.

While it is conceivable that non-axi-symmetric conditions may arise during autofrettage (for example localised deformation during hydraulic autofrettage or an un-aligned mandrel during swage autofrettage), such conditions are the exception to the mainstream and are sufficiently unpredictable to be ignored during the analyses presented in this thesis. It is likely that a tube autofrettaged under such conditions would be discarded.

2.4.1.2. Equilibrium Equation

Assessing the radial equilibrium of the element gives:

$$\left(\sigma_r + \frac{\partial\sigma_r}{\partial r}\cdot\delta r\right)(r+\delta r)\delta\theta\delta z - \sigma_r r\delta\theta\delta z - 2\sigma_\theta\delta r\delta z\sin\left(\frac{\delta\theta}{2}\right) + F_r\delta r\left(r+\frac{\delta r}{2}\right)\delta\theta\delta z = 0$$

Assuming $\delta\theta$ is small (i.e. $\sin(\delta\theta/2) \rightarrow \delta\theta/2$), taking $\delta r \rightarrow 0$, and dividing through by $r\delta r\delta\theta\delta z$ gives:

$$\frac{\partial \sigma_r}{\partial r} + \frac{\sigma_r - \sigma_\theta}{r} + F_r = 0$$

As explained above the body force, F_r, is assumed to be zero. As r is the only independent variable the partial derivative becomes total, giving the following equilibrium equation:

$$\frac{d\sigma_r}{dr} = \frac{\sigma_\theta - \sigma_r}{r} \tag{2.1}$$

2.4.1.3. Strain Relationship in cylindrical co-ordinates

Figure 2.6 displays the radial deflections (given in terms of u) observed during axi-symmetric expansion, at two radii – r and $r+dr$.

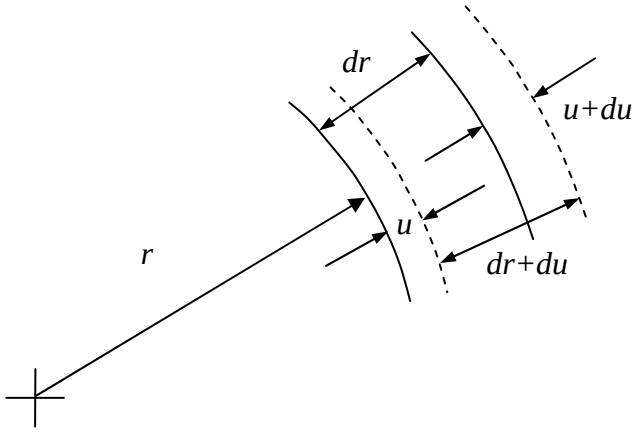

Figure 2.6: Deflection Diagram

Strains (deflection/original length) may then be defined as shown below.

Radial strain:

$$\varepsilon_r = \frac{du}{dr} \tag{2.2}$$

Hoop strain, given that circumference is $2\pi r$:

$$\varepsilon_\theta = \frac{2\pi(r+u) - 2\pi r}{2\pi r} = \frac{u}{r} \tag{2.3}$$

The following, standard, constitutive relations also apply:

$$E_t\varepsilon_r = \sigma_r - \nu_t(\sigma_\theta + \sigma_z) \tag{2.4}$$

$$E_t\varepsilon_\theta = \sigma_\theta - \nu_t(\sigma_r + \sigma_z) \tag{2.5}$$

$$E_t\varepsilon_z = \sigma_z - \nu_t(\sigma_r + \sigma_\theta) \tag{2.6}$$

2.4.2. Analytical Models

A selection of analytical models are presented below, starting with Lamé's elastic solution; while treatment of autofrettage inherently requires consideration of plasticity, Lamé's solution highlights the large tensile stresses found around the ID and allows the onset of yielding (sub-sub-section 2.4.2.2) to be predicted. Generally, it is only possible to create an analytical model (or closed form solution) of autofrettage using Hencky's total stress-strain relationship as the Prandtl-Reuss incremental stress-strain relations don't allow this.

This is followed by an assessment of some of the more prominent analytical elastic-plastic solutions of hydraulic autofrettage. While many other solutions have been developed, for brevity only those most relevant to this study are summarised here.

2.4.2.1. Lamé's Solution of a Thick-Walled Elastic Tube

The Lamé solution is the simplest treatment of stresses within a thick tube, and as such was the first aspect studied – Lamé elected to solve an elastic plane strain case using constitutive and compatibility relationships. The development of the solution, as given in the "Theory of Elasticity" [11] is repeated in Appendix A1.

Although in its pure form this solution is limited to elastic loading, it is utilised in later elastic-plastic models, as well as quasi-elastic models, making a thorough understanding of it important.

From Equation (11.4) it is noted that, at the inner diameter ($r = r_a$), p_i is the lower limit of hoop stress (σ_θ), reached when K tends to infinity. Thus in an elastically behaving vessel, even for impractically large values of K, the tensile hoop stresses at the inner diameter will always in practice exceed the internal pressure. Figure 2.7 shows the through wall hoop stresses for a range of elastic tubes.

In the context of high-pressure vessels, this directly limits the maximum allowable pressure and fatigue life. Accordingly some means of better distributing the hoop stresses, such as pre-stressing, must be adopted.

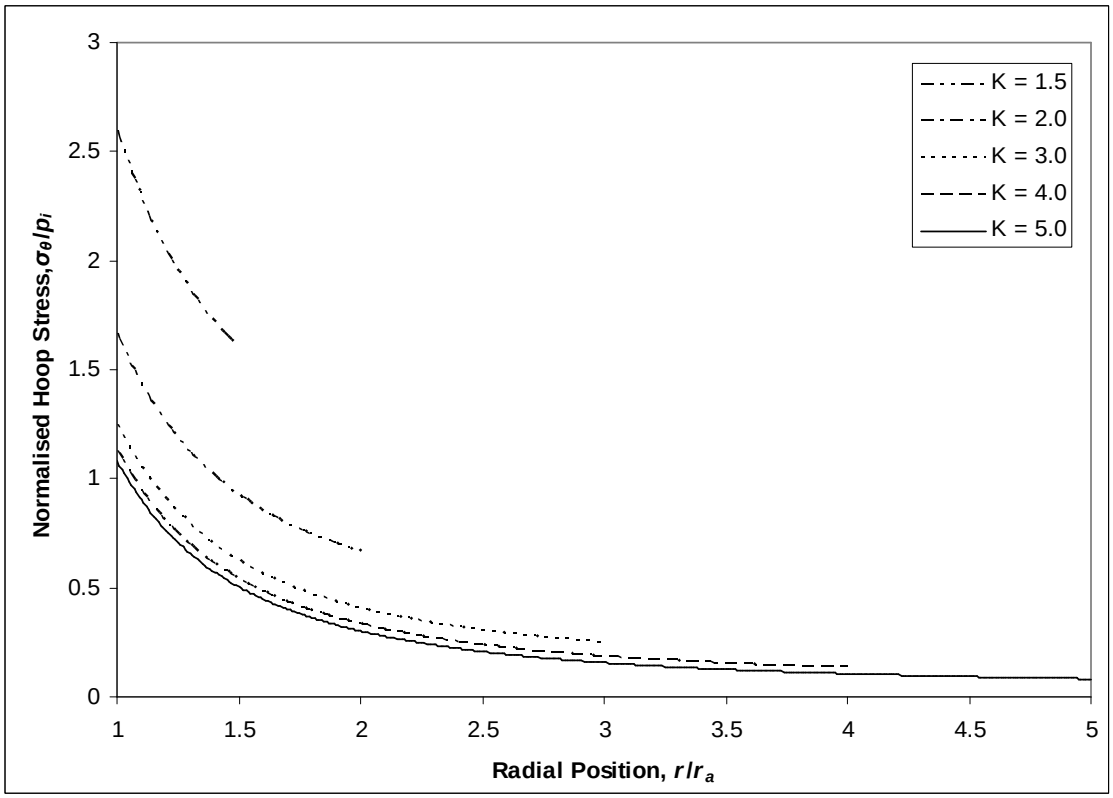

Figure 2.7: Hoop Stresses, in a series of Elastic tubes with a range of Wall Ratios

2.4.2.2. Elastic Limit and onset of Yield

Autofrettage induces compressive residual stresses at the inner diameter, by causing plastic deformation as a result of internal expansion; these residual stresses then reduce the size of tensile stresses encountered at the inner diameter. Lamé's model describes the elastic behaviour of a pressurised tube but predicts neither yielding nor subsequent plastic behaviour; therefore Lame's solution is not capable of simulating autofrettage.

Instead, a model that incorporates a yield criterion is required such that stresses within the tube wall are related to a stress value representative of the material's elastic limit. Yield criteria incorporate the following:

1. A means of translating a set of component/principal values into a single *equivalent* value,
2. An initial yield stress that is usually based on the yield stress either in simple tension (σ_{Y0}) or pure shear (k).

The two most common yield criteria, Tresca and von Mises (or Maxwell), are presented formally below, in terms of principal stresses [12].

Tresca Yield Criterion
Also called the Maximum shear stress criterion, as yielding is predicted to occur when the greatest of the three shear stresses reaches a critical value – the yield stress in pure shear, *k*.

$$|\sigma_1 - \sigma_2| \vee |\sigma_2 - \sigma_3| \vee |\sigma_3 - \sigma_1| = 2k \tag{2.7}$$

At the onset of yield in simple tension, $\sigma_1 = \sigma_{Y0}$, $\sigma_2 = \sigma_3 = 0$, hence $\sigma_{Y0} = 2k$.

von Mises Yield Criterion
Also called the Maximum shear strain energy criterion, as yielding is predicted to occur when the shear strain energy (or energy of distortion) per volume ($\tau^2/2G$) reaches a critical value. The energy of distortion, U_S, is given by:

$$U_S = \frac{1+\nu}{6E}\left[(\sigma_1 - \sigma_2)^2 + (\sigma_2 - \sigma_3)^2 + (\sigma_3 - \sigma_1)^2\right]$$

Substituting $E = 2G(1 + \nu)$, and equating the shear stress τ to the yield stress in pure shear, *k*, gives:

$$(\sigma_1 - \sigma_2)^2 + (\sigma_2 - \sigma_3)^2 + (\sigma_3 - \sigma_1)^2 = 6k^2 \tag{2.8}$$

At the onset of yield in simple tension, $\sigma_1 = \sigma_{Y0}$, $\sigma_2 = \sigma_3 = 0$, hence:

$$\begin{aligned} 2\sigma_{Y0}^2 &= 6k^2 \\ \sigma_{Y0} &= \sqrt{3}k \approx 1.7321k \end{aligned} \tag{2.9}$$

The above equations show the different relationships between the yield stresses in simple tension (σ_{Y0}) and pure shear (k) in the two yield criteria present.

This means that depending on the stress combination present (see Figures 2.8 and 2.9) the Tresca criterion will likely underestimate the strength of the material compared with the von Mises criterion.

To apply the above general formulae to this cylindrical case, $\sigma_\theta > \sigma_z > \sigma_r$ is assumed, hence:

Tresca's Yield Criterion gives:

$$\sigma_\theta - \sigma_r = \sigma_{Y0} = 2k \tag{2.10}$$

von Mises' Yield Criterion gives:

$$\frac{(\sigma_\theta - \sigma_r)^2}{2} + \frac{2}{3}\cdot\left(\sigma_z - \frac{\sigma_r + \sigma_\theta}{2}\right)^2 = \frac{2\sigma_{Y0}^2}{3} = 2k^2 \tag{2.11}$$

Tresca's Yield criterion was chosen for initial analyses (detailed in Chapter 3) due to the correlation between its stress equivalence (LHS of Equation (2.10)) and the numerator on the RHS of the equilibrium Equation (2.1). This allows separation of variables and subsequent integration of the equilibrium equation, leading to an explicit solution. The von Mises criterion was reserved for later use, as the lower accuracy of Tresca was not thought to be excessive during the early stages of this investigation. Some degree of error was expected, as (discussed above) the Tresca yield criterion tends to gives a more conservative estimation of material yield stress than the von Mises criterion does.

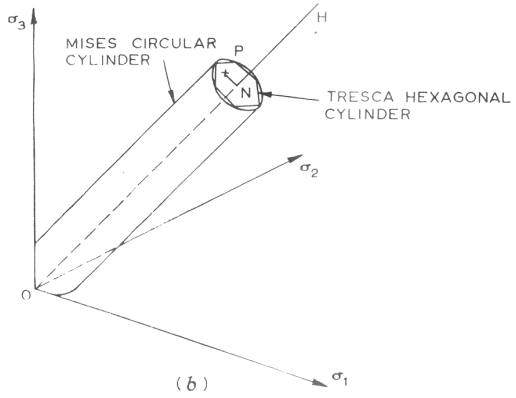

Figure 2.8: Yield Prisms

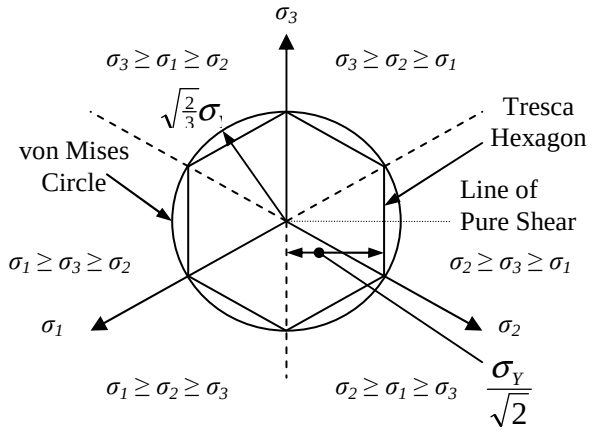

Figure 2.9: π-Plane Projection

Source: "Engineering Plasticity", Johnson, W and Mellor, P B, van Nostrand Reinhold, 1973

2.4.2.3. Hill's Model

Hill et al. [13] formulated a model of a non-strain-hardening hydraulically autofrettaged tube in plane strain that uses the Prandtl-Reuss stress-strain relationship. Importantly, it includes the effects of elastic strain components within the plastic region (i.e. it is considered compressible); many solutions neglect them. The Tresca yield criterion is used, allowing axial stress to be considered independently from radial and hoop stresses as it is the intermediate stress. However, it is shown that the solution is a close approximation of one based on the von Mises criterion (a 3% error in flow stress, that only occurs during the initial increment of plasticity for each element, is quoted for the given example).

The main finding is that an error of greater than 60% occurs (for the presented case) in axial stress if elastic strains in the plastic region are ignored.

2.4.2.4. Avitzur's Model

Avitzur developed a model [14,15] of an elastic-plastic tube undergoing hydraulic autofrettage, using the von Mises yield criterion for both plane strain and stress conditions. It models a smooth transition at r_p between an incompressible plastic portion and compressible elastic portion, but assumes axial stresses in the plastic zone, when pressurised, to be calculated using Hooke's law due to the elastic strains present (as plastic strains are of the same order of magnitude as elastic strains).

A substantial limitation is that the tube material is considered to be elastic, perfectly plastic; this does not exert a great influence over conditions at peak autofrettage pressure, but will significantly alter residual stresses. Arguably, the lack of accurate material representation will have a greater impact on residual stresses than the choice of the von Mises rather than Tresca yield criterion, given the early onset of non-linearity displayed by the materials of interest.

2.4.2.5. Huang's Model

Huang [16] developed a von Mises solution of an elastic-plastic tube, which is made possible by the following simplifications –

1. Incompressibility: $\varepsilon_r + \varepsilon_\theta + \varepsilon_z = 0$
2. Plane Strain: $\varepsilon_z = 0$

Although more restrictive than Avitzur's model, due to the incompressibility criterion, Huang's model very easily yields a solution making it of more practical use for comparison with other methods – specifically numerical methods. This makes it a considerable advancement in the field of analytical models of hydraulic autofrettage.

The incompressibility criterion means that the plane strain state is similar to the closed-ended case (which applies a tensile axial load of magnitude $p_i * r_a^2 * \pi$), due to the greater tensile axial stresses developed in the elastic region.

Crucially, the model includes an impressive degree of flexibility of modelling material stress-strain behaviour, allowing bi-linear or non-linear response to be specified independently for both loading and unloading procedures. Non-linear behaviour is restricted to power-law relationships but this allows reasonable flexibility, dependent on the desired stress-strain profile. With respect to the materials used in high pressure vessels, whose behaviour is dependent on prior plastic strain, the main limitation is that only one unloading profile may be used. The use of Huang's model is described in Chapter 3.

2.4.3. Numerical Models

When a particular set of equations cannot be solved analytically, it is often possible to numerically solve (usually to high and predictable accuracy) instead. This may be used when a differentiation or integration procedure cannot be achieved through normal means, or if variables cannot be separated sufficiently to allow direct solution. A selection of models that use these methods, to overcome some inherent restrictions of analytical solution of hydraulic autofrettage, are described below.

2.4.3.1. Chu's Method

Chu [17] made a good review of existing models, and developed a finite difference model of a hydraulically autofrettaged tube under general plane strain conditions. The autofrettaged tube may consist of a strain hardening material, be subject to end loads in addition to internal and external pressures, and behave according to von Mises yield criterion and Prandtl-Reuss incremental stress-strain laws. These combine to make an effective model of hydraulic autofrettage, which showed excellent agreement when compared with the models of Hill [13] and Hodge [18] for the autofrettage of an elastic, perfectly plastic tube.

Selection of a finite difference approach was pragmatic at the time the model was developed; computing resources were far scarcer than today, and commercial FEA packages were in their early stages. Chu notes that in the finite element method, stresses and strains must be determined via numerical differentiation, and that a fine mesh is required for accurate results. He then states, in reference to his method, "incremental stresses and strains at each nodal point are directly used as variables and, hence, numerical differentiation in the evaluation of stresses and strains is not required."

Given the development of computational resources and FEA packages to run on them, the use of the finite element method is now a much more viable, accessible and accepted means of creating an autofrettage model. Such packages automatically generate and solve the required FE equations, in addition to providing tools for the creation of model geometry and other features.

2.4.3.2. Jahed and Dubey's Method

Jahed and Dubey [19] developed a method for solving non-linear behaviour using a quasi-elastic analysis, which treats elastic properties as field variables such that the stress-strain state may be calculated for each location within the considered region. It builds on a method [20] for the solution of elastic-plastic conditions, using Hencky-Ilyushin total deformation theory, which transforms the constitutive relations into a form analogous to elastic relations. Effective elastic properties are iteratively applied, such that the desired stress-strain profile is followed, until a converged solution is

reached. Their method (expanded upon in Appendix A3, then used within FEA in Chapter 5) is then applied to a thick-walled tube undergoing hydraulic autofrettage, which is broken down into a series of strips to allow properties to be varied throughout the tube wall.

The authors investigate the effect of a variable Bauschinger Effect Factor (β), using empirical results from Milligan, Koo and Davidson [21], on the depth of reyielding following pressure removal, and residual hoop and axial stresses. Based on the material profile used, they conclude that the variable β only has significant impact on the three values when the degree of overstrain is relatively small. This is logical, as β is effectively constant for initial plastic strains of more than 2%, and the greater the degree of overstrain the greater the depth of tube that will have exceeded this threshold. However, they did not exploit the full potential of the method as the material did not exhibit non-linearity.

2.4.3.3. Hencky Programme

The Hencky Programme allows accurate simulation of hydraulic autofrettage for a wide range of end conditions (Plane strain and stress, open- and closed-ended) and materials, using von Mises yield criterion. It was developed by Parker [22] from a basic EMPRAP formulation by Jahed and Dubey [19] (described in Appendix A3) and allows radial variation of unloading properties (which are crucial when determining residual stresses) based on prior plastic strain experienced. Notably, the Hencky Programme can simulate the often significant nonlinearity exhibited by various candidate gun steels (e.g. A723, HY180, PH 13-8Mo) during unloading following initial plastic deformation.

It achieves this by considering a thick-walled tube to consist of a series of thinner, concentric, cylindrical shells. Each shell is obliged (via the formulation) to satisfy requirements of equilibrium and compatibility at its inner and outer interfaces where it interacts with its neighbours. The behaviour of the shells is treated elastically such that it may be modelled using Lamé's tube equations [23]; these provide the hoop and radial stresses in a cylinder, when subjected to internal and external pressure.

By using a large number (of the order of 100) of cylindrical shells, radial variation of material behaviour due to plastic strain can be easily modelled. Jahed and Dubey's method is employed to tailor the elastic properties (E and ν) of each shell, such that its stress-strain profile matches the desired material behaviour. This allows the hydraulic autofrettage (and subsequent unloading) of tubes in a variety of end conditions, consisting of virtually any material, to be accurately simulated. The range of end conditions is achieved by applying suitable constraints – for example, $\sigma_z = 0$ for plane stress, $\varepsilon_z = 0$ for plane strain.

Numerical modelling of the pressurisation phase of autofrettage begins with an initial quasi-elastic, or hypothetical, stress distribution (normally the elastic solution for the original homogeneous, isotropic material and selected bore pressure). From this solution initial yielding is assessed, and effective elastic properties (E_{eff} and ν_{eff}) are

calculated. The effective elastic properties are refined through a series of iterations. An iterative procedure is employed to refine E_{eff} for each strip, as illustrated in Figure 11.3, which represents three iterations, leading to E^{3}_{eff}. Convergence is monotonic, reasonably rapid, and easily assessed.

Loading and unloading phases are solved as separate phases, each using essentially the same procedure. However, whereas during loading there is a single profile associated with all radii, during unloading there is potentially a different profile associated with each radius, uniquely defined by the prior maximum plastic strain experienced at that radius. In terms of Figure 5.1, the 2-3- section of the plot is rotated through 180° and translated so that point 2 (now at the lower left of the line segment) lies at the origin of the graph. This is illustrated, for a given radius, in Figure 5.4.

The unloading stresses are calculated by the autofrettage (to the same pressure as was originally used) of a tube whose material loading profiles have been modified to be that of the unloading profiles. Finally, the total residual stresses are obtained by subtracting the unloading stresses from the loading stresses.

2.4.3.4. Single Effective Material (SEMAT)

The complexity of accurate material modelling (including the Bauschinger effect) that reflects radial variation within autofrettage models has acted as a major obstacle in the development of accurate models of hydraulic autofrettage. Various co-authors of Parker et al. [24] developed a method of representing a series of prior strain dependent unloading profiles with a single effective material (SEMAT) stress-strain profile. This is accomplished by selecting a material profile based on the final stress-strain loci that are observed within a hydraulically autofrettaged tube. When the material profile is applied to a hydraulic autofrettage simulation, this ensures that the final residual stress state is accurate, although the path taken is not; however, this is of little importance as partially unloaded stress states are rarely investigated.

It is demonstrated [24] that numerical solutions may be obtained using a single 'fictitious' material in this manner; whist this requires a very small number of iterations for accurate convergence, it dramatically reduces the material-modelling challenges. Furthermore, SEMAT may be implemented into an analytical procedure thereby permitting highly accurate modelling of a real material whose unloading behaviour varies with radius. Comparisons indicate that this is a robust, accurate procedure.

SEMAT was not utilised within the work presented in this thesis, partly due to being developed following the work in Chapter 6, and partly due to the focus on swage autofrettage. Unlike hydraulic autofrettage, a material's stress-strain behaviour throughout unloading is important in the development of shear stresses during swage autofrettage, making it crucial that any material used follow the correct stress-strain profile during the entire unloading process.

2.5. NUMERICAL METHODS

Whilst a range of analytical models of hydraulic autofrettage exist, all include simplifying assumptions which limit their applicability, especially in terms of material modelling. Additionally, no analytical models of swage autofrettage exist. As such, it was recognised that numerical modelling would be required to achieve the goals of this study.

Given the increase in computational capabilities of PCs in recent years, numerical methods are very much more practical than was previously the case; in particular, commercial Finite Element packages have become more widespread.

2.5.1. Numerical Modelling Procedure

Regardless of the method employed, the process generally involves the same three stages: pre-processing, solution and post-processing. These are described below, in the context of the mechanical stress analysis that will be utilised in this study.

Pre-Processing describes the process of assessing the system that is to be analysed, and formulating its properties within the selected modelling method such that solution may commence. This generally comprises the following stages:

- Rendering the model geometry into discrete portions, suitable for the selected method.
- Application of special properties, such as plane strain behaviour and appropriate symmetries.
- Formulation of governing equations (for example, element matrices in FEM).
- Specification of material behaviour.
- Application of boundary conditions and loads.

The Solution procedure encompasses the computation of results, as well as the setting of method-specific values such as the number of time steps to be used or accuracy tolerances.

Post-Processing covers the extraction of poignant data from the complete set computed during solution, as well as any subsequent calculations performed on them and arrangement for presentation.

2.5.2. Finite Difference Method

Finite differences are described as the discrete analogue of derivatives, and are often used to evaluate boundary value problems when the governing differential equations are known but the function is not. Pressurised thick-walled tubes may be addressed

using this method; typically the boundary values of radial stress (at r_a and r_b) will be known, and the equilibrium equation is a differential expression that relates radial and hoop stresses.

Essentially, finite difference terms are used to replace derivatives in differential equations; progressive numerical solution is then possible. While potentially of use, it was not expected that a reconfigurable model of swage autofrettage could practicably be formulated using finite differences.

2.5.3. Boundary Element Method

The boundary element method (BEM) again requires the considered region to be decomposed into discrete portions, but differs in that the boundary, not the entire region, is considered; this reduces the dimensionality of the problem by one order. Compared to the FEM, the BEM is a relatively recent development; it is based on the solution of partial differential equations, formulated as integral equations, via numerical means. Boundary conditions are used to fit boundary values into the integral equation selected for the problem; once this is achieved, the integral equation may be evaluated within the considered region to obtain the required solution data.

The BEM is in some cases less computationally demanding than, for example, the finite element method, particularly when the considered region has a small surface area to volume ratio. However, in many cases, the opposite is true as the computational cost (in terms of both memory requirements and processing) of BEM tends to increase with the square of the model size, whereas a more linear relationship is observed for finite element models.

An additional restriction on the applicability of the BEM is that for any problem that is considered, it must be possible to calculate a Green's function; this generally requires that the region consist of a linear homogenous medium. Non-linear properties may be modelled, but this generally requires the use of volume integrals, which in turn need to be decomposed into sub-sections and addressed numerically. This negates one of the main advantages of BEM over FEM, especially as a core component of this study will be material non-linearity.

Given the linear homogenous restriction, relative maturity of FEM tools and complexities of translating the transient displacement boundary condition imposed by the mandrel during swage autofrettage, the BEM was not used in this study.

2.5.4. Finite Element Method

The finite element method (FEM) concerns itself primarily with geometrical rationalisation of the considered region, by which means the problem is reduced to one

which may be solved numerically. Such rationalisation is achieved through the decomposition of an arbitrary region into a finite number of geometrically simple sub-regions, or elements, collectively termed a mesh. The field properties within elements may then be evaluated individually and assembled to obtain them for the whole region.

The decomposition of the considered region into elements reduces an otherwise intractable problem into a finite number of unknowns, which are then solved by expressing the unknowns (field variables) within each element in terms of the approximation (or interpolation) function. Such functions are defined in terms of nodal values; nodes are shared by adjacent elements, "stitching" the mesh together by ensuring continuity of field variables between elements.

Forces arising from the physical interaction of bodies modelled in FE may be calculated using *contact analysis*, which made the FEM a likely candidate for use in this research. Combined with the relative maturity of commercial FE packages (that would allow model geometry to be rapidly formulated), is the reason the FEM was selected for use.

2.6. SUMMARY

Gun barrels have been made for many hundreds of years, with growing understanding of the processes that influence their performance and lifetime. "Hooping," and "self-hooping" methods were developed to mitigate the high tensile stresses found at their bores when pressurised, and these have become the subject of study since the early twentieth century. Many models of hydraulic autofrettage have been developed (both analytical and numerical), each based on different assumptions of yield criterion, flow behaviour and, critically, material stress-strain profile – particularly when unloading from peak pressure, when the early onset of non-linearity occurs, described as the Bauschinger effect. However some models, particularly numerical, do achieve accurate behaviour in some or all of these respects.

Swage autofrettage has not been addressed to the same degree; the travelling, localised load, and associated shear stresses and non-plane behaviour put it beyond the reach of analytical solution, and make it complex to address numerically, especially if accurate material response is included.

However, in recent years the abilities of computers have developed rapidly, as have commercial FE packages. This means that swage autofrettage, with all its associated complexities, may now be more practically modelled.

2.7. PROGRAMME OF WORK

Initial work will focus on investigating material behaviour relevant to autofrettage, and the selection of existing hydraulic autofrettage models suitable for comparison with and validation of FE models of the same.

Models of hydraulic autofrettage will then be developed within FE, featuring simplistic material stress-strain profiles, and validated against the previously selected existing models.

Accurate material stress-strain behaviour will then be implemented within FE, and subsequently validated against existing models to confirm its behaviour.

A model of swage autofrettage will be developed, to emulate the physical process as closely as possible. This will be compared against the only known solution in open literature.

Finally, accurate material behaviour will be combined with the swage model, to allow accurate residual stresses to be calculated.

3. MATERIAL AND ANALYTICAL MODELS

3.1. INTRODUCTION

This chapter utilises the models introduced in Chapter 2, and assesses their suitability for use in validation of numerical models of autofrettage developed at later stages throughout this course of research.

The Tresca-based elastic-plastic model of hydraulic autofrettage is initially investigated and implemented. This is then extended to incorporate different responses to plastic strain, and subsequently a swage-like scenario in which the applied pressure is calculated from interference with a solid disc (mandrel).

Finally, an overview of a range of more suitable pre-existing hydraulic autofrettage models is presented, ready for use in subsequent verification of future models.

3.2. MATERIAL MODELS

When modelling a system, in addition to accurate representation of its geometry and applied loads, the stress-strain behaviour of its constituent material must be simulated. In the context of conventional thick-walled high-pressure vessels in general, and this study in particular, engineering metals are of interest – specifically, high strength, high alloy steels. The stress-strain behaviour of such materials is hence fundamental to this study, both pre- and post-yield.

3.2.1. Plasticity following Initial Yield

Engineering metals exhibit a linear stress-strain response within the elastic regime, up to their initial yield stress, σ_{Y0}; their post-yield stress-strain behaviour is described by one of the following models: bi-linear, multi-linear and non-linear. Figure 3.1 plots these behaviours.

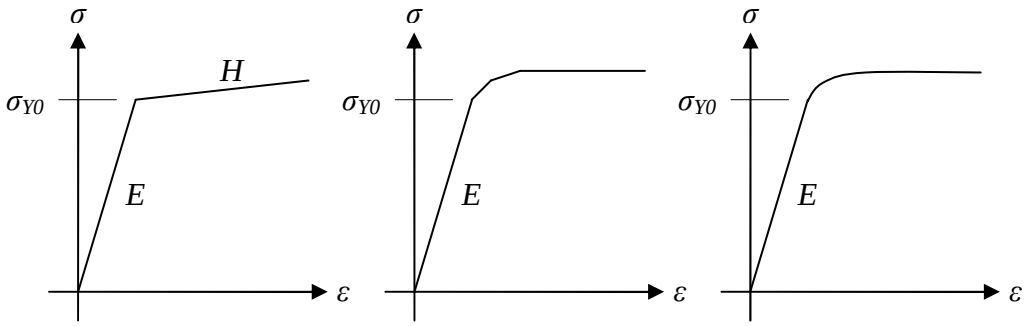

Figure 3.1: Post-Yield Stress-Strain Response

While they often display a small amount of non-linearity during initial yield, engineering metals can often be satisfactorily approximated by a bi-linear representation. A special case of the bi-linear model is that when no strain hardening occurs (the plastic modulus, *H*, equals zero) – the *elastic, perfectly plastic* (Figure 2.4) case. This is the simplest form of modelling plasticity, as the yield stress always equals the initial value (this fact is utilised by the derivation given in section 3.3).

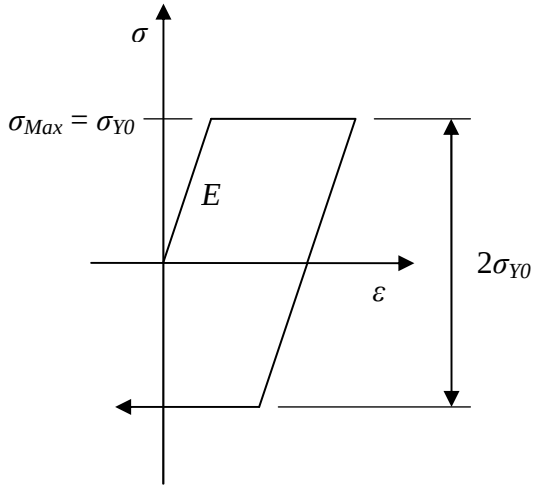

Figure 3.2: Stress-Strain Diagram of an Elastic, Perfectly-Plastic Material

3.2.2. Strain Hardening

Once the stress-strain behaviour in initial yield has been modelled, the response of the yield stress to plastic strain, when the direction of load is reversed, must be considered. One model assumes that the stress range, between peak tensile stress and the compressive yield stress, is twice the initial yield stress (kinematic hardening); the other that the stress range is twice the peak tensile stress (isotropic hardening). These are illustrated in Figure 3.3.

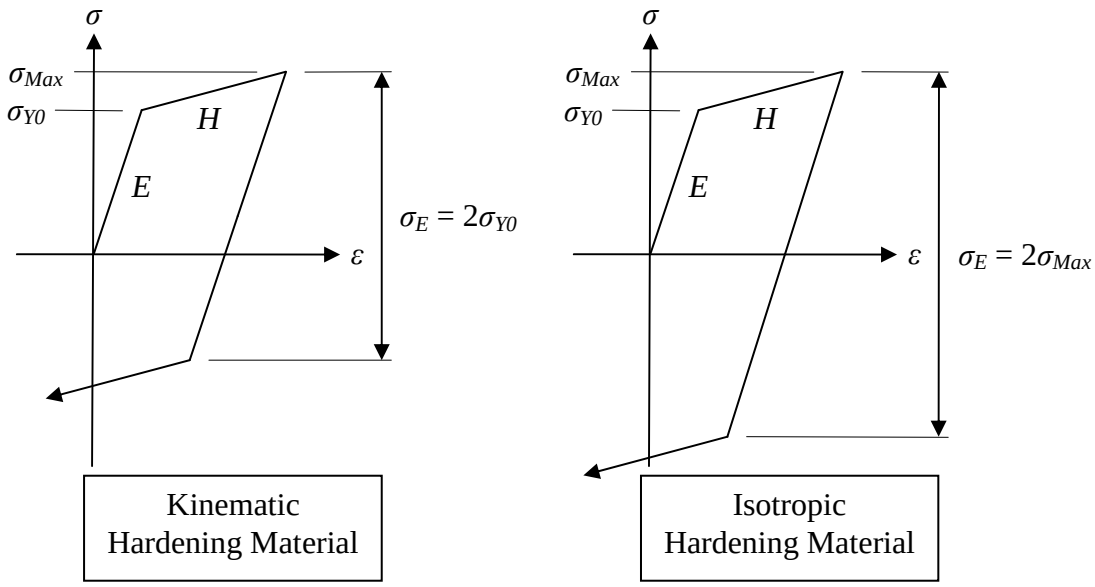

Figure 3.3: Material Hardening Models

The above diagrams compare uni-axial stresses and strains; the same behaviours, in multi-axial stress conditions, can be plotted on the π-plane (see Figure 2.9). When this is done, loci of equal equivalent stress can be plotted on the π-plane; if von Mises equivalence is used the locus forms a circle, and if Tresca equivalence is used the locus forms a hexagon. In both cases, the yield loci are centred on the zero deviatoric stress axis. In the von Mises case, the yield stress of the material is represented by a circle of radius σ_{Y0} (or the Tresca case, a hexagon circumscribed by a circle of radius σ_{Y0}). Subsequent descriptions will be based on the von Mises case, but will be applicable to the Tresca case also.

Once the initial yield stress of the material has been exceeded, the yield circle behaves differently depending on whether Kinematic or Isotropic hardening occurs; during Kinematic hardening the yield circle moves, and during Isotropic hardening the yield circle enlarges. The translation of the yield circle during Kinematic hardening causes yielding to occur at a lower stress on the opposite side of the zero deviatoric stress axis. However, given the relatively small plastic moduli of metals (often several orders of magnitude less than the elastic modulus), any significant movement/enlargement of the yield circle would generally require large plastic strains.

However, while the initial yield behaviour of steels may well be suitably described by the above models, neither describes the unloading behaviour (from maximum stress) well. Typically, when unloading from initial deformation, such materials experience an early onset of non-linearity (significantly earlier that that modelled even during Kinematic hardening), termed the *Bauschinger effect*. This is further explained in the following sub-section.

3.2.3. Bauschinger Effect

The Bauschinger effect [25] describes the early halt of linear elastic behaviour observed in most polycrystalline metals during load reversal when unloading from prior plastic strain, compared with that which would be predicted by the hardening models described above. The reduction of yield stress observed when the loading direction is reversed is generally explained in terms of dislocations within grains. Strain hardening occurs when the movement of dislocations is impeded, for example by grain boundaries. One explanation of the Bauschinger effect is that residual elastic stresses present in some grains (caused by their uneven plastic deformation) following plastic deformation allow dislocations to move more easily in the reverse direction. Another explanation is that dislocations of the opposite sign to those generated during initial deformation are created by the same sources. When unloading, the dislocations of opposite signs annihilate each other, reducing dislocation density and hence the strength of the material.

Again dependent on plastic strain, the location of the early non-linearity depends on the peak plastic strain encountered (typically in tension at peak pressure in the case of hydraulic autofrettage). It is quantified by the *Bauschinger Effect Factor, β*, (a function of prior plastic strain – see Figure 3.5) such that the reverse yield stress is defined by $-\beta\sigma_{Y0}$, as demonstrated in Figure 3.4:

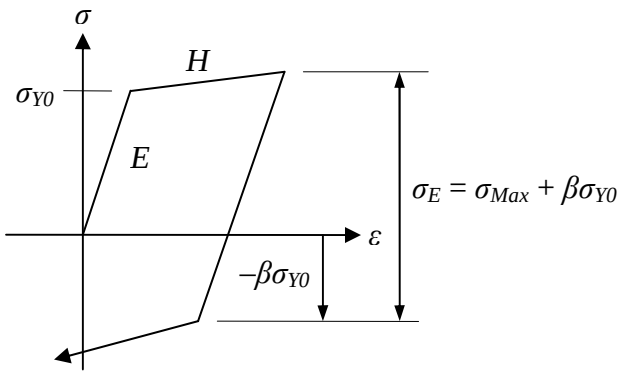

Figure 3.4: Material exhibiting the Bauschinger Effect and Strain Hardening

This early onset of non-linearity is significant with respect to the efficacy of the autofrettage procedure, given that compressive stresses are developed following tensile yielding, i.e. load reversal. This limits the size of compressive stresses that may be

applied to a thick-walled cylinder before reverse yielding occurs; clearly any accurate simulation of autofrettage must include it.

While the slight reduction in reverse yield stress present in Kinematic hardening may be described using β, Kinematic hardening is generally not an accurate model of material behaviour given that the plastic modulus, H, is often small hence $\beta \approx 1$. Figure 3.5 compares the elastic stress range, σ_E, between peak and reverse yield stresses, as the initial plastic deformation is varied, to illustrate this difference for the case of a gun steel named A723-1130 (see sub-section 5.1.1 for details of the material-fit).

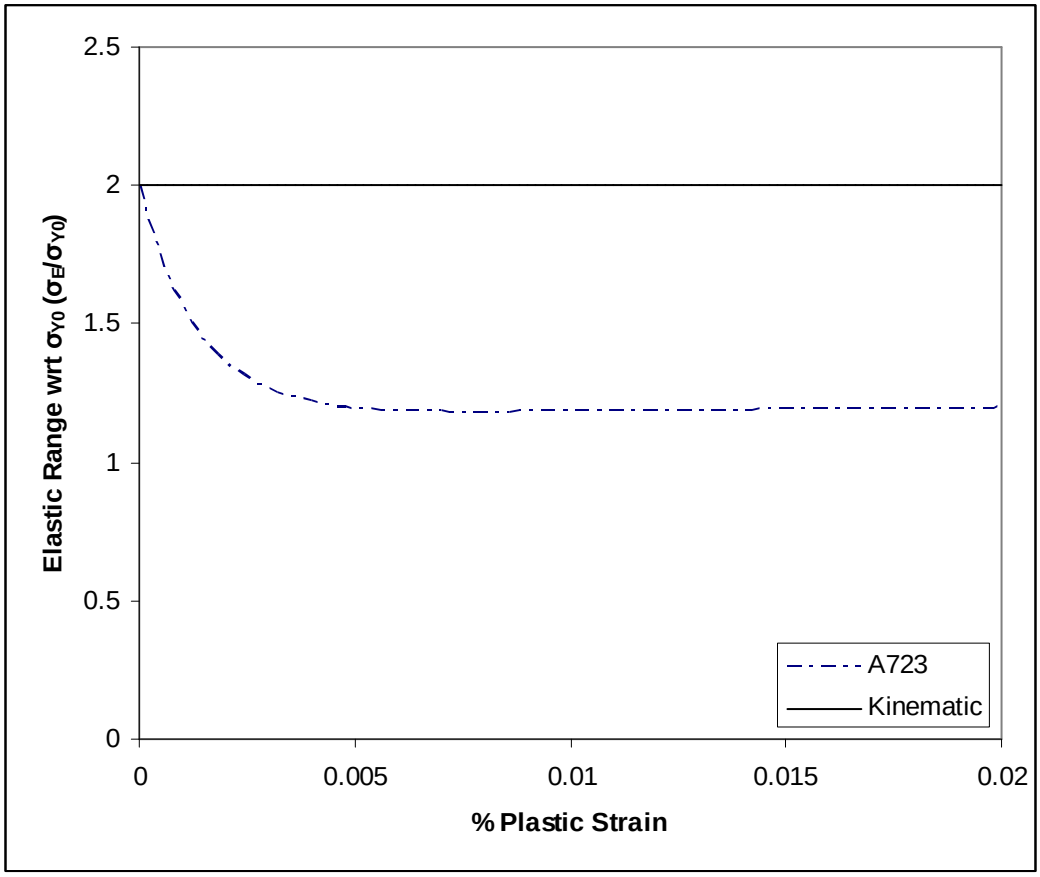

Figure 3.5: Comparison of Elastic Stress Range, σ_E, between Kinematic Hardening model and A723-1130

3.3. INITIAL AUTOFRETTAGE ANALYSIS

A model of a tube undergoing hydraulic autofrettage, in plane strain conditions, was created using Tresca's yield criterion to predict behaviour in the yield zone; elastic stresses in the region beyond this are calculated using Lamé's relationships. It is hence referred to as the *Tresca Elastic-Plastic solution*. While this model was developed [26] and expanded upon (e.g. by Bland [27]) many years prior to this study, it builds upon the Lamé solution to incorporate plasticity into an elegant analytical solution. This provides a convenient means of introducing many terms and concepts, so is included here. In addition it was used as the basis of an initial swage model, described in section 3.5. The development of the Tresca Elastic-Plastic solution is given in Appendix A2, and the resultant equations are summarised below.

3.3.1. Overview

Whether autofrettage is achieved hydraulically or through swaging, the process involves expansion and plastic deformation of the tube, followed by relaxation and the development of compressive stresses around the ID.

Consider a tube loaded by an internal pressure, p_i, which increases from zero to the final autofrettage pressure, p_{AF}. Once the pressure is high enough (p_e) tensile yielding initiates at the ID ($r = r_a$), propagating outwards as the pressure increases; Lamé's solution clearly shows that the Tresca equivalent stress is highest at the ID. When the applied pressure reaches p_{AF}, the maximum radius of plasticity is termed the *Primary Yield Radius*, r_p ($r_a \leq r_p \leq r_b$).

Upon removal of the autofrettage pressure compressive hoop stresses are developed within the expanded material found within the primary yield region ($r_a \leq r \leq r_p$), partnered by tensile hoop stresses in the elastic region ($r_p \leq r \leq r_b$). As in the pressure application phase, these compressive stresses are greatest around the ID. If the change in stress state (i.e. equivalent stress) between peak pressure and residual conditions exceeds the elastic stress range (σ_E), compressive yielding initiates at the ID and propagates outwards – the limit of this reyielding is termed the *Secondary Yield Radius*, r_s. As will be demonstrated, unless the tube material $r_a \leq r \leq r_p$ loses all strength ($\sigma_Y = 0$) following the plastic strain experienced during autofrettage, $r_s < r_p$. Figure 3.6 illustrates these radii.

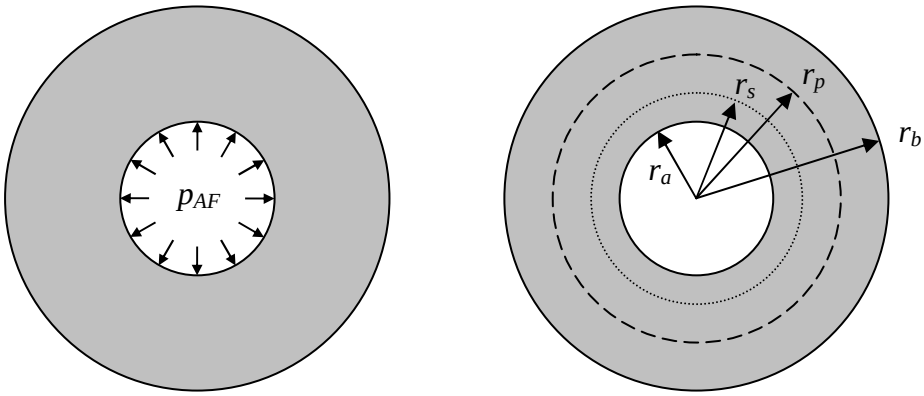

Figure 3.6: Yield Diagram

As noted towards the end of sub-section 2.4.2.2, the first elastic-plastic solution investigated is that based on Tresca's yield criterion, which allows for explicit solution of the stress field (within a hydraulically autofrettaged tube that remains plane throughout). An elastic, perfectly plastic material (i.e. $\sigma_Y^{comp} = \sigma_Y^{tension}$) is used which is the most simple stress-strain response that includes plasticity (see Figure 3.2).

3.3.2. Autofrettage Stresses

Plastic Region

$$\sigma_r = -\frac{\sigma_{Y0}}{2}\left[1-\frac{r_p^2}{r_b^2}+\ln\left(\frac{r_p^2}{r^2}\right)\right]$$

$$\sigma_\theta = \frac{\sigma_{Y0}}{2}\left[1+\frac{r_p^2}{r_b^2}-\ln\left(\frac{r_p^2}{r^2}\right)\right] \qquad r_a \le r \le r_p \qquad (3.1)$$

$$\sigma_z = E_t\varepsilon_z + \nu_t\sigma_{Y0}\left[\frac{r_p^2}{r_b^2}-\ln\left(\frac{r_p^2}{r^2}\right)\right]$$

Elastic Region

$$\sigma_r = -\frac{\sigma_{Y0}r_p^2}{2r_b^2}\left(\frac{r_b^2}{r^2}-1\right)$$

$$\sigma_\theta = \frac{\sigma_{Y0}r_p^2}{2r_b^2}\left(\frac{r_b^2}{r^2}+1\right) \qquad r_p \le r \le r_b \qquad (3.2)$$

$$\sigma_z = E_t\varepsilon_z + \nu_t\sigma_{Y0}\left(\frac{r_p^2}{r_b^2}\right)$$

The primary yield radius, r_p, cannot be determined through rearrangement or other direct means; instead, it must be found through a short iteration using the boundary

condition $\sigma_r = p_{AF}$ at the ID ($r = r_a$) applied to the radial stress expression from Equation (11.6). This was achieved (using Matlab, but any other suitable numerical method would quickly achieve a converged answer) by incrementing r from an initial value of r_a.

A special case of the radial stress from Equation (11.6) can be formed to give an expression for the minimum pressure required for yielding (or limiting elastic pressure) at the inner face, p_e. Setting r and r_p to r_a:

$$p_e = \frac{\sigma_{Y0}}{2}\left(1-\frac{r_a^2}{r_b^2}\right) = \frac{\sigma_{Y0}}{2}\left(1-\frac{1}{K^2}\right) \tag{3.3}$$

If the autofrettage load is hydraulic, a simple comparison of the applied pressure to the limiting elastic pressure, from Equation (11.8), will determine the presence of yielding.

3.3.3. Unloading Stresses

Unloading stresses are calculated in a separate process to the autofrettage stresses, and then subtracted from the autofrettage stresses to determine the residual stresses. Unloading from peak autofrettage conditions may occur either elastically or otherwise involve further plasticity; this is found to occur at the ID in the first instance, and may be detected by assessing the Tresca equivalent stress were the tube to remain elastic. This can be more easily seen by rearranging Equation (11.9), and making the substitution $r = r_a$:

$$\frac{\sigma_\theta - \sigma_r}{\left(1-\frac{p}{p_e}\right)} = \sigma_{Y0} \tag{3.4}$$

If unloading occurs elastically, residual stresses are calculated by superposing standard Lamé elastic stresses, caused by the application of p_{AF}, from Equations (11.4) upon those created during pressurisation If residual stresses are sufficient to cause reverse yielding, a secondary yield radius, r_s, must be designated and unloading stresses calculated by the following:

Plastic Region

$$\begin{aligned}
\sigma_r &= -\sigma_{Y0}\left[1-\frac{r_s^2}{r_b^2}+\ln\left(\frac{r_s^2}{r^2}\right)\right] \\
\sigma_\theta &= \sigma_{Y0}\left[1+\frac{r_s^2}{r_b^2}-\ln\left(\frac{r_s^2}{r^2}\right)\right] \qquad r_a \le r \le r_s \\
\sigma_z &= E_t\varepsilon_z + \nu_t\left(\sigma_r+\sigma_\theta\right)
\end{aligned} \tag{3.5}$$

Elastic Region

$$\sigma_r = -\frac{\sigma_{Y0} r_s^2}{r_b^2}\left(\frac{r_b^2}{r^2} - 1\right)$$

$$\sigma_\theta = \frac{\sigma_{Y0} r_s^2}{r_b^2}\left(\frac{r_b^2}{r^2} + 1\right) \qquad r_s \le r \le r_b \qquad (3.6)$$

$$\sigma_z = E_t \varepsilon_z + \nu_t(\sigma_r + \sigma_\theta)$$

The secondary yield radius, r_s, is found using the zero internal pressure after relaxation criterion. This means that the residual radial stress (from Equation (11.12)) summed with the radial stress during Autofrettage (from Equation (11.6)) must give an answer of zero (at $r = r_a$), as seen below.

$$-\frac{\sigma_{Y0}}{2}\left[1 - \frac{r_p^2}{r_b^2} + \ln\left(\frac{r_p^2}{r_a^2}\right)\right] + \sigma_{Y0}\left[1 - \frac{r_s^2}{r_b^2} + \ln\left(\frac{r_s^2}{r_a^2}\right)\right] = 0 \qquad (3.7)$$

As with r_p from Equation (11.6), r_s may be calculated by a short iteration; it will be found to be smaller than r_p. It can be seen from Equation (11.9) that as p/p_e increases from 2 (for the elastic, perfectly plastic case), secondary yielding occurs for radii progressively greater than r_a. Plots of residual hoop and axial stresses within a tube with Wall Ratio 3.0 can be seen in Figure 11.2.

3.3.4. Strains

While Equations (2.4) – (2.6) provide a means for assessing component elastic strains, they are not capable of calculating plastic strains; these are found by subtracting elastic strain components from the total values. Total hoop strains are found to be:

$$\frac{u_t}{r} = \underbrace{-\nu_t \varepsilon_z}_{Elastic} + \underbrace{(1-\nu_t)\frac{\sigma_{Y0} r_p^2}{2G_t r^2}}_{Plastic} + \underbrace{(1-2\nu_t)\frac{(\sigma_r)_t}{2G_t}}_{Elastic} \qquad r_a \le r \le r_p \quad (3.8)$$

Plastic hoop strains may then be found by subtracting elastic hoop strains, calculated by Equation (11.16), from the total value, Equation (11.21).

$$\varepsilon_\theta^p = (1-\nu_t^2)\left(\frac{\sigma_{Y0} r_p^2}{E r^2} - \frac{\sigma}{E}\right) \qquad (3.9)$$

Where σ represents the yield strength *during loading* of the material *at that position*. Hence when modelling the Bauschinger effect if there is no strain hardening present (i.e. $H = 0$) it equals σ_{Y0}, and when modelling strain hardening it increases according to

the hardening relationship defined. Also, given the associated integrated flow rule, plastic radial strain is given by:

$$\varepsilon_r^p = -\varepsilon_\theta^p \tag{3.10}$$

3.4. VARIATIONS ON THE TRESCA SOLUTION

The model described in section 3.3 incorporates an elastic, perfectly plastic material – this is a simplistic plasticity model, which maintains a constant equivalent stress of σ_{Y0} while in the plastic regime. As such, it is not representative of the stress-strain response of candidate steels to plastic deformation (especially during unloading), as described in section 3.2. In light of this, a series of adaptations are applied to the Tresca solution to reflect the different responses to plastic strain described in section 3.2.

Not only does the development of the variants allow the influence of these responses to be observed, it increases experience in the development of modelling autofrettage scenarios. The adaptations allow the following behaviours to be modelled:

1. Isotropic Hardening,
2. Kinematic Hardening,
3. Bauschinger Effect,
4. Pseudo von Mises.

3.4.1. Effects of Plastic Deformation

Equations (11.12) to (11.14) provide a means of assessing stresses within the tube subsequent to secondary yielding, providing the material properties of the tube remain unchanged. However, after tensile yielding (as experienced by the tube during either hydraulic or swage autofrettage), metallic materials experience changes to their properties, as described in section 3.2.

As can be seen from Figure 3.3, strain hardening alters the stress-strain state of a material once plastic deformation has begun. With respect to autofrettage, strain hardening would manifest as a reduction in r_p for a given value of p_{AF} as the material in the region $r_a \leq r < r_p$ would carry more pressure load than in an autofrettage tube of a perfectly plastic material (although the minimum pressure required for autofrettage, p_e, would be unchanged). This is most obviously true in a model that utilises the Tresca yield criterion, given the commonality with the equilibrium equation (used in Equation (11.5)). As strain hardening occurs, the difference between hoop and radial stresses increases, allowing for greater hoop stresses and hence greater pressure load. Subsequent unloading would also be affected; following the load reversal r_s would either be increased or decreased, for kinematic or isotropic hardening, respectively.

The Bauschinger effect occurs solely during unloading after plastic strain (Figure 3.4 shows this, and defines the *Bauschinger Effect Factor*, β); the primary yielding process is unaffected, hence r_p remains unchanged.

3.4.2. Implementation

Strain Hardening and the Bauschinger effect are modelled by multiplying the yield stresses from the Tresca yield criterion (Equation (2.10)) by a scaling factor. Stresses in both loading and unloading procedures must be altered, requiring a scaling factor for each case – designated F_{SL} and F_{SU} for loading and unloading, respectively.

During loading only strain hardening occurs as the Bauschinger effect does not influence yield stress until load reversal commences, hence only material within the deformed region ($r_a \le r \le r_p$) is affected; accordingly F_{SL} is only applied to the stresses equations within the deformed region. Hence, the autofrettage loading stress equations, adapted from Equations (11.6), are scaled using F_{SL}, becoming:

$$\begin{aligned} \sigma_r &= -\frac{F_{SL}\sigma_{Y0}}{2}\left[1-\frac{r_p^2}{r_b^2}+\ln\left(\frac{r_p^2}{r^2}\right)\right] \\ \sigma_\theta &= \frac{F_{SL}\sigma_{Y0}}{2}\left[1+\frac{r_p^2}{r_b^2}-\ln\left(\frac{r_p^2}{r^2}\right)\right] \\ \sigma_z &= E_t\varepsilon_z+\nu_t\left(\sigma_r+\sigma_\theta\right) \end{aligned} \tag{3.11}$$

Extending the principle of an altered yield stress into the unloading phase, a second scaling factor, F_{SU}, is introduced to alter yield during *unloading* – in this case to the unloading yield criterion, Equation (11.9).

During unloading both strain hardening and the Bauschinger effect influence yield stress; in addition, when isotropic hardening is present, the increased yield stress extends beyond the reyield region ($r_a \le r \le r_s$) to r_p, which must be reflected by the elastic stresses in the region $r_s \le r \le r_p$. F_{SU} is calculated to incorporate this behaviour (and must equal 1 in the undeformed region, $r_p \le r \le r_b$), and is used to scale unloading stress equations, adapted from Equations (11.12) and (11.13), in both elastic and plastic regimes:

$$\begin{aligned} \sigma_r &= -F_{SU}\sigma_{Y0}\left[1-\frac{r_s^2}{r_b^2}+\ln\left(\frac{r_s^2}{r^2}\right)\right] \\ \sigma_\theta &= F_{SU}\sigma_{Y0}\left[1+\frac{r_s^2}{r_b^2}-\ln\left(\frac{r_s^2}{r^2}\right)\right] \qquad r_a \le r \le r_s \\ \sigma_z &= E_t\varepsilon_z+\nu_t\left(\sigma_r+\sigma_\theta\right) \end{aligned} \tag{3.12}$$

$$\sigma_r = -F_{SU}\frac{\sigma_{Y0}r_s^2}{r_b^2}\left(\frac{r_b^2}{r^2}-1\right)$$
$$\sigma_\theta = F_{SU}\frac{\sigma_{Y0}r_s^2}{r_b^2}\left(\frac{r_b^2}{r^2}+1\right) \qquad r_s \le r \le r_b \qquad (3.13)$$
$$\sigma_z = E_t\varepsilon_z + \nu_t(\sigma_r + \sigma_\theta)$$

The secondary yield radius is then found by summing radial stresses at $r = r_a$, from Equations (3.12) and (3.11), to zero, forming Equation (3.14) (this is equivalent to the formulation of Equation (11.14)):

$$-\frac{F_{SL}\sigma_{Y0}}{2}\left[1-\frac{r_p^2}{r_b^2}+\ln\left(\frac{r_p^2}{r_a^2}\right)\right]+F_{SU}\sigma_{Y0}\left[1-\frac{r_s^2}{r_b^2}+\ln\left(\frac{r_s^2}{r_a^2}\right)\right]=0 \qquad (3.14)$$

In summary, F_{SL} and F_{SU} are used to control post-yield stress-strain relationships; it now remains to define F_{SL} and F_{SU} so as to give the desired behaviour during plastic deformation.

3.4.3. Plastic Strain

As both the Bauschinger effect and Strain Hardening are dependant on plastic strain, the (loading) plastic strain must be identified before they may be addressed. Plastic hoop and radial strains are given by Equations (11.22) and (11.23), and may be combined into the Tresca equivalent plastic strain using the following:

$$\begin{aligned}\varepsilon_{Tr}^p &= \varepsilon_\theta^p - \varepsilon_r^p \\ &= 2\varepsilon_\theta^p\end{aligned} \qquad (3.15)$$

At this stage, it was thought that making strain hardening proportional to the Tresca equivalent plastic strain was a sensible balance of accuracy versus simplicity.

Now the plastic strain which occurs during autofrettage has been quantified, it remains to formulate relationships between it and material yield stress.

3.4.4. Strain Hardening

The increased strength of the tube material during autofrettage in the deformed region ($r_a \le r \le r_p$) is represented by raising the yield strength above σ_{Y0} – in general, treating it as a function of Tresca equivalent plastic strain:

$$\sigma_\theta - \sigma_r = \sigma_Y = F\left(\varepsilon_{Tr}^p\right) \tag{3.16}$$

Assuming linear isotropic hardening, the altered yield stress of the strain-hardened material is given by:

$$F\left(\varepsilon_{Tr}^p\right) = \sigma_Y = \sigma_{Y0} + H\varepsilon_{Tr}^p$$

Where σ_Y is the modified yield stress of the material, and H (the Tangent modulus) is a constant, typically assumed to be 0.05 to 0.1 E. Substituting for Tresca equivalent plastic strain (Equation (3.15)) and rearranging, the Tresca yield criterion (from Equation (2.10)) in a linearly strain hardened tube is found:

$$\sigma_\theta - \sigma_r = \sigma = \frac{\sigma_{Y0}\left[1 + 2\left(1-\nu^2\right)\frac{Hr_p^2}{Er^2}\right]}{\left[1 + 2\left(1-\nu^2\right)\frac{H}{E}\right]} \tag{3.17}$$

Accordingly the yield stress scaling factor in loading, F_{SL}, is given by:

$$F_{SL} = \frac{\left[1 + 2\left(1-\nu^2\right)\frac{Hr_p^2}{Er^2}\right]}{\left[1 + 2\left(1-\nu^2\right)\frac{H}{E}\right]} \tag{3.18}$$

It must then be decided if the tube material behaves isotropically or kinematically in plastic deformation, such that the elastic stress range (σ_E) may be calculated. If isotropic hardening is desired, $\sigma_E = 2\sigma_{Max}$ hence $F_{SU} = F_{SL}$, or if kinematic hardening is desired, $\sigma_E = 2\sigma_{Y0}$ hence $F_{SU} = 1$ (F_{SU} operates on the stresses developed in Equations (3.12), which, as described in sub-section 11.2.5, already incorporate the stress range $\sigma_E = 2\sigma_{Y0}$).

Figure 3.7 plots the residual stresses within a kinematic hardening tube with Wall Ratio 3.0 subject to Strain Hardening of $H = E/10$, again with an autofrettage pressure ratio, p_i/σ_Y, = 1.0909. The normalised primary yield radius decreases to 0.4090, and the normalised secondary yield radius decreased to 0.0072 – resulting from the increased yield stress of the material.

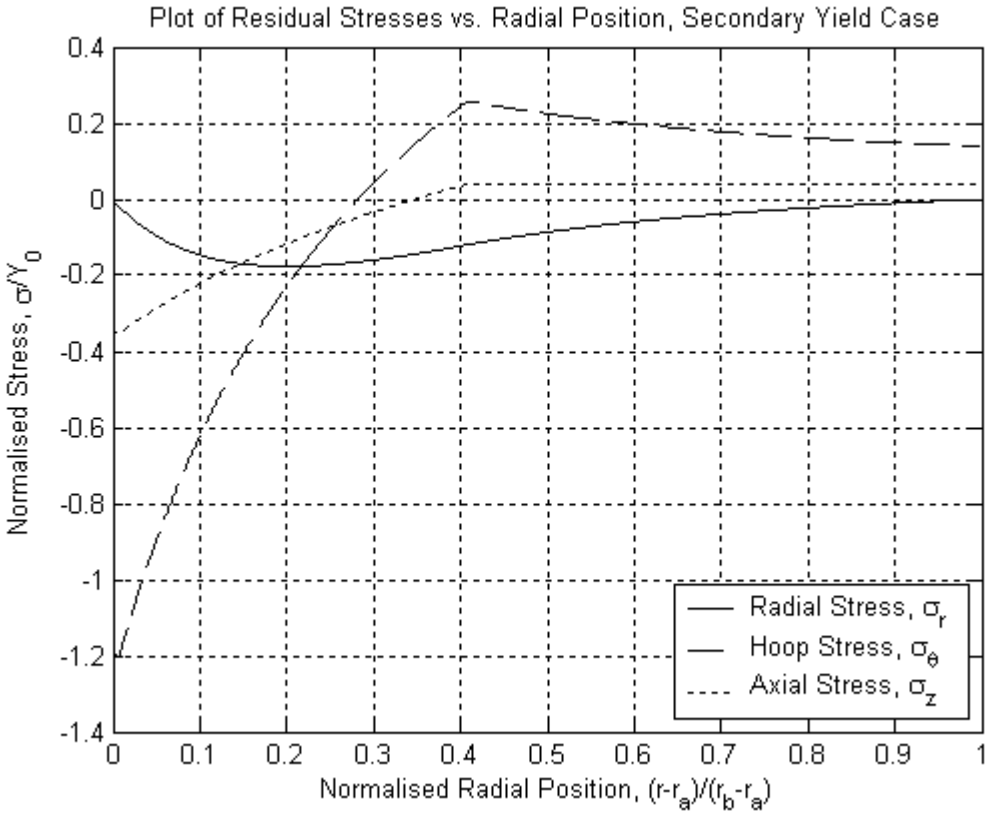

Figure 3.7: Residual Stresses in a Tube subject to Linear Strain Hardening

3.4.5. Bauschinger Effect

As described in sub-section 3.4.2, the Bauschinger effect was implemented through selection of the scaling factor in unloading, F_{SU} (given by Equations (3.12)).

The Bauschinger effect was addressed by considering the degree of weakening to be a function of Tresca equivalent plastic strain (ε_{Tr}^{p}), so that as initial plastic strain drops from a maximum at r_a to zero at r_p, β varies accordingly with radius in the tube.

As described above, the loading stage is unaffected by the Bauschinger effect (e.g. F_{SL} = 1), leaving F_{SU} to be defined. To model a decrease in yield strength:

$$F_{SU} = \frac{1+\beta}{2} \qquad 0 \le \beta \le 1 \qquad (3.19)$$

Milligan, Koo and Davidson [21] assessed the Bauschinger effect in high strength steels, providing a basis for the selection of values of the Bauschinger Effect Factor (β) used here.

The unloading profile of a material subject to the Bauschinger effect is determined by prior plastic strain – accordingly, as prior plastic decreases from a maximum at r_a to a minimum at r_p, β was varied in this region. In this study, it was thought that scaling the decrease in yield stress in proportion to prior Tresca equivalent plastic strain, ε_{Tr}^{p}, was a good approximation for this study, i.e.:

$$\beta = 1 - F_{S\beta} \cdot \varepsilon_{Tr}^{p} \tag{3.20}$$

Where $F_{S\beta}$ is a positive scaling factor. We may now apply an end constraint to identify $F_{S\beta}$ – if $\beta = \beta_0$ at $r = r_a$, then:

$$F_{S\beta} = \frac{1-\beta_0}{\varepsilon_{Tr}^{p}\Big|_{r=r_a}} \tag{3.21}$$

Now that β has been found, F_{SU} may be found using Equation (3.19); subsequently, Equations (3.12) and (3.13) may be evaluated to give unloading and hence residual stresses.

The formation of the above equations rely on the assumption that $r_s \leq r_p$; to confirm this, Equation (3.14) is evaluated with r_s is set to the limiting case of equality with r_p, $F_{SL} = 1$, giving:

$$-k\left[1-\frac{r_p^2}{r_b^2}+\ln\left(\frac{r_p^2}{r_a^2}\right)\right]+k(1+\beta)\left[1-\frac{r_p^2}{r_b^2}+\ln\left(\frac{r_p^2}{r_a^2}\right)\right]=0$$

$$(1+\beta)=1 \tag{3.22}$$

In view of Equation (3.22), it is clear that $r_s \leq r_p$ when $0 \leq \beta$; hence the range $0 \leq \beta \leq 1$ is valid without exception for Equations (3.12) and (3.13).

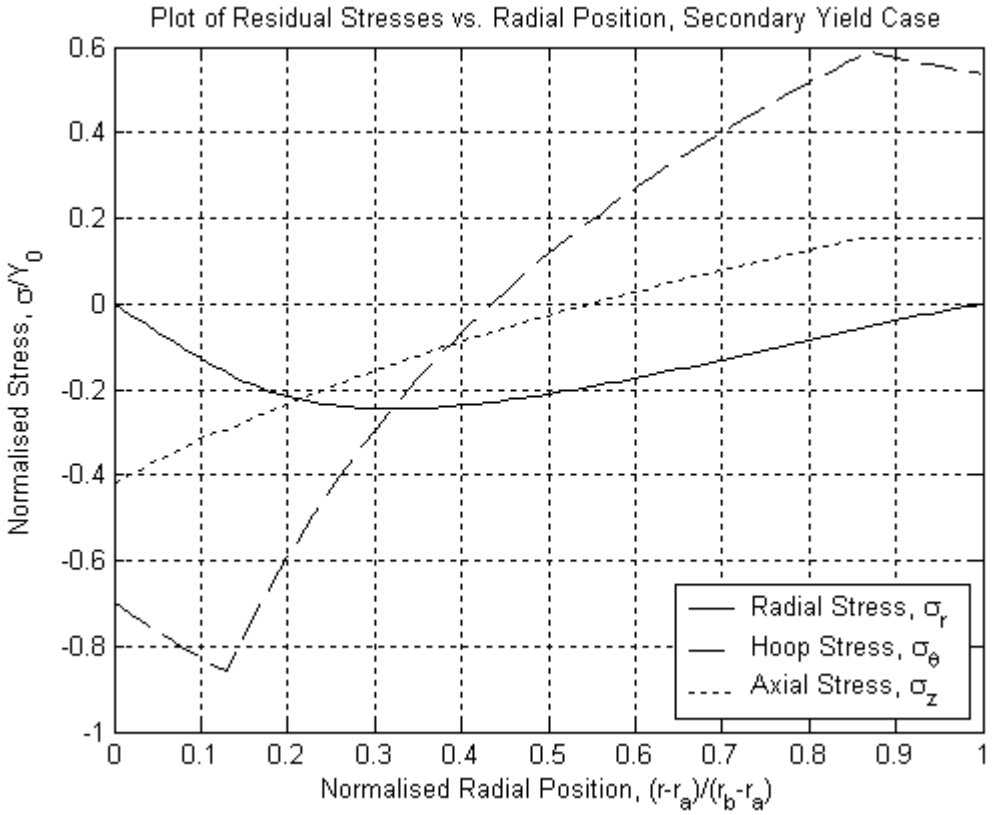

Figure 3.8: Residual Stresses in a Tube subject to the Bauschinger Effect

Figure 3.8 plots the residual stresses within a tube with Wall Ratio, K, = 3.0 subject to the Bauschinger effect (β_0 = 0.7)), again with an autofrettage pressure ratio, p_i/σ_Y, = 1.0909. Compared with the elastic, perfectly plastic case (Figure 11.2), the normalised primary yield radius remains at 0.8703 (the Bauschinger effect is an unloading phenomenon); however, the normalised secondary yield radius increased to 0.1291 – resulting from the reduced yield stress of the material under reverse loading. Additionally, the magnitudes of the stresses within the yielded region are reduced. This is unfavourable, as the size of residual stresses determines the amount of benefit obtained from autofrettage.

3.4.6. Pseudo von Mises

The Pseudo von Mises model uses the relationship between the yield stresses calculated by the Tresca and von Mises yield criteria, developed in sub-section 2.4.2.2, to scale the Tresca yield stress to the von Mises yield stress, *in plane stress*.

By assuming a plane stress (σ_z = 0) case, and approximating $\sigma_r = -\sigma_\theta$, we may then assume, using Equation (2.9), that k becomes the von Mises value, and increases in magnitude by ~15.5%. This new yield stress (in pure shear) may then be used in the

above Tresca method to approximate a von Mises solution of a plane *stress* tube. This should be used with caution, as it is not a state that generally exists in long tubes.

3.5. PSEUDO-SWAGE MODEL

Once an insight into stresses (and methods to find them) in pressurised tubes had been gained from Lamé's solution, the focus of work changed to form an analytical model of autofrettage. The process of pseudo-swage autofrettage is modelled by treating the mandrel as a short solid disc (in Plane Stress) travelling down a tube. It is assumed that the mandrel behaves elastically, while the tube is subjected to plastic deformations. However, as there are no axial variations incorporated, the model is effectively that of hydraulic autofrettage, albeit incorporating the interference fit of the mandrel – which gives an insight into the required mandrel size and deflections encountered.

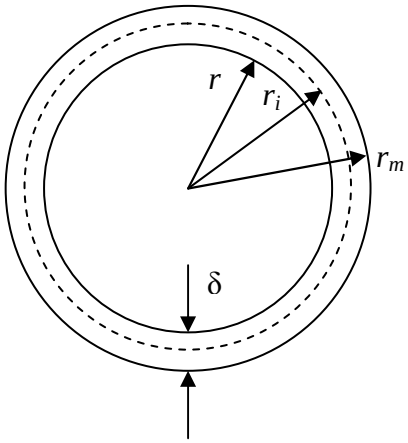

Figure 3.9: Interference Diagram

3.5.1. Initial Stages

First, the Compatibility criterion is introduced, on the basis that the inner surface of the tube is in contact with the mandrel, at some radius r_i (as shown in Figure 3.9), where $r_a \leq r_i \leq r_m$. Ensuing from this requirement, the combined deflection of the tube (u_t) and mandrel (u_m) must equal the difference between the mandrel radius (r_m) and the inner radius of the tube (r_a). Letting this difference (r_m - r_a) equal δ:

$$\delta = r_m - r_a \tag{3.23}$$

It also follows that:

$$\delta = -u_m + u_t \tag{3.24}$$

Sub-section 11.2.6 develops and number of strain relationships in tubes; in particular, Equations (11.15) and (11.16) are used to link strains to displacements, which are used below. Additionally, the tube and mandrel are also linked by the continuity of radial stress across the interface (at $r = r_i$) between them. Hence, at r_i:

$$\sigma_r = (\sigma_r)_m = -p_i \tag{3.25}$$

The tube and mandrel will now be addressed separately.

3.5.2. Mandrel

The mandrel is assumed to be an elastically behaving tube, of inner radius zero. As it is assumed to behave elastically, the stresses within the mandrel may be assessed using Lamé's case, Equations (11.2) and (11.3). However, as the mandrel is solid r decreases to zero at its centre; hence, the constant B must be set to zero to avoid singularities. This means:

$$\sigma_r = \sigma_\theta = A \tag{3.26}$$

It is now possible to assess the hoop stress in the mandrel (required for compatibility – Equation (3.24)). Substituting the Plane Stress criterion ($\sigma_z = 0$) into the general elastic hoop strain Equation (2.5), the following is obtained:

$$(\varepsilon_\theta)_m = \left(\frac{(\sigma_\theta)_m}{E_m} - \frac{\nu_m (\sigma_r)_m}{E_m} \right) \tag{3.27}$$

We may substitute for σ_θ in Equation (3.27), using Equation (3.26), obtaining the following simplification:

$$(\varepsilon_\theta)_m = \frac{(1-\nu_m)(\sigma_r)_m}{E_m} \tag{3.28}$$

By substituting for σ_r from Equation (3.25) into the above, the following equation is yielded.

$$(\varepsilon_\theta)_m = \frac{p_i(1-\nu_m)}{E_m} \tag{3.29}$$

Equation (11.16) is then used to change Equation (3.29) into a deflection expression.

$$u_m = (1-\nu_m)\frac{p_i r_m}{E_m} \tag{3.30}$$

Aside from the interface pressure, p_i, all terms on the right hand side of Equation (3.30) are known. It now remains to form an expression for the deflection of the tube, to solve the compatibility requirement between the mandrel and tube using Equation (3.24).

3.5.3. Tube Stresses

In the case of swage autofrettage the applied pressure results from the interference fit between mandrel and tube. The interface pressure is found by solving Equation (3.24), given the interference from Equation (3.23). The (elastic) mandrel deformation, u_m, is found from Equation (3.30) – an expression for the tube deflection is needed to solve Equation (3.24).

Sub-section 11.2.6 develops a relationship for the total hoop strain in an elastic-plastic tube, given by Equation (11.21). This can then be converted into a deflection equation by multiplying through by r (as when formulating Equation (3.30)). At the inner surface of the tube, where $r = r_a$ and $\sigma_r = -p_i$, this then becomes:

$$u_t = -r_a \nu_t \varepsilon_z + (1-\nu_t)\frac{kr_p^2}{G_t r_a} + r_a(1-2\nu_t)\frac{p_i}{2G_t} \tag{3.31}$$

Substituting Equations (3.30) and (3.31) into Equation (3.24), yields:

$$\delta = -r_a \nu_t \varepsilon_z + (1-\nu_t)\frac{kr_p^2}{G_t r_a} + r_a(1-2\nu_t)\frac{p_i}{2G_t} - (1-\nu_m)\frac{p_i r_m}{E_m} \tag{3.32}$$

A value for the axial strain, ε_z, must now be selected. As the length of the tube is considered to be large, it is appropriate to assume the *Plane Strain* case – meaning axial strain is set to zero. The radial stress at the inner surface of the tube, from Equations (11.6), is then used to introduce an expression for p_i, by substituting from Equation (3.25).

$$p_i = k\left[1 - \frac{r_p^2}{r_b^2} + \ln\left(\frac{r_p^2}{r_a^2}\right)\right] \tag{3.33}$$

This leaves Equation (3.32) with one unknown – r_p. While r_p cannot be separated and solved analytically, an iterative method quickly yields a value numerically. Once found, the value of r_p can then be used to evaluate Equations (11.6) and (11.7), to identify the stresses within the tube when deflected by the mandrel.

3.6. OTHER SOLUTIONS

A selection of solutions is presented below, both analytical and numerical; these were chosen on the grounds of their suitability for comparison and validation of numerical methods developed subsequently in this research. While they have been appraised in the Literature Review, this section expands upon their specific suitability and subsequent use.

3.6.1. Avitzur's Model

While Avitzur's method is quite general in terms of hydraulic autofrettage load cases it can model, it does not give an explicit solution for the component stresses or yield radii, and hence large amounts of iterations are required to obtain an output. This made it awkward to implement within a spreadsheet, and hence it was not used for validation of later numerical simulations. Although Avitzur's method offers an answer for hydraulic autofrettage using von Mises, the ultimate aim of this research is swage autofrettage. Critically, without the ability to model material non-linearity, Avitzur's model is of little use to this study, beyond its initial stage. As such, a more practical comparison model is required, even if more limited in terms of the end conditions which may be considered.

3.6.2. Huang's Model

Although restricted to the incompressible plane strain case, and hence more restrictive than Avitzur's model, Huang's model very easily yields a solution. This makes it of more practical use for comparison with numerical models developed later in this course of study. In addition Huang's model can represent both bi-linear and non-linear material behaviours, making it suitable for comparison with future autofrettage models (depending on the specific stress-strain relationship), with the noted exception that a single unloading profile must be used. The use of Huang's model is described below, which reuses the nomenclature used in the initial publication for clarity.

The model considers the tube material to behave linearly in the elastic phase (both loading and unloading), and either linearly or according to a power-law in the plastic phase (loading and unloading may be treated independently). Figure 3.10 shows a material following a power-law relationship in both loading and unloading. Yielding occurs in the loading phase at point 1, when the equivalent stress reaches σ_Y^+; during the unloading phase yielding occurs at point 3 when equivalent stress equals σ_Y^-.

Table 3.1 summarises the set of stress-strain relations, in both elastic and plastic regimes. As well as Young's Modulus (in both loading and unloading; as described in

sub-section 5.1.1, Young's Modulus can change following plastic strain), the relations require the following parameters to describe the plastic behaviour of the material: A_1, A_2, A_3, A_4, B_1 and B_2. The parameters form three groups: constant (A_1 and A_3), linear (A_2 and A_4) and exponential (B_1 and B_2).

Loading		**Unloading**	
Phase	Stress Response	Phase	Stress Response
0-1	$\sigma = E_1\varepsilon$	2-3	$\sigma^{UL} = E_2\varepsilon^{UL}$
1-2	$\sigma = A_1 + A_2\varepsilon^{B_1}$	3-	$\sigma^{UL} = A_3 + A_4\left(\varepsilon^{UL}\right)^{B_2}$

Table 3.1: Summary of Material Parameters, Huang's Method

A_1 and A_3 are selected such that the two sets of elastic and plastic equations produce continuous results at $\varepsilon_Y.E_1$ and $\varepsilon_Y^{UL}.E_2$ (points 1 and 3 on Figure 3.10) respectively:

$$A_1 = \varepsilon_Y E_1 - A_2\varepsilon_Y^{B_1} \tag{3.34}$$

$$A_3 = \varepsilon_Y^{UL} E_2 - A_4\left(\varepsilon_Y^{UL}\right)^{B_2} \tag{3.35}$$

A_2 and A_4 are multipliers in the plastic regime; when a bi-linear material is modelled they give the plastic slopes, and respectively are set equal to H_1 and H_2, the plastic slopes in loading and unloading. B_1 and B_2 are exponents of plastic strain; when a bi-linear material is to be modelled they are set to equal one, denoting linear stress response to plastic strain.

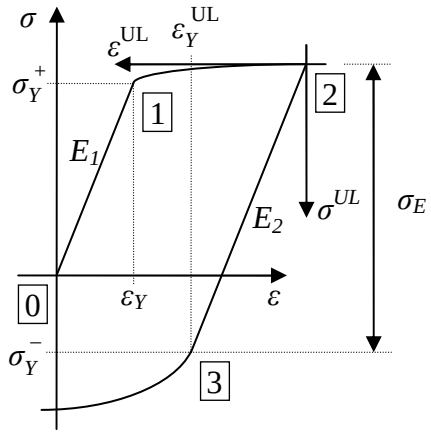

Figure 3.10: Stress-Strain Diagram of Material-Fit used by Huang

Huang's model is used in the comparisons presented in Chapter 4, where it is used with a bi-linear material model. It was considered for comparison with results from material models developed in Chapters 5 and 6, which allow representation of the gun steel A723-1130 (the material-fit is described in sub-section 5.1.1) within ANSYS. However it was thought that the single, fixed unloading profile used by Huang's Model, combined with the requirement for an incompressible material under zero axial strain

would complicate comparison; instead, only results from the Hencky Programme were used.

3.6.3. Hencky Programme

Given the ability of the Hencky Programme to model hydraulic autofrettage, using von Mises equivalence, over the full range of end conditions and including realistic material behaviour, it was deemed suitable for validation of hydraulic autofrettage models that would be created. It was used in Chapter 4 to simulate a bi-linear material behaviour, and in Chapters 5 and 6 to simulate a non-linear stress-strain response in unloading.

3.7. SUMMARY

A review of material models was conducted, with emphasis on response to plastic strain. The Tresca elastic-plastic solution was then implemented and subsequently adapted to reflect some of the plastic strain responses previously identified. Finally, the solution was extended to include an interference fit with a solid, elastic, cylinder within the tube's ID.

A review of analytical and numerical models suitable for comparison with future models of hydraulic autofrettage was then made.

4. HYDRAULIC AUTOFRETTAGE MODELS IN FEA

4.1. INTRODUCTION

After the investigation of analytical models in Chapters 2 and 3, Finite Element models were developed; this allowed a wider range of more realistic *hydraulic* autofrettage conditions to be simulated, than is practically possible through analytical methods. This will form the basis of future work, in particular the model of swage autofrettage – of crucial importance to this study.

To be useful to this study, it is essential that any method used meets the following criteria:

1. Uses the von Mises equivalence relation,
2. Offers suitable material modelling capabilities,
3. Allows constraints to be applied to suitably model a wide range of conditions,
4. Allows for batch processing of cases so that optimisation, convergence and parametric analysis may be conducted.

As ANSYS [28] was immediately available, it was assessed on the above criteria; it was found to fulfil all points, with the following notes:

1. Strong scripting through the ANSYS Parametric Design Language (APDL), allows for very effective parametric/batch modelling,
2. It includes a well developed means of customisation of many features, including material models, through User Programmable Features (UPFs).

It is accepted that most modern FE packages offer many or all of the required features, ANSYS's known strengths and immediate availability made it the clear choice.

The analyses presented in this thesis, conducted within the ANSYS FEA programme, utilise Lagrangian methods, as the amounts of deflection that occur in the various models are not sufficient to require Eulerian-based methods.

Eulerian methods represent the modelled geometry within a fixed frame of reference, making them more suitable for modelling flow (such as that which occurs during large plastic deformation); instead, Langrangian methods utilise a moving frame of reference more suitable for modelling discrete objects.

In terms of geometrical discretisation as used in FEA, the Lagrangian method considers a predefined section of material to be contained within the periphery of an element which deforms with the material, whereas the Eulerian method considers cells to remain stationary whilst material flows into, out of and through the cells.

This chapter describes the work conducted to model the hydraulic autofrettage process, and subsequent unloading, in a range of end-conditions. To this end, simplistic bi-

linear material models are used; elastic, perfectly plastic during the optimisation stage (section 4.6) and kinematic hardening for comparison with other methods (section 4.7).

This allows development work to focus on the modelling of the physical conditions of autofrettage, allowing errors to be rapidly identified and inconsistencies between models to be addressed with confidence. Accurate material representation will then be added at a later stage.

4.1.1. Summary of Hydraulic Autofrettage Models

The Hydraulic Autofrettage models created within ANSYS were designed to simulate the mid-section properties of a long internally pressurised tube, subject to a range of end conditions. Additionally, as simulation of the hydraulic case would serve as a precursor to that of swage autofrettage, modelling work done on the former should be transferable to the latter to avoid duplication of effort.

The first model simulated an r,θ section of tube, which allowed both plane strain (ε_z = 0) and plane stress (σ_z = 0) conditions to be created through application of element properties. Results from this initial model were suitable for comparison with those from analytical and numerical methods studied earlier (see Chapter 3), and gave good agreement.

As the r,θ section model was limited in the range of end conditions it could simulate, and could not include axial variation (which would be important when modelling swage autofrettage), it was then necessary to simulate an autofrettaged tube in another way, this time modelling an r,z section.

Using an r,z section it was possible to predict the stress distribution in both plane stress and general plane strain conditions (ε_z = constant w.r.t. r), comprising true plane strain as well as open-ends (net axial force sums to zero, or $\int_0^{2\pi}\int_{r_a}^{r_b}\sigma_z \cdot dr \cdot d\theta = 0$) and closed-ends (net axial force sums to $\int_0^{2\pi}\int_{r_a}^{r_b}\sigma_z \cdot dr \cdot d\theta = 2\pi r_a^2 p_{AF}$) conditions. Additionally, axial variations can be included, making the model an effective mile-stone towards simulating swage autofrettage.

As in the analytical models, gravitational effects are ignored in all FE models used in this study; given the tiny size of gravitational forces compared to those resulting from pressure loading, inclusion of gravitational forces would add needless complexity and preclude the use of axial symmetry in the r,z section model.

4.2. COMMON MODELLING NOTES

4.2.1. Model Optimisation

This sub-section describes the optimisation procedure, as applied to FEA; it is employed generically for all models, both described in this chapter and subsequently.

Once ANSYS models were confirmed to be generating suitable results, their meshes were optimised to balance computational size against accuracy of results; this dilemma is faced almost universally whenever a process is modelled. While the meshes described in this chapter remained relatively simple, allowing results to be obtained in 10-20 seconds, it was recognised that models can quickly become more complex. Accordingly, optimisation was crucial to minimise computational requirements while keeping element size small enough to resolve radial variation in material behaviour, particularly during unloading.

The optimisation was conducted in a relative manner – results from one mesh geometry were compared against those from the next mesh in the appropriate "fineness" series (i.e. a coarse mesh was compared against a slightly less coarse mesh).

This may seem counter-intuitive when like-for-like comparisons with different methods are possible, but relative error convergence is a useful measure (and in some cases necessary) due to the following:

1. Available Comparisons – like-for-like comparisons would not always be possible, especially as swage models were developed; accordingly it was important to confirm that ANSYS is able to generate sufficiently stable results to allow convergence to be monitored as element size is decreased.

2. Numerical Accuracy – even though different numerical and analytical models may be used to model identical conditions, differences in iterative procedures and rounding (some of which will not be known or controllable) will mean that no two methods ever give exactly the same answer. These inter-method differences may be small, but will skew convergence graphs.

Once the optimisation process had been conducted for each model, results from the optimised models were compared and validated against data from other sources (numerical or empirical), where available. For the Axial section model developed in this chapter (section 4.4), such comparisons are made in section 4.7.

4.2.2. Material Model

A bi-linear material model was chosen – while a simplistic representation, it allowed the structural aspects of the model to be developed without the complexities of material non-linearity (the implementation of which is detailed in Chapters 5 and 6). Such a model is defined in two stages in ANSYS; elastic and plastic behaviour. To model the apparent drop in reverse yield strength (see section 3.2) of steel, a kinetic hardening model was selected (rather than isotropic). While this is not an accurate model, it is generally more representative than isotropic hardening. ANSYS refers to such a material as BKIN.

4.3. HOOP SECTION MODEL

The following description has been kept brief, summarising early work, with notes on element selection and details of tests moved to section 4.5 to reduce the duplication of material between Hoop and Axial section models.

During the development of the model, familiarity was gained with ANSYS, and modelling methodologies were developed that would prove valuable when developing future models. For this reason, future models (such as the Axial Section) are presented in more detail.

4.3.1. Overview

After following initial tutorials contained within the ANSYS documentation, a transverse section of the tube was modelled. Figure 4.1 displays the dimensioning of the model, and Figure 4.2 describes the manner in which the model is loaded and constrained.

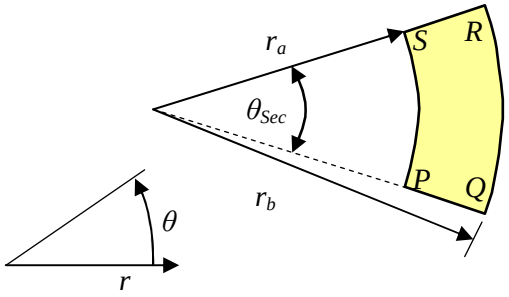

Figure 4.1: Hoop Section Model Geometry

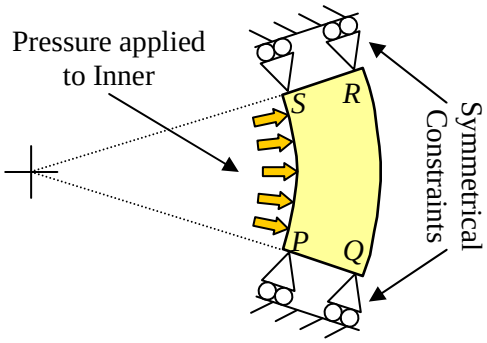

Figure 4.2: Hoop Section Model Constraint

Initially a single quadrant (Figure 4.3 was used to demonstrate that the developed stresses when autofrettaged were as expected, and that rotational symmetry could be used to reduce the model size. This was refined into a 1° segment (Figure 4.4)) to further exploit the rotational symmetry of the tube, allowing a finer mesh for a given number of elements. In both cases, the meshes were retained by constraining the section surfaces as lines of symmetry.

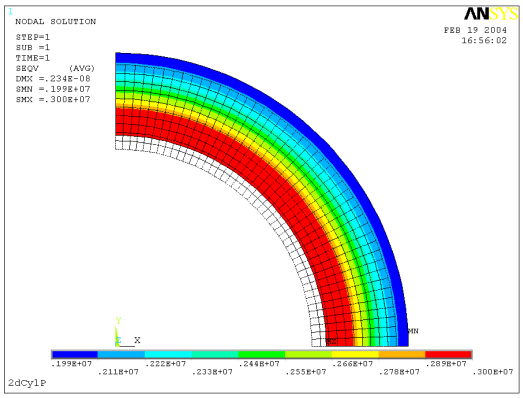

Figure 4.3: Initial Mesh

The first quadrant mesh, showing a contour plot of von Mises stress during autofrettage.

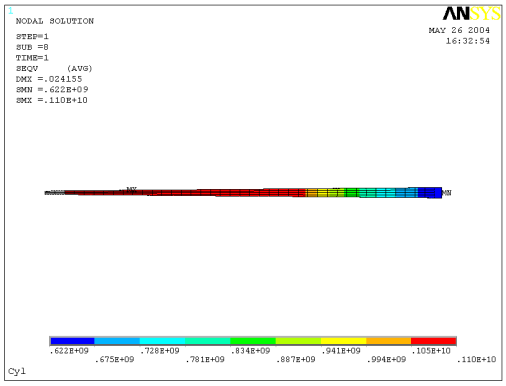

Figure 4.4: Refined Mesh

The above mesh gave finer radial granularity, allowing more accurate comparison of stresses.

Preliminary investigations showed that the angle of section (θ_{Sec}) had no influence on the generated results, which left mesh fineness as the next topic of study. Mesh fineness is effectively represented by two values, the number of division in the hoop and radial directions; these two variables were then investigated.

Initially, both the number of radial and circumferential divisions were varied, to determine which had the most influence on error. The number of radial divisions used were 10, 20, 30 and 40, and the number of circumferential divisions used were 1, 2, 3 and 4 (Figure 4.11 shows the mesh structure). θ_{Sec} was selected to give square elements at the ID (see Figure 4.11). The convergence plots, showing errors (relative to Huang's method) in radial and hoop stresses at the inner diameter during peak pressure conditions, are shown in Figure 4.5.

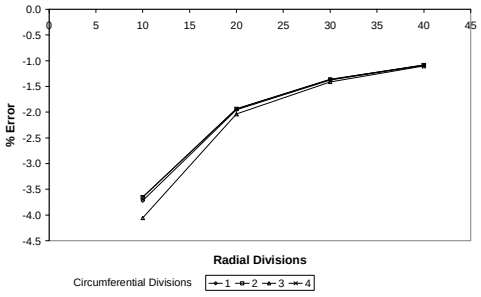

Convergence plot of Radial Stresses

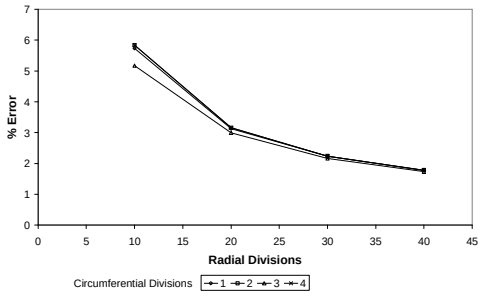

Convergence plot of Hoop Stresses

Figure 4.5: Initial Error Convergence Plots

Results were taken at the ID for an incompressible tube of K = 2, of bi-linear material (E = 209 GPa, ν = 0.4999999999, σ_{Y0} = 1,100 MPa, H = 20.9 GPa), autofrettaged to 791 MPa (nominally 50% overstrain). These were matched in Huang's model.

It was quickly discovered that while the number of circumferential divisions had virtually no effect on error (the data sets for different numbers of circumferential divisions are almost coincident), the number of radial divisions strongly influenced the

accuracy and smoothness of results. Consequently, the number of radial divisions then became the focus of a more thorough sensitivity analysis, described in section 4.6.

Following these initial investigations, optimisation of the number of radial divisions was systematically assessed, as described in sub-section 4.6.2.

4.4. AXIAL SECTION MODEL

4.4.1. Overview

Once initial work, developing the hoop section (r,θ) model, had been completed, a series of axial section (taken on the r,z plane) models were created. As well as allowing Open-Ends and Closed-Ends (in addition to true Plane Strain and Plane Stress) conditions to be investigated, axial variation would also be able to be incorporated. In turn, a similar model could be used as the basis for simulating swage autofrettage, as well as tapered sections and non-uniform pressure loading.

Switching to an axi-symmetric model had the additional benefits of effectively eliminating any unnecessary simulation overhead by reducing the considered angle of tube to zero, and presenting a rectangular area for meshing (avoiding problems with element geometry at high values of K).

General plane strain (in the context of tubes) describes the condition when initially plane sections remain plane while under load, i.e. ε_z is invariant with respect to radius. General plane strain is a collective term encompassing *engineering* plane strain – in which all sections of the tube possess an equal amount of axial strain – and *true* plane strain – a special case of engineering plane strain that occurs when $\varepsilon_z = 0$ throughout the tube wall.

In general, it would be necessary to model a long section of tube to allow accurate mid-section properties to be calculated (Saint-Venant's principle implies that stresses resulting from a point load applied to the end of a beam may be considered uniform when more than one thickness from its end). However, in the models described below the end constraints (on surfaces 1 and 3) are selected to reproduce the conditions found at the mid-sections of the respective tubes, eliminating the need for long models. For the general plane strain cases (i.e. all excepting the Plane Stress model), the end constraints maintain plane strain conditions (ε_z is constant throughout the tube wall) and apply an appropriate axial load; details are given with the model descriptions.

4.4.2. Axi-Symmetric Modelling

When creating an axi-symmetric model in ANSYS it is only necessary to represent one half of the section, as rotational symmetry equates to, is a special case of, reflectional symmetry. ANSYS requires that the axis of symmetry is placed on the global Y-axis – this means the following conversions apply when the polar co-ordinates of the considered section are translated to the Cartesian co-ordinates used: r to X, θ to Z, z to Y. This is shown in Figure 4.6.

Accordingly an axi-symmetric model is created by creating an area as described above, which is then meshed with a suitable planar element, to which has been applied the axi-symmetric property (through a `KEYOPT`).

Applying the axi-symmetric properties establishes a constitutive relationship between hoop and radial properties, much like that in the equilibrium equation (2.1). This provides effective constraint in the radial direction, requiring only the application of axial restraint to achieve a fully constrained model. In addition to restraining the model, axial constraint is used to control axial stresses within the section; accordingly the particulars of the constraints applied are specific to each end condition, and are hence given with the description of each end condition.

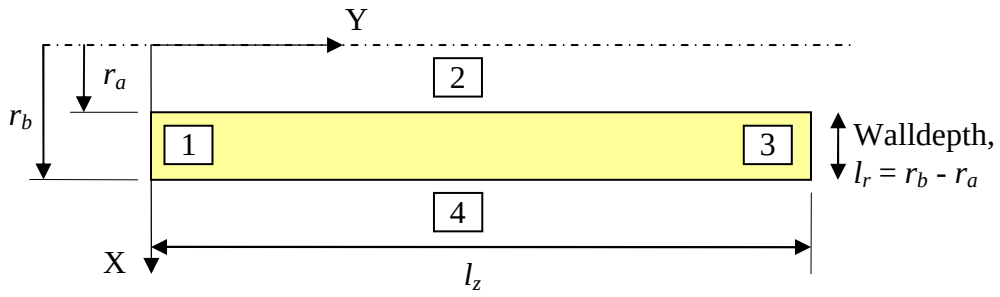

Figure 4.6: Co-Ordinate System and Model Dimensions

4.4.3. Notes Common to ANSYS Modelling

The following notes apply to all models.

4.4.3.1. Element Selection

As explained in sub-section 4.5.4, PLANE183 elements were again selected for this model, to which the axi-symmetric property was applied.

4.4.3.2. Model Geometry and Meshing

To represent a mid-section segment of a tube, only a simple rectangle is required; thus the model consisted solely of a rectangle, appropriately constrained. The aspect ratio of the rectangle was determined in a subsequent sensitivity analysis (see sub-section 4.6.3), but was based on the premise that the mesh would always contain two axial elements. When developing the initial model (prior to the sensitivity analysis) it was quickly determined that the number of axial elements had virtually no effect on the accuracy of the results. This would suggest the use of just one axial element. However, it was found that the *resolution* of results was improved slightly if they were taken along an element boundary. For this reason two axial elements were used, rather than one.

4.4.4. General Plane Strain Models

The three plane strain (True Plane Strain, Open- and Closed-Ends) conditions used identical meshes; one end of which (A-C, as shown in Figure 4.7) is constrained to zero axial displacement, the other (B-D) is constrained to create the desired end condition.

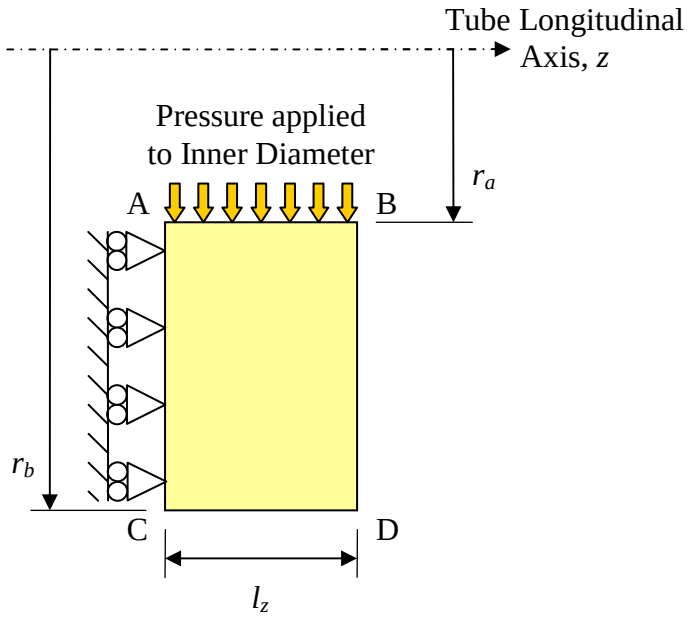

Figure 4.7: Geometry and Common Constraint of General Plane Strain Model

Descriptions of the three Plane Strain conditions, and the constraints required to achieve them, are given below; Figure 4.8 then provides a graphical summary.

4.4.4.1. True Plane Strain

The True Plane Strain condition specifies that total axial strain remains at zero throughout the autofrettage process (and subsequent unloading) at all points within the tube wall; this is achieved through the application of a zero axial displacement constraint to the free end of the section (B-D), as shown by the additional constraints applied to B-D on the left hand diagram of Figure 4.8. If required an arbitrary axial strain may be created within the tube, as the applied displacement need not be zero.

4.4.4.2. Open-Ends

The Open-Ends condition requires that the tube must carry no net axial load (axial stresses summed through the tube wall must sum to zero). Simply leaving the end (B-D) free would achieve this, but the section would not remain plane (indeed, for a thin section this would approximate the Plane Stress condition); instead, the axial displacements of the nodes along B-D are *coupled*. As the tube axis is perpendicular to the surface, this has the effect of keeping the section plane whilst avoiding a constraint load. This is shown by the dashed line along B-D on the central diagram of Figure 4.8.

The Open-Ends condition is one that conceptually would, due to its free end, have the greatest axial variation – to capture these details a long tube section would be required. Figure 2.1 describes the Open-Ends condition graphically.

4.4.4.3. Closed-Ends

The Closed-Ends condition represents a tube which experiences an additional tensile axial force, which results from the pressure of the autofrettage fluid acting on end caps that retain the fluid within the tube. These caps are attached to the ends of the tube (they are not free floating as in the Open-Ends case); essentially the tube develops the required reaction force to resist the pressure force.

The Closed-Ends condition is created within the section by coupling the nodes along B-D (as in the Open-Ends condition) and applying an additional load to that surface. The load is scaled to equal the reaction force of the autofrettage pressure acting over a circular area, of radius r_a. Figure 2.1 describes the Closed-Ends condition graphically.

$$F_{Ax} = P_{AF} \cdot \left(\pi \cdot r_a^2\right) \tag{4.1}$$

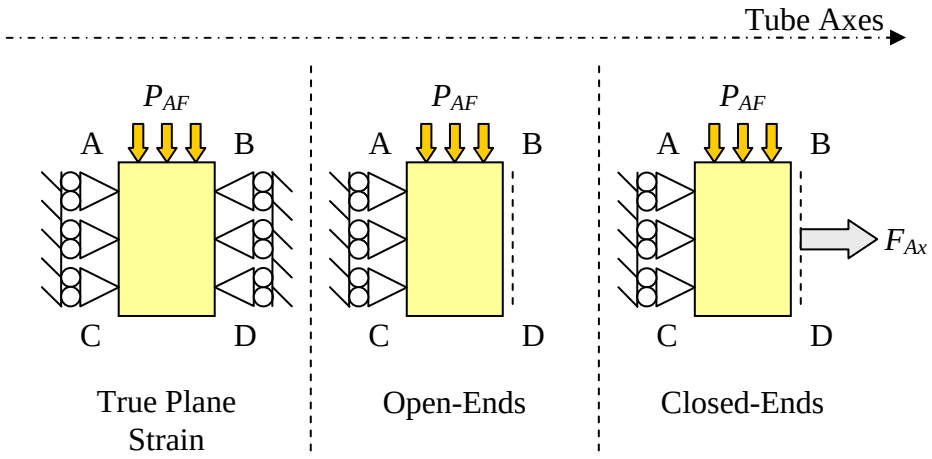

Figure 4.8: Constraint Diagrams, General Plane Strain Models

4.4.5. Plane Stress

The plane stress condition stipulates that there be no axial stresses present (i.e. stresses lie on the r-θ plane). Unlike the Hoop Section model, the Axial Section model cannot use through-plane properties to achieve plane stress (the tube axis now lies in-plane); instead it is accomplished using a very short section. In the absence of an applied pressure (such is the case for the free ends of the section), no normal stresses can exist at a free surface.

The short section is constrained by setting the axial displacement of a single node, at the mid-point of the ID, to zero. The final length was selected during the sensitivity analysis described in section 4.6.

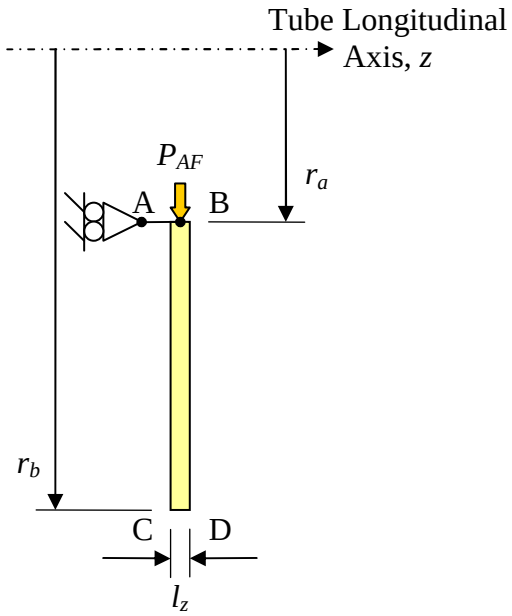

Figure 4.9: Geometry and Constraint Diagram, Plane Stress Model

4.5. FE MODELLING, AND SUMMARY OF COMPARISONS

This section describes how the four different end conditions were modelled within ANSYS; although the final sizing of elements within the models was not established until the section that follows, the models used for both optimisation and comparison shared the same constraint, loading and meshing methodologies.

For that reason, the above methodologies are presented in this section, alongside a summary of the two sets of tests that are detailed fully in the following two sections.

4.5.1. Summary of Comparisons

The comparisons were conducted in two stages to first ensure the stability of results from the ANSYS models, and secondly to assess the accuracy of results obtained from them.

The first stage (section 4.6) was accomplished by investigating the sensitivity of representative results to the size of element used; this allowed meshes to be identified that generated sufficiently accurate results while not being too onerous to solve.

The second stage (section 4.7) used results from the model optimised in the previous stage, and compared them with equivalent results from existing analytical and semi-analytical methods (respectively, Huang's model and the Hencky Programme).

4.5.2. Constraint

With the exception of the Axial Section Plane Stress case, *lines* are constrained in all models to retain the tube sections. In addition these constrained lines act as lines of symmetry, which is crucial for the Hoop section models as they do not include the axi-symmetric element property used in the Axial section models.

4.5.3. Loading

The pressure applied to the tube during the comparisons were determined iteratively based on the desired amount of overstrain, as detailed in section 4.7. Conversely, the precise amount of overstrain was not important for the optimisation process; instead, all models were loaded to a specific pressure (see below for the value). While it would be possible to apply load such that an equal amount of overstrain occurred in all models, the basis of the comparisons was to assess how the models respond to the same input.

Additionally, gauging the extent of plastic strain in the more coarsely meshed models is somewhat imprecise, and reliant upon manual interpolation.

All autofrettage pressures are applied to the lines representing the inner diameters of the respective models, using the ANSYS SFL command. The magnitude of loading would have to be sufficient to cause a significant amount of overstrain (greater than 50%), to provide a valid test of autofrettage conditions and residual stresses.

Selection of a suitable pressure required some initial experimentation which indicated a pressure of similar magnitude to the material yield stress would be suitable. For this reason, the material yield stress was used as the initial value of P_{AF}.

However during initial mesh sensitivity tests it became apparent that in the Plane Stress case, hoop stresses at the inner diameter at peak pressure tended to zero. This exaggerated the relative errors, making the trends effectively meaningless. It was subsequently realised that given a small amount of strain hardening (post-yield equivalent stress $\approx \sigma_{Y0}$), this would always occur in Plane Stress conditions when $P_{AF} = \sigma_{Y0}$; at the inner diameter $\sigma_r = P_{AF} = \sigma_{Y0}$, and $\sigma_z = 0$, so given the von Mises yield criterion, $\sigma_\theta = 0$.

For this reason, 10^9 Pa was selected as the value for P_{AF} for the optimisation process.

4.5.4. Meshing

For both the Hoop and Axial section models, a two-dimensional (planar) element was required. For a mechanical loading scenario, ANSYS includes four such elements:

Element	Number of Nodes
PLANE42	4
PLANE82	8
PLANE182	4
PLANE183	8

Table 4.1: Element Summary

While the two sets of elements (PLANE42 and PLANE182, and PLANE82 and PLANE183) are very similar, PLANE42 and PLANE82 do not support custom material models (see Chapter 6), which immediately ruled out their use. PLANE182 and PLANE183 do support custom material models – being more recently developed, their abilities are a superset of the earlier elements.

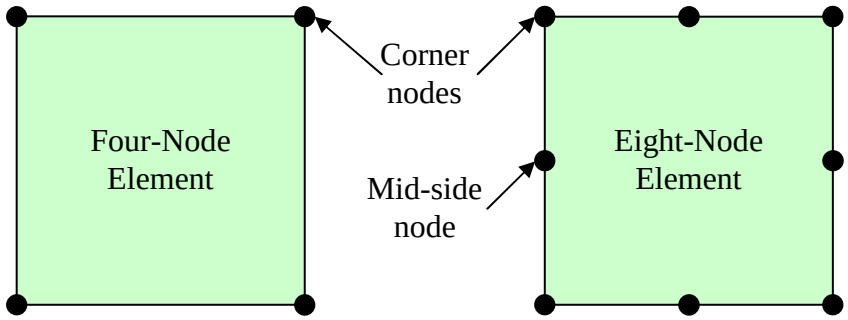

Figure 4.10: Element Nodal Configuration

The addition of mid-side nodes allows for non-linear (quadratic) deformation along the side of an eight-node element; similar results could be obtained using quadruple the number of four-node elements, compared to eight-node elements. It is arguable that the results obtained from the larger number of four-node elements may be somewhat more precise than those using the smaller number of eight-node elements, as a group of four, four-node, elements is more easily able to distort. This precision would require approximately 25% more nodes as well as four times the number of integration points (each of the elements mentioned has four).

However, for an otherwise identical mesh eight-node elements would generate more accurate results than would be the case if four-node elements were used. Also, due to the quadratic deformation which is possible along their sides, eight-node elements are better suited to model curved boundaries.

For this reason, it was decided to use eight-node elements – while this is little different from using four four-node elements, it would reduce the number of element, nodes and integration points required, and it would still be possible to increase the number of eight-node elements beyond the 1:4 ratio if required. Accordingly, PLANE183 elements were selected and used for both Hoop and Axial section models.

Given a section of constant size, the number of elements used to mesh has a great influence on the accuracy of results generated from the model. As such it is important to be able to readily refer to the number of elements specified in different directions along the model. Given the ability to explicitly set the number of divisions along a line when meshing an area in ANSYS, the number of divisions specified to a line was selected as a suitable measure of mesh fineness.

Given the three orthogonal dimensions (radial, axial and tangential), the variables representing the number of divisions were named as listed in Table 4.2:

Property	**Symbol**	**APDL Variable**
Number of axial elements	El_{Ax}	`Axi_Div`
Number of radial elements	El_{Rad}	`Rad_Div`
Number of tangential elements	El_{Tan}	`Tan_Div`

Table 4.2: Mesh Sizing Variables

These are illustrated in the mesh diagrams given in the following two figures.

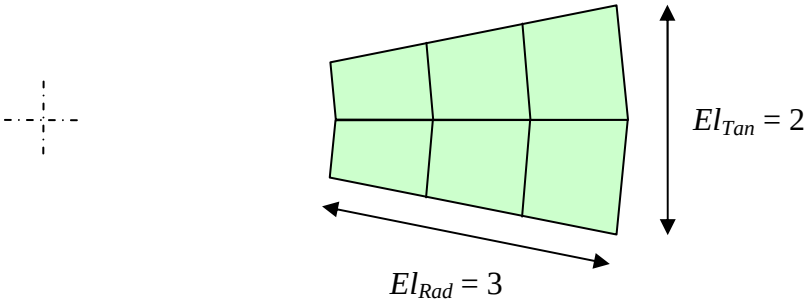

Figure 4.11: Hoop Section Mesh

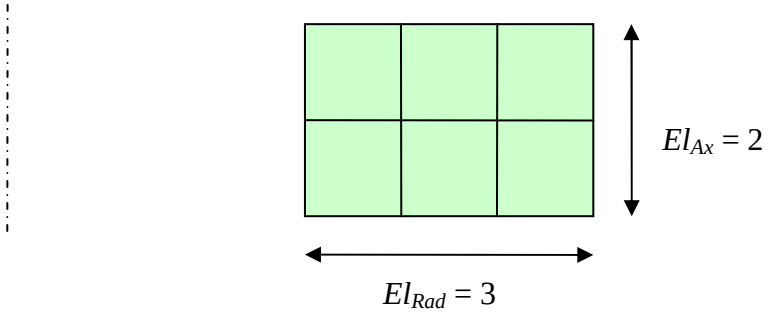

Figure 4.12: Axial Section Mesh

With regards to the axial section model, elements are initially created as square using the following relationship to determine axial length, l_z, from radial length, l_r (r_b - r_a):

$$l_z = \frac{El_{Ax}}{El_{Rad}} l_r \tag{4.2}$$

4.5.5. Material

As this stage work was focussed upon modelling of the autofrettage process and the different conditions in which it could occur, hence only a simplistic material was required. Accordingly a bi-linear, kinematic hardening material (see sub-section 3.2.2 for a description) was selected for the initial optimisation tests. This would allow for plasticity in both the loading and unloading sections of the process. Table 4.3 summarises the material properties applied.

Property	Value
E	209 GPa
v	0.3
σ_Y	1,130 MPa
H	$E/10^9$ = 209 Pa

Table 4.3: Material Properties

During the Comparison tests, to better approximate the early onset of yield following plastic strain, described by the Bauschinger effect, an artificial Bauschinger effect factor (β) was applied to the tube material during unloading. While the material model remains bi-linear, and hence only a rough approximation of the non-linear behaviour observed in metals, material behaviour is one step closer to that desired – a convenient first opportunity for tailoring material properties during unloading.

Alteration of the yield strength in unloading caused a greater degree of reverse yielding to occur, allowing a more meaningful comparison of residual stresses to be made, especially for smaller values of K. See Table 4.6 in section 4.7 for details of the material parameters used.

4.6. MESH SENSITIVITY AND OPTIMISATION

4.6.1. Overview of Tests

The discrete loading/unloading nature of the hydraulic autofrettage models lends them to be assessed both during peak pressure and after total removal of the applied pressure. All cases were assessed using the following tests:

1. Summation of Hoop Stresses at peak pressure
   Hoop stresses are summed throughout the tube wall, and compared with the applied pressure load (demonstrated by Figure 4.13), to investigate how well the internal hoop force agrees with the applied load.

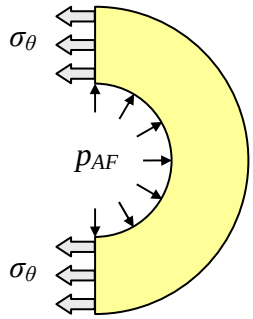

Figure 4.13: Virtual Longitudinal Section, showing Pressure-Hoop Stress Equilibrium

2. Summed residual Hoop Stresses
   The magnitude of residual hoop stresses are summed to determine how well the sum matches the zero pressure load applied. The measure is effectively a mean magnitude, which would equal zero in a perfectly accurate model.

3. Autofrettage and Residual Hoop Stresses at the Inner Diameter.

In addition to the above it was required that sufficient elements be used to allow a reasonable number of results to be taken without excessive interpolation, for meaningful comparison with other methods. It was felt that 100 data points would be a suitable number for such comparisons.

4.6.2. Hoop Section Model

As both the Plane Strain and Plane Stress models were effectively the same (excluding the through-element properties applied), they were both tested in the same ways.

Given the initial refinement of the model (reducing it from a 90° to 1° section), it was already known that the number of tangential element used had virtually no effect on the through-wall results. Accordingly, the mesh sensitivity investigation focused on the effect of the number of radial (through-wall) elements present.

The number of radial elements was varied from 10 to 200, while the number of tangential elements was kept at 2, the smallest number that would still allow results to be taken along element edges at the midpoint of the section. This is potentially more accurate, as the mid-side nodes of the PLANE183 element effectively double the number of nodes on the results path.

Solely varying the number of radial elements would be detrimental to element geometry, if the angle of section, θ_{Sec}, was not adjusted. For this reason the model was scripted to calculate θ_{Sec} on a case by case basis, to ensure near square element geometry at the inner diameter (where maximum stresses and strains are observed during autofrettage).

Figure 4.14 shows the mesh geometries resulting from the following values of El_{Rad}: 10, 30 and 100.

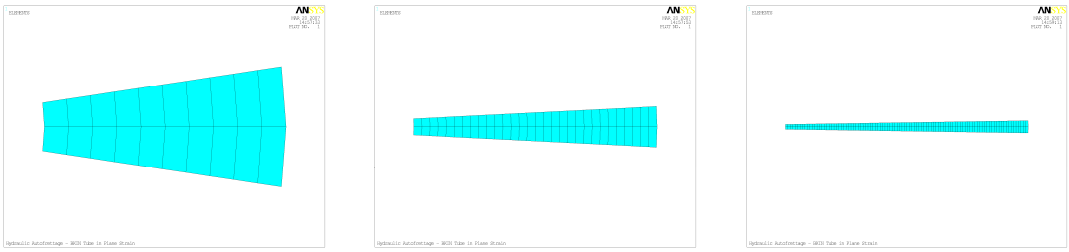

El_{Rad} = 10 El_{Rad} = 30 El_{Rad} = 100

Figure 4.14: Mesh Geometry of Hoop Section model as radial elements increase

The values of θ_{Sec} that result from the selected range of El_{Rad} values are summarised in Table 4.4.

El_{Rad}	θ_{Sec} (°)
10	17.189
20	8.594
30	5.730
40	4.297
50	3.438
60	2.865
70	2.456
80	2.149
90	1.910
100	1.719
110	1.563
120	1.432
130	1.322
140	1.228
150	1.146
160	1.074
170	1.011
180	0.955
190	0.905
200	0.859

Table 4.4: Angles of Section

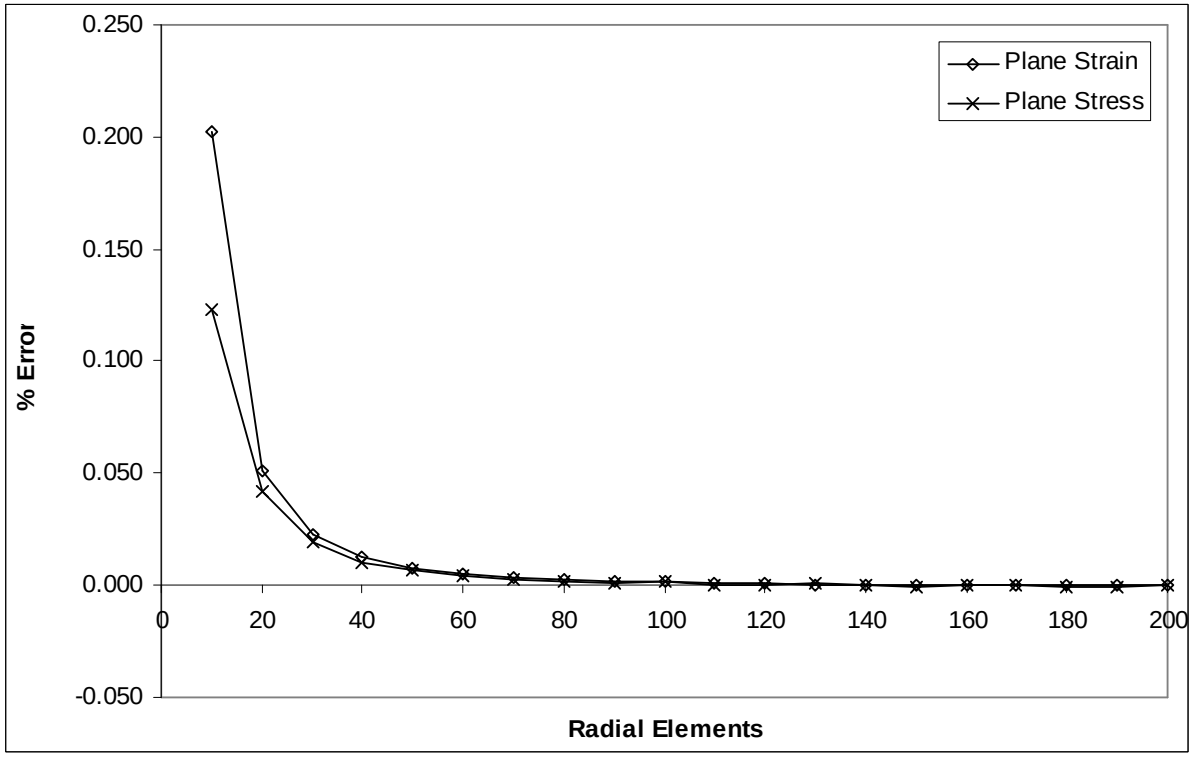

Figure 4.15: Relative Error of Summed Hoop Stresses at Peak Pressure

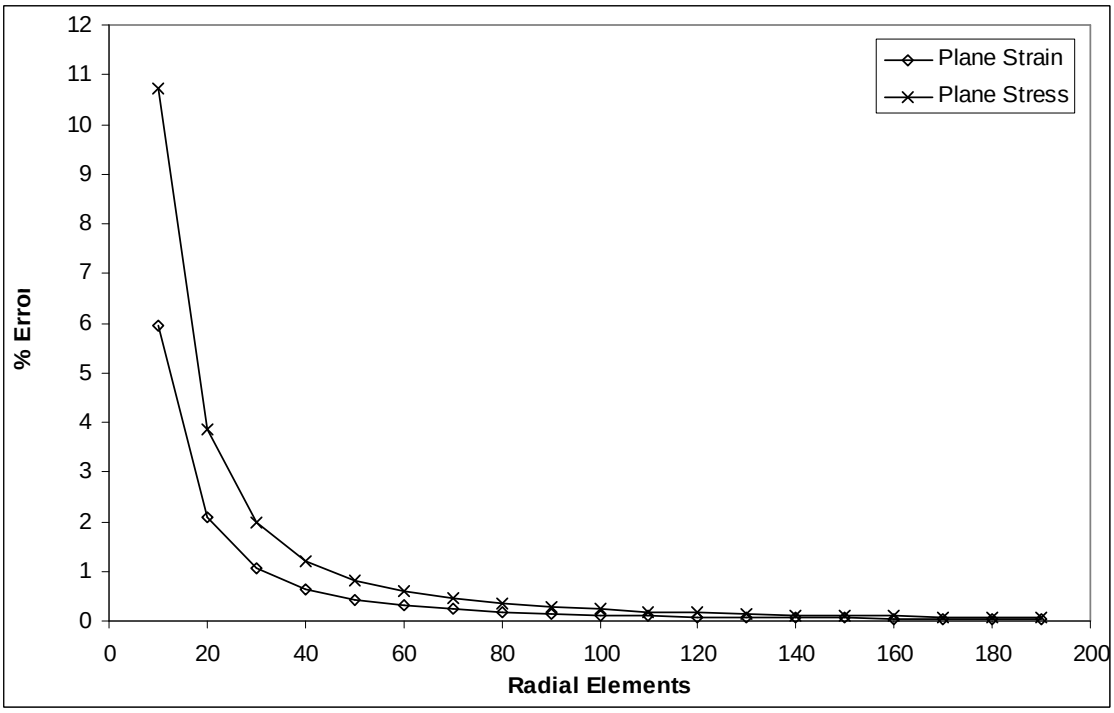

Figure 4.16: Relative Error of Hoop Stresses (at Peak Pressure) at the ID

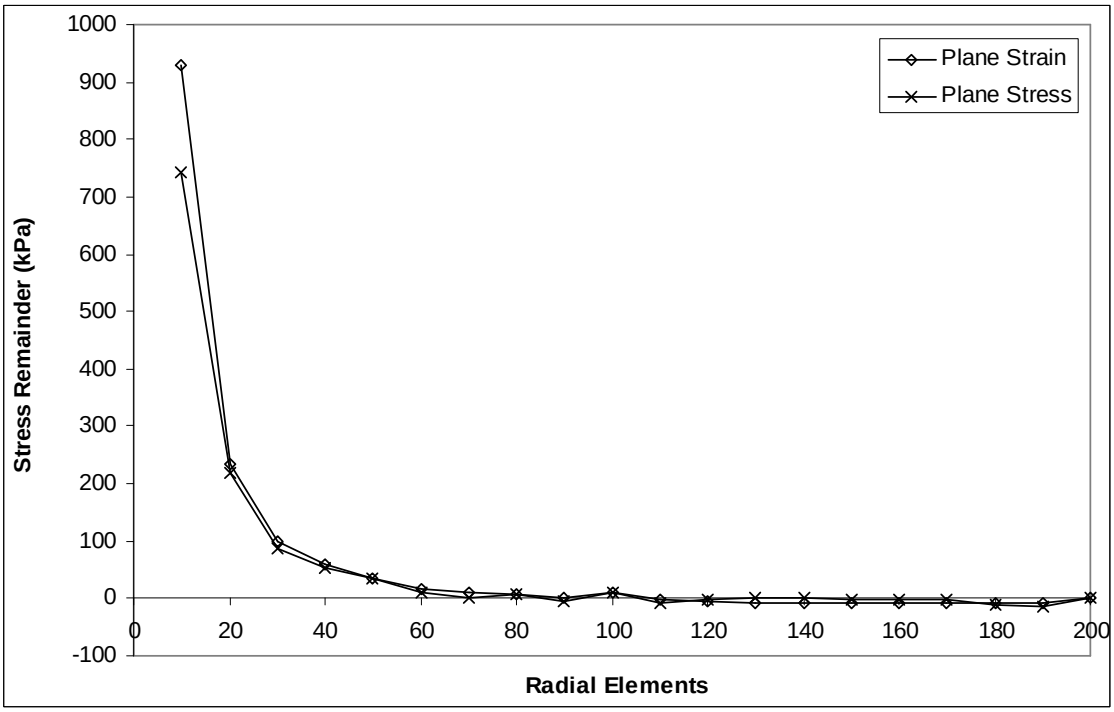

Figure 4.17: Summed Residual Hoop Stresses

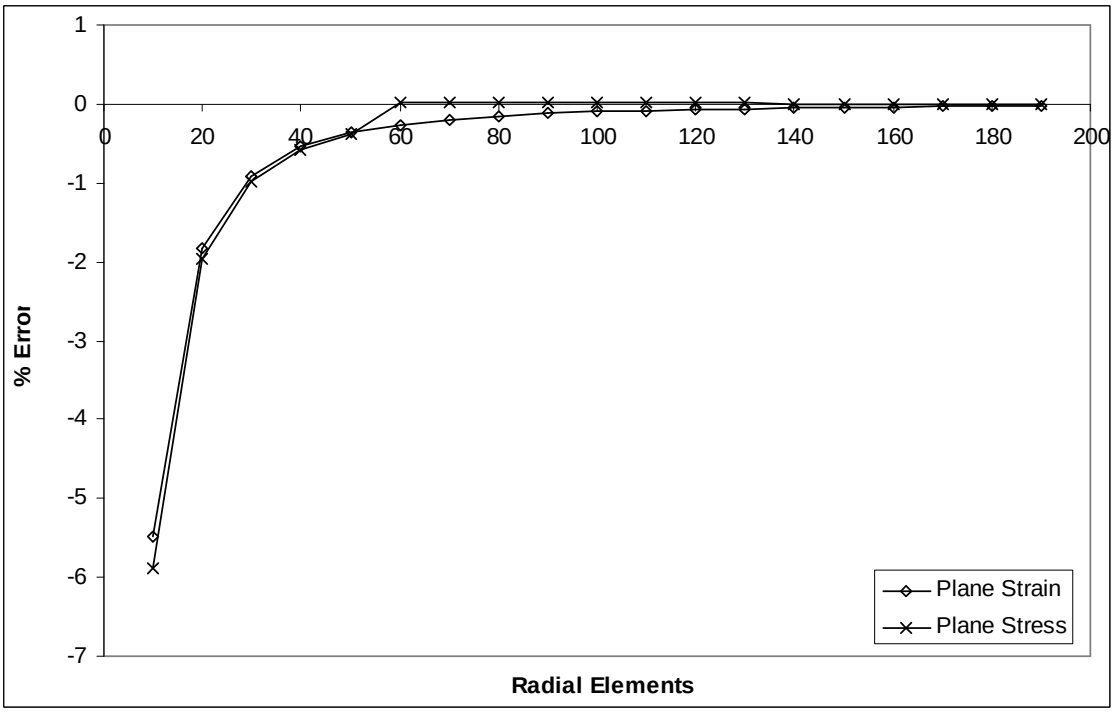

Figure 4.18: Relative Error of Residual Hoop Stresses at the ID

4.6.2.1. Discussion

The summed hoop stresses tend to approximate the applied pressure load closely; Figure 4.15 shows the errors exhibit relatively high value when El_{Rad} = 10 (approximately 0.020% and 0.0125% in the Plane Strain and Plane Stress cases, respectively), which decrease rapidly – error is within 0.01% for El_{Rad} = 50, and approximately 0.001% when El_{Rad} = 100. The slight fluctuation is likely due to the fact the axi-symmetry is not intrinsically understood by the model, and is hence reliant upon the applied constraints. That the fluctuations centre on the zero error line indicates internal force equilibrium is accurately achieved.

Figure 4.16 shows that in both cases the relative error of hoop stresses at the inner diameter decreases monotonically towards zero, and is comfortably less than 1% once El_{Rad} equals 50 or more.

The summed residual hoop stresses (relative error is not assessed as the value converges to zero) also decrease rapidly to within 50 kPa for values of El_{Rad} = 50 or more, as shown in Figure 4.17. This reduced to within 10 kPa once El_{Rad} equals 70 or more.

Aside from the first point, the plot given in Figure 4.18 shows a progressive decrease of the relative error of hoop stresses as El_{Rad} increases. Specifically, error reduces to less than 0.1% once El_{Rad} equals 50, and continues decreasing thereafter.

Based on the above observations of errors, it was apparent that a value of El_{Rad} = 70 or greater would give suitable accuracy. Hence, it was decided to use a value of El_{Rad} = 100 for future investigations; this increased value would allow 100 data points to be comfortably taken.

4.6.3. Axial Section Model

For all four Axial Section model, it was necessary to ensure that they possessed sufficient radial elements to allow for accurate results. In addition, it was also necessary to ensure the section used for the Plane Stress model was thin enough such that axial stresses were small enough to be neglected.

The Axial Section models were optimised using the same procedure as the Hoop section models, albeit by varying section length, l_z, (as opposed to θ_{Sec} that was varied in the Hoop section) to ensure square element geometry. In the Plane Stress case, the range of El_{Rad} values was adjusted to provide the thinner sections required to approximate plane stress. Figure 4.19 contains images of the meshes generated for three of the El_{Rad} values used in the optimisation.

El_{Rad} = 10 El_{Rad} = 30 El_{Rad} = 100

Figure 4.19: Mesh Geometry of Axial Section model as radial elements increase

The range of radial divisions used for the optimisation of both the general plane strain and Plane Stress model are listed in Table 4.5.

All four models were subjected to the tests laid out in sub-section 4.6.1, and additional tests were carried out on the Plane Stress model to ensure the plane stress state was being effectively simulated. The results are displayed in sub-sub-sections 4.6.3.1 and 4.6.3.3, respectively. The Plane Stress specific tests are also detailed in sub-sub-section 4.6.3.3.

Plane Strain, Open- and Closed-Ends		Plane Stress	
El_{Rad}	l_z/r_a	El_{Rad}	l_z/r_a
10	$3.000*10^{-1}$	200	$1.500*10^{-2}$
20	$1.500*10^{-1}$	400	$7.500*10^{-3}$
30	$1.000*10^{-1}$	600	$5.000*10^{-3}$
40	$7.500*10^{-2}$	800	$3.750*10^{-3}$
50	$6.000*10^{-2}$	1000	$3.000*10^{-3}$
60	$5.000*10^{-2}$	1200	$2.500*10^{-3}$
70	$4.286*10^{-2}$	1400	$2.143*10^{-3}$
80	$3.750*10^{-2}$	1600	$1.875*10^{-3}$
90	$3.333*10^{-2}$	1800	$1.667*10^{-3}$
100	$3.000*10^{-2}$	2000	$1.500*10^{-3}$
110	$2.727*10^{-2}$	2200	$1.364*10^{-3}$
120	$2.500*10^{-2}$	2400	$1.250*10^{-3}$
130	$2.308*10^{-2}$	2600	$1.154*10^{-3}$
140	$2.143*10^{-2}$	2800	$1.071*10^{-3}$
150	$2.000*10^{-2}$	3000	$1.000*10^{-3}$
160	$1.875*10^{-2}$	3200	9.375*10-^{4}
170	$1.765*10^{-2}$	3400	$8.824*10^{-4}$
180	$1.667*10^{-2}$	3600	$8.333*10^{-4}$
190	$1.579*10^{-2}$	3800	$7.895*10^{-4}$
200	$1.500*10^{-2}$	4000	$7.500*10^{-4}$

Table 4.5: Lengths of Section

4.6.3.1. Common Tests

The results to the tests described in sub-section 4.6.1 are given below. Figure 4.20 compares the summed hoop stresses throughout the tube wall at peak pressure with the applied pressure load. Figure 4.21 plots the relative error of hoop stresses at the ID between progressively finer meshes. Figure 4.22 sums the residual hoop stresses calculated. Figure 4.23 plots the relative error of residual hoop stresses at the ID between progressively finer meshes.

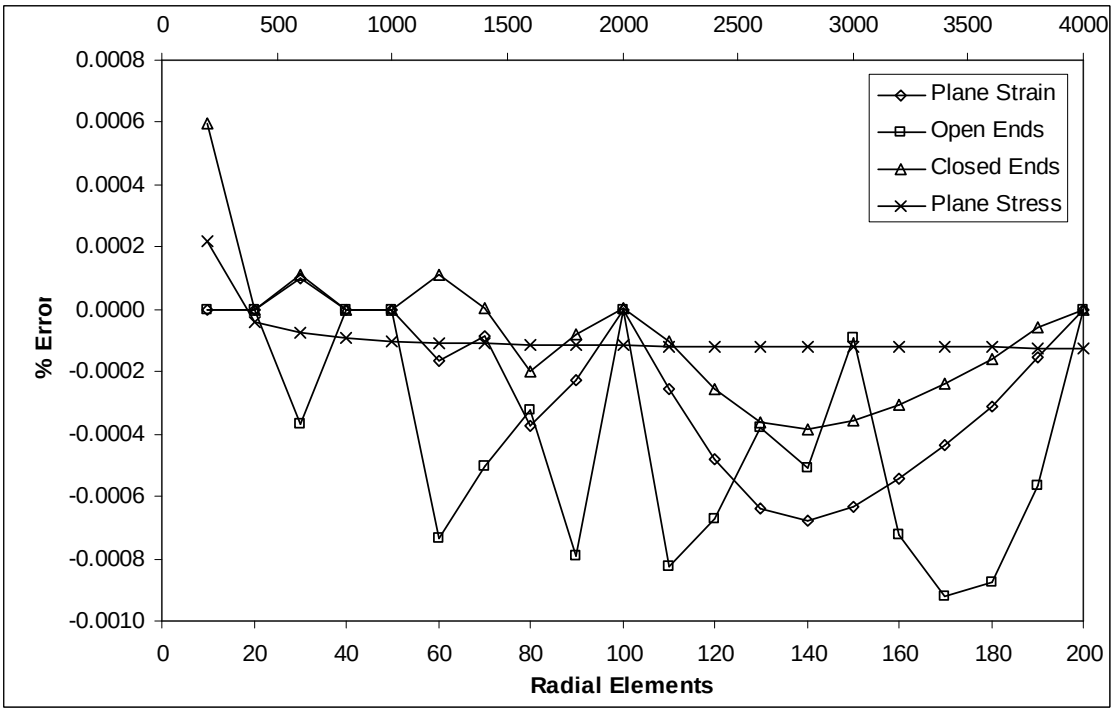

Figure 4.20: Summed Hoop Stresses at Peak Pressure (Plane Stress results plotted on second x-axis)

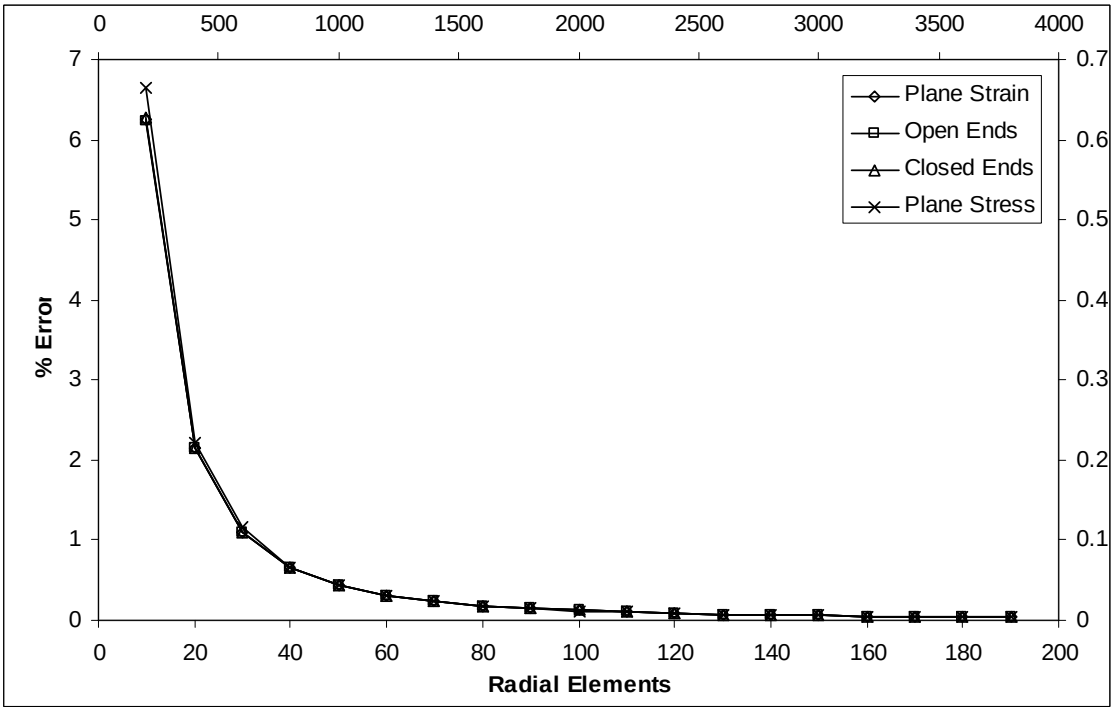

Figure 4.21: Relative Error of Hoop Stresses (at Peak Pressure) at the ID (Plane Stress results plotted on the second set of axes)

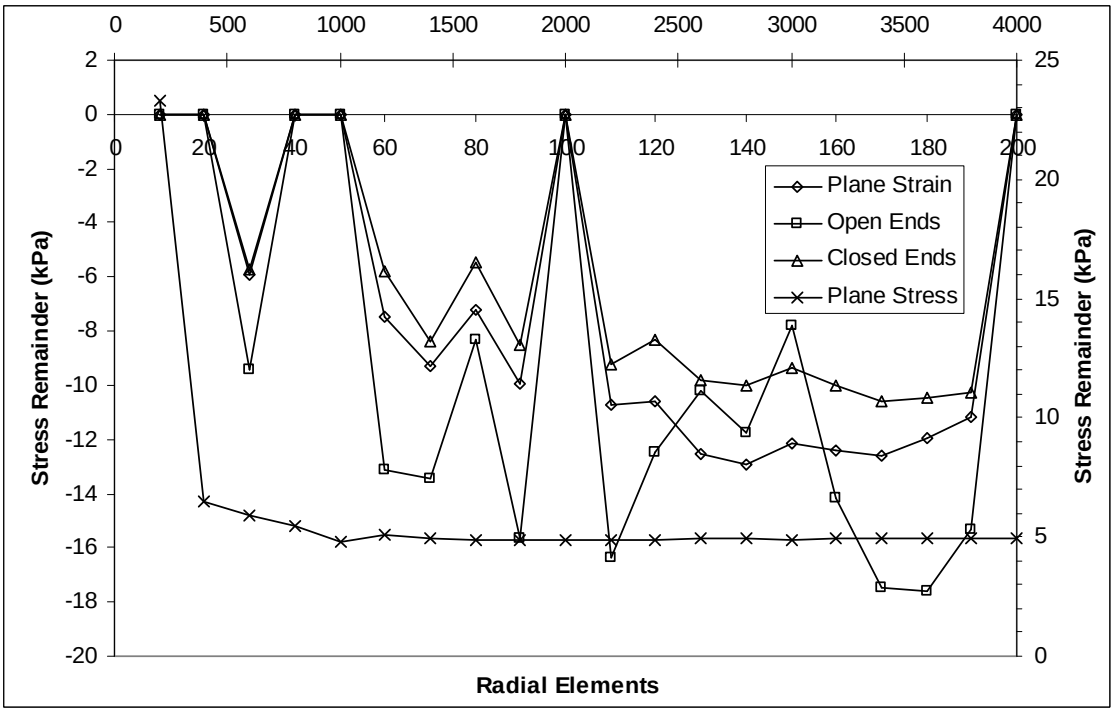

Figure 4.22: Summed Residual Hoop Stresses (Plane Stress results plotted on the set of axes)

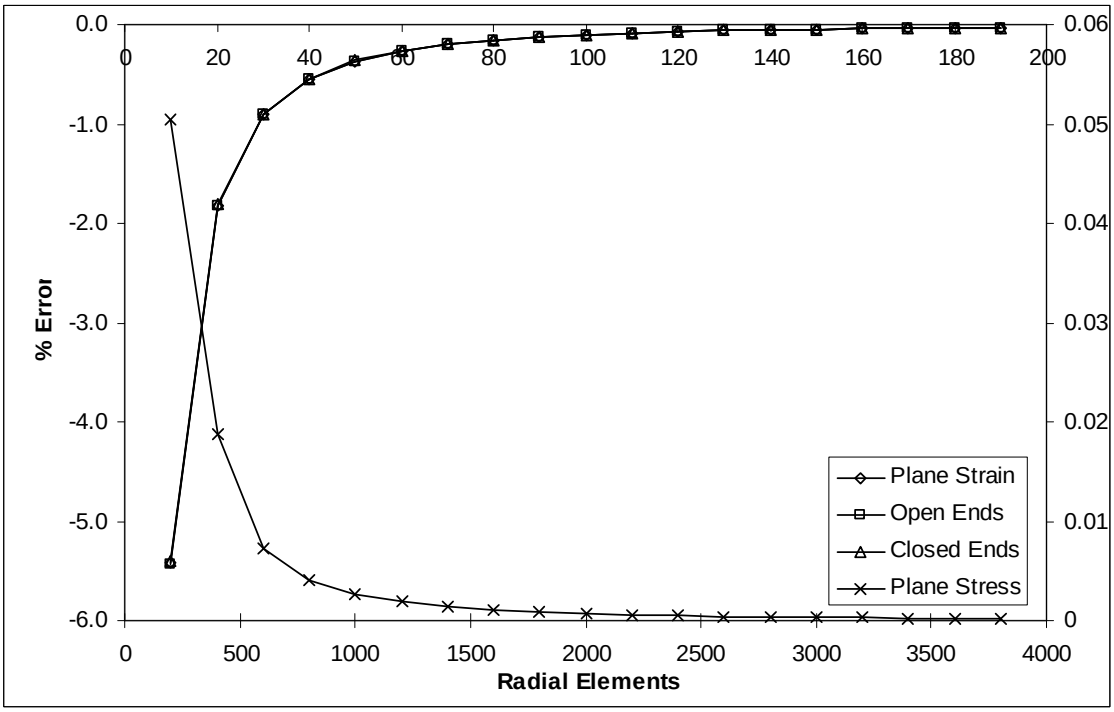

Figure 4.23: Relative Error of Residual Hoop Stresses at the ID (Plane Stress results plotted on the set of axes)

4.6.3.2. Discussion

The following Discussion makes no mention of the results from the Plane Stress model, as the high number of radial elements used caused errors to be well within acceptable levels; also the observed error decreases progressively with increasing El_{Rad}. Instead, the following observations apply solely to the general plane strain models.

No particular trend was observed (Figure 4.20) when comparing summed hoop stresses with the applied pressure; as the errors were consistently small, and given the range of radial divisions applied, it was judged that all meshes used satisfied the equilibrium criterion. Although the errors transition from negative to positive, given the small errors this pattern was thought to be insignificant.

This outcome was not unexpected, as the FE solution must reach equilibrium, even when using a coarse mesh, to attain a converged solution; a finer mesh would instead generate more accurate predictions of the *distribution* of stresses within the model.

The relative error of hoop stresses at the inner diameter (Figure 4.21) showed a stereotypical, non-linear decrease as the number of radial elements was increased – indicating that the calculated distribution of stresses becomes more accurate as the mesh is made finer. A relative error of 0.2% was obtained when 80 radial elements were used.

Similar to the summed hoop stresses during autofrettage, the summed residual hoop stresses (Figure 4.22) reveal little regarding the effect of mesh fineness on total residual stresses. As such, they do not provide any extra information for the optimisation of the mesh.

Conversely, the residual hoop stresses at the inner diameter (Figure 4.23) are a useful means of optimising the mesh; the data form another curve, showing progressive reduction of relative error. Relative error reduced to less than 1% once $El_{Rad} > 30$.

Taken together, the observations made on the above plots indicate that 70-80 radial elements would be required to give the required accuracy. Accordingly $El_{Rad} = 100$ was selected, which would also serve to give enough resolution when taking results along radial paths for meaningful future comparisons.

The Plane Stress results show much lower levels of error, as would be expected due to the far greater number of elements used. For this reason the above tests are not useful for sizing the mesh for the Plane Stress case; as described in sub-section 4.4.5, obtaining a sufficiently thin section would determine the model geometry, and hence mesh. Instead, the results serve as an indicator of how the errors vary for values of El_{Rad} much greater than were used for the general plane strain cases.

4.6.3.3. Plane Stress

As the Axial Section model does not have the facility to explicitly set the plane stress conditions, it must approximate it using a thin section (short l_z). For this reason, it was important to ensure that the approximation was good, so that axial stresses could be considered to be effectively zero (these checks were in addition to those described above for all Axial Section models).

This was achieved in two ways:

1. Summing the magnitude of axial stresses through the tube wall, to assess the total amount of stress present,
2. Comparison of peak axial stresses.

The requisite data were taken during the simulations used to generate the results for the hoop stress sensitivity checks (sub-sub-section 4.6.3.1), and are plotted below (stress values are normalised with respect to the initial yield stress, σ_{Y0}).

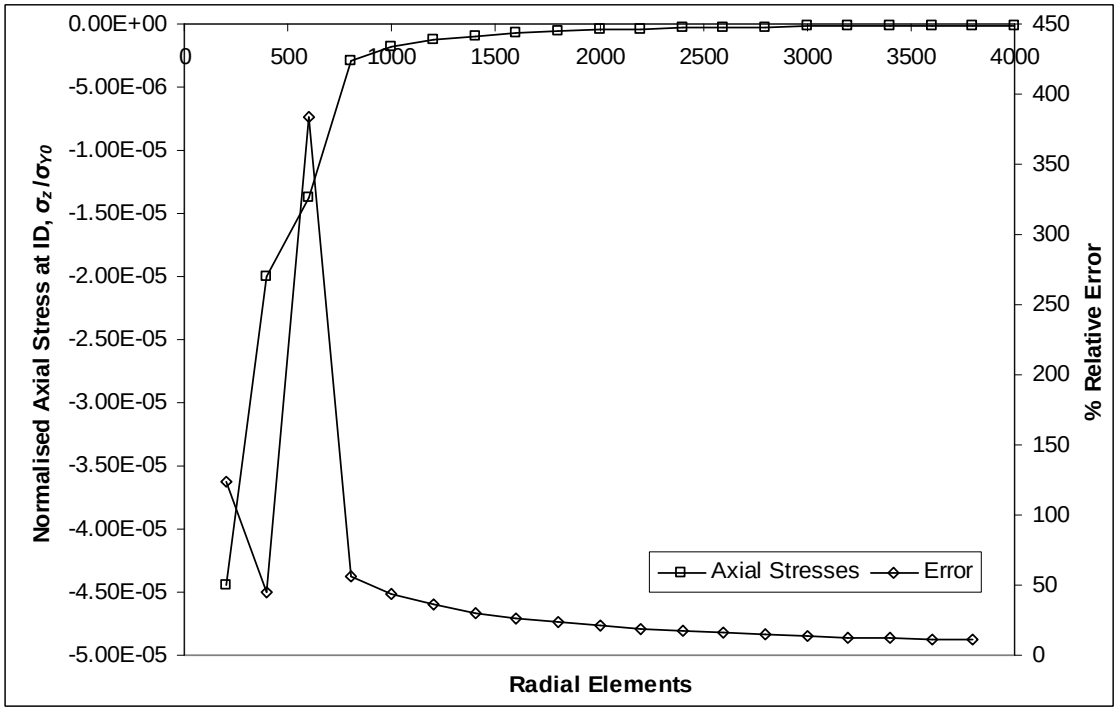

Figure 4.24: Peak Axial Stress during Autofrettage, and Relative Error

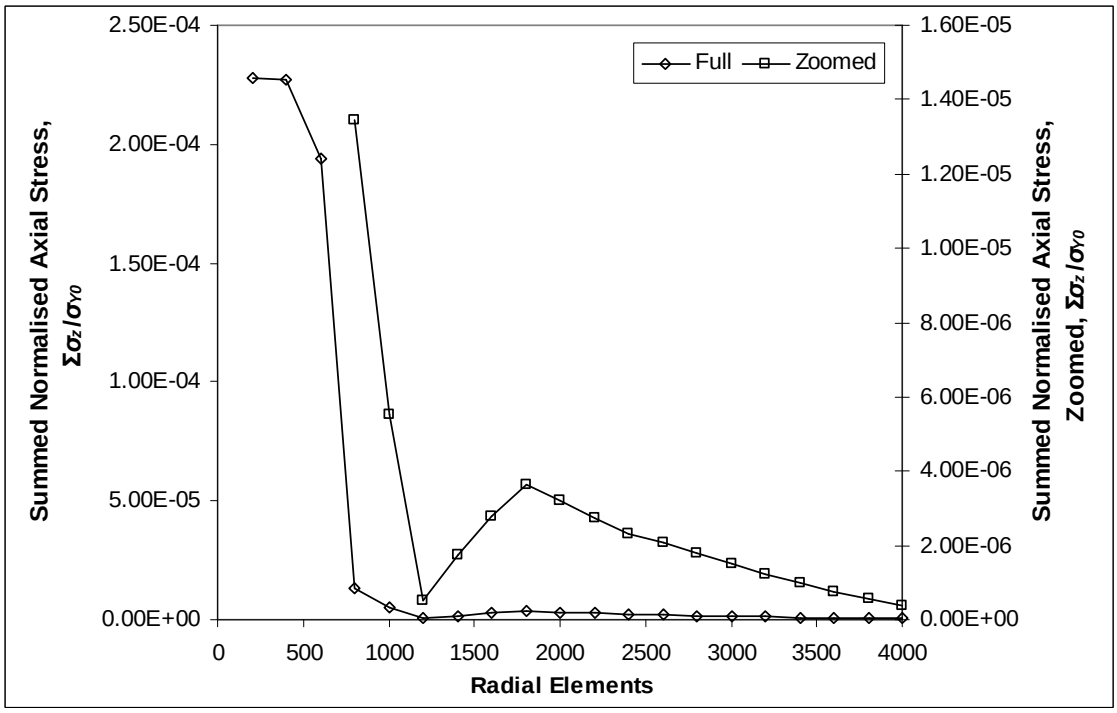

Figure 4.25: Summed Axial Stresses during Autofrettage

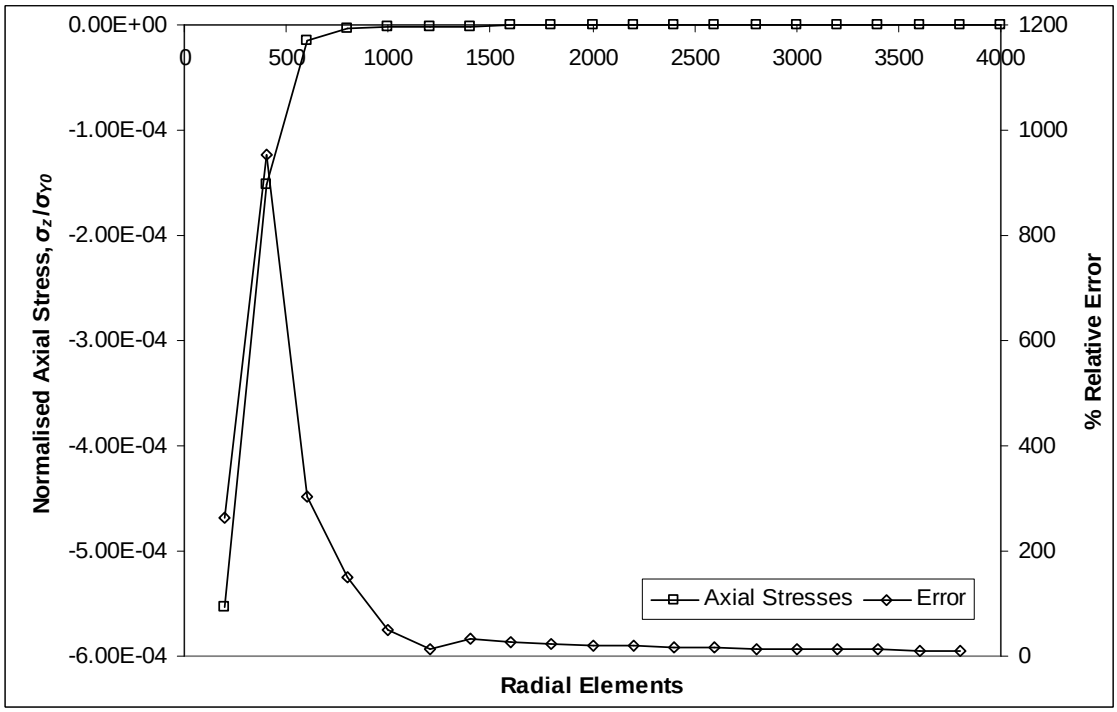

Figure 4.26: Peak Residual Axial Stress, and Relative Error

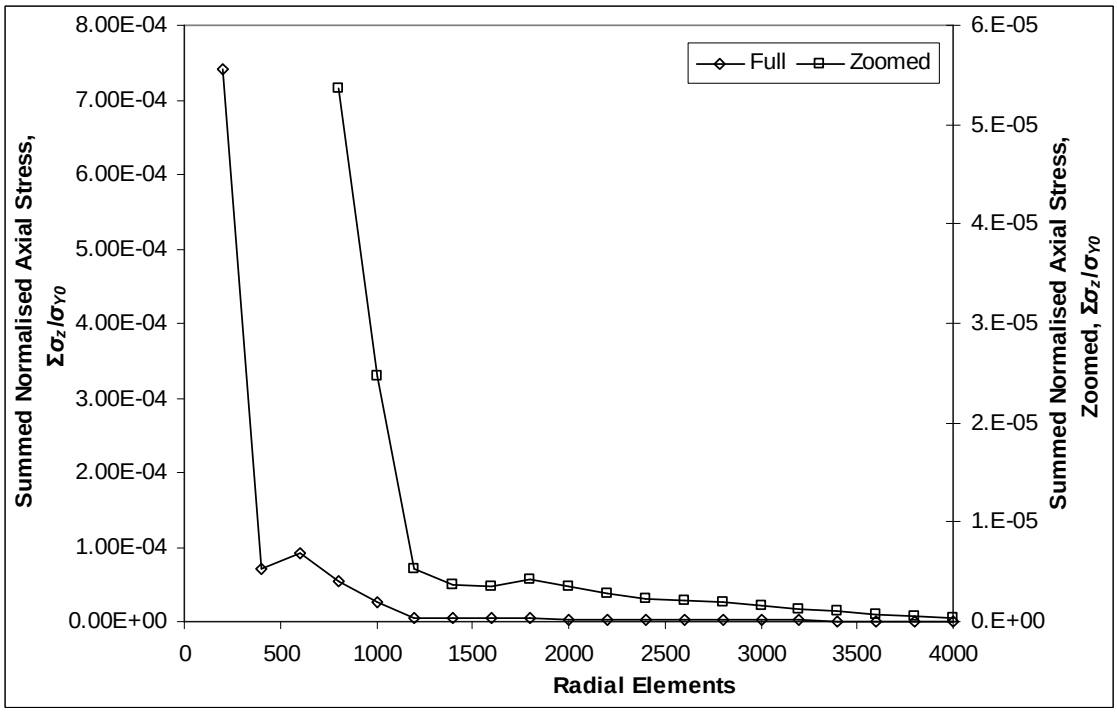

Figure 4.27: Summed Residual Axial Stresses

4.6.3.4. Discussion

The peak axial stress, shown in Figure 4.24, rapidly decreases until El_{Rad} = 800 by which point the value plateaus. Relative error is larger than would otherwise be expected as axial stress is converging towards zero (the reason the autofrettage pressure was adjusted, described in sub-section 4.5.3, to ensure hoop stress at the inner diameter in the Plane Stress case did not converge to zero).

Figure 4.25 shows summed axial stresses following a similar pattern to the peak value; the value rapidly drops until El_{Rad} = 800, after which decrease is more gradual.

Peak residual axial stresses (Figure 4.26) exhibit a pattern similar to that shown by the autofrettage values, albeit with the rapid decrease occurring by the point when El_{Rad} = 600. While the initial magnitude of the stresses are larger than in the autofrettage case they rapidly reach that of the autofrettage stresses, again once El_{Rad} = 600 or more.

Figure 4.27 shows the summed residual axial stresses rapidly decreasing in the range $200 < El_{Rad} < 400$, then undergoing a period of moderate reduction, until finally reaching a consistently low level once El_{Rad} = 1200.

The above observations show that axial stresses (peak and summed) generally reduce to acceptable levels once El_{Rad} exceeds 600-800, or in the summed residual case, 1200. Accordingly, 1500 was selected as a suitable value of El_{Rad} to use; comfortably above the values indicated by the sensitivity analysis, but not excessively so (keeping model

size manageable). This value also far exceeds that required to output results of a resolution suitable for comparison with other methods.

4.7. COMPARISON AND VALIDATION

4.7.1. Overview

Once the mesh sensitivity analysis had been completed, the Axial Section model was validated against two other existing methods (Huang's method, and the Hencky Programme) of simulating hydraulic autofrettage [29]. All three methods use the von Mises criterion to establish equivalent stresses and strains, and hence predict yielding and subsequent plasticity. At this stage it was decided that, whilst it produced accurate answers, the Hoop Section model was too limited in potential to be worth formal validation.

The tests carried out were intended to determine whether the physical process of autofrettage was accurately simulated by the ANSYS model, hence a simple bi-linear material representation was used. Non-linear material representation would be implemented and validated at a later stage, independent to this analysis; development of the customised material model commenced once the accuracy of modelling autofrettage under the range of four end conditions had been confirmed.

4.7.2. Comparisons

The FE model was tested in two sets of comparisons, to 70% overstrain: firstly, against both Huang's model and the Hencky programme in the incompressible, True Plane Strain condition; secondly, against the Hencky programme in a variety of end conditions (True Plane Strain, Plane Stress, Open- and Closed-ended) for a more standard material – $\nu = 0.3$. The modelling of the four end conditions is described earlier this chapter, in sub-sections 4.4.4 and 4.4.5. For each, two wall ratios were used, $K = 2.0$ and $K = 2.5$, to ensure the models were not limited to a specific geometry.

As stated above, the focus of this comparison was upon geometric accuracy rather than material fidelity – accordingly, a simplistic bi-linear kinematic hardening material was used, as well as keeping the Young's and Tangent moduli constant in loading and unloading (i.e. $E_1 = E_2 = E$, $H_1 = H_2 = H$). This allowed plasticity during both loading and unloading to be investigated, whilst leaving the physical constraints as the focus of the comparison.

It was desired to apply some rudimentary alteration to the material in unloading, so that the yield stress was defined by the Bauschinger effect (i.e. equals $-\beta\sigma_{Y0}$). For each method, once peak pressure had been released the reverse yield stress of the material was altered to equal $\beta\sigma_y$ (peak equivalent stress is not known prior to the calculation of the peak pressure state). This was desirable for the two wall ratios used, as it allowed and similar amounts reverse yielding to occur, both sufficient to be properly assessed. In addition, reverse yielding would occur to a radius more similar to that expected if a

realistic material model had been used. This was accomplished using *temperature profiles*; the means of achieving such alteration are described in sub-section 4.7.3.

Accordingly, two temperature profiles are defined (one for the loading process, one for unloading); between load steps, the material is swapped from the loading profile to unloading. Additionally, an extra solution control was set, to cause the material to be immediately changed, stepped rather than progressively interpolated between the two profiles during the course of the second load step.

Figure 4.28 gives a graphical interpretation of the material.

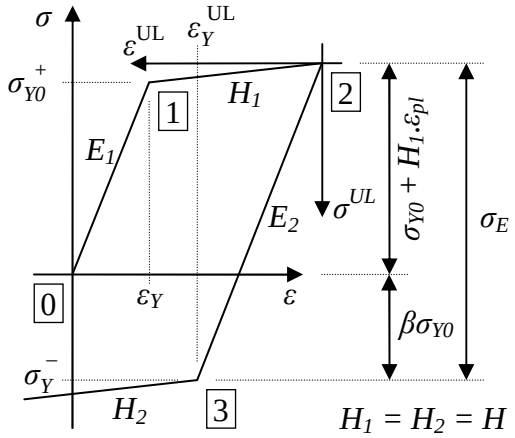

Figure 4.28: Bi-linear material model, incorporating the Bauschinger effect

The material parameters are summarised in Table 4.6 (compare with Tables 4.7 and 4.8, which contain the values used in Huang's Method). Two values of β were specified to ensure sufficient reverse yielding occurred to allow a useful comparison of it to be made between methods.

Property	Value
E	209 GPa
v	0.3
σ_{Y0}	1,100 MPa
H	E/10, 20.9 GPa
β	0.7, K = 2.5
β	0.45, K = 2.0

Table 4.6: Material Parameters for Comparison Tests

4.7.3. Specification of Material Model within ANSYS

To model the Bauschinger effect, between the loading and unloading load steps the tube material must be altered from the default kinematic hardening model; the Bauschinger effect is represented by changing the yield stress of the region of the tube which underwent plastic deformation – the primary yield zone ($r_a \leq r \leq r_p$).

It is not possible to directly edit material properties or change material during solution – in terms of the hydraulic autofrettage models described here, redefining the material properties assigned to the tube once autofrettage pressure is released, would cause the plastic strain history of the tube being lost. However, a different temperature profile may be selected without any such loss. This is a common method of altering material properties in FEA when it would not otherwise be possible, and doesn't necessarily involve *actual* temperature change. A material may be defined with multiple temperature profiles, each (for example) containing values for E, ν, σ_{Y0} and H.

In this case the process is considered to be isothermal, hence no consideration of temperature change is required. By default, ANSYS assumes a temperature change is a thermal process, and uses Rice's Hardening law to calculate stress relaxation due to temperature change; this is deactivated.

As stated in sub-section 4.7.2, two temperature profiles were used; the first matching the initial material state, the other the deformed material state, calculated between stages of the procedure. The deformed profile is again a bi-linear kinematic hardening material, but differs from the initial state as the initial yield stress (σ_{Y0}^{U}) is selected to ensure $\sigma_{Y0}^{U} = \sigma_E/2$, where, from Figure 4.28, $\sigma_E = \sigma_{Y0}\ (1 + \beta) + H_1.\varepsilon_{pl}$). Reverse yielding then begins at $2\sigma_{Y0}^{U}$ below the peak value (kinematic hardening), which equals σ_E. The peak equivalent stress experienced by the tube at its ID is used to determine $\sigma_{Y0} + H_1.\varepsilon_{pl}$.

To reiterate, the material properties are otherwise unchanged between the two temperature profiles – i.e. a change in *temperature* is *not* being simulated – as mentioned above, the titular change of temperature is merely a convenient method of tailoring the material properties to simulate the Bauschinger effect.

4.7.4. First Comparison

The following notes detail how the three models were configured for use in this comparison.

4.7.4.1. Huang's Model

As the Plane Strain, incompressible conditions are already present, only material properties need to be set. Material properties are defined through appropriate selection of the parameters used by the model; sub-sub-section 2.4.2.4 describes the model, with the material's governing equations given in Table 3.1, which are described in, and illustrated in Figure 3.10.

Calculation of A_1 and A_3 is described in sub-section 3.6.2, and B_1 and B_2 are exponents of plastic strain (which here equal one, denoting linear stress response to plastic strain).

Table 4.7 summarises the values used as the material parameters during the loading phase.

$K = 2.0$		$K = 2.5$	
A_1	990 MPa	A_1	990 MPa
A_2	20.9 GPa	A_2	20.9 GPa
B_1	1	B_1	1

Table 4.7: Loading Parameters, Huang's Method

Table 4.8 contains the three parameters relating to the unloading phase, which depend upon the prior plasticity in the tube. Accordingly, two sets of unloading parameters must be defined, one for each wall ratio. These account for the fact that for a given overstrain, the bore plastic strain, on which strain hardening and the Bauschinger effect depend, increases with wall ratio. Huang's method assumes a uniform response to plastic strain in the initial yield zone (as does the ANSYS model), meaning that the elastic range (from peak stress to reverse yield), σ_E, is the same throughout the primary yield zone.

$K = 2.0$		$K = 2.5$	
A_3	1,623 MPa	A_3	1,999 MPa
A_4	20.9 GPa	A_4	20.9 GPa
B_2	1	B_2	1

Table 4.8: Unloading Parameters, Huang's Method

4.7.4.2. ANSYS Model

Plane Strain conditions are applied, as described in sub-sub-section 4.4.4.1, and a Poisson's ratio, v, of 0.499999 (to match the incompressible assumption made by Huang's Model) is specified when defining the elastic material properties (using the `MPDATA` command).

Setting $v = 0.5$ is possible within ANSYS, but it will likely cause the solution to fail as singularities appear when calculating the stiffness matrix.

4.7.4.3. Hencky Programme

Plane Strain conditions are set within the Hencky Programme by specifying that all of the concentric shells possess zero axial strain. Also, v is set to 0.5 during direct comparison with Huang's (incompressible) model.

4.7.5. Second Comparison

The FE model was then tested against the Hencky Programme, across the full range of end conditions, using a compressible material. Configuration of the methods was as in the first comparison, albeit with ν set to 0.3, and the use of Plane Strain, Plane Stress, Open- and Closed-Ends conditions.

4.7.6. Results

The results obtained during this validation process are plotted below. During any analysis consisting of a number of stages (for example, this analysis treats autofrettage and subsequent unloading as separate stages), it is important to make comparison at each stage, thus allowing causes for deviation to be more readily identified. However, only one set of autofrettage stresses (for K = 2.0 in the first comparison) is displayed here, as during these analyses it was observed that autofrettage stresses were so similar that any more would be repetitious.

Indeed residual stresses are of more interest, both in this study and whenever fatigue life assessments are made, especially the hoop component at the inner diameter; consequently, all such results are displayed below. Additionally, as the unloading process is fundamental to the prediction of residual stresses, it is crucial that it be investigated.

4.7.6.1. Normalisation of Results

The radial position is normalised using the following expression to relate it to the tube wall thickness:

$$r_N = \frac{r - r_a}{r_b - r_a} \tag{4.3}$$

The stresses are normalised against the yield stress in simple tension (σ_{Y0}):

$$\sigma_N = \frac{\sigma}{\sigma_{Y0}} \tag{4.4}$$

4.7.6.2. First Comparison: Huang-Hencky-ANSYS, ν = 0.5

The results from the first stage of the comparison are shown below: Figure 4.29 plots the *Autofrettage* stresses (radial, hoop and axial) from the ANSYS model against those predicted by Huang's method and the Hencky Programme for K = 2.0; Figure 4.30

plots the *residual hoop* stresses from the ANSYS model against those predicted by Huang's method and the Hencky Programme for both K = 2.0 and 2.5. In both Figures, the results from the Hencky Programme and Huang's method are shown as lines (generally too close to be distinguishable), and the results from the ANSYS model are shown as symbols overlying the corresponding plots from the other two methods.

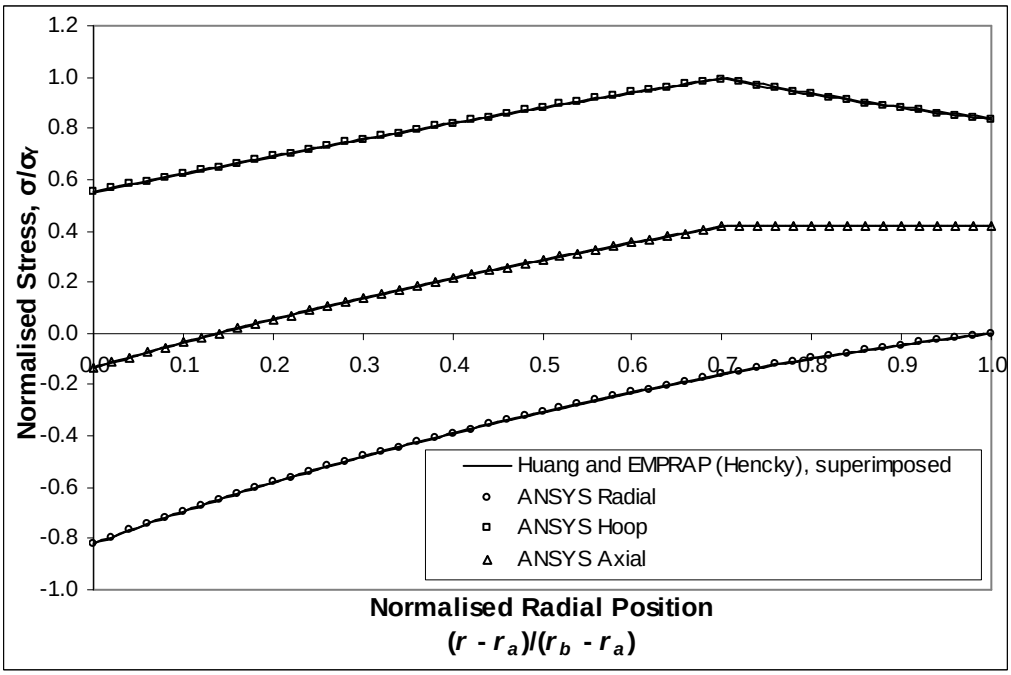

Figure 4.29: Comparison of Autofrettage Stresses, ν = 0.5, K = 2.0, β = 0.45

All three principal stresses show good agreement with the Hencky Programme and Huang's model. The plots for K = 2.5 showed similar agreement and are omitted in the interest of brevity.

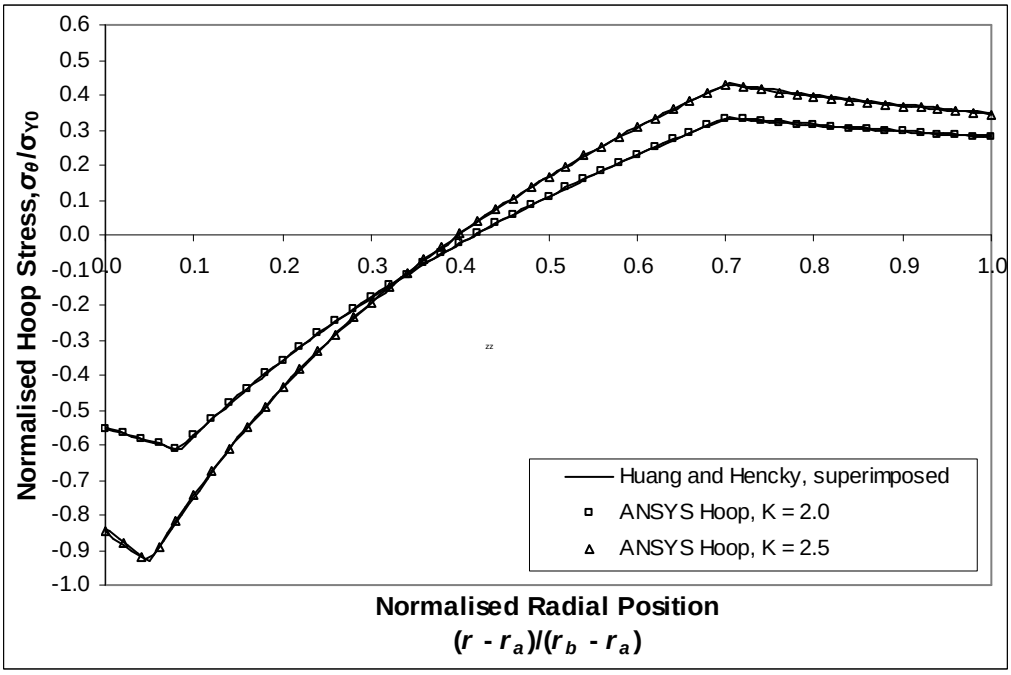

Figure 4.30: Comparison of Residual Hoop Stresses, ν = 0.5, for K = 2.0, β = 0.45 and K = 2.5, β = 0.7

Figure 4.30 shows a comparison of the ANSYS calculated values (shown by symbols) against those from the Hencky Programme and Huang's method. A very close agreement can be seen throughout the tube wall, including at the bore. This indicates the ANSYS model can accurately reproduce results from Huang's model, when using a bi-linear material.

4.7.6.3. Second Comparison: Hencky-ANSYS, ν = 0.3

The results from the second comparison, of the ANSYS model against the Hencky Programme for the four specified end conditions, are shown below in Figures 10-13 for K = 2.0 and 2.5.

The graphs plot the Residual hoop stresses throughout the tube walls – they show the ANSYS results as symbols overlaid on the continuous lines generated using the Hencky Programme results.

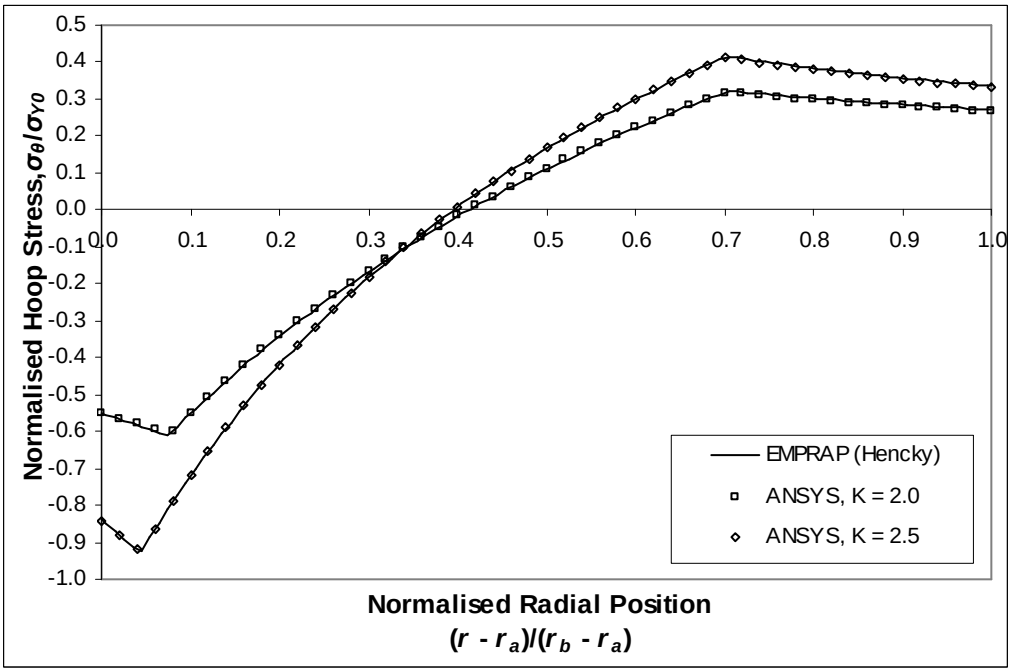

Figure 4.31: Residual Hoop Stresses for the Plane Strain Tube

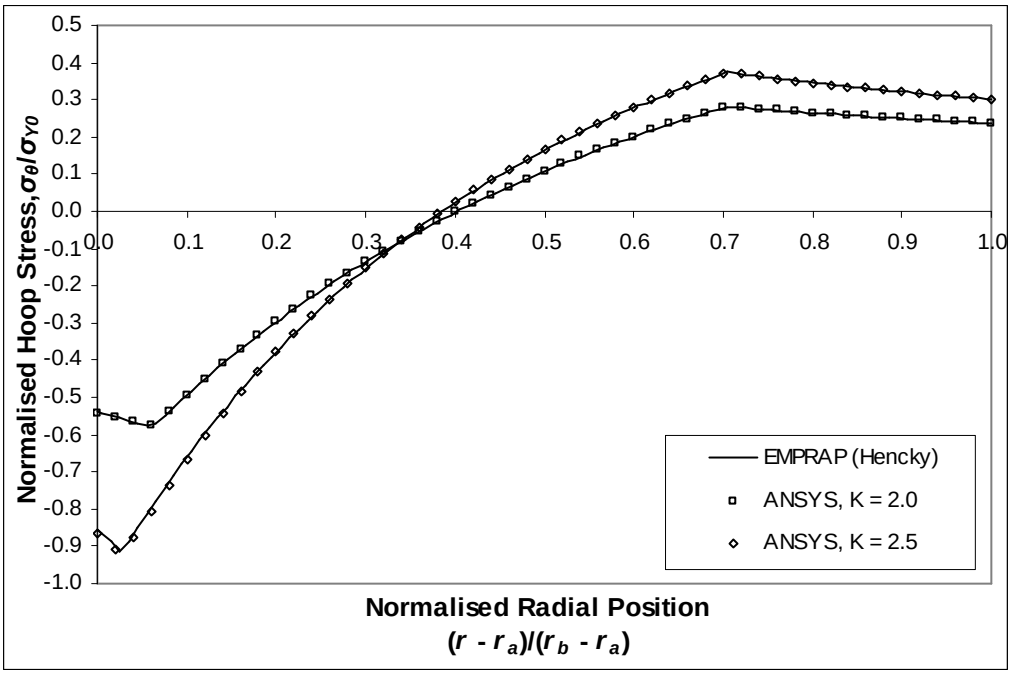

Figure 4.32: Residual Hoop Stresses for the Plane Stress Tube

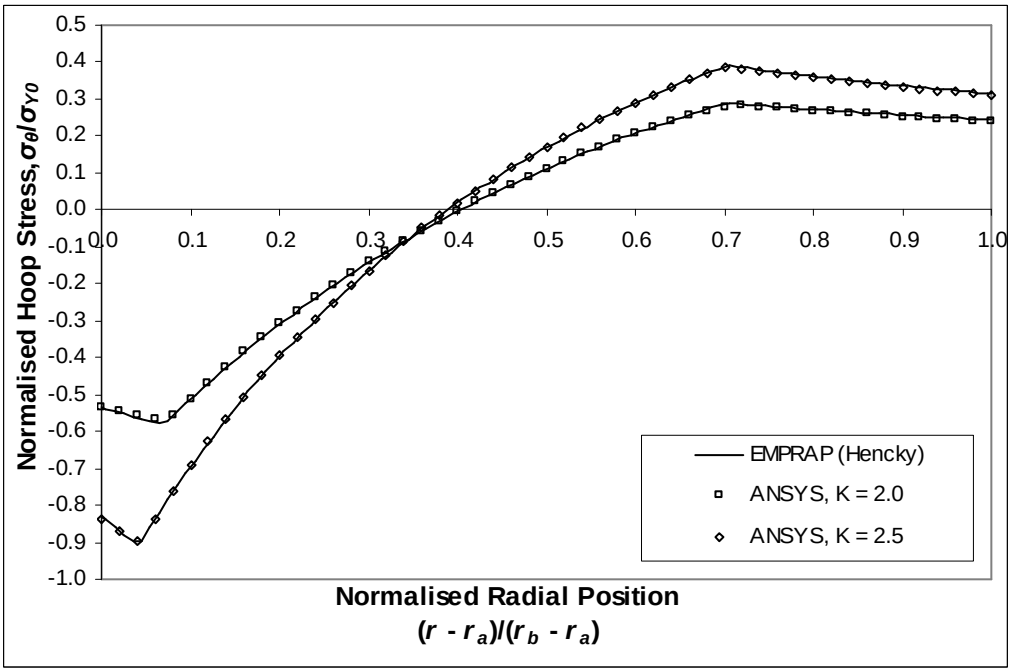

Figure 4.33: Residual Hoop Stresses for the Open-Ended Tube

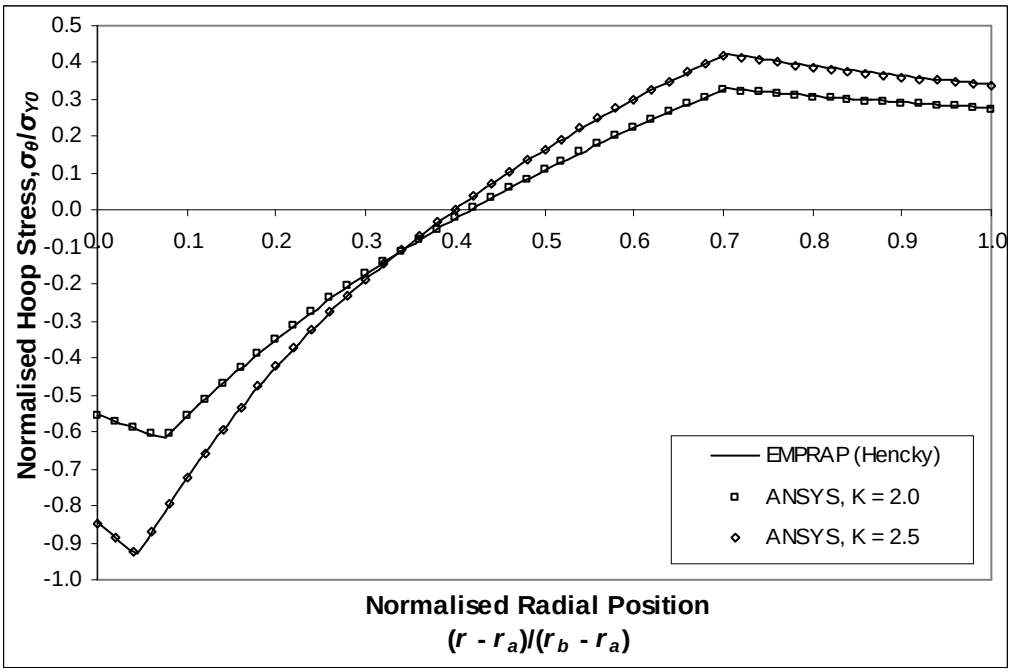

Figure 4.34: Residual Hoop Stresses for the Closed-Ended Tube

The Autofrettage pressures required to achieve 70% overstrain are listed in Tables 4.9 and 4.10.

	Pressure (MPa)	
End State	ANSYS	Hencky
Open-Ended	877.4	879.1
Closed-Ended	913.2	914.7
Plane Strain	906.5	908.4
Plane Stress	877.3	878.8

Table 4.9: Autofrettage Pressures, K = 2.0

	Pressure (MPa)	
End State	ANSYS	Hencky
Open-Ended	1220	1223
Closed-Ended	1254	1257
Plane Strain	1246	1249
Plane Stress	1224	1227

Table 4.10: Autofrettage Pressures, K = 2.5

4.8. DISCUSSION

The key property of all the residual hoop stress plots is the presence of secondary yielding near the bore which ultimately restricts the degree of pre-stressing possible in tubes. The reyielding depends on the autofrettage pressure (due to the compressive effects of its removal) and the strength of the material (altered from initial properties by deformation during loading).

For the incompressible conditions, Figures 4.29 and 4.30 show excellent agreement between the ANSYS model, the Hencky programme and Huang's model. This indicates that the ANSYS model can accurately predict stresses in such a case.

The comparisons between the ANSYS model and Hencky programme for the wider range of end conditions and a more realistic Poisson's ratio, are given in Figures 4.31 to 4.34. Again, a close match is exhibited. A slight variation may be seen in the reyield zones ($r_a \leq r \leq r_s$) away from the bore, more clearly visible for K = 2.0 and ν = 0.3; the ANSYS results show a small decrease in the magnitude of residual hoop stresses, and a slight, commensurate, increase of reyield radius (r_s).

The autofrettage pressures in Tables 4.9 and 4.10 show two sets of very similar values. The pressures for the Open-Ended condition are most similar to those for the Plane stress. This is not surprising since the former represents a tube in which the axial stresses sum to zero net force and the latter one in which all axial stresses are zero. The autofrettage pressures for the Closed-Ended condition are most similar to those for the Plane Strain condition. This is likewise unsurprising since they reduce to almost the same problem for the case of an incompressible material.

Finally, the fact that autofrettage pressure for plane strain/open-ends exceeds that for plane stress reflects the observations in [22]. This could also be inferred, using von Mises criterion, from the presence of an axial stress which, in the near-bore region, generally varies between 0.3 and 0.5 times hoop stress, depending upon Poisson's ratio.

From Tables 4.9 and 4.10 it can be seen that the pressure required for a given depth of autofrettage is affected by the chosen end condition. This is controlled by the von Mises yield criterion that considers all three principal stresses. The axial stress is the intermediate principal stress and is influenced by the chosen end condition; it therefore influences the degree of yielding. The variation between the various models in the near-bore reyield zone is modest.

4.9. SUMMARY

4.9.1. Mesh Sensitivity Tests

The sensitivity tests, documented in section 4.6, demonstrate how the four models react to variations in mesh density; the trends observed were used to select appropriate meshes that would deliver results of sufficient accuracy while consuming minimal time and computational resources.

The tests conducted on the general plane strain models, discussed in sub-sub-section 4.6.3.2, indicated that using 100 radial elements (El_{Rad} = 100) would provide ample accuracy (the results suggested that more than 70-80 were needed), while keeping model size small enough for rapid solution. Likewise, for the Plane Stress model it was observed that setting El_{Rad} equal to 600-800 (or in the summed residual case, 1200) generally achieved the desired accuracy. Accordingly, 1500 was selected as the value of El_{Rad} to be used; sufficient to make any quantisation error negligible while keeping the model size acceptable.

In both cases, two axial elements are used (sub-sub-section 4.4.3.2); to maintain square element geometry, the length of section, l_z, is scaled from the wall depth, l_r, using Equation (4.2).

4.9.2. Comparison Tests

During the comparison tests, described in section 4.7, good agreement was observed between the results generated by the ANSYS FE model, the Hencky numerical programme and Huang's analytical model. This demonstrates that given a correctly calculated degree of plastic strain at the bore, an accurate value of residual stress may be predicted by the ANSYS model for a number of end conditions. However, the bi-linear stress-strain profile used here is an approximation. To obtain more realistic

values of residual stress a more accurate material model is required that properly follows the non-linear unloading and also encompasses the varying degree of plastic strain experienced by the material throughout the tube wall. These enhancements, achieved through implementation of an EMPRAP and use of ANSYS User Programmable Features, are detailed in Chapters 5 and 6 respectively.

5. AN INITIAL APPROACH TO MODELLING NON-LINEAR MATERIAL BEHAVIOUR

5.1. INTRODUCTION

Hydraulic autofrettage modelling in ANSYS, described in Chapter 4, centred on modelling four different end conditions, and the constraints required to achieve those conditions. In addition, the use and modification of the Bi-linear Kinematic hardening (BKIN) material was investigated. Effectively, the physical conditions of hydraulic autofrettage had been accurately simulated, but the material model used was not representative of high-strength steels. Figure 5.1 shows the general stress-strain relationship of a typical gun steel, specifically the non-linearity exhibited by such steels during unloading, following prior plastic strain (experienced during autofrettage); this is not represented by the BKIN material.

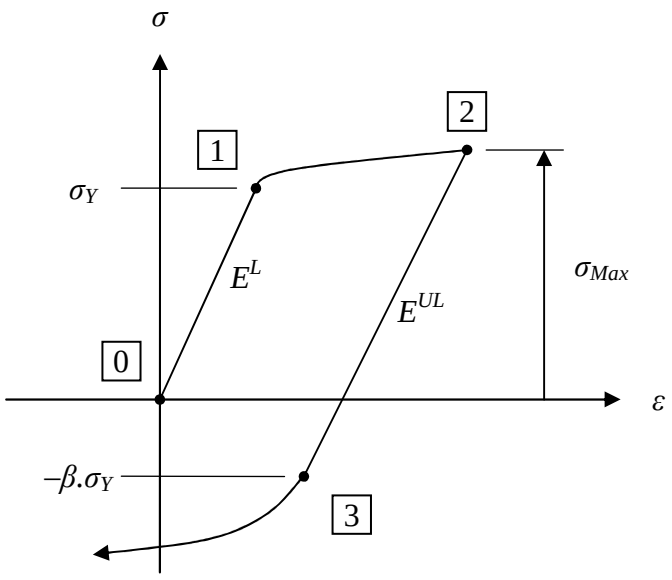

Figure 5.1: Generalised Stress-Strain relationship for a typical gun steel

This was significant as the region around the inner diameter is of the most interest when investigating autofrettage, which also experiences the greatest amount of plastic strain during hydraulic autofrettage. This region will hence unload with the greatest degree of non-linearity, with a commensurate divergence from the residual stresses predicted using a bi-linear material.

The next step towards achieving the overall goal is the development of a method to model the non-linear unloading of materials following the plastic strain experienced by tubes during autofrettage, which varies with radius. The first stage of such material modelling is described in this chapter.

As mentioned at the end of Chapter 4, two means of achieving the desired non-linear unloading were identified: User Programmable Features (UPFs) or an "Elastic Modulus and Poisson's Ratio adjustment procedure" (EMPRAP). A UPF was thought to be the most useful in the long term, but initially an EMPRAP was selected because it permitted implementation of real (experimentally determined) material behaviour within FEA, and will provide an independent validation of UPF in due course.

Accordingly, an EMPRAP was the first means of customised non-linear material modelling developed, and is described in Appendix A3. Note that the EMPRAP is limited to modelling hydraulic autofrettage, but such results could still be compared with any UPF analysis of swage autofrettage.

5.1.1. Selected Material Model

A723-1130, was selected as a suitable material for use throughout the course of this research; a gun steel which displays the characteristic non-linearity when unloading from prior plastic strain, central to these studies. A set of material-fit equations (given below) was developed for A723 by Parker et al. [30] from uni-axial tension-compression tests, and are summarised by Figure 5.2:

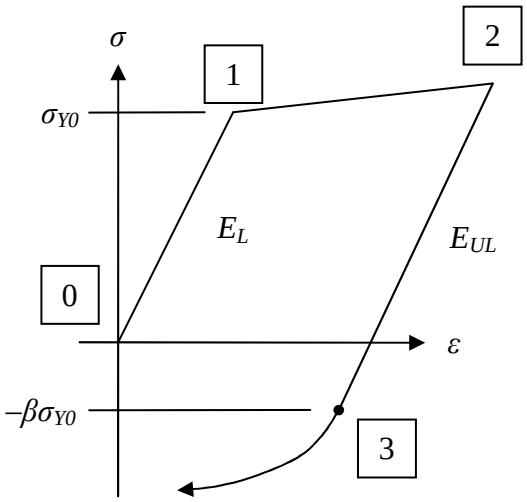

Figure 5.2: Material Stress-Strain Model

The loading/unloading cycle can be broken up into four parts:

0-1 – Elastic Loading
Behaviour defined by Hooke's Law using the modulus E_L.

1-2 – Plastic Loading
Material stress given by

$$\sigma_L^p = \sigma_{Y0}\left(1 + a\tanh\left[c\cdot\varepsilon_L^p\right] + d\cdot 100\cdot\varepsilon_L^p\right) \tag{5.1}$$

Slope given by

$$\frac{d\sigma_L^p}{d\varepsilon_L^p} = a \cdot c \cdot \text{sech}^2\left(c \cdot \varepsilon_L^p\right) + 100 \cdot d \cdot \sigma_{Y0} \tag{5.2}$$

2-3 – Elastic Unloading
Behaviour defined by Hooke's Law, albeit with an altered modulus E_{UL}.

3- – Plastic Unloading
Material stress given by

$$\sigma_{UL}^p = -\sigma_{Y0}\left(\left[1 + a - \beta\right]\tanh\left[\gamma \cdot 100 \cdot \varepsilon_{UL}^p\right] + \beta + d \cdot \varepsilon_{UL}^p\right) \tag{5.3}$$

Slope given by

$$\frac{d\sigma_{UL}^p}{d\varepsilon_{UL}^p} = -\sigma_{Y0}\left(\left[1 + a - \beta\right] \cdot 100 \cdot \gamma\left\{1 - \tanh^2\left[100 \cdot \gamma \cdot \varepsilon_{UL}^p\right]\right\} + d\right) \tag{5.4}$$

For A723-1130, the values of the three constants are given in Table 5.1. A723-1130 is used throughout the comparisons presented in this thesis.

Parameter	Value
a	0
c	0
d	0.013

Table 5.1: Material-fit Parameters

The Bauschinger Effect Factor, β, is given by:

$$\beta = 0.1684\left[\tan\left(1 - 100\varepsilon_L^p\right)\right]^{3.6} + 0.17 \qquad 0 < \varepsilon_L^p < 0.01$$
$$\beta = 0.17 \qquad \varepsilon_L^p \geq 0.01$$

The unloading parameter, γ, is given by:

$$\gamma = 1.2858 \cdot \left(100 \cdot \varepsilon_L^p\right)^{-0.323}$$

The above material fit is assumed to be a function only of strain, although it is recognised that other factors such as temperature, strain rate and time (for creep analysis) would be required for a full constitutive relationship. However, it is felt that the presented relationship is suitable for the analyses described in this thesis, as deformation rates are very small and temperature variation (resulting from stress-strain hysteresis and, in the case of swage autofrettage, friction) is felt to be small enough to be ignored.

5.2. IMPLEMENTATION WITHIN ANSYS

5.2.1. Overview

The meshes developed and optimised in Chapter 4 are used for the analysis presented in this chapter, allowing the implemented material model to be tested in the range of end conditions described therein: general plane strain (Plane Strain, Open- and Closed-Ends) and Plane Stress. Instead of the bi-linear kinematic hardening material used in the previous model, a continually altered elastic material was used in this model, befitting the EMPRAP.

The EMPRAP developed by Jahed and Dubey was used to govern the manipulation of E and v, such that the non-linear behaviour of an elastic-plastic material was emulated by the purely elastic material employed. Their model was extended, in the same way as was done in the Hencky Programme, such that both material non-linearity and position dependency were incorporated. This was necessary to model the variable plastic strain throughout the wall of an autofrettaged tube, and the selected material, A723-1130 (see sub-section 5.1.1).

While only one material (A723-1130) is used in the comparisons presented in this chapter, neither the EMPRAP nor the implementation of it within ANSYS is limited for use with it; the methods are general, and all that would be required to simulate another material would be alteration of the material-fit expression to match the desired material.

5.2.2. Implementation of the EMPRAP

Given the nature of the EMPRAP, it is clear that the tube material's elastic properties must be altered progressively during the solution process, in response to encountered plastic strain. Moreover, as plastic strain varies throughout the tube wall it is necessary to alter material properties on a fine-grained basis; this was achieved by defining a material for *each element*, so that material properties for each element could be altered dependent on the simulated plastic strain experienced by the element.

The models were created as follows:

1. Linear elastic materials are defined (as the actual material's E and v values) for each element (to be created), and data arrays are created to store the iterated solution data,
2. Geometries are created, meshed, constrained and loaded as described in Chapter 4,
3. Each element has its own material assigned to it (using the MPCHG command).

In addition, using normal methods it is not possible to alter material properties during ANSYS's solution process (such control becomes possible when using UPFs), meaning

a model based on an EMPRAP cannot be solved in a single solution. Instead, a series of solutions must be run, in between which material properties are altered. To allow this, the solution state must be retained outside of the normal ANSYS database; this was achieved using parameters within the ANSYS environment.

The modelling process and the iteration solution procedure, described above, are summarised by the flow diagram given in Figure 5.3.

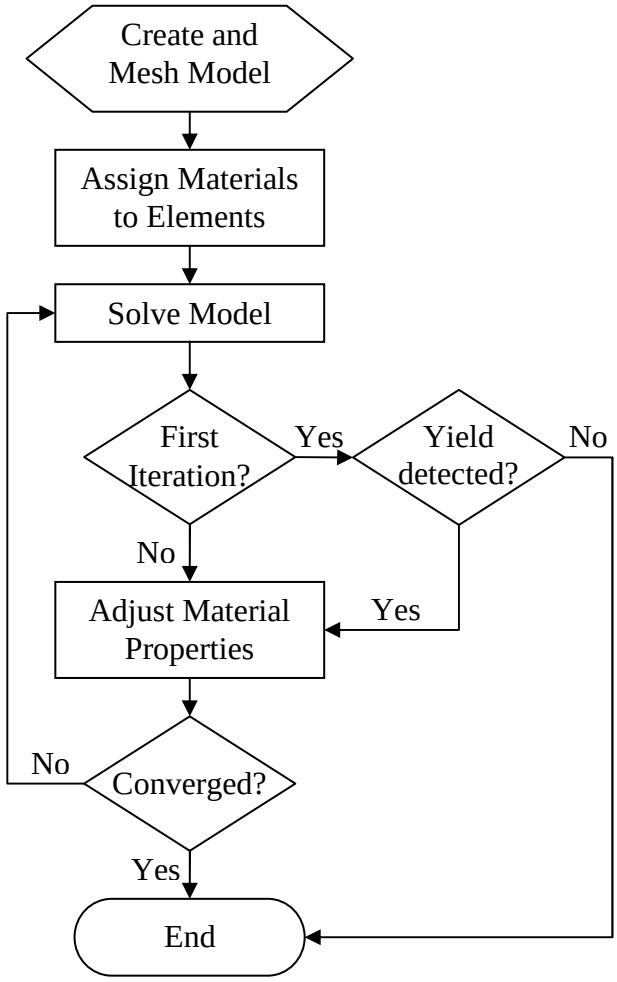

Figure 5.3: EMPRAP Solution Process

The fact that a material must be created and assigned to each element, and data must be retained and incremented for each element, strengthens the case for the optimisation documented in Chapter 4 – all consume memory, so it is important to minimise element numbers. In addition, the large number of elements (and hence, materials) used, when combined with the multiple iterations required to obtain a converged solution, made manual manipulation of parameters impractical; instead, the model was automated using APDL.

The drawback of this method is its reliance on elastic analysis; if the applied hydraulic pressure were released following autofrettage, the tube would completely and elastically unload to its original size with no residual stresses present. Accordingly, it is not possible to simulate the application and removal of pressure simply by mapping the two stages of the procedure onto their FE analogues, as was done within the models based on bi-linear materials in Chapter 4. For the same reason, swage autofrettage may not be modelled using such a quasi-elastic material as it is inherently a single continuous process; once the load is removed the tube would contract back to its original size, with no residual stresses present. This is reflected upon in the summary of this chapter (section 5.6).

Instead two separate pressurisation procedures are conducted, corresponding to the loading and unloading processes; the unloading stresses represent the changes in component stresses between their autofrettage (peak pressure) and residual states.

The unloading analysis is conducted in the same way as loading, albeit with material properties in the initial deformed region of the tube ($r_a \leq r \leq r_p$) altered to reflect the plastic strain experienced at that radius. The unloading stresses are calculated by autofrettaging the modified tube, *to the same pressure* as that used for the initial autofrettage procedure. Initially the elements constituting the deformed region of the tube have their Young's modulus altered to E_{UL}; the iterative solution then proceeds as in the loading phase. If the yield stress (which here equals σ_{ER}, as explained below) is exceeded, E and v are again adjusted so that the stress-strain response matches the unloading section of the material-fit curve, as illustrated in Figure 5.4 (compare with Figure 5.1).

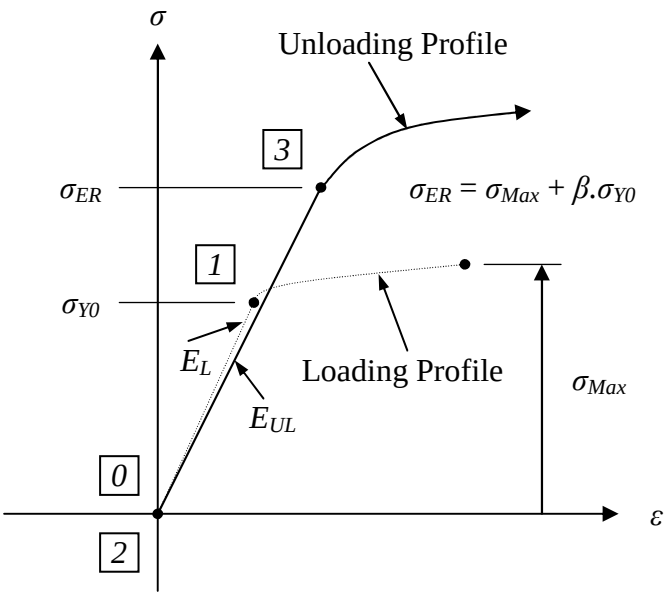

Figure 5.4: Stress-Strain relationship showing unloading profile mapped onto the loading profile

Again, material alteration is conducted on an element-by-element basis, using the plastic strain calculated for that element during the loading stage. Specifically:

1. The unloading Young's modulus, E_{UL}, is altered (generally reduced) – in the case of A723-1130:

$$E_{UL} = E_L\left[1 - 0.15\tanh\left(1.2\times 100\varepsilon_L^p\right)\right]$$

2. The yield stress is altered to equal the elastic range, σ_{ER}, from peak autofrettage stress to reverse yield:

$$\begin{aligned}\sigma_{ER} &= \sigma_{Peak} + \sigma_{Y0} \quad & \varepsilon_L^p &= 0\\ \sigma_{ER} &= \sigma_{Max} + \beta\sigma_{Y0} \quad & \varepsilon_L^p &> 0\end{aligned}$$

σ_{Peak} is the stress experienced during autofrettage; this is used as a dummy value such that reverse yield occurs at $-\sigma_{Y0}$. While reverse yield will never occur in this region ($r_p \leq r \leq r_b$) in the absence of an external pressure (meaning no reverse yield stress is strictly required), σ_{Peak} is calculated to keep the model as general as possible, allowing more potential for future use.

Once the solution of the unloading phase is complete, residual stress components are calculated using super-positioning; the unloading stresses are subtracted from the loading stresses, on a component-by-component basis. Equivalent stress is then calculated from the residual components that result.

In summary, avoiding the use of UPFs meant that all material modification had to be scripted within ANSYS using APDL. This was achieved by conducting a series of elastic analyses, between which the elastic properties (Young's modulus, E, and Poisson's ratio, v) were altered using Jahed and Dubey's method [19] according to material-fit parameters by Parker et al. [30], based on the results from the previous analysis stage.

5.2.3. Solution Control

For any numerical solution, a convergence criterion must be set; in this case as E and v are the altered properties, they are used here to determine convergence. The innermost element (that in contact with the bore) is used for convergence checking as it undergoes the greatest plastic strain and hence changes in E_{eff} and v_{eff}, quantified by the expressions in Equations (5.5).

$$E_\Delta = \left|1 - \left|\frac{E_{eff}^n}{E_{eff}^{n-1}}\right|\right| \qquad \nu_\Delta = \left|1 - \left|\frac{\nu_{eff}^n}{\nu_{eff}^{n-1}}\right|\right| \tag{5.5}$$

As E_{eff} and v_{eff} converge over successive iterations, E_Δ and v_Δ converge to zero from a positive value. They are summed to give Δ (see Equation (5.6)), which also converges to zero with its components.

$$\Delta = E_\Delta + \nu_\Delta \tag{5.6}$$

Δ is used as the convergence variable; once it has dropped below a set value (the convergence criterion), convergence is assumed. A suitable value for Δ was determined by a sensitivity analysis, documented in sub-section 5.3.2, and is used during subsequent comparisons.

As these differences are relative to the values from the previous iteration, a given value of convergence criterion yields a more converged answer than would be the case if differences were relative to the initial value of the variables.

5.2.4. Progression of Solution

In the case of an autofrettaged tube, during the first solution a relatively small depth around the bore will experience stress greater than the yield stress. In subsequent solutions, as the modulus of these over-stressed portions decreases, more of the load must be carried by the outer regions of the tube, progressively causing a larger degree of yielding. This continues until a converged solution, gauged using Equation (5.6), is developed.

It should be noted that the Jahed and Dubey method operates using *equivalent* stresses and strains; therefore aside from the loss of deformation following load removal, there is no reason, in principal, why it would not be applicable to swage autofrettage, in which the tube behaves in a non-plane fashion. In this case, the von Mises equivalent stress and strain are calculated from the direct and shear components present (or from principal values).

Typical autofrettage stresses can be seen in Figure 5.6, found within the Results section (5.4) – in this case for the Plane Strain case.

5.3. SUMMARY OF TESTS

This section describes the tests conducted to ascertain the accuracy of the implemented EMPRAP. The model utilises the previously developed and optimised meshes (see Summary of Chapter 4), which allowed material modelling immediately to become the focus of investigation.

As before, the tests constitute both a sensitivity analysis and a comparison with an established model (the Hencky Programme). The sensitivity analysis focussed on optimisation of the value of the convergence criterion, Δ; as such the tests were limited in scope, and their findings are given later in this section (sub-section 5.3.2). The comparison investigated how well results, generated when using the optimised criterion, agreed with those from an established method (the Hencky Programme).

5.3.1. Common Features

Both the sensitivity tests and the comparison feature a tube of Wall Ratio 2.5, consisting of the material A723-1130, autofrettaged such that $P_{AF} = \sigma_Y$. The stress-strain behaviour of A723-1130 is described fully in sub-section 5.1.1, but salient aspects are summarised below for convenience along with tube and autofrettage parameters.

Property	**Value**
Wall Ratio, K	2.5
Autofrettage Pressure, P_{af}	1130 MPa
Young's Modulus, E_{UL}	209 GPa
Poisson's Ratio, ν	0.3
Yield Stress, σ_{Y0}	1130 MPa

Table 5.2: Model Parameters

5.3.2. Preliminary Convergence Sensitivity Analysis

To investigate the effect of the convergence criterion, Δ, its magnitude was varied whilst keeping model and loading parameters constant. This was conducted for the Plane Strain model, using the following values of Δ: 10^{-1}, 10^{-2}, 10^{-3}, 10^{-4}, 10^{-5}, 10^{-6}, 10^{-7}.

Table 5.3 lists the iterations required for solution, alongside the respective values of Δ. The number of required iterations increases, including the sharp increase between $\Delta = 10^{-2}$ and 10^{-3} cases. Solution time may be considered to be effectively proportional to the total number of iterations, because plasticity very rapidly propagates through the tube. This means that during most iterations (for any value of Δ), the majority of

elements within $r_a \leq r \leq r_p$ must be operated upon. Also, as autofrettage is to the same pressure (and hence very similar depth, or overstrain), r_p is effectively constant.

	Iterations		
Δ Values	Loading	Unloading	Total
10^{-1}	5	2	7
10^{-2}	6	3	9
10^{-3}	21	5	26
10^{-4}	31	6	37
10^{-5}	40	8	48
10^{-6}	51	9	60
10^{-7}	60	11	71
10^{-8}	70	12	82

Table 5.3: Iterations required for Solution using the EMPRAP Implementation, varying the Convergence Criterion

The relative errors for the cases enumerated above were calculated, and are presented in Table 5.4. The errors decrease monotonically as the convergence criterion is reduced, with a significant change (more than an order of magnitude) between the $\Delta = 10^{-2}$ and 10^{-3} cases, reflecting the increase in iterations to solution also observed.

	% Relative Error		
Δ Values	Loading	Unloading	Residual
10^{-1}	-1.8655	3.5101	5.0977
10^{-2}	-1.0452	1.3668	2.1017
10^{-3}	-0.0709	0.0119	0.0372
10^{-4}	0.0378	0.0120	0.0041
10^{-5}	-0.0014	0.0002	0.0007
10^{-6}	-0.0002	0.0001	0.0001
10^{-7}	$-8.193*10^{-6}$	$3.829*10^{-7}$	$3.123*10^{-6}$
10^{-8}	n/a	n/a	n/a

Table 5.4: Relative Error using the EMPRAP Implementation, varying the Convergence Criterion

To make a cost-benefit analysis of the above data, the total number of iterations to solution (Table 5.3) was multiplied by the percentage error values for the residual hoop stresses (Table 5.4). The residual stresses were selected as the most relevant to this study, and the total number of iterations to solution was most representative of total solution time.

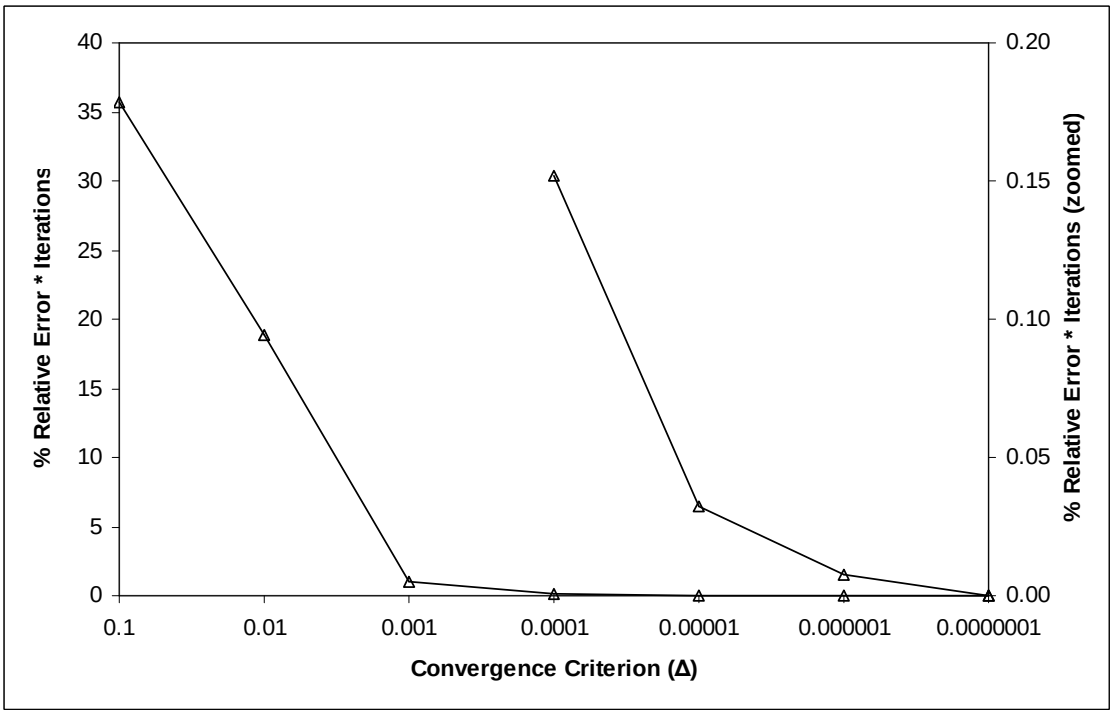

Figure 5.5: EMPRAP Implementation Error/Solution Time Comparison

While the product of relative error and number of iterations to solution rapidly approach zero, the absolute size of the decrease in error rapidly decreases also. For this reason, it was deemed that $\Delta = 10^{-4}$ was suitable; solution is then achieved in approximately 40 iterations, and the relative error is within a few hundredths of a percent.

5.3.3. Comparison with Hencky Programme

The ANSYS model, implementing Jahed and Dubey's EMPRAP, was assessed via comparison with like-for-like hydraulic autofrettage results from the Hencky Programme. The comparisons were conducted over a range of end conditions (Plane Strain, Plane Stress, Open- and Closed-Ends), with matched material and autofrettage parameters (see Table 5.2); results from both methods during both autofrettage and residual conditions were compared. In each case, a pressure equal to σ_{Y0} (1130 MPa) was applied to the tubes.

A convergence criterion, Δ, equal to 10^{-4} was selected for the ANSYS model based on the convergence study (sub-section 5.3.2); as in the convergence tests, the model used the mesh developed during the earlier mesh sensitivity analysis (Chapter 4).

5.4. RESULTS

This section presents the results generated from the comparison between the ANSYS model and the Hencky Programme, described in sub-section 5.3.3.

For the sake of brevity, only results from the Plane Strain case (both the sensitivity analysis and the comparison) are shown here; the remainder (for the Plane Stress, Open- and Closed-ended cases) are presented in Appendix A4. Specifically, results from the ANSYS implementation (EMPRAP(ANSYS)) of the Jahed and Dubey EMPRAP are overlaid as data points upon equivalent results from the Hencky Programme (EMPRAP(Hencky)), depicted as continuous lines.

Three sets of results (Loading, Unloading and Residual stresses) are displayed, each in component form.

5.4.1. Comparisons

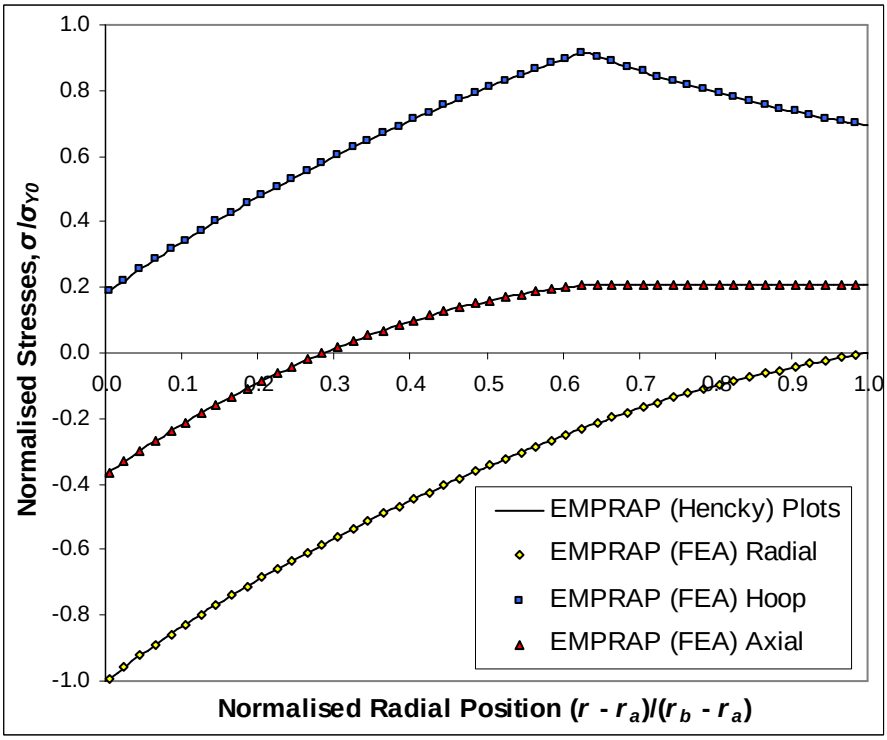

Figure 5.6: Autofrettage Stresses in a Plane Strain Tube

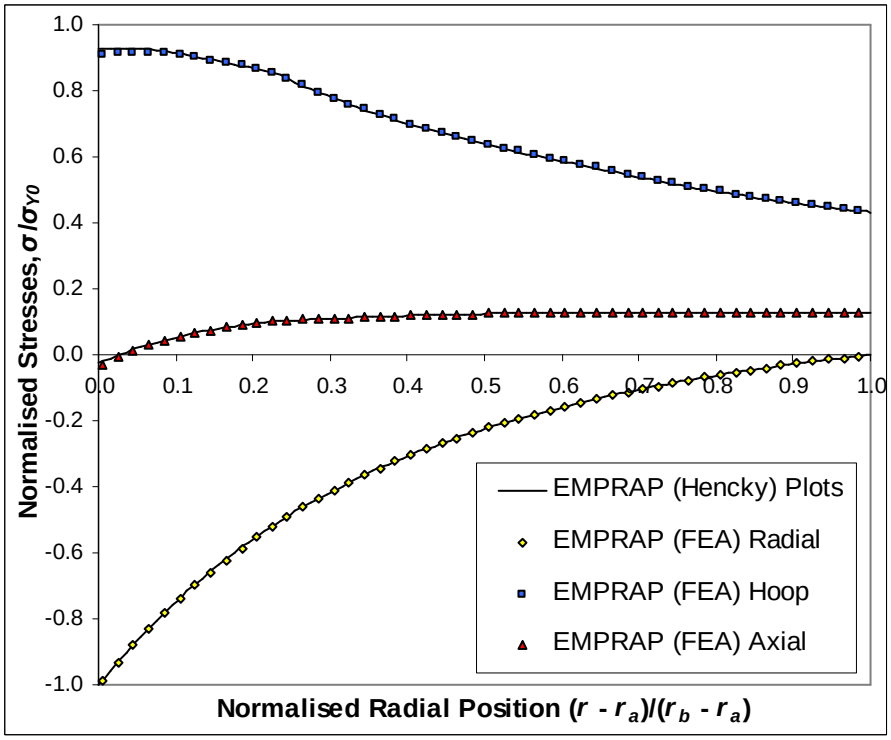

Figure 5.7: Unloading Stresses in a Plane Strain Tube

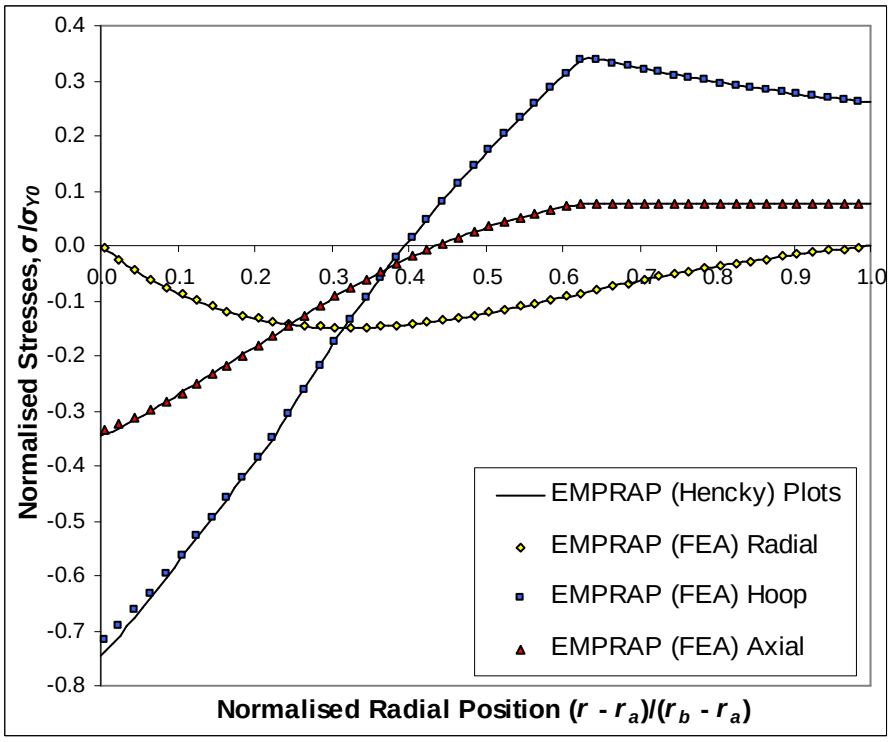

Figure 5.8: Residual Stresses in a Plane Strain Tube

	Residual Hoop Stress at ID, normalised w.r.t. σ_{Y0}		
End Condition	**EMPRAP (Hencky)**	**EMPRAP (ANSYS)**	**% Error**
Plane Strain	-0.74534	-0.71719	-3.77743
Plane Stress	-0.80373	-0.77178	-3.97588
Open Ends	-0.74258	-0.71248	-4.05410
Closed Ends	-0.74636	-0.71935	-3.61824

Table 5.5: Residual Hoop Stresses at the ID and errors, w.r.t. Hencky results

5.5. DISCUSSION

The Preliminary Convergence Sensitivity analysis identified how the required number of iterations varied as the magnitude of the relative error criterion was reduced. It was found that a convergence criterion (Δ) of 10^{-4} typically achieved complete solution within 40 iterations; taking approximately 31 iterations for the loading phase and 6 for the unloading phase. This tallies with what would be expected and is logical, given that the EMPRAP method iterates to find the elastic-plastic stress-strain state. As a greater degree of plastic strain (both quantity and extent) is observed in the loading process, compared to the unloading process, a much higher number of iterations would be expected to solve for the greater plastic strain encountered.

The autofrettage stresses show excellent agreement, indicating that the material has been modelled accurately in loading. However, the unloading stresses do show a small disagreement – specifically the hoop stresses (and to a lesser degree, the axial stresses) calculated by the ANSYS model are slightly less than those obtained from the Hencky programme. This leads to the ANSYS model slightly underestimating the residual hoop stresses by approximately 4% when compared to the Hencky programme.

Given the mesh sensitivity (Chapter 4) and convergence (sub-section 5.3.2) analyses conducted, numerical error is thought to be unlikely; instead, the different structural representations are thought to be responsible.

The two models employ the same method of material representation, but represent the tube structure differently; the Hencky Programme simulates a series of concentric cylinders each behaving according to Lamé's solution, and the ANSYS model uses an axi-symmetric mesh. Hence the most significant influence of such modelling differences would be upon the inter-relation of stress components, as is seen in the results – radial stress distributions agree much more closely than the hoop (and to a lesser degree, axial) stress distributions.

However each method is internally consistent, in that when summed through the tube wall, the hoop stresses equal the applied pressure load (in both loading and unloading processes). This supports the above observation regarding the inter-relation of stress components, as small variations would alter the precise distribution of stresses even though the summed stresses reached equilibrium with the applied pressure load. Given the lower amount of yielding that occurs during unloading, it is likely that a small error in the amount predicted would be more noticeable in unloading. On this basis, it is felt the difference between the unloading results is probably due to small differences in the detection of yield and calculation of plastic increment within the two models.

As would be expected, given the pre-existing constraint sets used, the results also indicate that the four end conditions are well simulated by the ANSYS model. This suggests that the material representation and end conditions are sufficiently independent to allow either to be changed as needed during future analyses, while retaining the integrity of the solution.

No abrupt changes in gradient are observed in the residual stress plots (Figure 5.8) at the reyield radius, r_b, compared with equivalent results from the bi-linear kinematic case in Figure 4.31. This is due to the stress-strain profile associated with A723 (Figure 5.2), which also shows no sudden change at the onset of reverse yield; the opposite is true for the bi-linear kinematic model used in Chapter 4 (Figure 3.3).

Although not compared here, the implementation within ANSYS of the EMPRAP is generic enough to be capable of simulating virtually any material (certainly any of interest in the context of pressure vessels). All that would be required to adapt it to another material is the replacement of the stress-strain relationships in the loading and unloading stages, along with the required material parameters.

5.6. SUMMARY

An existing mesh and constraint set, optimised and developed in Chapter 4, was utilised to provide the basis for a model in which the Jahed and Dubey EMPRAP could be implemented. The EMPRAP was used to represent the gun steel A723-1130, which exhibits non-linear unloading from plastic strain, within an ANSYS model; the model was then used to simulate the hydraulic autofrettage of a series of thick-walled tubes. With the exception of a small discrepancy in the unloading stresses near the ID, the calculated stresses matched very well against equivalent results from the Hencky programme. This supports its use in comparisons with future material models developed.

In addition, there is no reason why the model, in principle, would not be able to simulate the hydraulic autofrettage of tubes of more complex geometry, featuring tapers or steps for example. Combined with its flexibility in terms of material modelling, this method potentially allows a wide range of hydraulically autofrettage tubes to be modelled.

This method is well suited to modelling hydraulic autofrettage due to the discrete nature of the loading and unloading allowing residual stresses to be calculated using super-positioning; however, swage autofrettage is not so easily modelled due to the continuous nature of the process. Effectively, as the material is inherently elastic it will always return to it original unstressed state when the load is removed – ergo after the passage of the mandrel such a tube would return to its un-deformed, unstressed state. This also would affect the peak stress state, and predicted depth of plasticity, as the peak stress point is influenced (via shear stresses) by the tube both in front and behind the mandrel, the latter would be altered by the absence of residual stresses behind the mandrel. This necessitated the development of a different form of material modelling, described in Chapter 6. Additionally, although ANSYS seemed to contain no explicit limit to the number of definable material models (1,000,000 models were defined to investigate), its performance is reduced by excessive numbers of materials.

In summary, an FEA procedure for simulating non-linear stress-strain behaviour during hydraulic autofrettage has been implemented and investigated.

Whilst it is unsuitable for modelling swage autofrettage, a single continuous process during which stresses vary axially, it has provided valuable experience of implementing real material behaviour into FEA.

In addition, it is a source of results suitable for comparison with special cases such as the UPF, which was subsequently developed; this work is described in the next chapter.

Hence modelling swage autofrettage *with accurate material representation* remains the key focus for future work. A possible method is the use of a bi- or multi-linear ANSYS (elastic-plastic), which would retain the plastic strain experienced during loading; non-linear unloading would again be achieved through the modification of elastic

properties. This assumes that stresses in the non-linear unloading region remain below the reverse yield stress calculated by the ANSYS material, and that the loading profile of the material may be satisfactorily modelled using a bi-/multi-linear representation.

6. DEVELOPMENT OF AN FE ROUTINE TO MODEL REAL MATERIAL BEHAVIOUR

(Chapter 6 may be omitted on a first reading of the thesis.)

6.1. INTRODUCTION

This chapter details the adaptation of an ANSYS *User Programmable Feature* (UPF) to create an accurate model of a real world material, and its subsequent use in a simulation of hydraulic autofrettage. This is necessary in order to provide an accurate material model for use in simulation of swage autofrettage; as documented in Chapter 5, the EMPRAP material is not suitable for such circumstances.

The accuracy of the customised material behaviour is verified through:

1. Comparison of uni-axial stress-strain results with data taken directly from the material-fit equations,
2. Comparison in Hydraulic autofrettage with the Hencky Programme and the ANSYS EMPRAP model (developed in Chapter 5), both employing the same material-fit.

Given that the ANSYS EMPRAP model could satisfactorily be used in the simulation of hydraulic autofrettage, the main purpose for developing the UPF-based material model is for its later use simulating swage autofrettage.

6.2. USER PROGRAMMABLE FEATURES (UPFS)

ANSYS provides a set of customisable routines that may be employed to achieve non-standard behaviours; collectively they are referred to as *User Programmable Features* (UPFs).

UPFs are supplied as individual source code (Fortran 90) files, which generally recreate a standard feature in ANSYS. These files may then be altered to achieve the desired behaviour, after which they are compiled and statically linked with the main ANSYS object file, creating a second customised version of ANSYS containing the UPF. With the necessary compiler installed, the custom executable file is easily created – the "Relink" option is selected from the ANSYS Admin utility. This runs a batch file which runs through the required procedures, resulting in a custom executable file. Static linking, as opposed to dynamic linking, creates a single executable file containing all compiled and linked code, rather than dynamically linking the external code at run time.

A wide variety of UPFs exist, but those of interest are those that alter the stress-strain behaviour of a material in a mechanical analysis. Of these, the USERMAT routine is of particular interest as it allows the stress-strain state in both elastic and plastic regimes to be controlled. It is important to be able to control the elastic behaviour, as some metals (A723, for example) exhibit a slight change in their Young's Modulus during unloading subsequent to plastic loading.

6.2.1. ANSYS Solution Procedure

Before explaining the function of USERMAT, it is appropriate to describe the ANSYS solution procedure and where material sub-routines, such as USERMAT, are used within it.

ANSYS divides its solution hierarchy into three layers: load steps, sub-steps and equilibrium iterations. Load steps are user defined, and separate the solution into successive stages which reflect the details of the applied loading on the system being modelled; in the hydraulic autofrettage model used in this study, load steps are used separately to model the loading and unloading procedures.

Sub-steps divide load steps into shorter periods, between which the applied loads are (by default) altered to achieve gradual progression between the initial and final values defined for the load step. Minimum, maximum and suggested numbers of sub-steps may be defined by the user; sufficient must be employed to capture the details of loads, especially when transient (such as the sliding contact present during swage autofrettage), while keeping the simulation computationally tractable.

During each sub-step, ANSYS employs a series of equilibrium iterations to gauge a suitable increment of the input (during mechanical analyses, strain increments are the input), by assessing the output from the selected sub-routine (in this case, USERMAT) for the analysis.

6.2.2. USERMAT and its Sub-Routines

In a nutshell, USERMAT accepts increments of total strain as inputs, and outputs both the stress and plastic strain state. In addition, it outputs a stress-strain Jacobian matrix (the best linear approximation to a differentiable function near a given point; in this case, the multi-axial stiffness) which is used to help estimate the next set of total strain increments. Like a standard material USERMAT is called for at each integration point, during each equilibrium iteration.

USERMAT consists of a number of components – the first determines the complexity of the load case, and then calls the suitable component specific to the load case. The degree of complexity is primarily determined by the number of strain components, which in turn depends on the element selected. The range of load cases is listed in Table 6.1, along with the related sub-routine. Note: the number of shear strain components equals the difference between the number of strain and direct strain components.

Load Case	Strain Components	Direct Strain Components	Sub-Routine Called
One Dimensional	1	1	*usermat1d*
Three Dimensional Beam	3	1	*usermatbm*
Plane Stress	3	2	*usermatps*
Plane Strain or Axi-Symmetric	4	3	*usermat3d*
Three Dimensional	6	3	*usermat3d*

Table 6.1: Summary of USERMAT Sub-Routines

Of the listed sub-routines *usermat3d* was adapted and used due to its utility in the axi-symmetric case, in addition to the three dimensional case (which was used to create uni-axial specimens, described in sub-section 6.4.3). In addition, *usermat1d* was used as an intermediary during the customisation of *usermat3d*, allowing development to progress without dealing with multi-component stress-strain.

6.2.3. Using the USERMAT Routine

The custom executable, once compiled and relinked, may either be selected from the ANSYS Profile Manager, or may be invoked (in the case of ANSYS 11.0) using the following command:

```
ansys110 -custom <filename>
```

The USERMAT UPF is activated in much the same way as a normal material mode. First, the *state variable* environment is initialised, in this case with three components. The `TB,STATE` command specifies `nStatev`, which in turn sizes `statev`, the array that contains the state variables between Newton-Raphson iterations:

```
TB,STATE,1,,3,
TBDATA,1,C1,C2,C3,
```

The state variable retains equivalent plastic strain, component plastic strains and current yield stress; thus for the bi-linear isotropic model supplied, its size must equal the number of strain components (from Table 6.1) plus two. Effectively, it maintains the state of the solution for each integration point as the procedure iterates through them, throughout the sequence of sub-steps that constitute the solution. In addition, the state variable may be dimensioned to retain extra data to suit the requirements of the customised USERMAT (as was done in this case).

Then the material properties are assigned to the material:

```
TB,USER,1,1,4
TBTEMP,1.0
TBDATA,1,E1,nut,YS1,UniAxPlMod
```

The above example would be used to initialise a single temperature profile for the unmodified, bi-linear isotropic hardening material supplied with ANSYS. The four properties listed are: Young's Modulus, Poisson's Ratio, Yield Stress and Uni-Axial Plastic Modulus.

The user material may then be used with a number of elements: LINK180, SHELL181, PLANE182, PLANE183, SOLID185, SOLID186, SOLID187, BEAM188, BEAM189, SOLSH190, SHELL208 and SHELL209. For the purposes of this work 8-node PLANE183 elements will be used in two-dimensional analyses.

Prior to the quoted code, a number of "housekeeping" tasks are carried out – the subroutine is *passed* a number of variables, most notably the total strain increments and the contents of the state variable; the subroutine's local variables are then declared. After each invocation of the sub-routine, it passes data back to the main programme and stores it for use in subsequent iterations.

The initial preparation code is followed by the "functional" code, given below in section 6.2.4; the code is that supplied with ANSYS 9.0, due to difficulties encountered (described in section 8.1) adapting the code for ANSYS 11.0.

6.2.4. Documentation of Supplied USERMAT Code

The code shown here in boxes, labelled as “Code Blocks”, is in the Fortran language, and is distinct from the APDL (ANSYS Parametric Design Language) scripts that are used to automate the execution of the ANSYS programme. Line length is limited to 72 characters, and may be continued using the “&” character.

The first section creates the local variables based on the information passed to the sub-routine by the main ANSYS executable, and calculates the equivalent plastic modulus (`dsigdep`) from the uni-axial value, and shear modulus (i.e. the 2nd Lamé Constant, μ). Finally, the elastic stiffness (stress-strain) matrix (`dsdeEl`) is calculated. In this one-dimensional case the matrix has only one component, but in the axi-symmetric case it has 4x4 components, and 6x6 in the full three-dimensional case.

```
      keycut   = 0
      dsigdep  = ZERO
      pleq_t   = statev(1)
      pleq     = pleq_t
c *** get Young's modulus and Poisson's ratio, initial yield stress
c       and others
      young    = prop(1)
      posn     = prop(2)
      sigy0    = prop(3)
c *** calculate plastic slope
      dsigdep  = young*prop(4)/(young-prop(4))
      twoG     = young / (ONE+posn)
c *** define tsstif(1) since it is used for calculation of
hourglass stiffness
      tsstif(1) = HALF * twoG
c *** calculate elastic stiffness matrix
c
      dsdeEl(1,1)= young
```

Code Block 6.1

The second section uses the elastic stiffness matrix as an initial value for the plastic stiffness matrix, `dsdePl`, which is then used as the Jacobian matrix (if plastic deformation occurs, `dsdePl` is modified – see Code Block 6.6). The stress (`sigElp`) is then incremented elastically using `dsdeEl`, and the strain increment vector, `dStrain`. In the one-dimensional case presented here, both matrices and the vector have only one component, but higher-order cases utilise appropriately dimensioned tensors.

The second half of the code block determines the sign and von Mises equivalent of the incremented stress; `signTens` assumes the value of 1 or -1 (respectively, tensile or compressive), and `qEl` equals the von Mises equivalent stress. The tensile/compressive check is not made in the higher-dimensional models as the state is not readily apparent. In this case however, it is a useful example of the kind of checks than can be made to establish the load status of the material.

Finally, the current yield stress, `sigy`, is calculated based on the initial yield stress (`sigy0`), the plastic slope (`dsigdep`) and current equivalent plastic strain (`pleq`).

```
c *** calculate the trial stress and
c     copy elastic moduli dsdeEl to material Jacobian matrix
      sigElp(1)   = stress(1)
      dsdePl(1,1) = dsdeEl(1,1)
      sigElp(1)   = sigElp(1) + dsdeEl(1,1) * dStrain(1)
c *** sign of predicted stress
      signTens = sign (ONE, sigElp(1))
c *** compute von-mises equivalent stress
      qEl = abs(sigElp(1))
c *** compute current yield stress
      sigy    = sigy0 + dsigdep * pleq
```

Code Block 6.2

Code Block 6.3 checks for yielding – if the equivalent stress, `qEl` is less than the current yield stress, `sigy`, `fratio` takes a value below zero. The `IF` statement is then

satisfied, and the `GO TO` command instructs the execution point to jump ahead, skipping the plasticity-handling code. If `qEl` exceeds `sigy` the reverse happens, and the plasticity code is executed.

```
      fratio = qEl / sigy - ONE
c *** check for yielding
      IF (sigy .LE. ZERO.or.fratio .LE. -SMALL) GO TO 500
```

Code Block 6.3

If the yield stress has been exceeded, and plasticity has been detected, Code Block 6.4 is executed. The yield stress from the start of the iteration is recorded as `sigy_t`, and the plastic strain increment (`dpleq`) is found by dividing the difference in the current equivalent and yield stresses by Young's Modulus.

The equivalent plastic strain (`pleq`) is then incremented, and a new yield stress is calculated by adding the product of the plastic slope (`dsigdep`) and increment plastic strain to the initial yield stress.

```
      sigy_t   = sigy
c *** initial guess of incremental equivalent plastic strain
      dpleq    = (qEl - sigy) / young
      pleq     = pleq_t + dpleq
      sigy     = sigy0 + dsigdep * pleq
```

Code Block 6.4

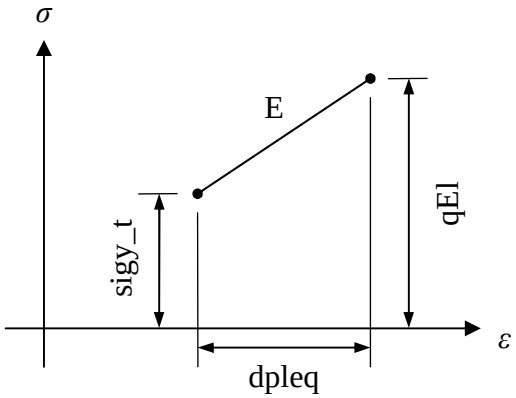

Figure 6.1: Estimation of Plastic Strain Increment, dpleq

Code Block 6.5 increments the sole plastic strain component (`epsPl(1)`) with `dpleq` (sign is determined by `signTens`) and sets the value of stress. As this is a one-dimensional example the stresses and strains present have only one component, which each equal the equivalent value. This is not so for the higher-dimensional cases, in which the components are calculated individually. The sole stress component (`stress(1)`) is then assigned the value of the final yield stress (`sigy`) – this value is multiplied by `signTens` as the yield stress is a scalar property.

```
c ***  update plastic strains, stresses
      epsPl(1) = epsPl(1) + dpleq * signTens
      stress(1) =  signTens * sigy
```

Code Block 6.5

Code Block 6.6 uses `pleq` (an internal variable) twice to define values to be returned to the main ANSYS programme – once to set the value of `statev(1)` (which is used to define `pleq_t` in the following iteration) and secondly to set the value of `epseq` (which the main ANSYS programme uses).

It then estimates the plastic work increment, `sedPl`, using the trapezium rule (this gives an exact value for the linear plasticity model used by the supplied material), as demonstrated in Figure 6.2.

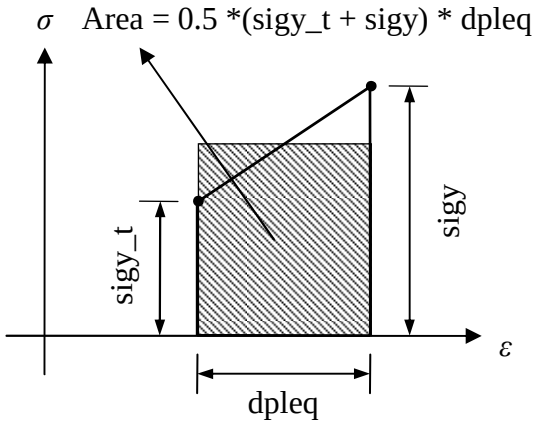

Figure 6.2: Estimation of Plastic Work Increment

Finally the Jacobian matrix (the `dsdePl` matrix) is calculated, for the plastic case.

```
c ***  update plastic strains
      epseq  = pleq
c *** Update state variables
      statev(1) = pleq
      statev(2) = epsPl(1)
c *** Update plastic work
      sedPl = sedPl + HALF * (sigy_t + sigy) * dpleq
c
c *** Material Jcobian matrix
c
      dsdePl(1,1) = dsdeEl(1,1) * dsigdep /(dsdeEl(1,1) + dsigdep)
c *** Allow a small number for Jcobian matrix if it is an ideal
c       plasticity
      if(dsdePl(1,1).LE.ZERO) dsdePl(1,1) = SMALL*dsdeEl(1,1)
c
      goto 600
```

Code Block 6.6

Code Block 6.7 starts with a continue statement, which resumes the execution path following the goto statement in Code Block 6.3. The single line of code given below copies the stresses determined by elastic analysis (`sigElp`) into the `stress` vector, which is output to the main programme. (In the one-dimensional case shown only one stress component is present.)

```
  500 continue

c *** Update stress in case of elastic/unloading
      stress(1) = sigElp(1)
```

Code Block 6.7

Code Block 6.8 is executed during both elastic and plastic behaviour (the continue statement resumes the plasticity code path, following the goto statement in Code Block 6.6). The elastic work (`sedEl`) is calculated based on the area of a triangle (representing the area under the elastic loading ramp), using the stress and elastic strain present. Finally, the last entry of the state variable, `statev(nStatev)`, is updated with the current value of the yield stress and the sub-routine ends.

```
  600 continue
c *** elastic strain energy
      sedEl = HALF * stress(1) * (Strain(1)+dStrain(1)-epsPl(1))
c *** update state variables
      statev(nStatev) = sigy
c
      return
      end
```

Code Block 6.8

6.2.5. Modifications to Model A723

The description of the modifications made to the USERMAT routine will be made in two sections; firstly, how the desired stress-strain behaviour was applied to the one-dimensional variant of the material, *usermat1d*, and secondly, how these modifications were applied and adapted to *usermat3d*, material variant used for axi-symmetric and three-dimensional analyses. This reflects the nature of the development work conducted on the material routine, and splits the description logically so that material representation issues and load cycle position are treated separately.

The main difference between the supplied BISO material and the behaviour of A723 is the response to plastic strain; the BISO model retains the peak equivalent stress as the future yield strength, whereas A723 displays the Bauschinger effect and significant non-linearity in unloading dependant on the degree of plastic strain in loading.

Indeed the isotropic property of the BISO material means that regardless of the configuration of the applied stress components the material retains equal yield strength,

whilst the Bauschinger effect means that A723 begins to yield at lower stress in compression following tensile plastic strain.

The above makes it clear that to successfully simulate A723, the material model must be altered to record the peak plastic loading strain experienced. Without this the characteristic plastic strain-dependent unloading profile, crucial for an accurate assessment of residual stresses, would not be achieved.

6.3. ONE-DIMENSIONAL MODEL

As mentioned in sub-section 6.2.5, the one-dimensional model, *usermat1d*, was the first to be modified, to allow the material representation to be perfected without the complexities of multi-component stress-strain.

Specifically, it is trivial to determine whether loading or unloading is occurring as strain increments are either positive (loading) or negative (unloading). In addition to this, no equivalent values (stress or strain) need be calculated.

The modifications to *usermat1d* were designed to allow it to be tested in simplistic tension-compression model, made up of a single link element. Thus the load cycle would be kept simple allowing the position within the cycle to be determined via rudimentary checks.

6.3.1. Overview of Modifications

To adapt the supplied sub-routine to allow it to model the desired non-linear stress-strain profile (given in Figure 5.2), a number of alterations were required. The *raison d'être* for the alterations are detailed below.

Specification of Material Constants
Material-fit equations generally require additional parameters to be assigned for their proper evaluation. These must either be supplied through the material definition, or "hard coded" into the sub-routine. It was decided to hard code (specify values within the Fortran source code) any required parameters, given space limitations within the `TBDATA` variable and infrequent changes of material-fits.

Initial Elasticity and Yield left unchanged
No material models of relevance (especially not the A723 model used here) include anything other than linear elastic behaviour for non-deformed material, of constant Young's Modulus and initial yield stress.

Stresses during Initial Plasticity altered
While the material models of interest generally prescribe a linear response to initial plasticity, the slopes are often case specific and given by a fit equation. As such the sub-routine was altered to use such equations, and to use their derivatives as the uni-axial plastic gradient (used to calculate `dsigdep`).

Values Retained at Peak Stress
In order to track unloading of properties (stress and strain) from peak values, it was necessary to retain these peak values within the state variable. In the one-dimensional case (*usermat1d*) only the peak plastic strain needed to be retained (hence the state variable is enlarged from three to four entries), with other values calculated from it.

The extra values requiring retention for the three-dimensional case (*usermat3d*) are detailed in section 6.4.2.

Detection of Unloading from Prior Plastic Strain
Given the change in properties (Young's Modulus and reverse yield stress) that occur following prior plastic strain, it is essential that unloading be detected and its presence declared to the relevant portions of code. This is simply done for the one-dimensional case, and is done informally where needed. The three-dimensional case required more formal treatment, including an unloading flag, to avoid excess repetition.

Reverse Plasticity and Yield Stress altered
When unloading is detected, both Young's Modulus and the reverse yield stress are calculated, dependent on prior plastic strain.

Non-Linearity during reverse Yielding
Once the material is detected to have exceeded the reverse yield stress calculated at that point, non-linear unloading commences in accordance with the material-fit equations.

6.3.2. Narration of Modifications

The modifications made to the one-dimensional case, *usermat1d*, the reasons for which are given in sub-section 6.3.1, are presented below in the order they appear in the code.

The first additional task that must be conducted is reading the value of maximum tensile plastic strain in from the state variable. This is achieved by the contents of Code Block 6.9, which is placed after the line assigning a value to `pleq` in Code Block 6.1, which reads the value into the local variable `tensepeq`. The value is returned to the state variable by Code Block 6.15 (the description for which explains the assignment of values to the different entries within the state variable).

```
      Tensepeq = statev(3)
```

Code Block 6.9

An additional array, `MatParms`, is added to the list of those defined during the initialisation portion of the sub-routine. Its four entries are used to contain the material-fit constants (*a*, *c* and *d*), and γ once unloading commences. Code Block 6.10 assigns the values of *a*, *c* and *d*.

```
      MatParms(1) = 0.d0
      MatParms(2) = 0.d0
      MatParms(3) = 0.013d0
```

Code Block 6.10

It is then necessary to determine whether the material is unloading, and if so conditionally set or modify values. This is easily achieved in the one-dimensional tension-compression case investigated here – given prior plastic strain, the sign of the strain increment (`dStrain`) defines whether loading or unloading is occurring. (It was recognised that this is not a rigorous check, but was satisfactory for the limited scope in which the *usermat1d* sub-routine was used.)

Code Block 6.11 checks for unloading; if detected the relevant variables, listed below, are altered appropriately, dependant on the degree of tensile plastic strain experienced.

- Young's Modulus (`young`),
- Bauschinger effect Factor (`BEF`),
- γ (`MatParms(4)`),
- Maximum Equivalent Stress (`MaxEqSig`) – used for calculating the amount of elastic unloading strain,
- Reverse Elastic Strain (`RevElStrn`), used to determine reverse plastic strain,
- Initial Reverse Equivalent Plastic Strain (`Revpleq_t`).

Figure 6.3 helps explain these terms.

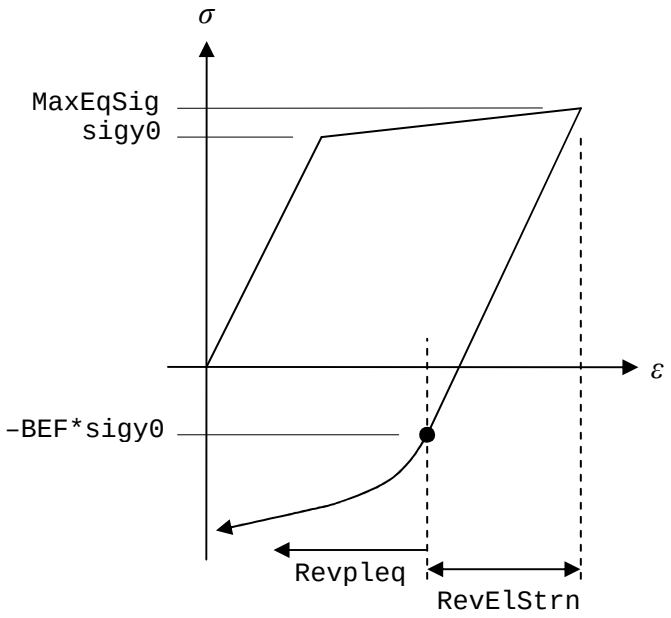

Figure 6.3: Strains in Unloading

As well as the calculations made, the final line within the IF structure checks to ensure `Revpleq_t` does not assume a negative value, which would be nonsensical in terms of the material representation.

```
      IF (dStrain(1) .LT. ZERO .and. Tensepeq .GT. ZERO) THEN
        young = prop(1) * (ONE - 0.15d0*DTANH(1.2d0*Tensepeq*1.d2))
        IF (Tensepeq .GE. 0.01d0) BEF = 0.17d0
        IF (Tensepeq .LT. 0.01d0) BEF = 0.1684d0 *
     &    (DTAN(ONE - Tensepeq*1.d2))**3.6d0 + 0.17d0
        MatParms(4) = 1.2858d0 * (Tensepeq*1.d2) ** -0.323d0
        MaxEqSig = sigy0 * (ONE + MatParms(1) * DTANH
     &    (MatParms(2) * Tensepeq) + MatParms(3) * Tensepeq * 1.d2)
        RevElStrn = (MaxEqSig + BEF*sigy0)/young
        Revpleq_t = (Tensepeq+sigy0/prop(1) - RevElStrn) - Strain(1)
        IF (Revpleq_t .LT. ZERO) Revpleq_t = ZERO
      END IF
```

Code Block 6.11

Code Block 6.12 checks for loading/unloading by inspecting both the total strain increment and tension-compression status; this means that the tensile yield stress is retained while unloading down the line 2-3 until the stress becomes compressive. In addition, initial and final yield stresses (`sigy_t` and `sigy`, respectively) are calculated directly using the material-fit equations and initial and final plastic strains, not the plastic slope, `dsigdep`. This means that `dsigdep` (now calculated in Code Block 6.14) is only required when calculating the Jacobian matrix.

```
      IF (dStrain(1) .GT. ZERO .and. signTens .GT. ZERO) THEN
        sigy_t = sigy0 * (ONE + MatParms(1) * DTANH(MatParms(2) *
     &   pleq_t) + MatParms(3) * pleq_t * 1.d2)
      ELSE IF (dStrain(1) .LT. ZERO .and. signTens .LT. ZERO) THEN
        sigy_t = sigy0 * ((ONE+MatParms(1)-BEF) * DTANH
     &  (MatParms(4)*Revpleq_t*1.d2) + BEF + MatParms(3)*Revpleq_t)
      END IF
```

Code Block 6.12

Code Block 6.13 then calculates the incremented reverse equivalent plastic strain, and ensures it is positive, in the same way the initial value was obtained.

```
      IF (dStrain(1) .LT. ZERO) Revpleq = Revpleq_t-dStrain(1)
      IF (Revpleq    .LT. ZERO) Revpleq = ZERO
```

Code Block 6.13

Code Block 6.14 again checks for loading/unloading and calculates the incremented yield stress, in the same way that the initial yield stress is calculated in Code Block 6.12. The `Stress` array, due to be passed back to the main ANSYS programme at the end of the current pass through the material sub-routine, is then updated. Finally the plastic modulus, `dsigdep`, is calculated as the gradient between the initial and final yield stresses.

During reverse yielding, this will slightly over-estimate the actual gradient that will be encountered during the following iteration as the gradient of A723 reduces as reverse plastic strain increases. However, given the prescribed displacement that will be applied to the one-dimensional test model (which means the strain increment, `dStrain`,

is calculated directly from the applied displacement), the precise value of the slope is not important. However, *usermat3d* will need to include an accurate means of predicting the required slope for the next iteration as the applied loads are not displacement based.

```
      IF (dStrain(1) .GT. ZERO .and. signTens .GT. ZERO) THEN
        sigy = sigy0 * (ONE + MatParms(1) * DTANH(MatParms(2) *
          pleq)
     &   + MatParms(3) * pleq * 1.d2)
      ELSE IF (dStrain(1) .LT. ZERO .and. signTens .LT. ZERO) THEN
        sigy = sigy0 * ((ONE+MatParms(1)-BEF) * DTANH
     &  (MatParms(4)*Revpleq*1.d2) + BEF + MatParms(3)*Revpleq)
      END IF
```

Code Block 6.14

The final alteration, as shown in Code Block 6.15, updates the maximum tensile plastic strain for the integration point if the current value exceeds that stored in the state variable. The state variable is enlarged by the APDL code that assigns the custom material to the ANSYS model – the original size of the state variable for the one-dimensional version of the USERMAT sub-routine is three entries, and this was increased to four to store the maximum tensile plastic strain.

For this and higher dimensional variants of the sub-routine, it was decided not to store the maximum tensile plastic strain as the final value in the array, as the modified yield stress (`sigy`) is always stored as such, and accessed using `statev(nStatev)`. Instead, it was stored between the plastic strain vector and the yield stress value.

```
      IF (pleq .GT. statev(3)) statev(3) = pleq
```

Code Block 6.15

Following the modifications detailed above, usermat1d.f was compiled and linked with ANSYS, which was then ready to be used in the test model.

The changes described above were made incrementally, to allow different portions to be developed separately and errors to be identified quickly – the stages are given below:

1. The supplied bi-linear material was altered and its responses to them observed,
2. The initial tensile behaviour was programmed to model that of A723 in loading,
3. The initial tensile behaviour was programmed to model that of A723 in unloading from initial tensile plastic strain,
4. Loading and unloading behaviours were combined, creating the code described above.

6.3.3. ANSYS Test Model

As described at the beginning of section 6.3, as simple tension-compression model was required to test the customised *usermat1d* sub-routine. To do so, a model consisting of a single LINK180 element was created, one end of which was fully constrained while the other was displaced along the axis of the element. This is shown in Figure 6.4.

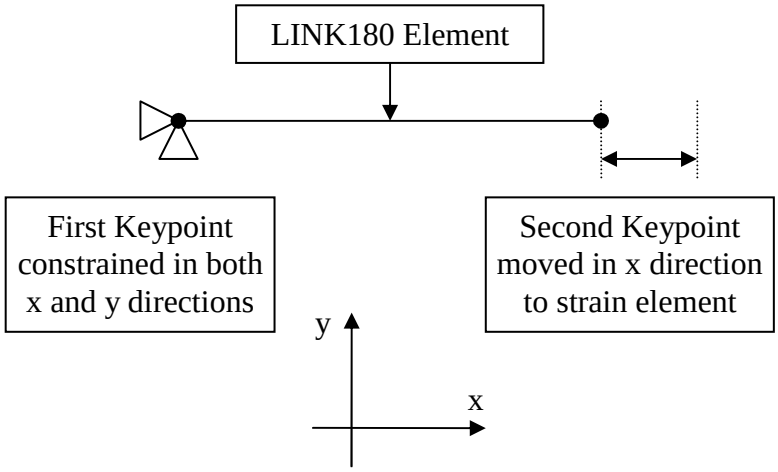

Figure 6.4: Uni-Axial Test Model

The above model was first progressively loaded in tension to a maximum value (sufficient to cause plastic deformation), and then progressively unloaded from this maximum value. At each increment the stress-strain state in the element was recorded into a table, from which the results could easily be compared and plotted against those calculated from the material-fit equations.

These procedures were scripted and automated using APDL to reduce the time taken for requisite stages to be completed; this allowed a range of maximum strains and material parameters to be tested, to further verify the model.

6.3.4. Results

Figure 6.5 plots the results obtained from the model, detailed in sub-section 6.3.3, using the custom material. The link element was extended such that the total strain equalled several multiples (1.5, 2, 2.5 and 3) of the yield strain, ε_Y, and material parameters were as specified.

The results from ANSYS are plotted against those obtained directly from the material-fit equations, for the same conditions.

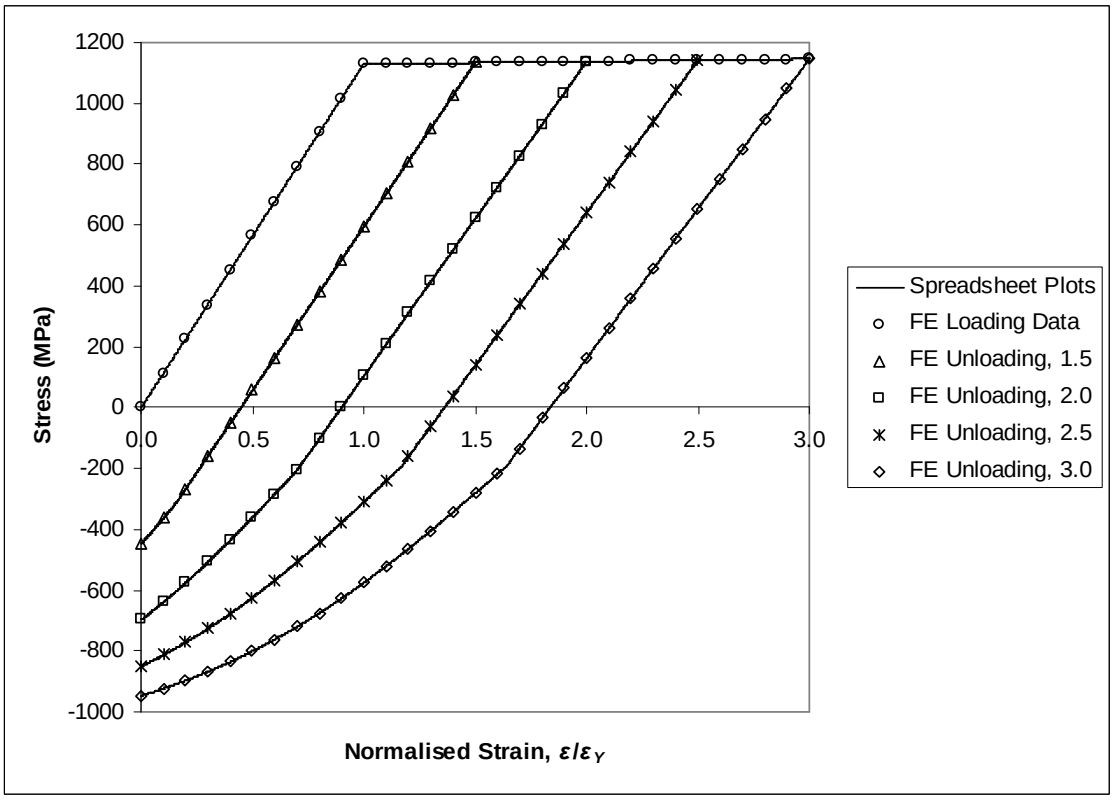

Figure 6.5: Tensile-Compressive Profiles, *usermat1d*

6.3.5. Summary of One-Dimensional Material

The results from the ANSYS custom material, presented in Figure 6.5, show excellent agreement when compared against those from the material-fit equations, across a range of maximum initial strains. In additional, results were compared across a range of variations of material parameters (*a*, *c* and *d*), which all showed equally close matching (results are omitted for brevity).

6.4. THREE-DIMENSIONAL MODEL FOR AUTOFRETTAGE SIMULATION

Once the one-dimensional model had been adapted and verified, the three-dimensional model became the focus for development. This section first describes the extra complexity required to model multi-component stress-strain, and then the additional modifications made to the source code to achieve the desired material behaviour.

6.4.1. Differences between the one- and three-dimensional models

To calculate initial elastic stresses, the sub-routine uses the stiffness matrix, **K**, to calculate the stress increments from the strain increments. This is from Hooke's Law, and is given by Equation (6.1):

$$\{\sigma\} = [K]\{\varepsilon\} \tag{6.1}$$

Fully expanded to the six component (three direct, three shear) case, the above becomes that given in Equation (6.2) – the form used by the material sub-routine:

$$\begin{Bmatrix} \sigma_1 \\ \sigma_2 \\ \sigma_3 \\ \sigma_{12} \\ \sigma_{23} \\ \sigma_{31} \end{Bmatrix} = \begin{bmatrix} \lambda+2\mu & \lambda & \lambda & 0 & 0 & 0 \\ \lambda & \lambda+2\mu & \lambda & 0 & 0 & 0 \\ \lambda & \lambda & \lambda+2\mu & 0 & 0 & 0 \\ 0 & 0 & 0 & \mu & 0 & 0 \\ 0 & 0 & 0 & 0 & \mu & 0 \\ 0 & 0 & 0 & 0 & 0 & \mu \end{bmatrix} \begin{Bmatrix} \varepsilon_1 \\ \varepsilon_2 \\ \varepsilon_3 \\ \varepsilon_{12} \\ \varepsilon_{23} \\ \varepsilon_{31} \end{Bmatrix} \tag{6.2}$$

Standard elastic relationships, given in Equations (6.3) and (6.4), are used to determine the two Lamé constants:

$$\lambda \equiv \frac{\nu E}{(1+\nu)(1-2\nu)} \tag{6.3}$$

$$\mu \equiv \frac{E}{2(1+\nu)} = G \tag{6.4}$$

The following, in Code Block 6.16, is used to populate the elastic stiffness matrix, `dsdeEl`. `G` is a small mask vector (*not* shear modulus), the first three values (`G(1)` to `G(3)`) equalling one, the last three equalling zero. The `DO` loops at the end exploit the diagonal symmetry of the matrix to save calculation time by mirroring 16 of the values

over into the opposite corner. The mask vector is used solely to allow the calculations to be encoded more succinctly.

When used in Plane Strain and Axi-Symmetric cases only four strain components exist (three direct, one shear); accordingly the upper left 4x4 block of matrix values are used. In the full three-dimensional case, the entire 6x6 matrix is used as six strain components are present (three direct, three shear).

```
      dsdeEl(1,1)=(elast1+TWO*elast2)*G(1)*G(1)
      dsdeEl(1,2)=elast1*G(1)*G(2)+elast2*TWO*G(4)*G(4)
      dsdeEl(1,3)=elast1*G(1)*G(3)+elast2*TWO*G(5)*G(5)
      dsdeEl(1,4)=elast1*G(1)*G(4)+elast2*TWO*G(1)*G(4)
      dsdeEl(1,5)=elast1*G(1)*G(5)+elast2*TWO*G(1)*G(5)
      dsdeEl(1,6)=elast1*G(1)*G(6)+elast2*TWO*G(4)*G(5)
      dsdeEl(2,2)=(elast1+TWO*elast2)*G(2)*G(2)
      dsdeEl(2,3)=elast1*G(2)*G(3)+elast2*TWO*G(6)*G(6)
      dsdeEl(2,4)=elast1*G(2)*G(4)+elast2*TWO*G(1)*G(4)
      dsdeEl(2,5)=elast1*G(2)*G(5)+elast2*TWO*G(1)*G(5)
      dsdeEl(2,6)=elast1*G(2)*G(6)+elast2*TWO*G(2)*G(6)
      dsdeEl(3,3)=(elast1+TWO*elast2)*G(3)*G(3)
      dsdeEl(3,4)=elast1*G(3)*G(4)+elast2*TWO*G(5)*G(6)
      dsdeEl(3,5)=elast1*G(3)*G(5)+elast2*TWO*G(5)*G(3)
      dsdeEl(3,6)=elast1*G(3)*G(6)+elast2*TWO*G(6)*G(3)
      dsdeEl(4,4)=elast1*G(4)*G(4)+elast2*(G(1)*G(2)+G(4)*G(4))
      dsdeEl(4,5)=elast1*G(4)*G(5)+elast2*(G(1)*G(6)+G(5)*G(4))
      dsdeEl(4,6)=elast1*G(4)*G(6)+elast2*(G(4)*G(6)+G(5)*G(2))
      dsdeEl(5,5)=elast1*G(5)*G(5)+elast2*(G(1)*G(3)+G(5)*G(5))
      dsdeEl(5,6)=elast1*G(5)*G(6)+elast2*(G(4)*G(3)+G(5)*G(6))
      dsdeEl(6,6)=elast1*G(6)*G(6)+elast2*(G(2)*G(3)+G(6)*G(6))
      do i=1,ncomp-1
        do j=i+1,ncomp
          dsdeEl(j,i)=dsdeEl(i,j)
        end do
      end do
```

Code Block 6.16

Next, the plastic stiffness matrix is created using the values from the elastic stiffness matrix as the first value; as in the one-dimensional case, `dsdePl` is output to the main programme as the Jacobian matrix, so unless plasticity occurs this equals **K**. At the same time, the elastic component trial stresses (`sigElp`) are incremented, in accordance with the standard method of evaluating matrices.

```
      do i=1,ncomp
         sigElp(i) = stress(i)
         do j=1,ncomp
            dsdePl(j,i) = dsdeEl(j,i)
            sigElp(i) = sigElp(i)+dsdeEl(j,i)*dStrain(j)
         end do
      end do
```

Code Block 6.17

Code Block 6.18 calculates the hydrostatic stress, and hence obtains the deviatoric stresses, `sigDev`, from which the equivalent stress, `qEl`, is determined.

```
c *** hydrostatic pressure stress
      pEl = -THIRD * (sigElp(1) + sigElp(2) + sigElp(3))
c *** compute the deviatoric stress tensor
      sigDev(1) = sigElp(1) + pEl
      sigDev(2) = sigElp(2) + pEl
      sigDev(3) = sigElp(3) + pEl
      sigDev(4) = sigElp(4)
      sigDev(5) = sigElp(5)
      sigDev(6) = sigElp(6)
c *** compute von-mises stress
      qEl =
     &  sigDev(1) * sigDev(1)+sigDev(2) * sigDev(2)+
     &  sigDev(3) * sigDev(3)+
     &  TWO*(sigDev(4) * sigDev(4)+ sigDev(5) * sigDev(5)+
     &  sigDev(6) * sigDev(6))
      qEl = sqrt( ONEHALF * qEl)
```

Code Block 6.18

None of the above procedures was altered – as in the one-dimensional case, the altered elastic stiffness following plasticity is achieved by modifying Young's Modulus (and any other elastic values derived from it) before being entered into the procedures. Thus suitable stress increments may be calculated.

In overview, Code Block 6.19 calculates the increment in plastic strain (`dpleq`), then the incremented plastic strain, `pleq`, and resultant equivalent stress magnitude (based on linear hardening), `sigy`. It then updates the vectors of stress components, `stress`, and plastic strain components, `epsPl`, which are output to ANSYS.

```
c *** compute derivative of the yield function
      DO i=1, ncomp
         dfds(i) = threeOv2qEl * sigDev(i)
      END DO
      oneOv3G  = ONE / threeG
      qElOv3G  = qEl * oneOv3G
c *** initial guess of incremental equivalent plastic strain
      dpleq    = qElOv3G - sigy * oneOv3G
      pleq     = pleq_t + dpleq
      sigy     = sigy0 + dsigdep * pleq
c
c ***  update stresses
      DO i = 1 , ncomp
         stress(i) =  sigElp(i) - TWOTHIRD * (qEl-sigy) * dfds(i)
      END DO
c
c ***  update plastic strains
      DO i = 1 , nDirect
         epsPl(i) = epsPl(i) + dfds(i) * dpleq
      END DO
      DO i = nDirect + 1 , ncomp
         epsPl(i) = epsPl(i) + TWO * dfds(i) * dpleq
      END DO
```

Code Block 6.19

The flow rule is used to calculate the stress and strain increments – as the stress function used is also the yield function, this then becomes the associative flow rule

(meaning plastic strains occur in the direction of the normal to the yield surface [31). The different components of the partial derivative are stored within the `dfds` vector.

Equation (6.5) shows the general form of the associative flow rule [32]:

$$\dot{\varepsilon}^p = \dot{\lambda}\left(\frac{\partial f}{\partial \sigma}\right) \tag{6.5}$$

ANSYS employs the discrete form, such that small increments of plastic strain are used, rather than derivatives, as shown in Equation (6.6):

$$\Delta\varepsilon_i^p = \Delta\varepsilon_{eq}^p\left(\frac{\partial f}{\partial \sigma_i}\right) \tag{6.6}$$

`dfds` corresponds with the partial derivative of *f*, the plasticity criterion function (which defines the yield surface, $f = 0$), and `dpleq` to $\Delta\varepsilon_{eq}^p$, the multiplier of time-independent plasticity.

Code Block 6.20 then stores the equivalent (`pleq`) and component (`epsPl(i)`) plastic strain values in the state variable, and increments the plastic work, `sedPl`.

```
c *** Update state variables
      statev(1) = pleq
      do i=1,ncomp
         statev(i+1) = epsPl(i)
      end do
c *** Update plastic work
      sedPl = sedPl + HALF * (sigy_t+sigy)*dpleq
```

Code Block 6.20

Code Block 6.21 calculates the current plastic Jacobian matrix, `dsdePl`.

```
c *** Material Jcobian matrix
c
      IF (qEl.LT.sqTiny) THEN
         con1 = ZERO
      ELSE
         con1 = threeG * dpleq / qEl
      END IF
      con2 = threeG/(threeG+dsigdep) - con1
      con2 = TWOTHIRD * con2
      DO i=1,ncomp
         DO j=1,ncomp
            JM(j,i) = ZERO
         END DO
      END DO
      DO i=1,nDirect
         DO j=1,nDirect
            JM(i,j) = -THIRD
         END DO
         JM(i,i) = JM(i,i) + ONE
      END DO
      DO i=nDirect + 1,ncomp
         JM(i,i) = HALF
      END DO
      DO i=1,ncomp
         DO j=1,ncomp
            dsdePl(i,j) =    dsdeEl(i,j) - twoG
     &           * (  con2 * dfds(i) * dfds(j) + con1 * JM(i,j) )
         END DO
      END DO
c
      goto 600
```

Code Block 6.21

Code Block 6.22 copies the elastic trial stresses to the output stress vector if no plastic deformation occurred during the current iteration.

```
  500 continue

c *** Update stress in case of elastic/unloading
      do i=1,ncomp
         stress(i) = sigElp(i)
      end do
```

Code Block 6.22

Code Block 6.23 iterates through each component present to calculate the current elastic work, `sedEl`, stores the current yield stress, `sigy`, in the state variable, then exits the sub-routine.

```
  600 continue
      sedEl = ZERO
      DO i = 1, ncomp
        sedEl = sedEl + stress(i)*(Strain(i)+dStrain(i)-epsPl(i))
      END DO
      sedEl = sedEl * HALF
      statev(nStatev) = sigy
c
      return
      end
```

Code Block 6.23

6.4.2. Modifications made to the three-dimensional model

Having successfully created a one-dimensional material model of the gun steel A723, the main tasks necessary to formulate a three-dimensional version were:

1. Develop more robust loading/unloading detection
2. Introduce the use of equivalent stresses and strains
3. Add in automatic selection of behaviour when employed in plane strain/axi-symmetric and three-dimensional cases.

The most important of the above tasks is detection of loading/unloading. To accomplish this reliably and succinctly, once unloading for a given integration point is detected, the decision (see Code Block 6.26) is stored as a flag within the state variable. Within the sub-routine, the value was assigned the name `UnldFlag` (unloading flag).

To properly determine the current stress-strain state when multiple components are present, equivalent values must be used. In addition to this, a separate set of unloading variables must be maintained, just as the reverse plastic strain (`Revpleq`) was in *usermat1d*. The retained values were:

1. Peak (total) component strains,
2. Peak component stresses,
3. Reverse component stresses,
4. Reverse (plastic) component strains.

A summary of the calculation process used is given below, which is followed by a more detailed explanation interspersed with the source code that achieves the described features.

The peak stresses and strains were stored to allow reverse values to be calculated as the material contracts. Specifically, the current (total) reverse strains are calculated; from these reverse strain increments, reverse elastic trial stresses are incremented (as in the "forwards" case).

These reverse elastic trial stresses are then assessed against the reverse yield stress, $\sigma_{Max} + \beta^*\sigma_{Y0}$; as in the forwards case, an extra stage of plasticity calculations are conducted

if the reverse yield stress is exceeded, otherwise the elastic stress components are taken as the final reverse stress components for that iteration. The final reverse stress components are then subtracted from the peak component stresses to determine the final values of the "forward" stress components for that iteration.

Code Block 6.24 handles reading in the values of both `Tensepeq` and `UnldFlag` from the state variable at the start of each pass through the sub-routine. In addition, several other values are read in from the state variable and/or calculated from other parameters: peak total strain is read into `PeakStrn`, peak stress is read into `PeakStress`, reverse stresses are read into `RevStress`, reverse strains and strain increments are calculated and stored in `RevStrain` and `dRevStrain`, respectively.

The initial reverse yield stress, `Revsigy_t`, is also read in from the state variable, the value of which is also used as the incremented reverse yield stress, `Revsigy`.

As different numbers of components are present in the three-dimensional and axi-symmetric/plane strain cases, `statev` varied in size to accommodate this. Thus, it was important to ensure references to `statev` reflected its variable size, and hence were relative and/or procedural; for example, `UnldFlag` and `Tensepeq` are respectively third and second from last, and are referenced relative to the last entry. Finally, the initial reverse plastic strain, `Revpleq_t`, is calculated.

```
      pleq_t   = statev(1)
      pleq     = pleq_t
      DO i = 1, ncomp
        PeakStrn(i)   = statev(i + (ncomp+1))
        PeakStress(i) = statev(i + (2*ncomp+1))
        RevStress(i)  = statev(i + (3*ncomp+1))
        RevStrain(i)  = Strain(i) - PeakStrn(i)
        dRevStrain(i) = -dStrain(i)
      END DO
      Revsigy_t = statev(nstatev-3)
      Revsigy   = Revsigy_t
      UnldFlag  = statev(nstatev-2)
      Tensepeq  = statev(nstatev-1)
      Revpleq_t = Tensepeq - pleq_t
```

Code Block 6.24

Following the extra code used to read in values, the first addition, given in Code Block 6.25, to *usermat3d* was the calculation of a set of equivalent total strain values. The peak value (`MaxTotStrn`), the initial value (`qStrn_t`) and incremented value (`qStrn`) for the current iteration (based on the `Strain` array and the element-by-element sum of the `Strain` and `dStrain` arrays, respectively). The calculations are conducted in three stages to allow for the variable number of shear components that may be present.

Finally, the maximum stress at the integration point experienced in loading (`MaxEqSig`) is calculated, by substituting the value of maximum plastic strain in loading (`Tensepeq`) into the material-fit equation (see sub-section 5.1.1). This peak stress value is used when calculating the reverse yield stress.

```
      MaxTotStrn = (PeakStrn(1)-PeakStrn(2))**2
     &+ (PeakStrn(2)-PeakStrn(3))**2 + (PeakStrn(3)-PeakStrn(1))**2

      qStrn_t = (Strain(1)-Strain(2))**2 + (Strain(2)-Strain(3))**2
     &   + (Strain(3)-Strain(1))**2

      qStrn = ((Strain(1)+dStrain(1))-(Strain(2)+dStrain(2)))**2
     &   +      ((Strain(2)+dStrain(2))-(Strain(3)+dStrain(3)))**2
     &   +      ((Strain(3)+dStrain(3))-(Strain(1)+dStrain(1)))**2

      DO i = 4, ncomp
        MaxTotStrn = MaxTotStrn + 1.5d0*PeakStrn(i)**2
        qStrn_t = qStrn_t + 1.5d0*Strain(i)**2
        qStrn = qStrn + 1.5d0*(Strain(i)+dStrain(i))**2
      END DO

      MaxTotStrn = DSQRT(MaxTotStrn) / (DSQRT(TWO)*(ONE+posn_eff))
      qStrn_t = DSQRT(qStrn_t) / (DSQRT(TWO)*(ONE+posn_eff))
      qStrn = DSQRT(qStrn) / (DSQRT(TWO)*(ONE+posn_eff))

      MaxEqSig  = sigy0 * (ONE + MatParms(1) * DTANH
     &(MatParms(2) * Tensepeq) + MatParms(3) * Tensepeq * 1.d2)
```

Code Block 6.25

Code Block 6.26 conditionally sets the unloading flag, `UnldFlag`, to indicate to following code that the material is unloading *from prior plastic strain* (determined by the outer `IF` statement), using the tolerance value `UnldFact` to help prevent false positives of unloading detection.

Given the potential for a more complex load cycle it was important that the code be able to cope with small drops in equivalent strain before peak strain is reached, and small increases in strain during unloading from peak strain. The `IF` statements in Code Block 6.26 ensure that once equivalent strain drops below the peak value encountered, and only resumes loading (by setting `UnldFlag` to zero) if strain exceeds the previous maximum.

Using a numerical value for the unloading flag allows for convenient future expansion, through the addition of extra material states. This would be material dependent, but could allow ratchetting or re-autofrettage to be investigated.

```
      IF (Tensepeq .GT. ZERO) THEN
        IF (qStrn .LT. qStrn_t) UnldFlag = ONE
        IF (qStrn .GT. MaxTotStrn) UnldFlag = ZERO
      END IF
```

Code Block 6.26

If unloading is detected, Code Block 6.27 calculates the requisite values for subsequent unloading stress calculations: Young's Modulus (`young`), multiples of the shear modulus (`twoG` and `threeG`), the Bauschinger Effect Factor (`BEF`) and gamma (stored in `MatParms(4)`). In addition to these, the initial value of reverse yield stress (`Revsigy_t`) is calculated if the current iteration is the first in which unloading follows loading (this means that if unloading is briefly detected during loading, `Revsigy_t` will

be correctly recalculated when unloading restarts – reflecting the true peak stress during loading). For any case other than initial unloading, `Revsigy_t` is read in from the state variable by Code Block 6.24.

```
      IF (UnldFlag .EQ. ONE) THEN
        young = prop(1) * (ONE - 0.15d0*DTANH(1.2d0*Tensepeq*1.d2))
        twoG    = young / (ONE+posn)
        threeG  = ONEHALF * twoG
        IF (Tensepeq .LT. 1.d-2) BEF = 0.1684d0 *
     &   (DTAN(ONE - Tensepeq*1.d2))**3.6d0 + 0.17d0
        IF (Tensepeq .GE. 1.d-2) BEF = 0.17d0
        IF (statev(nstatev-2) .EQ. ZERO .and. UnldFlag .EQ. ONE)
     & THEN
          Revsigy_t = MaxEqSig + BEF*sigy0
          Revsigy = Revsigy_t
        END IF
        MatParms(4) = 1.2858d0 * (Tensepeq*1.d2) ** -0.323d0
      END IF
```

Code Block 6.27

The elastic stiffness matrix, `dsdeEl`, is then calculated (as described in Code Block 6.16) which means that it reflects the value of the elastic constants whether in loading or unloading. The value of the elastic stress increments is then calculated, as given in Code Block 6.17, which is followed by a conditional `GOTO` command (Code Block 6.28) that jumps to the elastic unloading segment (at execution point 400) if `UnldFlag` equals one.

```
      IF (UnldFlag .EQ. ONE) GOTO 400
```

Code Block 6.28

If unloading is not present, and the above `GOTO` is not followed, the elastic loading path is followed. This is unchanged, apart from writing the elastic stresses to the `stress` vector (which is later written to the state variable) when behaviour remains elastic (it was previous done at execution point 500).

If unloading is detected, an equivalent set of calculations is made for a set of dummy "reverse" variables, as would be made for the "forward" variables. This is accomplished by Code Block 6.29.

```
      DO i=1,ncomp
        RevsigElp(i) = RevStress(i)
        DO j=1,ncomp
          dsdePl(j,i) = dsdeEl(j,i)
          RevsigElp(i) = RevsigElp(i) + dsdeEl(j,i)*dRevStrain(j)
        END DO
      END DO
c *** Reverse hydrostatic pressure stress
      RevpEl = -THIRD * (RevsigElp(1) + RevsigElp(2) +
     &  RevsigElp(3))
c *** compute the reverse deviatoric stress tensor
      DO i=1,nDirect
        RevsigDev(i) = RevsigElp(i) + RevpEl
      END DO
      DO i=nDirect+1,ncomp
        RevsigDev(i) = RevsigElp(i)
      END DO

      RevqEl = ((RevsigElp(1)-RevsigElp(2))**2 +
     & (RevsigElp(2)-RevsigElp(3))**2 +
     & (RevsigElp(3)-RevsigElp(1))**2)/TWO +
     & 3*(RevsigElp(4)**2 + RevsigElp(5)**2 + RevsigElp(6)**2)
      RevqEl = DSQRT(RevqEl)

      Revfratio = RevqEl/Revsigy_t - ONE
      IF (RevqEl .EQ. ZERO) Revfratio = ZERO
```

Code Block 6.29

As in the “forward” case, yielding is determined by the ratio of the equivalent stress to the current yield stress. In this “reverse” case, `Revfratio` is the name assigned to the variable. If no reverse yielding is detected (`Revfratio` is zero or less), Code Block 6.30 assigns the elastic reverse stress components as the final reverse stress components for the iteration, subtracts these values from the peak component stresses to find the current “forward” values, and stores the reverse stresses in the state variable. Finally it jumps to execution point 600. If yield is detected, execution jumps to the reverse plasticity section (440).

```
      IF (Revsigy_t .LE. ZERO .or. Revfratio .LE. -SMALL) THEN
        DO i = 1, ncomp
          RevStress(i) = RevsigElp(i)
          stress(i) =  PeakStress(i) - RevStress(i)
          statev(i + (3*ncomp+1)) = RevStress(i)
        END DO
        GOTO 600
      END IF

      GOTO 440
```

Code Block 6.30

As in the elastic case described above, the plasticity code comprises two paths: loading and unloading. A plasticity path is followed if its respective elastic precursor calculated a trial stress that exceeded the current yield stress.

The plastic case in loading was altered little from that supplied with the bi-linear isotropic material. Specifically, the incremented yield stress (`sigy`) calculation was changed to match that given by the material-fit, and the uni-axial plastic modulus (here named `TM_UniAx`) is calculated as the derivative of the material-fit equation. These are summarised by Code Block 6.31.

```
      sigy = sigy0 * (ONE + MatParms(1)*DTANH(MatParms(2)*pleq)
     & + MatParms(3) * pleq * 1.d2)

      TM_UniAx = sigy0*MatParms(3)*100.d0
```

Code Block 6.31

The plastic case in unloading was, like the elastic case in unloading, a new addition that was based on the structure supplied with the isotropic case. Code Block 6.32 lists the code which computes the values for the dummy "reverse" variables – from calculation of reverse plastic strain increment (`dRevpleq`) and new reverse yield stress (`Revsigy`), to updating the reverse stress (`RevStress(i)`) and plastic strain (`RevepsPl(i)`) components.

```
      threeOv2RevqEl = ONEHALF / RevqEl

c *** compute derivative of the reverse yield function
      DO i = 1, ncomp
        Revdfds(i) = threeOv2RevqEl * RevsigDev(i)
      END DO
      oneOv3G  = ONE / threeG

c *** initial guess of incremental equivalent plastic strain
      dRevpleq = (RevqEl - Revsigy_t) * oneOv3G
      Revpleq  = Revpleq_t + dRevpleq
      Revsigy = MaxEqSig + sigy0 * ((ONE+MatParms(1)-BEF) * DTANH
     & (MatParms(4)*Revpleq*1.d2) + BEF + MatParms(3)*Revpleq*1.d2)

c ***  update reverse stresses
      DO i = 1, ncomp
        RevStress(i) = RevsigElp(i) -
     &   TWOTHIRD * (RevqEl-Revsigy) * Revdfds(i)
      END DO

c ***  update reverse plastic strains
      DO i = 1, nDirect
        RevepsPl(i) = RevepsPl(i) + Revdfds(i) * dRevpleq
      END DO
      DO i = nDirect+1, ncomp
        RevepsPl(i) = RevepsPl(i) + TWO * Revdfds(i) * dRevpleq
      END DO
```

Code Block 6.32

Once the "reverse" variables are calculated, the "forward" variables are determined using them, as shown in Code Block 6.33. The variables used are the same as those in the supplied material, with the exception of the additional values (reverse stress

components, `Revstress(i)`, and reverse plastic strain components, `RevepsPl(i)`) written to the state variable array by the final `DO` loop.

```
c *** update equivalent plastic strain
      dpleq   = -dRevpleq
      pleq    = Tensepeq - Revpleq
c *** compute derivative of the yield function
      DO i = 1, ncomp
        dfds(i) = -Revdfds(i)
      END DO
c *** update actual stresses
      DO i = 1, ncomp
        stress(i) =  PeakStress(i) - RevStress(i)
      END DO
c *** update actual plastic strains
      DO i = 1 , nDirect
        epsPl(i) = epsPl(i) + dfds(i) * dpleq
      END DO
      DO i = nDirect + 1, ncomp
c *** BEGIN MODIFICATION 009.08
        epsPl(i) = epsPl(i) + TWO * dfds(i) * dpleq
      END DO
      epseq  = pleq
c *** Update state variables
      statev(1) = pleq
      DO i = 1, ncomp
        statev(i+1) = epsPl(i)
        statev(i + (3*ncomp+1)) = RevStress(i)
        statev(i + (4*ncomp+1)) = RevepsPl(i)
      END DO
```

Code Block 6.33

Once the “forward” values are determined, the plastic work and Jacobian matrix are calculated – the latter to give ANSYS a hint for when it formulates the conditions for the next iteration.

Given the non-linear behaviour that is simulated in unloading, formulating the “hint” is not straight forwards without knowing the strain increment for the following iteration. As the strain increment is determined in some part by the Jacobian matrix output by the material routine, and not knowing the precise method by which ANSYS formulates the strain increment, it is impossible to explicitly calculate an exact Jacobian matrix.

```
c *** Update plastic work
      sedPl = sedPl + HALF * (Revsigy_t+Revsigy)*dRevpleq
c *** Estimate plastic slope for next iteration
      dsigdep = (Revsigy - Revsigy_t)*0.75d0/dRevpleq
c *** Material Jacobian matrix
      IF (RevqEl.LT.sqTiny) THEN
        con1 = ZERO
      ELSE
        con1 = threeG * dRevpleq / RevqEl
      END IF
      con2 = TWOTHIRD * (threeG/(threeG+dsigdep) - con1)
      DO i=1,ncomp
        DO j=1,ncomp
          JM(j,i) = ZERO
        END DO
      END DO
      DO i = 1, nDirect
        DO j = 1, nDirect
          JM(i,j) = -THIRD
        END DO
        JM(i,i) = JM(i,i) + ONE
      END DO
      DO i = nDirect + 1, ncomp
        JM(i,i) = HALF
      END DO
      DO i = 1, ncomp
        DO j = 1, ncomp
          dsdePl(i,j) = dsdeEl(i,j) - twoG
     &     * (con2*Revdfds(i)*Revdfds(j) + con1*JM(i,j))
        END DO
       END DO
```

Code Block 6.34

Once the stress calculations have been made (be they in loading or unloading, elastic or plastic), the final section of the sub-routine is run. This is mostly unaltered from the supplied code, aside from the extra values that are written to the state variable array; Code Block 6.35 details how this is accomplished. The values are: peak total component strain (if the incremented equivalent strain exceeded the previous maximum), reverse yield stress, unloading flag and peak tensile plastic strain.

```
      IF (qStrn .GT. MaxTotStrn) THEN
        DO i=1, ncomp
          statev(i + (ncomp+1)) = Strain(i)+dStrain(i)
        END DO
      END IF
      statev(nstatev-3) = Revsigy
      statev(nstatev-2) = UnldFlag
      IF (pleq .GT. statev(nstatev-1)) statev(nstatev-1) = pleq
```

Code Block 6.35

6.4.3. Uni-Axial Testing

As an initial check, *usermat3d* was used in the simulation of a uni-axial sample. This used a three dimensional model of high aspect ratio, to minimise through-section stresses, to allow stress from a tension-compression cycle to be compared with those from the material-fit equations. This follows the same methodology as the comparison of the results from *usermat1d* with spreadsheet data, allowing the accuracy of the material-fit to be easily assessed in simple stress conditions (no shear stresses present).

The model consisted of a tall cuboid (see Figure 6.6) – its "height" (in the z-axis) was 100 times its depth and width (in the x- and y-axes). Its base area was constrained to zero z-displacement, and two lines around the base were constrained – one to zero x-displacement and one to zero y-displacement (the lines lying along the y- and x-axes, respectively). The upper surface was then displaced in the z-axis to achieve the tensile-compressive load cycle.

The model was meshed using 100 SOLID185 elements, such that each element is cube-shaped in its undeformed state. SOLID185 elements are 8-noded (one at each corner) elements, which makes them well suited to this investigation (the stress distribution is uniform, so there is no need of higher-order elements to improve the resolution of results).

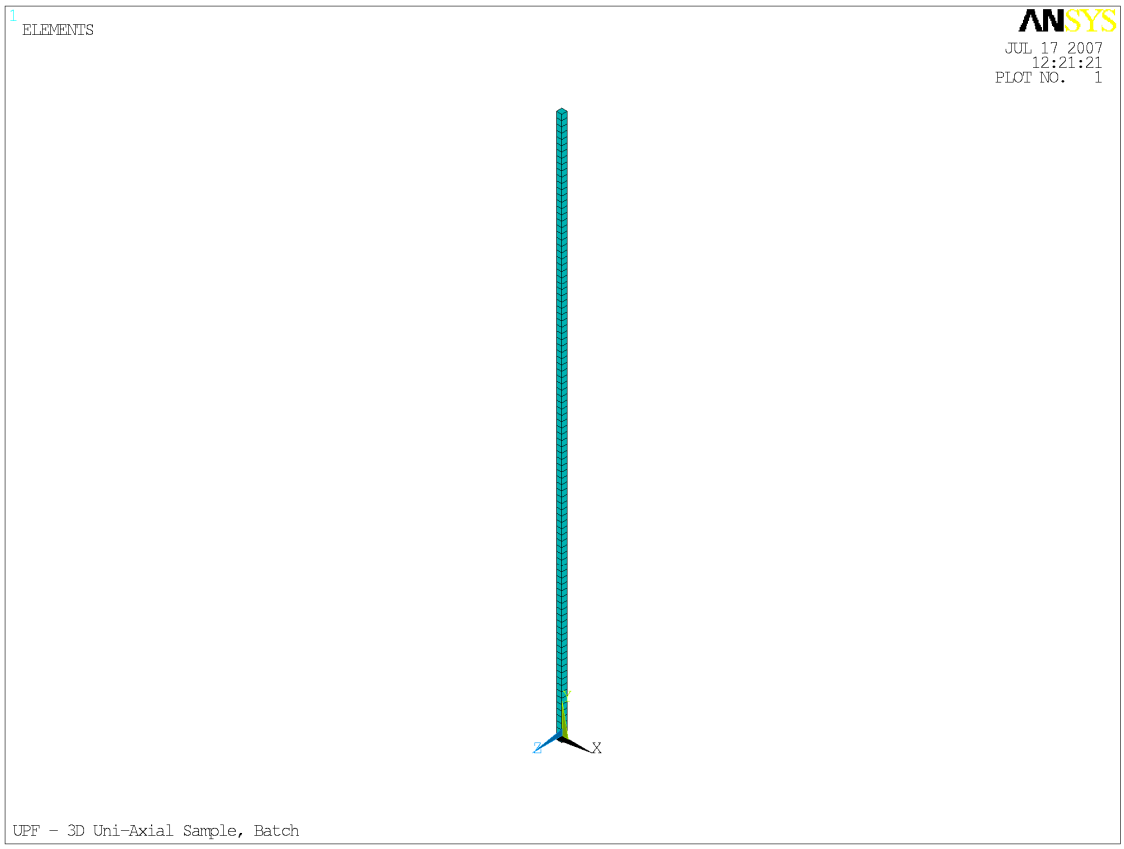

Figure 6.6: Uni-Axial Sample Mesh

The results are given in Figure 6.7. Agreement is generally very good, aside from a slight underestimation of the stress made by the FEA results in the moderate reverse plastic strain region. Inspection of the other stress components reveals that they are of the order of 10 kPa in this same region (they are much lower elsewhere), indicating the equivalent stress is accurate. While undesirable, this is understandable given the following:

1. The stress components are entirely dependent on the increments of component strain that are input to the sub-routine.
2. In turn, component strain increments are determined in part by the stress-strain Jacobian matrix output by the sub-routine in the previous iteration.
3. Given the unknown strain increment for the current iteration, it is impossible to calculate an effective gradient for the non-linear stress-strain relationship during the previous iteration. The Jacobian matrix cannot then be accurately calculated.

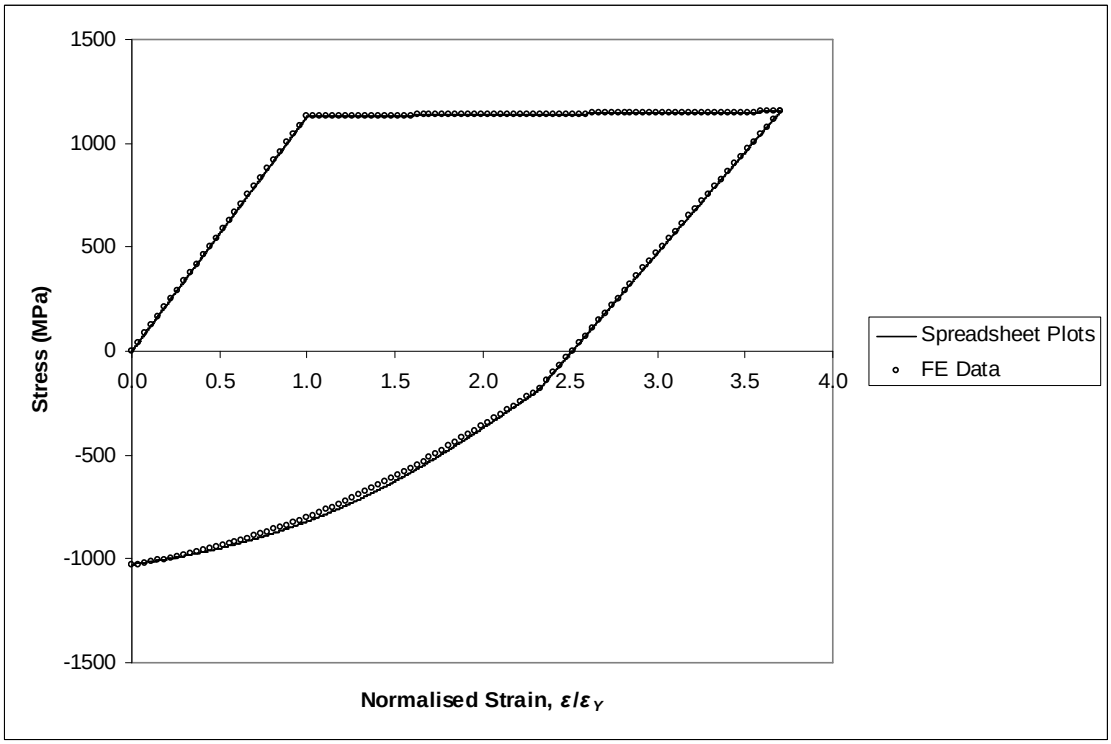

Figure 6.7: Tensile-Compressive Profiles, *usermat3d*

6.5. COMPARISON AND VALIDATION

Following the verification of both the one- and three-dimensional models in their ability to simulate uni-axial conditions, *usermat3d* was tested in a series of hydraulic autofrettage simulations. Results from the material model, used within ANSYS, were used in a set of comparisons with two other models, previously reported by Gibson et al. [33].

6.5.1. Details of Comparisons

The custom material, *usermat3d*, was compared with two other methods: the Hencky Programme and the ANSYS implementation of the EMPRAP (described in Chapter 5). Respectively, the methods are referred to as ANSYS (UPF), EMPRAP (Hencky) and EMPRAP (FEA) in subsequent tables and figures. Each method was programmed to model A723-1130, the behaviour of which is defined in sub-section 5.1.1.

As was the case in Chapter 5, the three methods were compared in four different end conditions (Plane Strain and Plane Stress, Open- and Closed-Ends), for two different Wall Ratios (2.0 and 2.5).

The meshes developed in Chapter 4 (and also used in Chapter 5) were retained and again used here for both the ANSYS (UPF) and EMPRAP (FEA) models. This meant that any variation between the two sets of results would be directly attributable to the different material representations.

6.5.2. Results

Autofrettage pressures for each of the configurations are presented in Table 6.2. Table 6.3 and Table 6.4 respectively show the peak autofrettage plastic equivalent strains at the ID at peak pressure for $K = 2$ and $K = 2.5$ respectively.

	Pressure (MPa)	
End Condition	K = 2.0	K = 2.5
Plane Strain	873.9	1092.8
Plane Stress	849.1	1067.4
Open-Ends	853.2	1081.7
Closed-Ends	877.3	1095.0

Table 6.2: Autofrettage Pressures

End Condition	Strain (%)			% Error UPF, w.r.t. Hencky
	ANSYS (UPF)	EMPRAP (FEA)	EMPRAP (Hencky)	
Plane Strain	1.21	1.20	1.22	-0.81
Plane Stress	1.28	1.34	1.35	-5.18
Open-Ends	1.08	1.08	1.09	-0.93
Closed-Ends	1.26	1.26	1.27	-0.68

Table 6.3: Peak Plastic Equivalent Strains at ID during AF, *K* = 2.0

End Condition	Strain (%)			% Error UPF, w.r.t. Hencky
	ANSYS (UPF)	EMPRAP (FEA)	EMPRAP (Hencky)	
Plane Strain	1.51	1.51	1.53	-1.08
Plane Stress	2.17	2.44	2.45	-11.27
Open-Ends	1.43	1.44	1.45	-1.11
Closed-Ends	1.55	1.55	1.57	-0.98

Table 6.4: Peak Plastic Equivalent Strains at ID during AF, *K* = 2.5

Figure 6.8 shows equivalent plastic strains throughout the tube at peak pressure under Plane Strain. Figure 6.9 shows the same results in the near-bore region. Tables 6.5 and 6.6 show residual hoop stresses at the bore for K = 2 and K = 2.5, respectively.

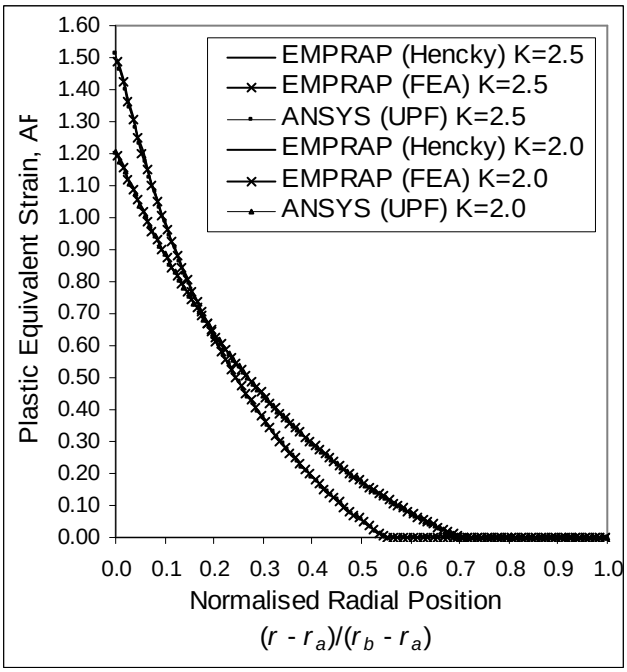

Figure 6.8: Equivalent Plastic Strains at Peak Pressure in Plane Strain

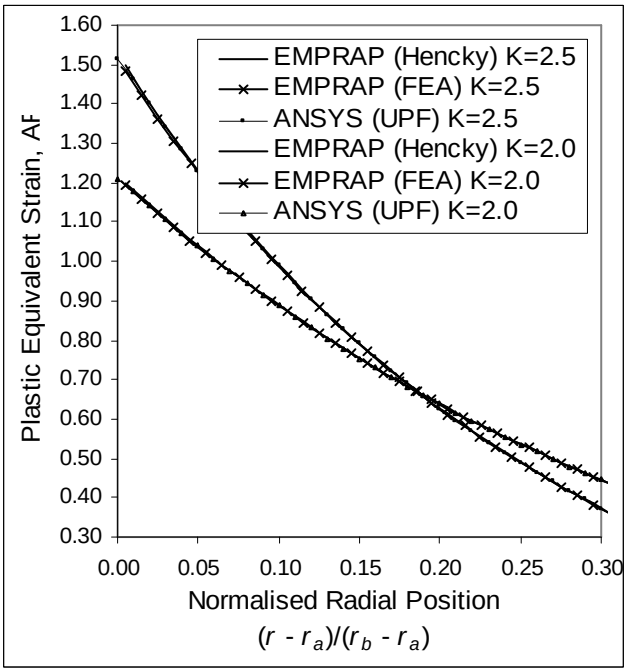

Figure 6.9: Equivalent Plastic Strains at Peak Pressure in Plane Strain, Expanded

End Condition	Stress (MPa)			% Error UPF, w.r.t. Hencky
	ANSYS (UPF)	EMPRAP (FEA)	EMPRAP (Hencky)	
Plane Strain	-651.3	-667.4	-676.0	-3.64
Plane Stress	-629.6	-635.1	-644.1	-2.25
Open-Ends	-622.1	-638.0	-647.2	-3.88
Closed-Ends	-657.3	-674.6	-682.1	-3.63

Table 6.5: Residual Hoop Stresses at Bore, K = 2.0

End Condition	Stress (MPa)			% Error UPF, w.r.t. Hencky
	ANSYS (UPF)	EMPRAP (FEA)	EMPRAP (Hencky)	
Plane Strain	-781.3	-787.3	-808.4	-3.35
Plane Stress	-828.0	-814.4	-834.5	-0.77
Open-Ends	-768.0	-773.4	-795.1	-3.41
Closed-Ends	-784.5	-791.2	-811.6	-3.35

Table 6.6: Residual Hoop Stresses at Bore, K = 2.5

Figures 6.10 – 6.13 show full residual hoop stress profiles for Plane Strain, Plane Stress, Open Ends and Closed Ends respectively. Tables 6.7 and 6.8 show residual plastic equivalent strains at ID, for K = 2.0 and K = 2.5 respectively. Figures 6.14 and 6.15 show variation through the wall under plane strain.

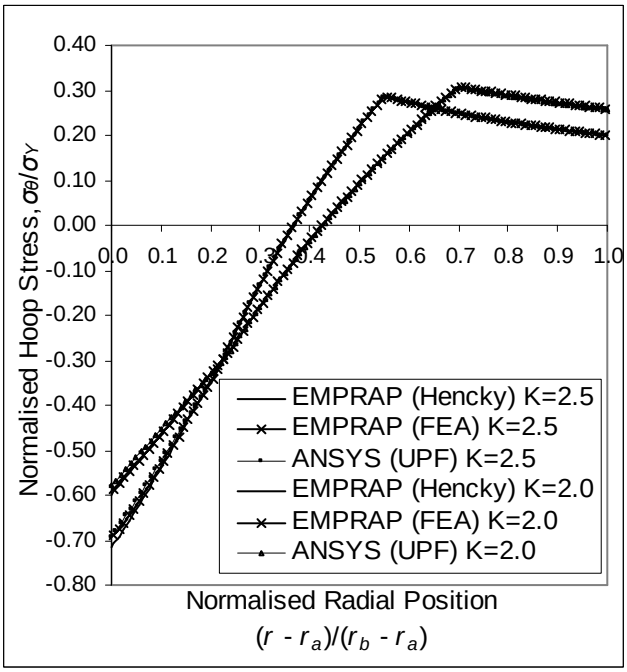

Figure 6.10: Residual Hoop Stresses in Plane Strain

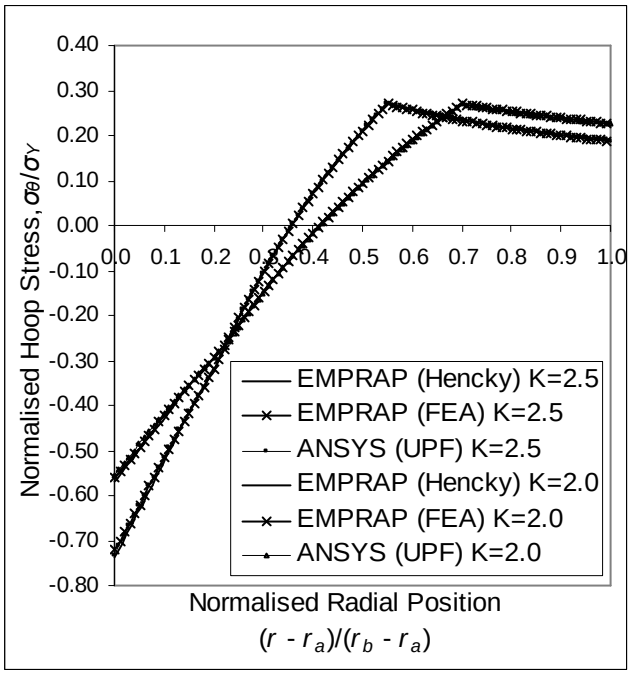

Figure 6.11: Residual Hoop Stresses in Plane Stress

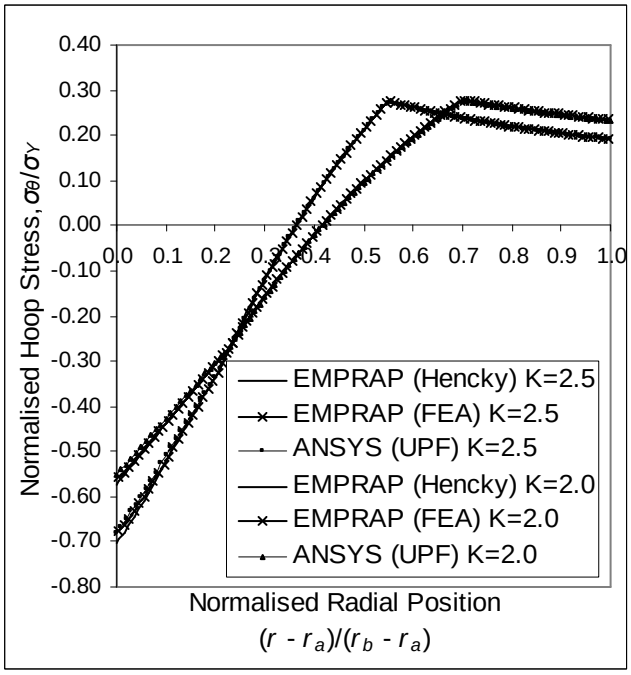

Figure 6.12: Residual Hoop Stresses, Open Ends

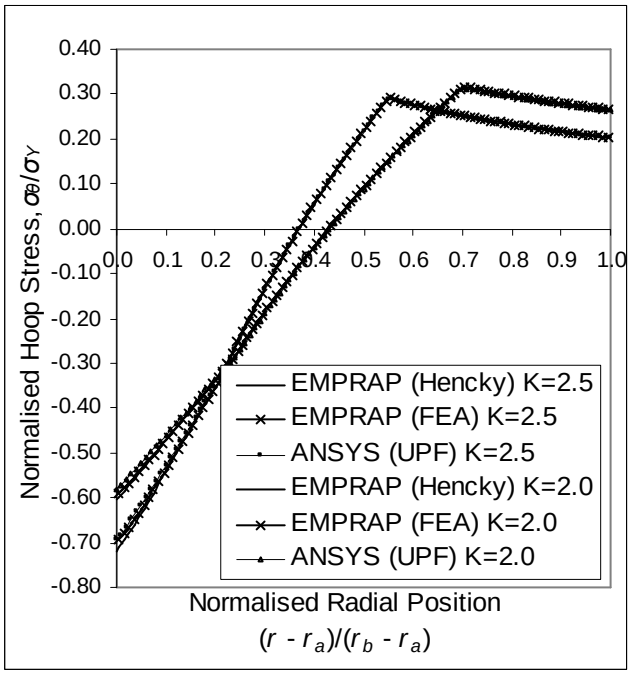

Figure 6.13: Residual Hoop Stresses, Closed Ends

End Condition	Strain (%)			% Error UPF, w.r.t. Hencky
	ANSYS (UPF)	EMPRAP (FEA)	EMPRAP (Hencky)	
Plane Strain	0.87	0.86	0.85	1.74
Plane Stress	0.97	1.02	1.01	-4.25
Open-Ends	0.77	0.76	0.75	1.82
Closed-Ends	0.91	0.89	0.89	1.73

Table 6.7: Residual Plastic Equivalent Strains at ID, K = 2.0

End Condition	Strain (%)			% Error UPF, w.r.t. Hencky
	ANSYS (UPF)	EMPRAP (FEA)	EMPRAP (Hencky)	
Plane Strain	1.02	1.01	1.00	1.89
Plane Stress	1.71	1.94	1.93	-11.29
Open-Ends	0.96	0.95	0.94	1.93
Closed-Ends	1.05	1.04	1.03	1.88

Table 6.8: Residual Plastic Equivalent Strains at ID, K = 2.5

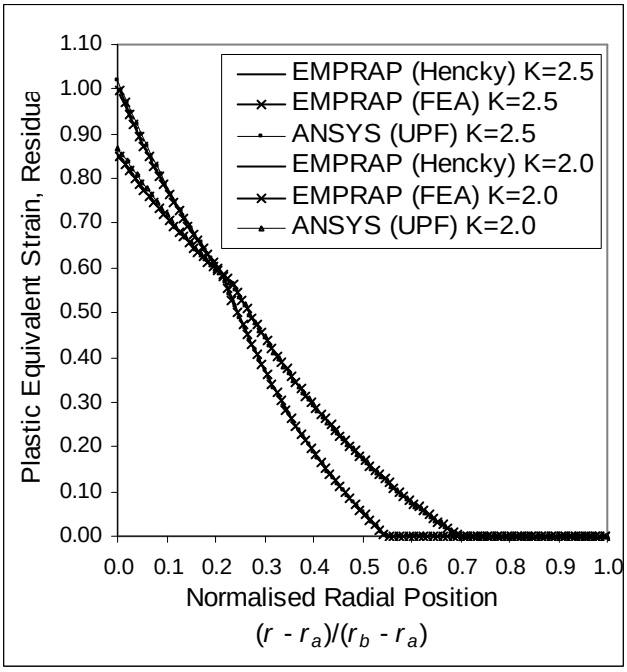

Figure 6.14: Residual Equivalent Plastic Strains in Plane Strain

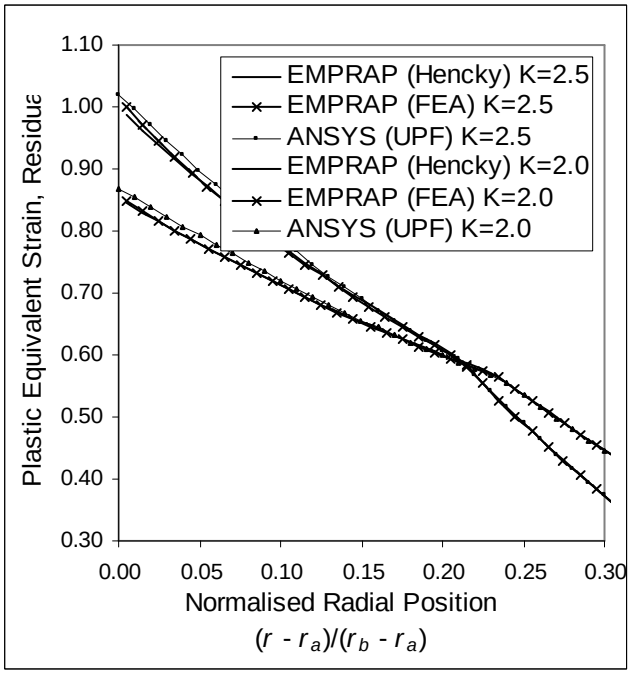

Figure 6.15: Residual Equivalent Plastic Strains in Plane Strain, Expanded

These results are assessed in section 6.6.

6.6. DISCUSSION

The initial set of results (sub-section 6.3.4) demonstrates the high accuracy with which the one-dimensional implementation of the material model (*usermat1d*) is able to match spreadsheet-derived data, within the iterative solution procedure used by ANSYS. The uni-dimensional stress-strain model makes it trivial to determine when unloading begins, based on the sign of the strain increment. In addition it means that no ambiguity exists when calculating the Jacobian matrix, which is used by ANSYS when it determines the strain increment for the next iteration.

The second comparison (results given in sub-section 6.4.3, Figure 6.7) investigates how well the three-dimensional material model (*usermat3d*) is able to match the same spreadsheet-derived data when used in a uni-axial model. Not only did this test how well the material model was able to detect the loading/unloading state, but also how the sub-routine interacted with ANSYS to recreate the uni-axial stress that should be present. The two issues are not exclusive, as the off-axis stress components contribute to the equivalent value, on which yielding is determined. Hence, although the stress-strain data from ANSYS generally matched those from the spreadsheet closely, the region in which agreement is less close (for mid-range values of reverse plastic strain) is also the region in which off-axis stresses are at their maximum.

Stress increments are determined by the strain increments, which are supplied as inputs to the sub-routine by ANSYS. In turn, ANSYS uses the Jacobian matrix which is returned to it by the sub-routine, to determine the strain increments for the next iteration. Taking this and the results of the first investigation together, indicates that the material stress calculations are accurate, while the value of the Jacobian matrix does not equal that which would be expected by ANSYS.

The third comparison (section 6.5) utilises the three-dimensional material model to simulate the stress-strain state within a series of autofrettaged tubes. Consequently it experiences three direct stress components (no shear stresses are present), which makes the comparison a good test of how accurately the material calculates these components, as well as detecting unloading. As the custom material was developed for use in autofrettage simulation (while being as general as possible), this comparison warrants more comprehensive treatment, given below.

The two EMPRAP models both implement a non-linear material in the same way but differ structurally – the EMPRAP (FEA) model uses an FE mesh while the EMPRAP (Hencky) model considers the thick-walled vessel to be a series of concentric thin cylinders behaving according to Lamé's equations. The EMPRAP (FEA) model and the ANSYS (UPF) model are identical structurally (they use the same mesh geometry), but implement material behaviour differently.

Note that subtle differences between the three constant axial strain cases relate to the interplay between axial stress distribution, dominated by end-load, and the other principal stresses. In the case of an incompressible material, the plane strain state is

similar to the closed-ended case. Throughout the autofrettage cycle, at each radial location, the axial stress is the mean of the hoop and radial stress. In more general cases, axial stress continues to be the intermediate principal stress and to make a contribution to the residual stress outcomes. For a given overstrain this contribution differs with end conditions, producing some small differences in hoop stress.

During the loading phase, for each configuration, autofrettage pressures to achieve 70% and 55% overstrain (K = 2.0 and 2.5, respectively) were within 0.1% across the three models. Peak hoop stresses were also well within 0.1% agreement. Given the diversity of the models, this is a strong validation of their elastic-plastic response to autofrettage pressure loading.

Equivalent plastic strains and associated hoop stresses at peak autofrettage pressure were compared. The Plane Strain, Open- and Closed-Ends conditions all show good agreement between the three methods. In the Plane Stress condition plastic strains are much larger than in the other three conditions, and there is a larger disparity between the ANSYS (UPF) results and those from the two EMPRAP methods. Pressures, stresses and strains for plane strain and open-end conditions were compared with available data and discussed in detail in [22]. The EMPRAP (Hencky) results presented herein use the same numerical model as in [22]. The agreement between EMPRAP (Hencky), EMPRAP (FEA) and ANSYS (UPF) is therefore reassuring.

Although the hoop stress values at the ID at peak pressure differ between configurations, it can be confirmed that the hoop stresses sum throughout the tube wall to equilibrate the autofrettage pressure. The fidelity of the plastic strain response of the three models was confirmed by overlaying stress-strain data from the ANSYS (UPF) model on a plot generated from the material-fit equations, showing very close agreement.

Unloading, and residual values show fairly acceptable agreement across the three models; typically, ANSYS (UPF) predicted slightly less compressive residual bore hoop stress than EMPRAP (FEA) (2.5% difference) and EMPRAP (Hencky) (4% difference).

There is a subtle but significant issue here. For each configuration, the stress fields at peak pressure were in very close agreement. Differences therefore arose principally during the depressurization process, during which the Bauschinger effect occurs. Considering the case K = 2, Open-Ends, the range of hoop stress during unloading is circa. 920 MPa. Using this value to estimate differences during the unloading phase the 4% and 2.7% values referred to above reduce to 2.7% and 1.7%. These values are typical for a non-linear numerical solution.

In addition to the results presented here, the customised USERMAT was used in comparison [24] with hydraulic autofrettage results from the SEMAT method of material representation, and subsequently used to implement the SEMAT within ANSYS. Close agreement is generally observed between the various implementations (using the Hencky Programme, Huang's method and the ANSYS model presented here) of cases including full unloading profiles and the SEMAT approach.

6.7. SUMMARY

The first, one-dimensional material model was created to gain familiarity with the ANSYS solution procedure, and determine how to programme the desired material within it. The close match between the results generated using it, with data from the material-fit equations confirm that the sub-routine calculates stress states accurately, and in a manner that allows ANSYS to reach solution normally.

The three-dimensional material model (*usermat3d*) was created to be used in all autofrettage simulations (hydraulic and swage), hence confirmation of its accuracy was vital. The uni-axial tests (sub-section 6.4.3) demonstrate a generally close match between results from the material model and the material-fit equations. Agreement is less complete where off-axis (direct) stresses increase in magnitude, altering the relationship between equivalent and axial stress. These off-axis stresses arise from the circular relationship between the Jacobian matrix output to ANSYS from the sub-routine, and the resultant strain increments that ANSYS supplies in return.

The three-dimensional material model was then used in a series of hydraulic autofrettage simulations, under a range of end conditions. The results showed good agreement; disparities are in line with the variations expected from the different numerical methods. Apart from the plastic strains calculated for the Plane Stress case, all residual stress and strain values showed very close agreement. Differences between constant-strain end condition cases may be explained by variations in the axial stress which is the intermediate principal stress.

It is inferred that variations of stresses and plastic strains between models is most likely due to subtle differences in the way each model calculates component stress.

Overall, with some reservations regarding the Plane Stress case, the ANSYS (UPF) model accurately calculates the stress-strain state resulting from the hydraulic autofrettage in a single procedure.

In summary, a custom material model of a real world gun steel (A723-1130) has been programmed utilising the USERMAT feature within ANSYS. USERMAT behaves as a standard material and, crucially, retains plastic strains; this makes the customised material suitable for use in more general load cases than allowed by the EMPRAP method – in particular, simulating swage autofrettage of a pressure vessel.

Hence this custom FE material model may now be used with reasonable confidence to simulate the swage autofrettage process. This work is described in Chapter 8, following an investigation of the influence of friction on the swaging process, using a moving band of pressure, in Chapter 7.

Such analyses will be conducted in an axi-symmetric model, but should the need for a full three-dimensional model arise the custom material will be suitable for such use

(subject to a small amount of additional verification, over that done in sub-section 6.4.3).

7. BAND OF PRESSURE MODEL

7.1. INTRODUCTION

To help demonstrate the differences between Hydraulic and Swage autofrettage, the Band of Pressure models were created. This would separate the influences of shear stresses and axial forces, thought to be the main differentiators between hydraulic and swage autofrettage, allowing the influence of each on residual stresses to be investigated.

The models allow a band of pressure to be applied to the bore of the modelled tube in two ways: as a static band which expands longitudinally (starting from the centreline and working towards the ends) and as a moving band. The models are fully parameterised to allow tube geometry, tube material, end conditions, applied pressure, and band properties to be altered easily.

The models utilise the inbuilt ANSYS BKIN material; although it does not simulate non-linear material unloading (after prior plastic strain), accurate material representation was not required as the loading mechanism is the focus of this portion of the investigation.

7.2. CONCEPTUAL NOTES

Given the ability to investigate autofrettage in the presence of shear stresses, without the frictional and axial stresses that arise during swaging, several issues needed to be investigated to help understand the reasons for the different residual stress fields created by hydraulic and swage autofrettage (the differences between which are explored in sub-section 7.2.2). The main issues identified were:

1. Increase in pressure as band width decreases (for constant autofrettage depth),
2. The relationship between shear stresses, band width and pressure,
3. Whether there is an optimum pressure band width,
4. When residual stress patterns transition from Hydraulic to Swage,
5. Similarity between the end effects in Band of Pressure and Swage cases.

7.2.1. Plan of Work

It was decided to first investigate the relationship between the width of the band of pressure and autofrettage depth – the band of pressure would initially act on the entire length of tube (i.e. hydraulic autofrettage), and during subsequent simulations the band width would be systematically shortened while keeping pressure constant.

Pressure for each case would then be adjusted to achieve the initial depth of autofrettage for each value of band width (the results would be used to inform the choice of pressure in the moving band case). Shear stresses would be recorded and investigated at the same time. Once the response during loading was identified, the effects of band of pressure loading on residual stresses would be investigated.

The second stage of the investigation would then investigate how shear stresses near a moving band of pressure varied over the length of the tube section, which would help to reveal the exact causes of asymmetry near the tube ends. Additionally, and crucially, residual stresses would be compared with those hydraulic autofrettage results developed in earlier chapters.

These results would then be available for comparison with results from swage autofrettage (presented in Chapter 8). For the mid-section of a long tube (along which a constant contact pressure would be expected), the main difference between the band of pressure and swage loading mechanisms would be the absence of friction, and the resultant axial and shear stresses.

It was realised that the application of a band of high pressure (rather than a displacement-based load, similar to that experienced by a tube during swaging) could cause large deformation of the tube, especially in the presence of a small plastic modulus, as the applied pressure remains constant while the tube expands. However, this would likely only occur near the ends of a tube, which are generally discarded following autofrettage, so this was felt to be of secondary importance (although potentially worthy of future work).

7.2.2. Comparison of Autofrettage Methods

Swage and hydraulic autofrettage differ mostly due to:

1. Hydraulic autofrettage is applied equally to the whole length of the tube, while swage autofrettage applies localised loading leading to non-uniform deflection along the length which results in through-wall shear stresses, as shown in Figure 7.1,

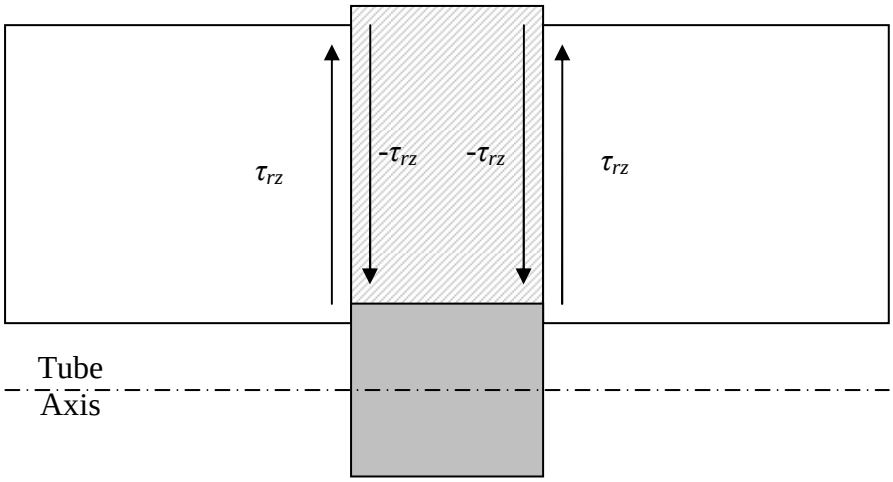

Figure 7.1: Shear Stresses in Swage Deflected Region

2. Hydraulic autofrettage generates axial stresses (which are independent of axial position), which may result in a net axial load (depending on the end conditions). Conversely, swage autofrettage definitely generates an axial load, equal to the swage driving force, which varies with axial position. The axial load results from both friction between the mandrel and tube, and a greater mean pressure on the forward face (P_{ff}) of the mandrel than on the rear face (P_{rf}), due to stress-strain hysteresis reducing the tube stiffness on unloading, and plastic deformation. In Figure 7.2, this translates into P_{ff} being larger than P_{rf}.

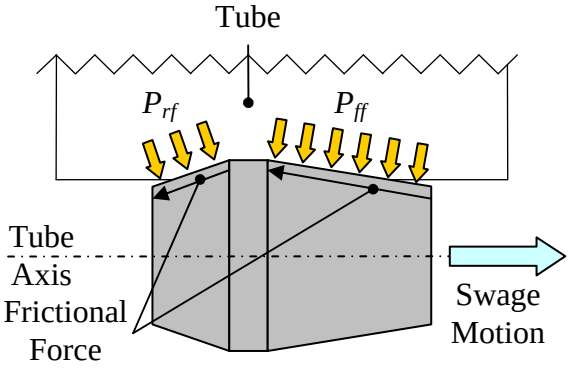

Figure 7.2: Swage Contact Forces

7.2.3. Modified Element Diagram

Graphically assessing the stresses acting upon an element within a tube, lying on the *r*-*z* plane, gives the diagram shown in Figure 7.3. This differs from diagram shown in Chapter 2 in that shear stresses are present and the fact that stresses may vary with axial position, allowing the effects of a localised load, such as a band of pressure, to be investigated. The tube is still considered to be axi-symmetric, precluding any variation of any property with θ, and requiring that $\tau_{r\theta} = \tau_{\theta z} = 0$, and initially plane sections are assumed to remain plane.

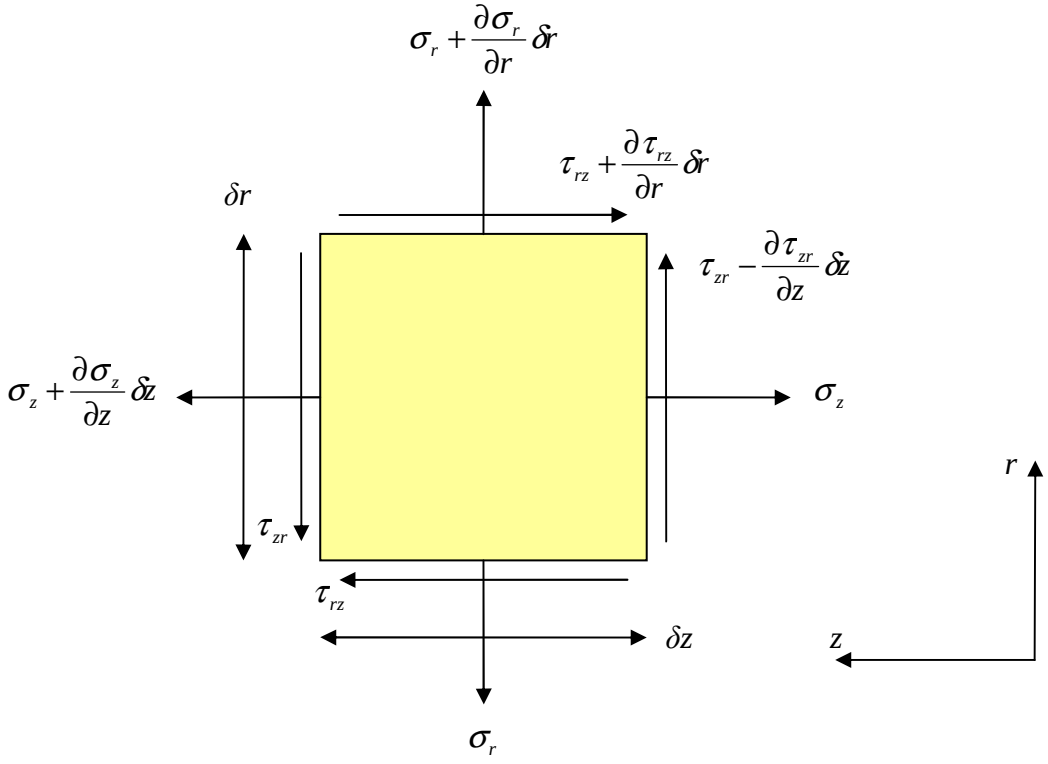

Figure 7.3: Shear Stresses acting on an element in the r-z plane

7.2.4. Equilibrium Equations

Applying the equilibrium criterion to the element shown in Figure 7.3 yields the following expressions.

Rotational

Summing the moments about the centre of the element yields the following:

$$\left[\tau_{zr}+\left(\tau_{zr}-\frac{\partial\tau_{zr}}{\partial z}\cdot\delta z\right)\right]\cdot\delta r\cdot r\delta\theta\cdot\delta z/2-\left[\tau_{rz}+\left(\tau_{rz}+\frac{\partial\tau_{rz}}{\partial r}\cdot\delta r\right)\right]\cdot r\delta\theta\cdot\delta z\cdot\delta r/2=0$$

Cancelling by $r\delta r\delta\theta\delta z/2$, and rearranging gives:

$$\tau_{zr}\left(2-\frac{\partial\tau_{zr}}{\partial z}\cdot\delta z\right)=\tau_{rz}\left(2+\frac{\partial\tau_{rz}}{\partial r}\cdot\delta r\right)$$

Taking δr and δz as tending towards zero, the following simplification can be made:

$$\tau_{zr}=\tau_{rz} \tag{7.1}$$

***z*-Axis**

$$\left[\left(\sigma_z+\frac{\partial\sigma_z}{\partial z}\cdot\delta z\right)-\sigma_z\right]\delta r\cdot r\delta\theta-\left[\left(\tau_{rz}+\frac{\partial\tau_{rz}}{\partial r}\cdot\delta r\right)-\tau_{rz}\right]r\delta\theta\cdot\delta z=0$$

$$\frac{\partial\sigma_z}{\partial z}\cdot\delta r\cdot\delta z=\frac{\partial\tau_{rz}}{\partial r}\cdot\delta r\cdot\delta z$$

$$\frac{\partial\sigma_z}{\partial z}=\frac{\partial\tau_{rz}}{\partial r} \tag{7.2}$$

***r*-Axis**

$$\left[\left(\sigma_r+\frac{\partial\sigma_r}{\partial r}\cdot\delta r\right)(r+\delta r)-\sigma_r\cdot r\right]\delta\theta\cdot\delta z-2\sigma_\theta\cdot\delta r\cdot\delta z\cdot\sin\left(\frac{\delta\theta}{2}\right)$$
$$+\left[\left(\tau_{zr}-\frac{\partial\tau_{zr}}{\partial z}\cdot\delta z\right)-\tau_{zr}\right]\cdot\left[(r+\delta r)^2-r^2\right]\delta\theta=0$$

$$\frac{\partial\sigma_r}{\partial r}(r+\delta r)\delta r\delta\theta\delta z+(\sigma_r-\sigma_\theta)\delta r\delta\theta\delta z-\frac{\partial\tau_{zr}}{\partial z}2r\delta r\delta z\delta\theta=0$$

Cancelling by $r\delta r\delta\theta\delta z$, and taking $\delta r \rightarrow 0$:

$$\frac{\partial\sigma_r}{\partial r}+\frac{(\sigma_r-\sigma_\theta)}{r}=2\frac{\partial\tau_{zr}}{\partial z} \tag{7.3}$$

7.3. MODELLING NOTES

7.3.1. Overview

The Band of Pressure model was based on previous hydraulic autofrettage models, with the main difference being axial length (l_z). The previous models were loaded by a uniform pressure acting along the whole of the modelled length with only mid-section properties assessed, but in this case localised loading was achieved through the application of a band of pressure – resulting in significant axial variation in stresses.

For this reason, the modelled section was long enough to capture variation resulting from the end effects. The end effects arise from the axial stresses caused by model constraints (not present in a tube uniformly loaded along it length), which in turn alter the proportions of the stress components when calculating equivalent stresses.

It is generally good practice when modelling to exploit whatever symmetry there is present to reduce the size of the modelled region (so that for a given number of elements, resolution is increased). Unlike the Hydraulic Autofrettage models (developed in Chapter 4), no axial symmetry existed in the Band of Pressure model, due to the axial variation inherent that results from the localised loading used. This precluded extensive use of such methods to achieve large reductions in the length of tube modelled.

The in-built bi-linear kinematic hardening material model (BKIN) was used for this investigation; while it was felt that using A723 would yield interesting results, the lack of empirical results for comparison would render them of little use. Instead, a simple material behaviour was selected, to allow easy observation of the effects of this unusual loading scenario. Young's Modulus, Poisson's ratio, yield stress and plastic modulus were selected to match that of A723 1130 during initial loading (the values are also used by the BKIN model during unloading and subsequent yielding).

To control the application of pressure, it was applied to elements along the ID rather than to entire line (as was done in the hydraulic autofrettage models).

7.3.2. Model Geometry

The model used to simulate hydraulic autofrettage (featured in Chapters 4-6) was largely suitable for use in the Band of Pressure model, with exception of the length of tube represented. To produce results that were comparable to those from swaging along the full length of a tube, the Band of Pressure model would need to represent a section of similar length; accordingly a section length of ten times the wall depth was selected ($l_z = 10l_r$). Thus, the mid-length position was five times the wall depth from the applied constraints and hence the axial stresses resulting from such could be

considered uniform (using St. Venant's principle), equalling zero given the zero net axial force from the end constraint.

The wall ratio (K) was also selected to allow broad comparability with swage, in that it would need to be large enough to induce reverse yielding (a crucial aspect when considering the residual stresses developed). To achieve this, K = 2.5 was selected; therefore normalised wall depth, l_r/r_a, equalled 1.5. Figure 7.4 depicts these dimensions.

Property	Value
Wall Ratio, K	2.5
Section Length, l_z	$10l_r$
Young's Modulus, E	209 GPa
Poisson's Ratio, v	0.3
Yield Stress, σ_{Y0}	1130 MPa
Plastic Modulus, H	1469 MPa

Table 7.1: Summary of Input Parameters

7.3.3. Model Constraint

Choice of constraint was determined by two factors:

1. Retaining similarity with previous hydraulic autofrettage models to allow comparison,
2. Ensuring results taken from the Band of Pressure model would be suitable for comparison with those to be generated by the Swage model.

The first criterion essentially required the constraint set to generate end conditions matching one or more of those used by the hydraulic models used in Chapters 4-6. The second criterion required that the constraints be suitable for application to long, but finite length, tube sections, and should match the conditions created by the retention mechanisms used during swaging (described in sub-section 2.3.2).

Of the four end conditions used in the hydraulic models, Plane Stress was immediately rejected as it applies only to thin sheets (i.e. very short sections). However, general plane strain conditions (Plane Strain, Open- and Closed-Ends) may be applied to a long section.

Given the three general plane strain conditions, Open-Ends best matches the constraint of a tube being swaged as it doesn't apply an axial load (as does Closed-Ends) or prescribe a length (as does Plane Strain).

As a long section is being used, it would initially seem logical to leave the ends of the tube free. However, to fulfil the first criterion, the end nodes of the tube must again be coupled such that when the pressure band is applied to the whole tube, the modelled state is equivalent to that used in the hydraulic autofrettage models (see Figure 4.8). In addition were a real-life tube hydraulically autofrettaged under Open-End conditions,

pressure would not be applied to the whole length of the tube – the floating bungs would be inset (as shown in Figure 2.1). Otherwise, with a constant pressure applied to the whole length, the unconstrained ends of the tube would undergo significant yielding. Accordingly, the model was constrained as shown in Figure 7.4, with the axial displacements of the nodes along the tube end A-C were coupled, such that the initially plane end remains so (and perpendicular to the axis), and end B-D constrained to zero axial deflection.

This results in zero axial load, both during and following the application of pressure.

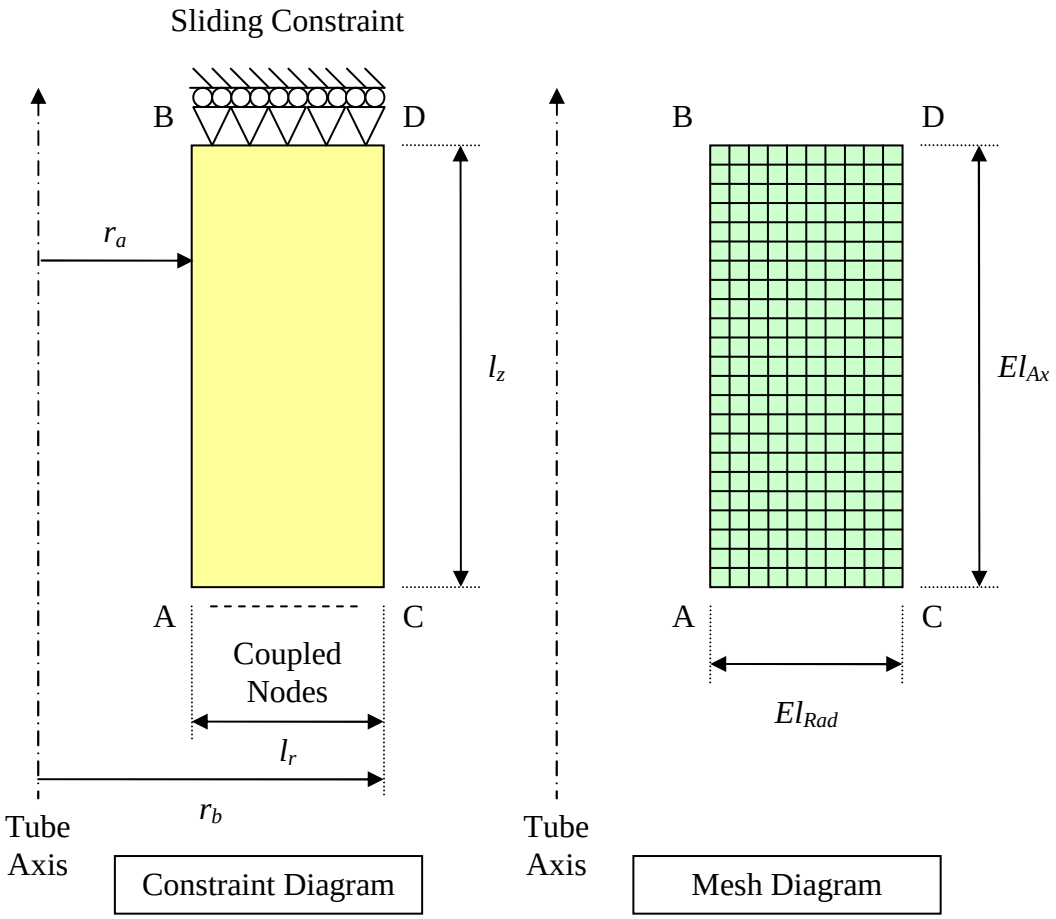

Figure 7.4: Model Geometry and Mesh

7.3.4. Meshing

The geometry of the model used here differs significantly from that of the model used during the hydraulic autofrettage investigation; previously the intention was to shorten the tube length as much as possible, while the opposite is true in the model described here. Additionally, while important (as in any investigation), absolute accuracy of the generated results is not the primary objective. Instead, the focus was upon the trends

observed while the band of pressure is altered, either in length or position. Lastly, retaining such small element size over the length of the tube could lead to an intractable model, in terms of both memory requirements and solution time.

Consequently, principally using Figure 4.21, the element size was increased such that the number of radial divisions, El_{Rad}, of the mesh was 20; the number of axial elements, El_{Ax}, was scaled from this using the ratio of length (l_z) to wall depth ($r_b - r_a$) to give $El_{Ax} = 100$ for the static band and $El_{Ax} = 200$ for the moving band.

7.3.5. Loading

Both static and moving band models achieved the desired pressure load to the desired section of tube by determining the appropriate elements along the ID of the tube and applying pressure to their exposed face (previous models had applied pressure to the entire line representing the ID). In the static case, the length over which the band of pressure was applied is termed l_{BW}.

For the static case a uniform pressure, P_{SB}, was applied to all elements; however, to better reflect the tapered profile of a mandrel, a gradient was applied to the pressure band in the moving case. As well as making the results from the moving band model more comparable to those from swaging, the pressure gradient made the individual stages of the solution easier to solve (and hence more rapid) as excessive element distortion was avoided. This was important as the model required many such stages. The gradient was achieved by applying the specified pressure, P_{MB}, to a single element, and applying progressively smaller pressures to each set of neighbouring elements towards the edge of the fringe. The difference in the pressures applied to successive elements was termed ΔP, itself a multiple of P_{MB}. The loading mechanisms for both models are given in Figure 7.5.

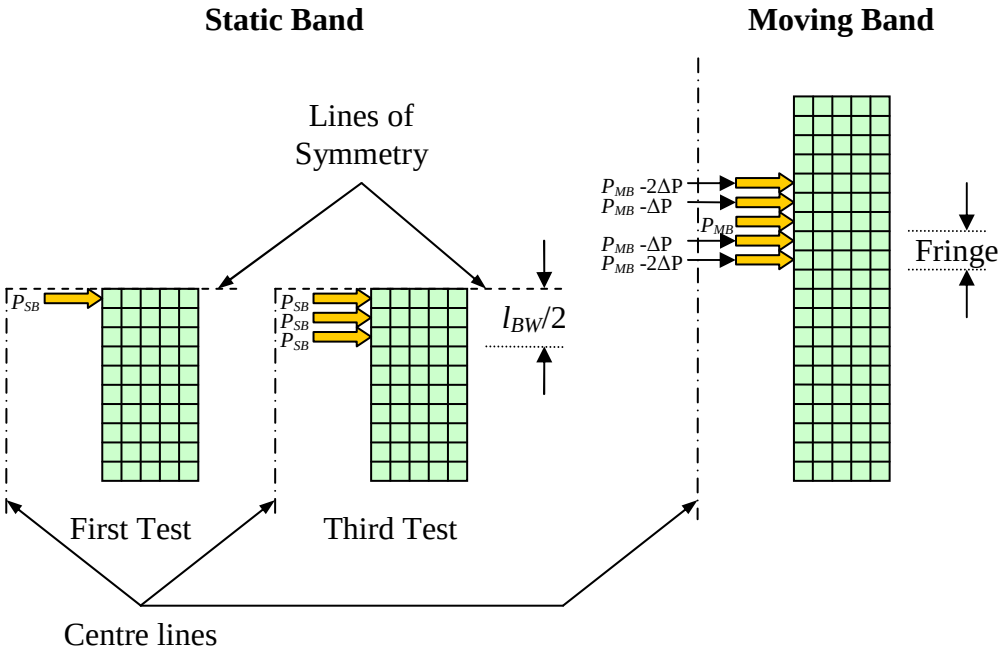

Figure 7.5: Mesh Loading Diagram

7.3.6. Recorded Results

In addition to the results taken along a single radial path in the hydraulic autofrettage models, it was important that extra results were recorded to allow axial variation and shear stresses to be investigated. Specifically, results were also taken along a radial path aligned with the edge of the pressure bands; as shown in Figure 7.6, results were taken from the forward edge of the Expanding Band, and both forward and rear edges of the Moving Band.

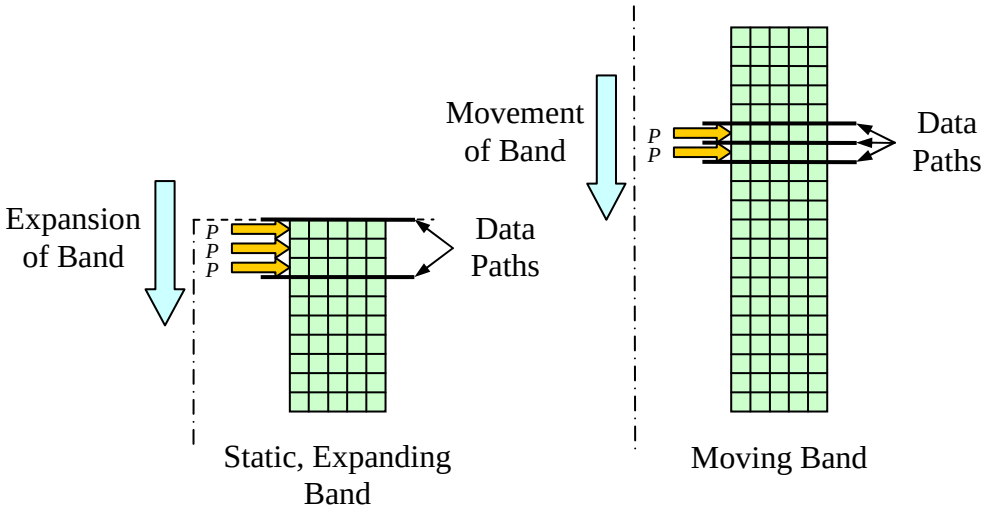

Figure 7.6: Data Path Diagram

7.4. STATIC, EXPANDING BAND

The Static band model was the first investigated, to explore the nature of the relationship between width of band and autofrettage depth; this would then be compared with data from the swage case to help determine the effects of friction and the slopes on the front and rear faces of the mandrel.

The first of results was gained by applying a constant pressure, P_{SB}, to a progressively larger portion of the ID, until hydraulic autofrettage was achieved when the portion equalled the full length, l_z. The pressure applied (1050 MPa) was that which was found to cause 55% overstrain when used in hydraulic autofrettage for the Open-Ends condition, with the material parameters given in Table 7.1. The second results were obtained by increasing P_{SB}, in the cases from the first set where depth of autofrettage had dropped below 55%, until overstrain again equalled 55%.

Figure 7.5 illustrates how the tube is progressively loaded, during the first three tests of the series, from its mid-point to its ends, until hydraulic autofrettage conditions are achieved.

7.4.1. Results

Figure 7.7 plots the overstrain (depth of autofrettage), plus equivalent and hoop plastic strains, against the width of the applied pressure band.

Figure 7.8 plots the mid-length residual hoop stress found at the ID, against the width of the applied pressure band.

Figure 7.9 plots the pressure required to achieve a consistent overstrain (55%) against the width of the applied pressure band. Also included is a fit line based on a rudimentary assessment of the stress state within the tube, describe in sub-section 7.4.2.

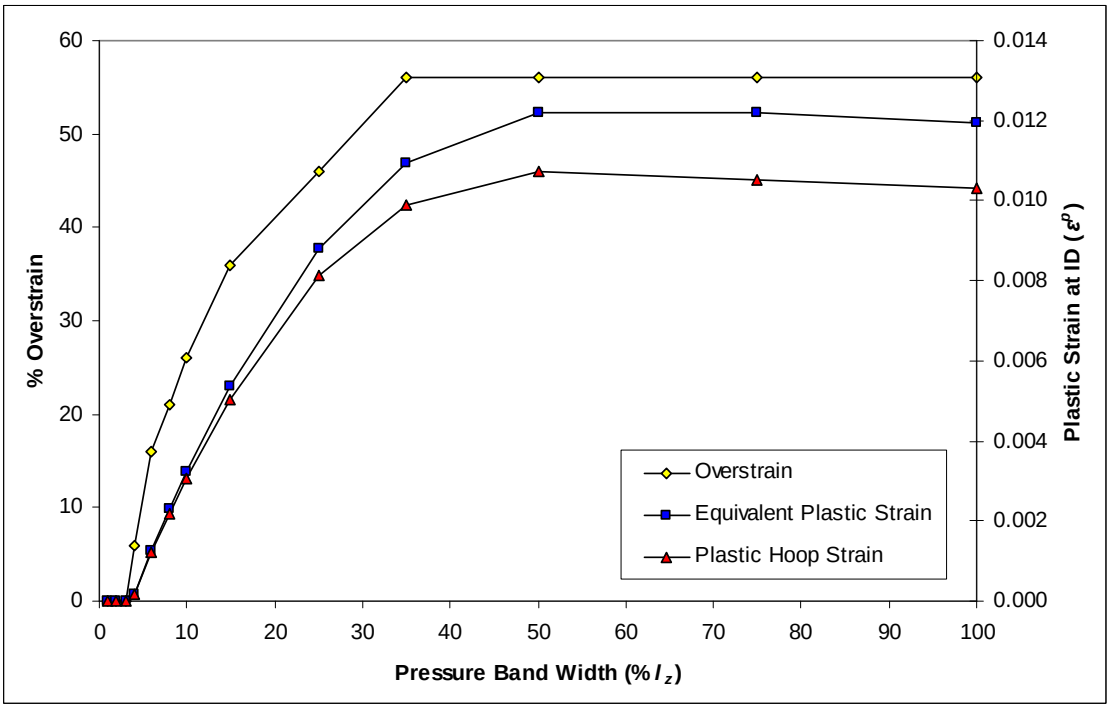

Figure 7.7: Overstrain, Equivalent Plastic Strain and Plastic Hoop Strain at ID for constant pressure, variable width Band

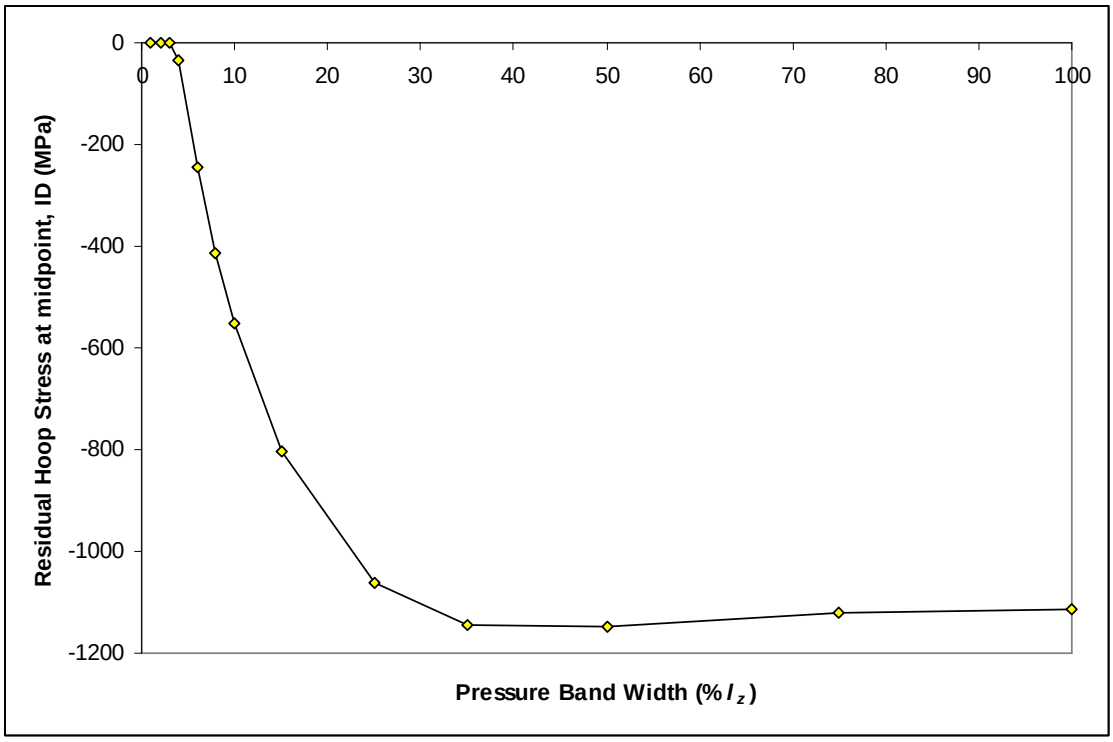

Figure 7.8: Residual Hoop Stress at midpoint, ID for constant pressure, variable width Band

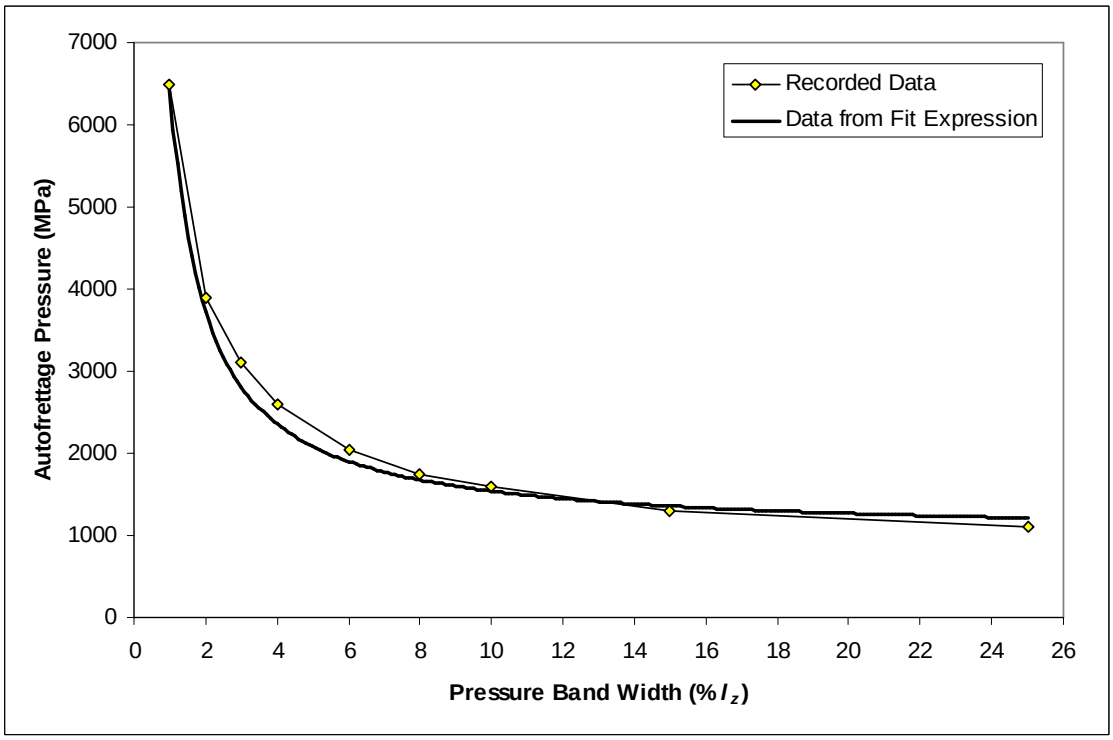

Figure 7.9: Autofrettage Pressure required for constant Overstrain as band width varies

7.4.2. Discussion of Results

It was noted (see Figure 7.7) that equivalent plastic strains at the ID drop slightly from their peak at band width of 50%; this results from decreased equivalent stress, which in turn results from the decreasing contribution of the ($\sigma_\theta - \sigma_z$) term, as σ_z becomes less negative (as the full section length is exposed to the applied pressure). The ($\sigma_r - \sigma_\theta$) and ($\sigma_z - \sigma_r$) terms peak at 100% band width, but their rate of increase is less than the rate of decrease of ($\sigma_\theta - \sigma_z$) in the 50-100% band width range.

This pattern is also observed for the plastic hoop strains during autofrettage (also Figure 7.7), which is then reflected by residual hoop stresses at the ID (Figure 7.8) which peak at a band width of 50%.

The second set of results (Figure 7.9) reveal that the required pressure increases rapidly as the band width decreases, in a form similar to an inverse proportionality. Indeed, it may be imagined that when the majority of the tube is unpressurised, the restraining force it applies is constant, which must be overcome by the pressure, as well as the strength of the loaded section (constant per unit length). This assessment is formalised by (7.4).

$$P_{SB} = m \cdot \frac{l_z - l_{BW}}{l_{BW}} + P_{AF} \tag{7.4}$$

The constant value, P_{AF}, is the pressure required for 55% overstrain when the full length of the tube is loaded (i.e. hydraulic autofrettage), hence P_{AF} = 1,050 MPa. The multiplicative constant, *m*, represents the restraining force of the unpressurised section. A value for *m* was obtained by making it the subject of the above equation, and entering the recorded data into the resulting expression. The mean value of 54.43 MPa was obtained from the data points for l_{BW} values of 1 to 10% of l_z, inclusive.

While this over-simplifies the details of the stress state in the tube, particularly in the yielding region, the concept appears to be well supported by the agreement between the FEA data and proposed relationship.

7.5. MOVING BAND

The second series of tests assessed the differences resulting from autofrettaging with a moving band of pressure, rather than an application of pressure to the whole tube length simultaneously. The influence of the width of pressure band and pressure gradient were investigated, which are analogous to mandrel length and taper angle, respectively.

Initially, the fringe width was varied, while maintaining an overstrain of 55% by altering the applied pressure, P_{MB} (that at the centre of the band); see Figure 7.5 for a diagram of fringe width. As 200 elements were used to mesh the tube along its length, each element represents 0.5% of the tube length. The following values were used:

Fringe Width (elements)	% Tube Length	Pressure, P_{MB} (MPa)
2	1.0	3,170
3	1.5	2,750
4	2.0	2,500
5	2.5	2,300

Table 7.2: Moving Pressure Band, Fringe Width Investigation Inputs

The results from the investigation of the effects of fringe width are given in sub-section 7.5.1.

Once the effects of fringe width had been investigated, the influence of the pressure gradient was assessed by varying it while keeping fringe width constant at 4. Between each successive element away from the central band, the applied pressure decreased by ΔP, where ΔP is given by the gradient, G_P, multiplied by the central pressure, P_{MB}. The following values of G_P were used:

G_P	ΔP (MPa)	Pressure, P_{MB} (MPa)
0%	0.0	2,200
5%	117.5	2,500
10%	275.0	2,750

Table 7.3: Moving Pressure Band, Pressure Gradient Investigation Inputs

The results from the investigation of the effects of pressure gradient are given in sub-section 7.5.2.

7.5.1. Fringe Width Investigation Results

Figure 7.10 and Figure 7.11 plot the hoop and axial stresses, respectively, through the tube wall at mid-length, when the pressure band is also at the mid-length position of the tube. For comparison, Figure 7.10 also plots the peak pressure hoop stresses for a hydraulically autofrettaged (i.e. uniform pressure along its whole length) open-ended tube of wall ratio 2.5 (as would be obtained from the model used in Chapter 4, with an

autofrettage pressure of 1082 MPa). Figure 7.12 and Figure 7.13 plot the residual (i.e. once the pressure band has finished acting on the tube) hoop and axial stresses, respectively, at the mid-length position.

Figure 7.14 plots the residual plastic axial strains through the tube wall at mid-length. Figure 7.15, Figure 7.16 and Figure 7.17 each show the shear stress (σ_{rz}) through the tube wall at mid-length, respectively at the forward edge, middle and rear edge of the pressure band.

All radial positions, r, are normalised w.r.t. the wall thickness (giving r_N), and stresses are normalised w.r.t. the initial yield stress, σ_{Y0}.

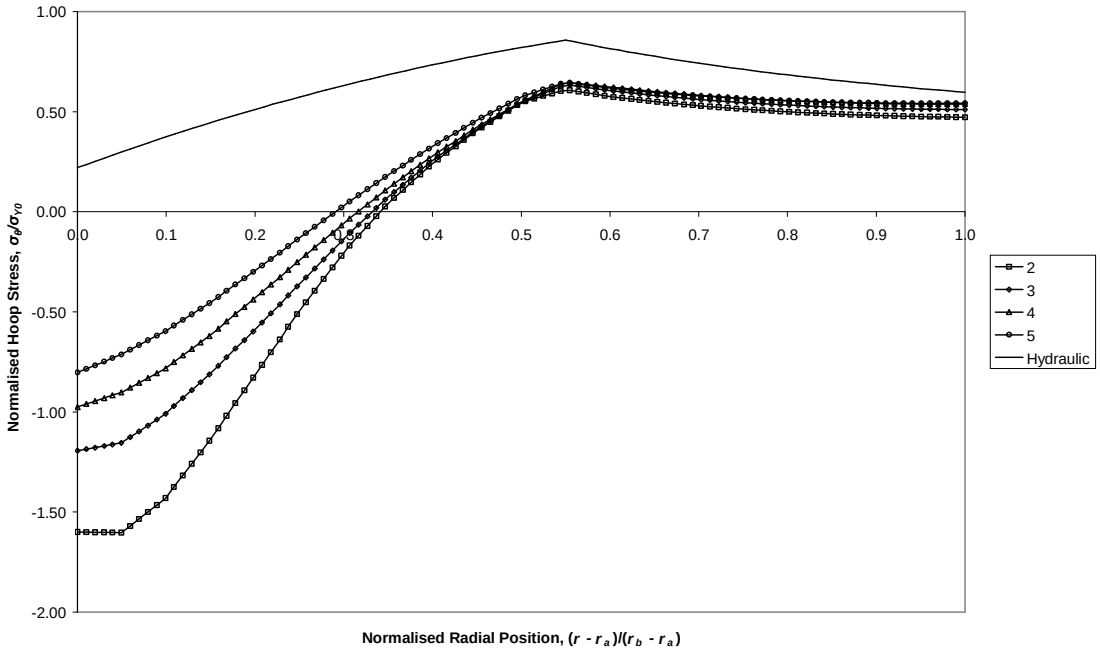

Figure 7.10: Hoop Stresses during Autofrettage at Mid-Length

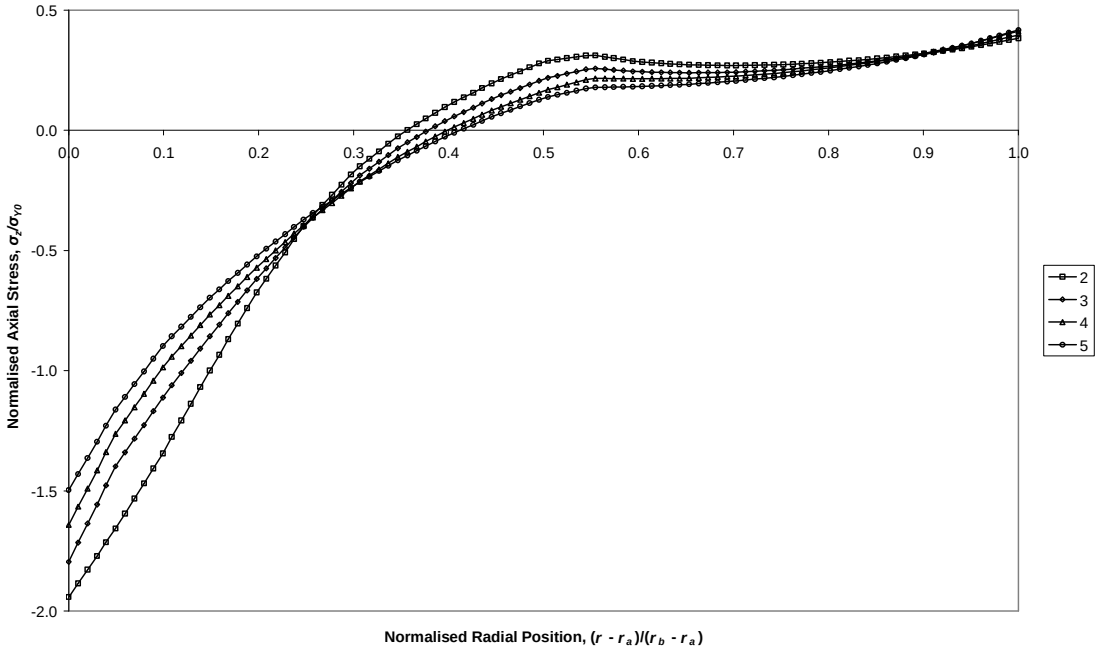

Figure 7.11: Axial Stresses during Autofrettage at Mid-Length

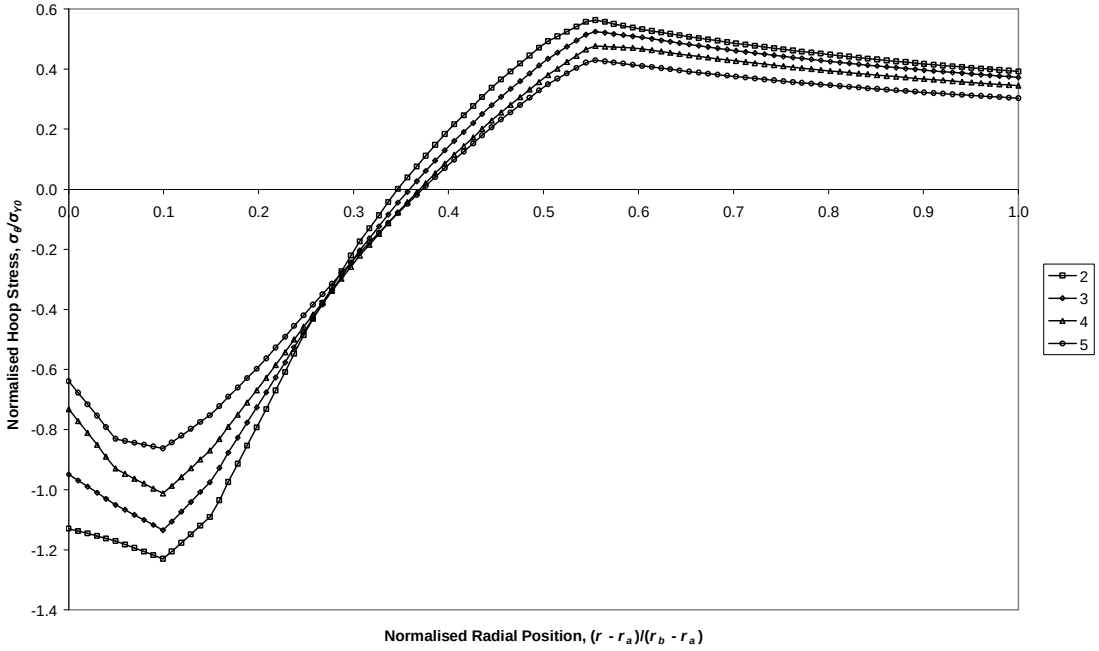

Figure 7.12: Residual Hoop Stresses at Mid-Length

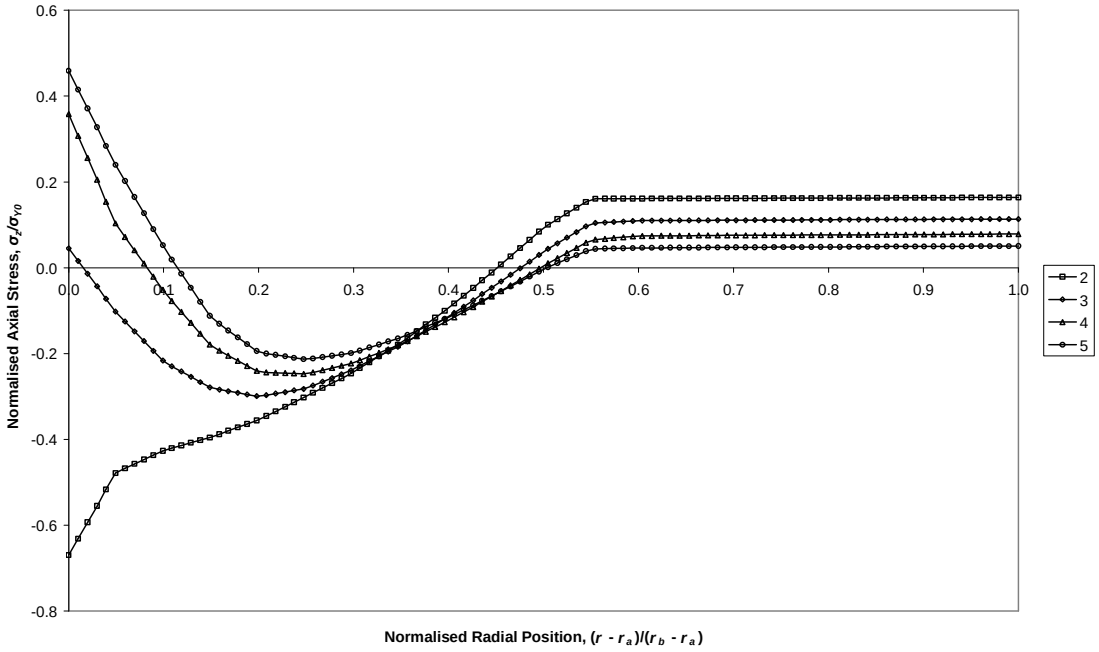

Figure 7.13: Residual Axial Stresses at Mid-Length

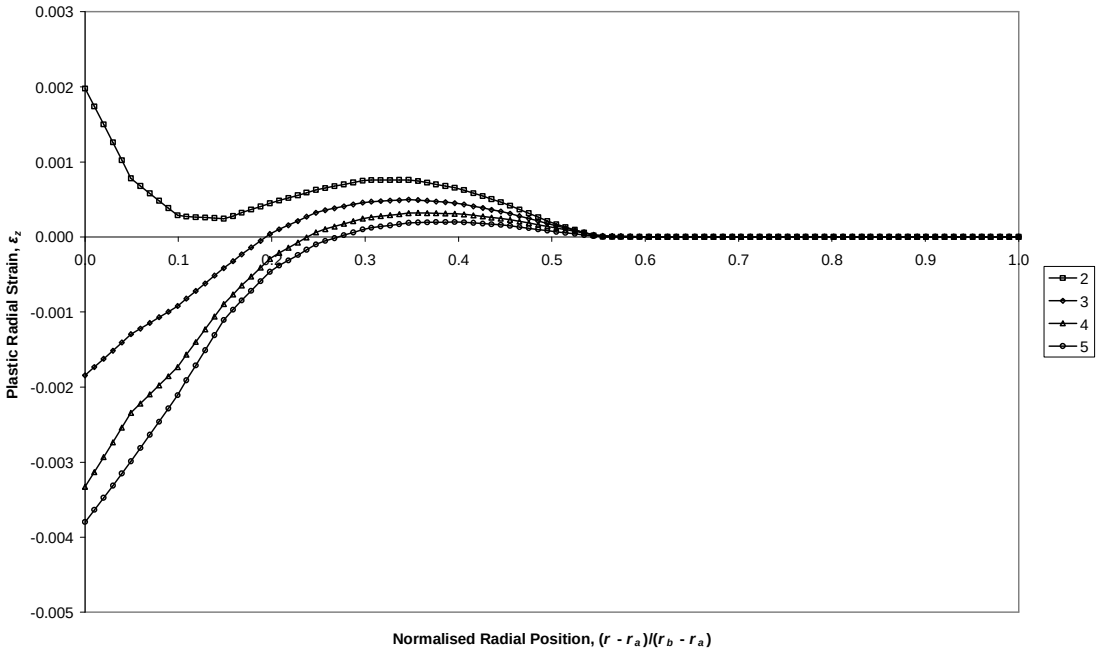

Figure 7.14: Residual Plastic Axial Strains at Mid-Length

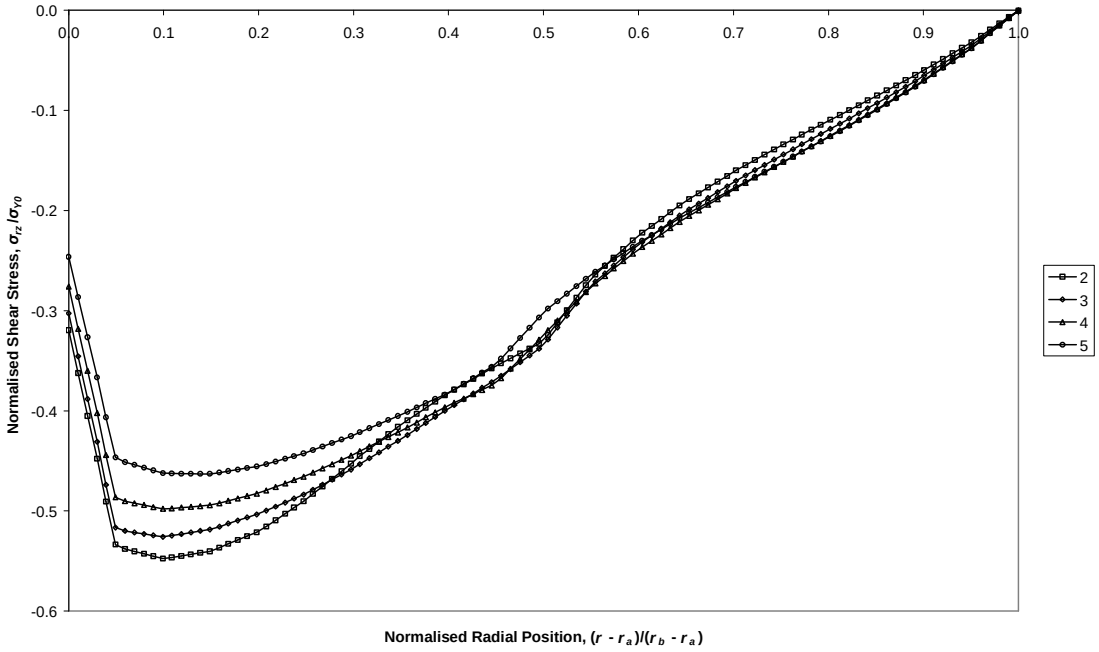

Figure 7.15: Shear Stresses at Forward Edge of Pressure Band, at Tube Mid-Section

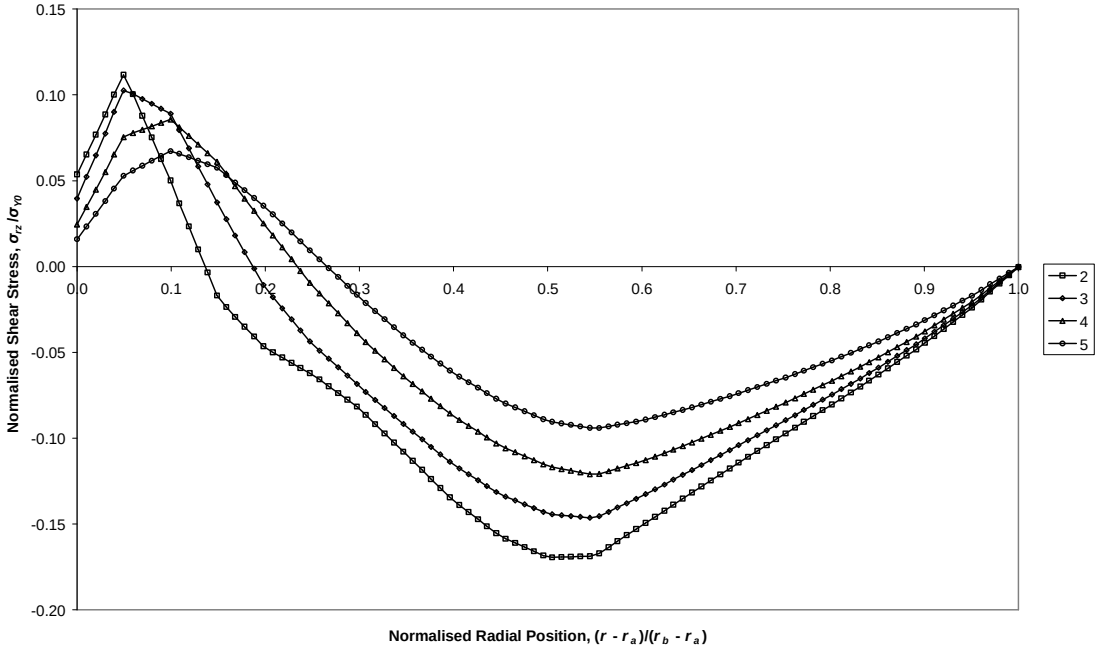

Figure 7.16: Shear Stresses at middle of Pressure Band, at Tube Mid-Section

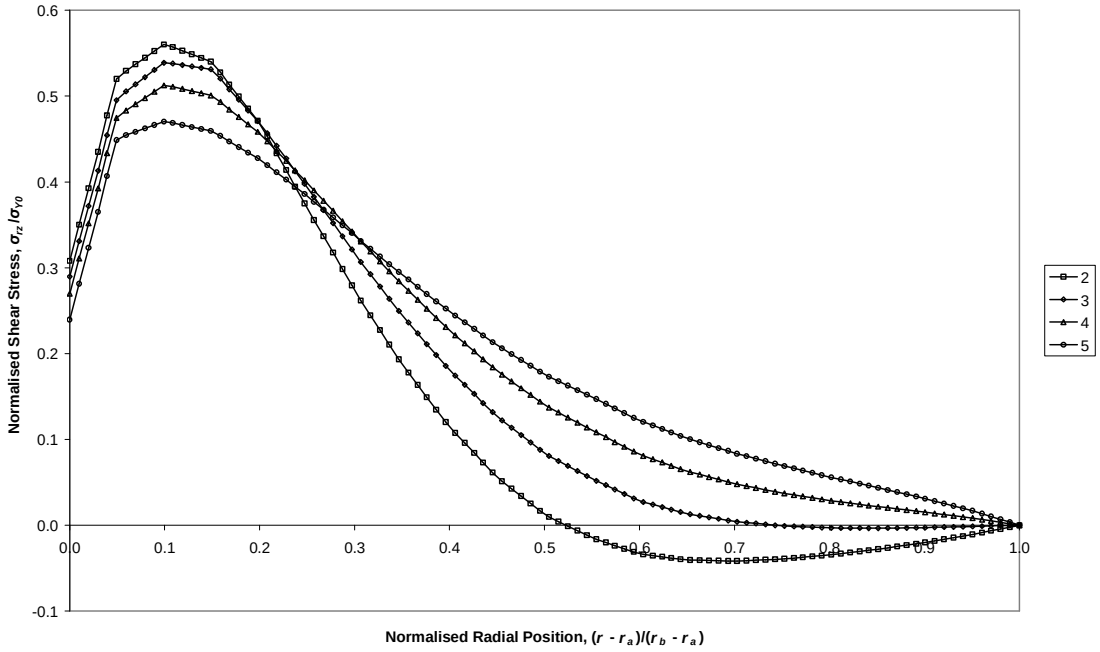

Figure 7.17: Shear Stresses at Rear Edge of Pressure Band, at Tube Mid-Section

7.5.2. Pressure Gradient Investigation Results

Figure 7.18 and Figure 7.19 plot the residual (i.e. once the pressure band has finished acting on the tube) hoop and axial stresses, respectively, at the mid-length position of the tube. These compare with Figure 7.12 and Figure 7.13 from the Fringe Width investigation.

All radial positions, *r*, are normalised w.r.t. the wall thickness (giving r_N), and stresses are normalised w.r.t. the initial yield stress, σ_{Y0}.

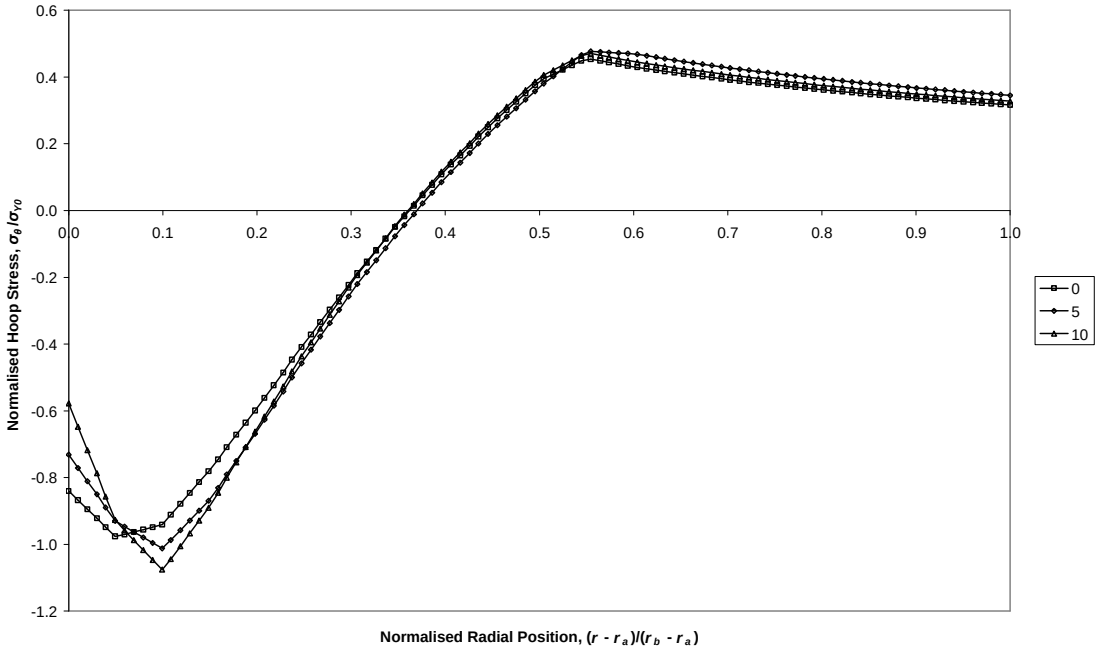

Figure 7.18: Residual Hoop Stresses at Mid-Length

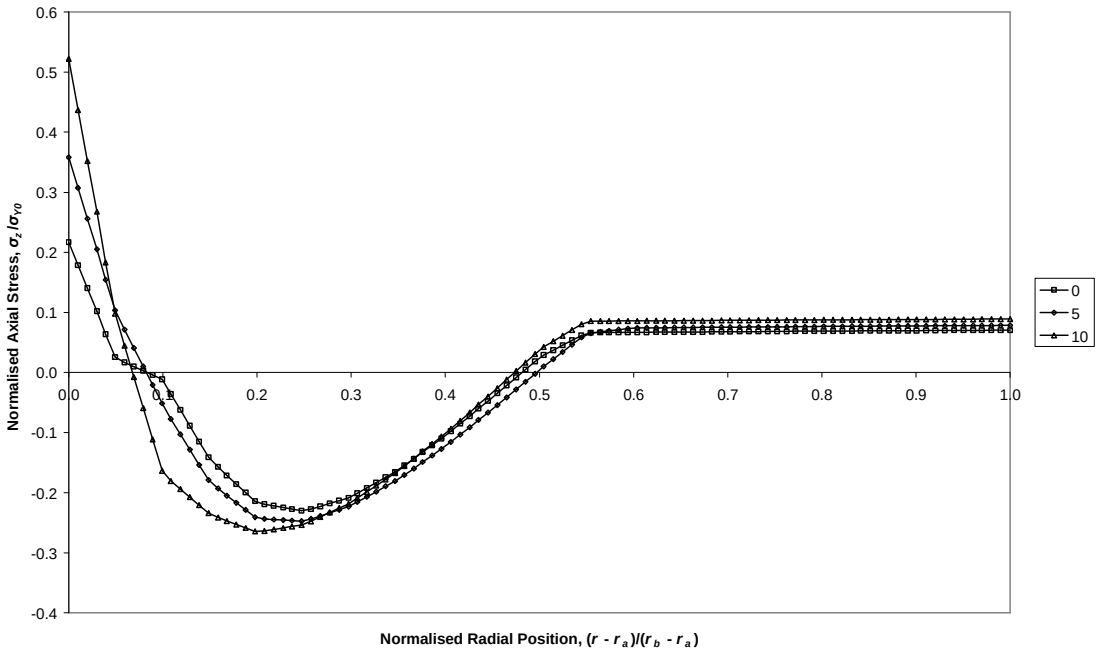

Figure 7.19: Residual Axial Stresses at Mid-Length

7.5.3. Discussion of Results

The following points of discussion refer to the variable fringe width results, unless they specifically reference the variable pressure gradient results.

As expected, it was found (Table 7.2) that the narrower the pressure band, the higher the pressure required to achieve a given depth of overstrain. This is logical, given the local nature of loading; as discussed in for the Static, Expanding band case (section 7.4.2), the pressure band not only has to overcome the strength of the material surrounding the band, it also has to overcome the supportive force of the tube – in front of, and behind the band. For a given band pressure, as the width of band decreases these supportive forces become a larger relative to the applied load.

The intensity of shear stresses was also seen to increase (Figure 7.15 to Figure 7.17), which is a natural consequence of the support forces discussed above; such forces are exerted on the pressurised section primarily through shear stress, and partially through axial stresses, given the outwards deflection of the pressurised section of tube.

From Figure 7.10 it is apparent that the through-wall hoop stresses at the centre of the pressure band do not equal the applied load (if the load on a single element is compared to the through-wall hoop stresses of a tube section one element long). This is another symptom of the pressurised section being supported via shear stresses, by neighbouring non-loaded sections.

The negative hoop stresses seen around the ID during peak pressure represents an outwards force by that section of the tube; this may seem counter-intuitive, given the net inwards force produced by the tube as a whole. However, this reflects the shear stresses present in the region surrounding the ID at the forward and rear edges of the pressure band (shown in Figure 7.15 and Figure 7.17), which apply a net inwards force to the loaded section. This fact tallies with the above observation that summed hoop stresses in the loaded region do not equal the applied load; indeed the inwards force resulting from the shear stresses is sufficient that a net outwards force is required from the hoop stresses to maintain force equilibrium. The radial location of the region of compressive hoop stresses is determined by the distribution shear stresses, which are in turn determined by the relative radial deflections of the loaded and surrounding sections.

The magnitude of residual hoop stresses (Figure 7.12) found at the ID increases as the pressure band width decreases. A similar pattern was observed in the variable pressure gradient case; Figure 7.18 shows residual hoop stress magnitude increasing with pressure gradient (and mid-band pressure). This results from the less positive values of residual axial stress found at the ID as band width decreases (Figure 7.13), or pressure gradient increases (Figure 7.19); the decreased difference between hoop and axial, and radial and axial stress components allows for a more negative residual hoop stress for a given equivalent stress. The process by which less negative axial stresses are developed is explained in the following paragraphs.

The nature of radial load transferral via shear stresses is described by Figure 7.3. Considering a pressure band progressing along a tube in the direction of z (coincident with the tube axis) increasing, such that the forward edge of the band first encounters the right hand side of the considered element; an inwards force applied to the surface via τ_{zr} would have a negative sign – this is observed in Figure 7.15. The converse occurs at the left hand side of the element; a positive τ_{zr} would be expected, and is indeed observed in Figure 7.17.

The shear stresses at the forward and rear edges of the pressure band (Figure 7.15 and Figure 7.17) show a large degree of similarity near the ID, but the plots begin to diverge once $0.25 < r_N$ with the narrower pressure bands showing greater amounts of divergence. Once beyond $r_N \approx 0.25$, the magnitude of the shear stresses decreases (relative to those at the forward edge of the pressure band), and plots from fringe widths of 2 and 3 even cross the axis. This may be explained by the deformation and expansion of the section of tube behind the pressure band; the loaded section is less dissimilar in radius to the non-loaded but previously deformed section, so that shear strains are smaller and hence so are shear stresses. The shear stresses remain similar (albeit of opposite sign) near the ID due to the close proximity of the pressure load discontinuity.

The large compressive residual axial stresses observed in Figure 7.13 at and around the ID (resulting from the tensile plastic strains found there, as seen in Figure 7.14), for the case fringe width equals two, are explained by the large tensile deformation experienced by the region near the ID, shortly after the centre of the band of pressure passes. This is shown by Figure 7.20.

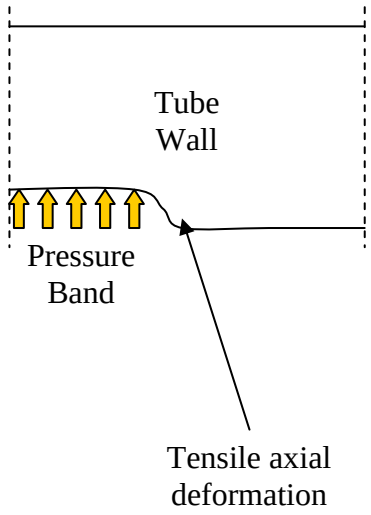

Figure 7.20: Tensile Axial deformation at rear edge of pressure band

The high pressure found at the band edge in this case differentiates it from the wider pressure band cases. This rapid change of axial stress experienced as the pressure band passes (compare with the highly compressive axial stresses experienced by the tube ID at the centre of the pressure band, in Figure 7.11) suggests, via Equation (7.2), a higher rate of change of τ_{rz} w.r.t. r (and hence τ_{zr}, from Equation (7.1)). This would agree with

the more intense shear stress observed for the narrower pressure band cases; the greater the magnitude and the shorter the length over which it varies, the greater the value of its derivative.

The same pattern is observed, without developing tensile residual axial stresses at the ID, in the variable pressure gradient case (Figure 7.19), resulting from the increased shear stresses at the edge of the pressure band resulting from decreased pressure gradient.

Note: whilst the shear stress inclusive equilibrium equations, developed above, assume that initially plane sections of tube remain so non-plane behaviour is observed. It is felt however, the principles remain true and hence the equations remain useful for qualitative description of the stress field near the applied pressure band.

7.6. SUMMARY

The results from the static band model supported the observation that the required pressure for a constant depth of autofrettage increases as the width of the pressure band decreases.

The relationship between band width and pressure was observed to follow a pattern similar to an offset inverse ratio; based on this, a representative relationship (7.4) was created, the results from which (Figure 7.9) showed reasonable agreement with the data.

The results from the moving band model showed the same trend; the narrower the fringe width, the greater was the pressure needed to obtain a given depth of overstrain. As would also be expected, shear stress magnitude near the band was seen to increase as fringe width decreased due to the greater step size between the applied pressure and zero pressure in the non-loaded section.

Shear stresses switched sign appropriately, given the element diagram in Figure 7.3, between the front (Figure 7.15) and rear (Figure 7.17) edges of the pressure band.

Through wall hoop stresses at peak pressure (Figure 7.10) were found to be markedly different from those observed at peak pressure during hydraulic autofrettage; indeed, at and around the ID, they were seen to be strongly negative (compressive) – creating a net outwards force for that section. This is due to the propagation, via shear stresses, of the applied load to more than just the directly loaded section.

Residual hoop stresses at the ID were seen to increase in magnitude as the pressure at the band edge increased (found with lower fringe widths and pressure gradients); the increasing curvature resulting from the more sudden change in pressure causes decreasingly tensile residual axial stresses at the ID, allowing more compressive residual hoop stresses to be developed.

While compressive axial stresses are found at the ID at the centre of the pressure band (Figure 7.13), towards the edges of the band stresses become increasingly tensile. If the band is narrow enough, this can cause sufficient tensile axial plastic strains to result in significant compressive residual axial stresses at the ID, as was the case when fringe width equalled 2.

The deflections resulting from the pressure-based loading used in this investigation are not identical to those resulting from the essentially displacement-based loading that occurs during swage autofrettage (for example, the ID of the tube cannot be deflected beyond the size of the mandrel). In addition, the selected pressure profile was intended to be representative of that found over the mandrel's surface but not particularly accurate (for example, it is symmetrical). However, the investigation was nonetheless useful, allowing the above assessments to be made, and the influence of localised loading and shear stresses to be understood and documented.

8. DEVELOPMENT OF A METHOD OF MODELLING SWAGE AUTOFRETTAGE

8.1. INTRODUCTION

Once the material model had been completed, and experience of simulating long tube sections had been gained, it was then appropriate to formulate a model of swage autofrettage. Given the paucity of open literature investigations of the swaging of long tube sections, it was important to follow this route, and then conduct additional sensitivity analyses to investigate both mesh fineness and contact parameters.

While it is recognised that mandrels are used to pre-stress structures in other contexts, such as holes within panels of aerospace vehicles [34,35], they have not been assessed in this thesis. This is based on the differences that arise between such panels and long tubes, due to the dissimilar length/radius ratios of the pre-stressed hole, as well as the prevalence of aluminium alloys in the different classes of components. The principles of the model developed in this chapter could be relevant to such applications.

Once the initial swage model had been formulated, and the means of adding a contact to the ANSYS model investigated, it was used to generate results for comparison with those from an earlier model developed by O'Hara [9] using the ABAQUS FEA package. It featured a relatively short section length, reasonably sparse mesh, and a bi-linear kinematic hardening material, making it ideal for a first check of the model described here. Additionally, the comparison was a suitable test bed to confirm the mandrel-tube contact had been specified correctly.

All results given in this chapter use the ANSYS bi-linear kinematic (BKIN) material. Between the customisation of the USERMAT sub-routine and the development of the swage model presented here, a change of ANSYS version (v9.0 to v11.0 SP1) was required for licensing reasons, introducing some changes to the format of the USERMAT sub-routine. This also required a change of Fortran compiler (from Compaq Visual Fortran 6.6A to Intel Visual Fortran 8.1). Unfortunately, some combination of the change in ANSYS version and Fortran compiler caused the material model developed in Chapter 6 to cease working as intended; solution failed upon unloading from prior plastic strain. After some work, the material was altered such that the solution would fail when unloading, but the stress-strain profile was erroneous when unloading into reverse plasticity. Insufficient time was available to correct this behaviour, so the decision was made to conduct these analyses using an inbuilt material. While the exact value of the results calculated may not be fully reflective of experimental values, it is nonetheless felt that the trends observed and conclusions drawn remain true.

8.2. MODEL DEVELOPMENT

8.2.1. Overview

The geometry and material used for the tube were initially based on that created for the moving Band of Pressure model (the tube was later refined following a sensitivity analysis), with loading applied via contact with an additional body (the mandrel) which passes along the ID of the tube. To enable the stresses resulting from the tube-mandrel interference to be assessed, a *contact pair* was created from the ID of the tube and outer surface of the mandrel. When the two surfaces intersect the contact pair applies compatibility, linking the deflections of both surfaces, from which strain and thence stresses are calculated (in the manner described in Chapter 6).

The model is considered isothermal (temperature is not considered and is assumed to be constant and uniform), despite the fact that, in addition to material hysteresis, heating would result from friction at the sliding contact between mandrel and tube. This is largely due to absence of information on the temperature dependent properties of the model, namely:

1. Softening of material due to temperature, altering reverse yielding,
2. Nature of friction relationship.

In essence this is equivalent to assuming the process is carried out very slowly. Although it cannot be verified, it was felt that material softening would have a relatively small effect on reverse yielding as the temperature increase would likely be modest. In addition, it was possible that the temperature increase might mitigate the Bauschinger effect, counter-acting the conventional softening.

The friction relationship is a closed-loop problem, as without knowing its temperature dependency it is impossible to calculate the incremental frictional heating, so the iterated friction properties cannot be calculated accurately, etc.

In summary, it was felt that ignoring temperature effects was a sensible compromise for this model; they could then be investigated in future studies.

8.2.2. Geometry

The tube was dimensioned largely as that in the moving Band of Pressure model, in Chapter 7; namely, long enough to capture the significant axial variation implicit between those regions near and far from the tube ends. As in the Band of Pressure model, representative dimensions of Wall Ratio, K, of 2.5 and a provisional length, l_z, of $10l_r$ were selected.

As described in Chapter 2, the mandrel consists of three main sections – the forward slope, parallel section and rear slope; this is shown in Figure 8.1, along with the critical dimensions.

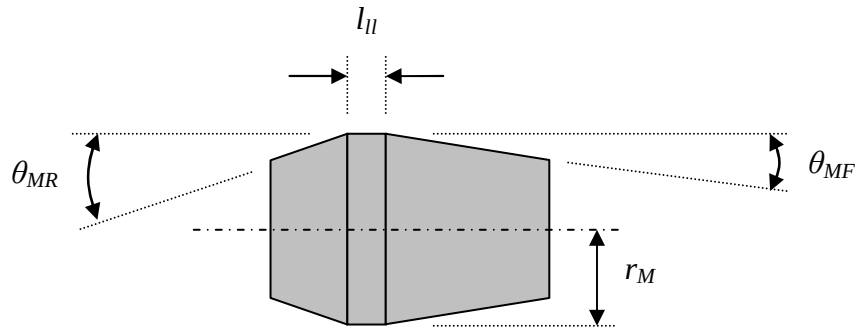

Figure 8.1: Mandrel Geometry

8.2.3. Contact Analysis

It was at this time that contact between two bodies was introduced. In all of the investigations documented earlier in this thesis, loading had been achieved entirely through the application of pressure. Accordingly, contact analysis and its use within ANSYS to simulate swage autofrettage, is described here; the ANSYS Contact Technology Guide [36] and a textbook by Madenci and Guven [37] were referred to during the implementation of the contact analysis.

In general, the initial considerations that must be made of contacting bodies is where and when they will contact, and the nature of friction between the two bodies (as mentioned in sub-section 8.2.1). The time and location of contact between the tube and mandrel are easily identified, eliminating the first of these concerns. However information is sparse regarding the nature of friction between the bodies, which depends on, among other properties, surface finish, contacting materials, lubrication, pressure and temperature.

For this reason it was decided to make the friction force proportional to the contact pressure (the Coulomb friction model), via a coefficient, μ, of constant value; this is defined by Equation (8.1).

$$\sigma_{rz} = \mu \sigma_r\big|_{r=r_a} + \text{Cohesion} \tag{8.1}$$

This type of friction was defined within ANSYS, selecting the isotropic variant. O'Hara [9] used a value for μ of 0.015, but Bihamta, Movahhedy and Mashreghi [38] suggest a higher value, $0.05 \leq \mu \leq 0.18$. However, to allow comparison with O'Hara's results, an initial value of $\mu = 0.015$ was chosen. O'Hara does not specify a value for cohesion, so it was set as zero. For comparison, in the case of a lubricated sliding contact between two surfaces of hardened steel, $\mu \approx 0.05$-0.15 [39].

It was then necessary to determine the type of contact, based on the relative rigidities of the contacting bodies (both material and geometry based). The options are either Rigid-Flexible (R-F), where the rigid body is non-deformable, or Flexible-Flexible (F-F). The use of an R-F contact is not realistic as, although the mandrel is stiffer (both its material and geometrically), it still deforms due to the contact pressure. Accordingly F-F contact was selected, in which special elements are added to the contacting surfaces to detect the contact and enforce compatibility between the boundaries.

ANSYS contains three contact models: node-node, node-surface and surface-surface. Of these, only the surface-surface contact type is suitable as the mandrel and tube surfaces will undergo a large amount of sliding during contact. Node-node contacts are not suitable when a large amount of sliding will occur, and the geometry of the two bodies is not suitable for a node-surface contact.

F-F analyses may be of two forms: asymmetric and symmetric. In the asymmetric case "target" elements are applied to one boundary, and "contact" elements to the other. The choice is not always obvious (section 3.5 of the ANSYS Contact Technology Guide gives several criteria to inform the decision), but generally the stiffer boundary would be defined as the target surface. Indeed, in an R-F contact, the rigid boundary would be the target surface. Symmetric analysis requires that both boundaries are designated both target and contact, which is required if the choice of target/contact is not clear, and/or excessive penetration occurs at the contact surface.

While it was recognised that the mandrel is stiffer than the tube (in terms of both geometry and material), it was not apparent whether the difference was enough to justify an asymmetric contact, and would need to be tested. Two cases were run using the initial values (for the contact pair, model and geometry) described in section 8.3; the first used asymmetric contact (with the mandrel designated the target, the tube the contact), the second used symmetric contact. TARGE169 and CONTA172 elements were used to mesh the target and contact surfaces, respectively, using the same number of divisions applied to the tube ID and mandrel surfaces. They are each 3-node line elements, and are the optimum elements with which to mesh the boundaries of the 8-node PLANE183 elements used within the tube and mandrel.

The test showed that contact pressure and equivalent plastic strain were slightly (approximately 0.75%) higher in the symmetric case than in the asymmetric case. This was due to the zero penetration condition applied to the tube by its designation as a target. Residual hoop stresses were also greater in magnitude at the ID in the symmetric case, reflecting the slightly larger initial plastic strains. Processor time increased to 1,348 s for the symmetric case, compared to 1,275 s for the asymmetric case; this is a 5.8% increase, although the total time taken would lengthen by a ratio of effectively half this value, as the ANSYS solution stage was observed to be disc-bound for approximately 50% of the time.

Given the importance of accurate calculation of initial deformation to this study, it was felt that it warranted the small increase in solution time required for the use of symmetric contacts.

The remainder of the settings for the contact pair are specified through two methods:

1. Defining a set of "real" constants, and associating the contact/target elements with them,
2. Applying KEYOPTs to the contact elements.

The properties specified via KEYOPTs are summarised in Table 8.1, with those values changed from the default are shown in bold text. Section 3.8.2, of the ANSYS Contact Technology Guide [36], details the full range of properties that may be specified via KEYOPTs, for all contact algorithms.

KEYOPT	Description	Setting
1	Selects DOF	0 – UX and UY.
2	Contact algorithm	0 – Augmented Lagrangian.
3	Stress state when super-element is present	0 – no super-elements present.
4	Location of contact detection point	0 – Gaussian points.
5	**CNOF/ICONT adjustment – initial gap or penetration reduction.**	**3 – Either closes the initial gap or reduces penetration, to enhance conditioning.**
5	CNOF/ICONT adjustment – initial gap or penetration reduction.	0 – bodies are well constrained so do not require restraint from the contact, and contact is made/broken smoothly.
6	**Contact stiffness variation**	**1 – Make a nominal refinement to the allowable stiffness range, to allow stiffness variation from KEYOPT(10) more latitude.**
7	Element level time increment control	0 – automatic time stepping is activated, and contact status is steady.
8	Asymmetric contact selection	0 – no automatic selection.
9	Effect of initial penetration or gap	0 – Include both initial geometrical penetration or gap and offset.
10	**Contact stiffness update**	**2 – update stiffness every equilibrium iteration (entire movement is modelled by one load step).**
11	Beam/shell thickness effect	0 – No such elements present.
12	Behaviour of contact surface	0 – Standard (non-rough, non-bonded, may separate).

Table 8.1: Contact Parameters specified via KEYOPTs

The most important setting made via the KEYOPTs is the selection of contact algorithm (that used to evaluate compatibility between the contacting boundaries); the default Augmented Lagrangian algorithm was selected. The Augmented Lagrangian algorithm iterates using the "penalty method", and augments contact pressure and frictional stress during equilibrium iterations, until the calculated penetration is within the specified tolerance. The penalty method uses "spring" stiffnesses between the contacting boundaries to calculate contact properties. In comparison the Augmented Lagrangian method generally leads to better conditioning of the contact, and is less sensitive to the magnitude of the contact stiffness. Section 3.8.3 of the ANSYS Contact Technology Guide [36] explains the choice of contact algorithms.

Additional parameters were then specified by defining a set of real constants for the pair. The Augmented Lagrangian algorithm (and the penalty method) requires normal and tangential contact stiffnesses, FKN and FKT respectively. The normal stiffness influences the amount of penetration between contact and target surfaces, and the tangential stiffness influences the amount of slip in sticking contact. Allowable penetration and slip tolerances, FTOLN and SLTO, are used to ensure the contact simulation remains within desired behaviour; the values must be within the tolerances for the equilibrium iteration to be deemed to have converged.

ANSYS provides default values of 1.0 for both FKN and FKT, which the manual describes as appropriate for most cases. The manual recommends FKN = 1.0 for bulk deformation problems, and FKN = 0.1 for those with bending deformation; as swaging deforms slightly more than 50% of the tube section, an intermediate value of FKN = 0.5 was felt appropriate. In addition, setting KEYOPT(10) = 2 allows the programme to update the value each equilibrium iteration, and setting KEYOPT(6) = 1 gives it slightly more range when doing so, so it was felt sensible to use the default values unless they proved problematic. The same applies to FTOLN and SLTO; FTOLN defaults to 0.1 (i.e. allowable penetration is 10% of the thickness of the underlying element), and SLTO defaults to 1% of the mean contact length within the pair. These defaults were retained for the initial analysis.

The Newton-Raphson (controlled using the NROPT command) solver was left with its default setting of “Auto”, which allows ANSYS to determine the influence of frictional stresses on the overall displacement field and select which algorithm to use. If the influence is small, ANSYS uses a symmetrical solver, if it is large it uses an unsymmetrical solver. The former is less computationally demanding but can require many iterations to solve, whereas the latter is more computationally intensive but allows for a more timely convergence when large frictional stresses are present. The output of the initial analysis would be checked to determine which algorithm was used; if the unsymmetrical was widely used, it would be engaged by default for future analyses.

8.2.4. Meshing

The ANSYS Contact Technology Guide suggests the use of similar sized elements for each contacting body. This was borne out by initial tests; not only does this tend to yield more consistent stresses along the contact, but also allows a converged solution to be reached more rapidly. With this is mind, it was important to identify the smallest length scale (which must be meshed by an integer number of elements) within the contacting region, and scale the mesh from this. The smallest feature was the parallel section of the mandrel.

8.3. INITIAL COMPARISON WITH O'HARA

8.3.1. Introduction

O'Hara [9] developed a model of swage autofrettage, the primary aim of which was the calculation of the resultant residual stress field – much like the aim of this investigation. His analysis was conducted using ABAQUS, an FEA package capable of modelling the required contacts between bodies and non-linear material behaviour. Additionally, the solution was made computationally feasible using axial symmetry to reduce a three-dimensional geometry to two dimensions, and solved on a Convex C-220. The computational abilities of the C-220 far exceeded those of standard PCs at the time of publication – for a machine in 1991, 64 bit processors, 256 megabytes of RAM and 16 gigabytes of hard disc space was astounding.

The key assumptions incorporated into O'Hara's model were:

1. Axi-symmetry of the geometry,
2. Bi-linear behaviour of the material, obeying kinematic hardening.

An equivalent model was constructed in ANSYS, using the dimensions and material properties given below (sub-section 8.3.2) along with the contact parameters described in sub-section 8.2.3. The comparison of the two models acted as an initial check of the contact model, and then as a first stage of optimisation; the mesh fineness was progressively increased, and successive sets of results were assessed relative to each other.

8.3.2. O'Hara's Model

O'Hara [9] modelled the swage autofrettage of a relatively short length of steel tube, l_z = 0.405 m, r_a = (0.105/2) m, hence l_z/r_a = 7.714, of moderate wall ratio, K = 2.257. The mandrel was considered to consist of tungsten carbide, of 2.5% interference (with respect to the tube ID) along a parallel section of 0.0063 m ($0.12r_a$). The forward slope, θ_{MF}, equalled 1.5°, and the rear slope, θ_{MR}, equalled 3.0°. Axi-symmetry of the section was created by using CAX8 (8-node, rectangular axi-symmetric) elements, and axial restraint was achieved by constraining the second node from the entrance end, at the OD, to radial displacement only. This represents the practice of clamping a real-world tube around a groove cut near the entrance end, and hence develops a net axial force within the tube. 64 elements are used along the ID of the tube, which morphs to 32 along the OD, and 6 through the tube wall (306 elements, after modification of mesh at the constraint point, rather than 384 had the tube been meshed with rectangular elements); Figure 8.2 illustrates the mesh used. This form of mesh topology allows more effective investigation of the stress field near the ID, for a given amount of computer memory, than would a mesh of uniform rectangular elements.

The interface between the swage and tube was modelled as a “softened contact”; this treats the interface pressure as an exponential function of separation, using a starting value of 17.2 MPa at a separation of 2.7 μm. The contact surfaces were modelled as “slide lines” – one covering all 64 elements of the ID of the tube, the other the contacting surface of the mandrel.

The contact was modelled with a coefficient of friction equal to 0.015, simulating a stearate-based high pressure lubricant held at the contact surface in a porous phosphate coating. The contact length on the mandrel is five elements, with the parallel section made up of one element.

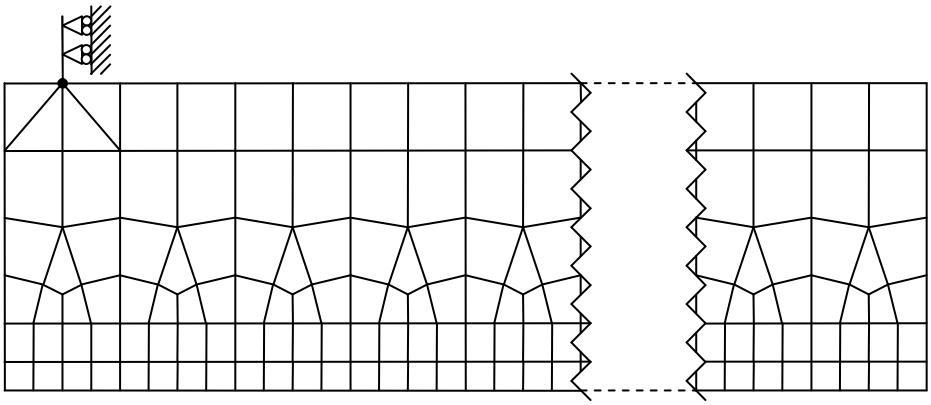

Figure 8.2: Mesh Diagram of O'Hara's Model

The mandrel is pushed by a solid block, representing a short length (length is half its diameter, which in turn is assumed, from Figure 1 in [9], to be slightly less than the ID of the tube) of solid steel ram, to the rear surface of which is applied a moving constraint. A coefficient of friction of 0.05 (he states the exact value isn’t particularly important as little sliding occurs, and this author agrees with him) is applied between the ram and mandrel. Residual stress data is taken from a radial path at the mid-length position of the tube. Figure 8.3 illustrates these properties.

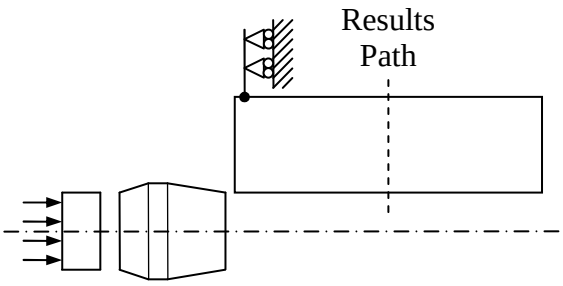

Figure 8.3: Diagram of O'Hara's Model

O'Hara's model also included tapers at both the entry and exit ends of the tube (see Figure 8.4); this reflects the actual geometries used in the workshop during swaging operations to make the process more readily achievable, primarily by easing the alignment of the mandrel with the tube. The slopes would somewhat alter the simulated driving force, and would potentially make solution of the contact pair more easily achieved, but would have little or no effect on the residual stresses developed at the mid-length position. For this reason, these slight tapers were omitted from the ANSYS model, but it was recognised they may have an effect if driving force were to be studied. Also, solution of the contact pair was achieved without difficulty.

One last point is that O'Hara does not specify the length of the short taper at the entry end of the tube, making a precise like for like comparison impossible. Normalisation of the final radius at the exit, r_{exit}, end w.r.t. r_a yields r_{exit}/r_a = 1.0126, and the 13 mm length of its taper is approximately 1/32nd of the section length or two elements in the O'Hara model.

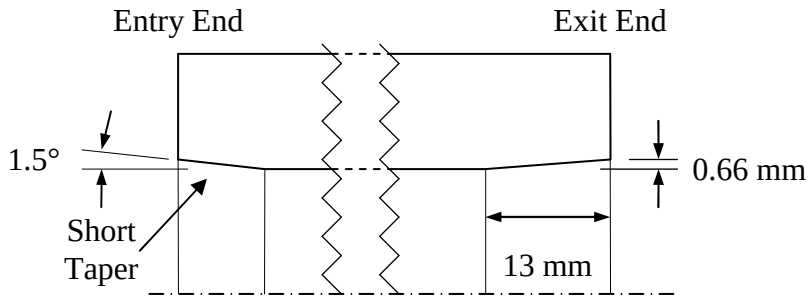

Figure 8.4: Taper Details

As stated, O'Hara used a bi-linear kinematic hardening material of yield stress, σ_{Y0}, equalling 1,195 MPa, which hardened to 1,332 MPa at a plastic strain of 0.0368. Young's Modulus and Poisson's ratio are not given, but are assumed to be 209 GPa and 0.3, respectively. The stress values equate to a plastic modulus, H, of (1,332 - 1,195)*10^6/0.0368 = 3.723 GPa, or E/H = 56.14.

The mandrel material is stated only as being Tungsten Carbide, and no mention is made of yielding (which would not be expected for a reusable mandrel), so it is assumed the mandrel behaves elastically. The following properties: Young's Modulus, E_m = 500 GPa, Poisson's ratio, v_m = 0.24. Different sources state a range of values for the Young's Modulus of Tungsten Carbide (450-650 GPa and 668.35-713.82 GPa), so an intermediate value of 500 GPa was used.

The motion of the mandrel is achieved by applying a moving constraint to the rear of the ram, which in turn moves the swage. O'Hara adds an extra constraint to prevent free body motion of the swage as it exits the tube.

560 time increments were used to simulate the progression of the mandrel through the tube – as with the ANSYS analyses described earlier, O'Hara states that this definition of time is merely to control the solution process, not to dictate rate effects, and as such the solution is termed quasi-static.

8.3.3. ANSYS Model

8.3.3.1. Geometry

To ensure a meaningful comparison, the ANSYS model was dimensioned to the same ratios as that used by O'Hara; specifically, this meant that the values of wall ratio, K, length ratio, l_z/r_a, length of parallel section of mandrel, l_{ll}, and the mandrel's forward and rear slopes, θ_{MF} and θ_{MR}, were matched. Figure 8.5 shows the mandrel dimensions used; as the lengths of the sloped sections are not stated by O'Hara, they are terminated when the radius reduces to r_a.

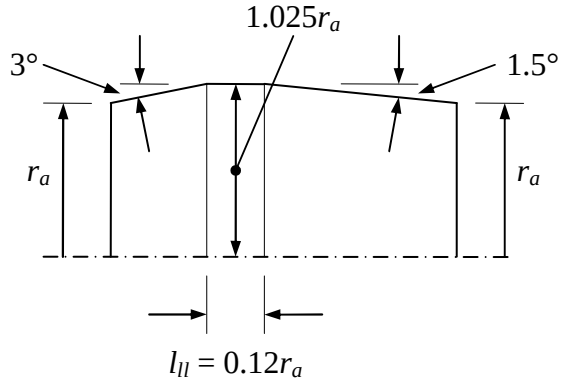

Figure 8.5: Mandrel Dimensions

The tapers featured in O'Hara's model, at the tube entrance and exit were omitted; they are used primarily to align the mandrel with the tube when it is swaged, which is not strictly needed in an FE model due to the alignment and constraints present. The tapers would have a secondary effect on mandrel driving force and residual stresses within the tube, but they are thought to be of very small magnitude.

It was also felt that the inclusion of a short section of ram, to apply the axial force to the mandrel, would have little or no effect. Given the stiffness of the mandrel, it was thought that applying a uniform displacement directly to its rear surface (such that it moves and remains plane) would be indistinguishable from applying it via the ram.

To determine the influence of the ram, the analyses were run twice; once with ram section, once without (residual hoop stresses from both cases are compared in Figure 8.13). Whilst the presence of the ram is of little consequence when replicating the mesh used by O'Hara on a modern computer, computational load increases with increased mesh fineness. Any computer model is a compromise between precision and speed of solution, and any modification that reduces complexity, and helps improve the compromise, must be sought.

The ram-mandrel contact was specified as asymmetric as both surfaces are flat (minimising penetration) and the mandrel is noticeably stiffer than the ram. In addition, as yielding was unexpected at the interface (and none was observed, and the

stresses were well below the yield stress), there was not the same requirement to minimise penetration as there was at the tube-mandrel interface. The Augmented Langrangian algorithm was again used, configured as at the tube-mandrel interface apart from setting FKN to 0.1 as no yielding was expected.

8.3.3.2. Mesh

The tube, mandrel and ram were meshed with PLANE183 elements. A mapped meshed was applied to the mandrel, allowing continuous horizontal and vertical lines of elements that followed the form of the mandrel.

To correctly model the "corners" of the mandrel, it was necessary to ensure that a node was present at each. These could not be mid-side nodes (before deformation, elements are quadrilateral), meaning the parallel section of the mandrel would have to be meshed with an integer number of elements. This element size, normalised with respect to r_a, is given by the (normalised) length of the parallel section divided the number of elements along it:

$$l_{El} = \frac{l_{ll}}{El_{Ax-ll}} \tag{8.2}$$

l_{El} is then used to scale the elements within the rest of the mandrel, ram and tub, as similarly sized elements are one of the key requirements for an accurate contact analysis. The number of radial and axial elements in the tube is hence determined by the results of the following, rounded to the nearest integer:

$$El_{Rad} = \frac{r_b - r_a}{l_{El}}, \quad El_{Ax} = \frac{l_z}{l_{El}} \tag{8.3}$$

Due to "top-down" approach used to create the model, it was decided to mesh the tube with rectangular elements; the uniformity lent itself well to scaling the mesh via scripting using APDL, allowing the sensitivity analysis to be automated. While not as efficient as the mesh used by O'Hara (requiring 640 rather than 306 elements), the mesh would be no less accurate. The ram was also meshed with rectangular elements.

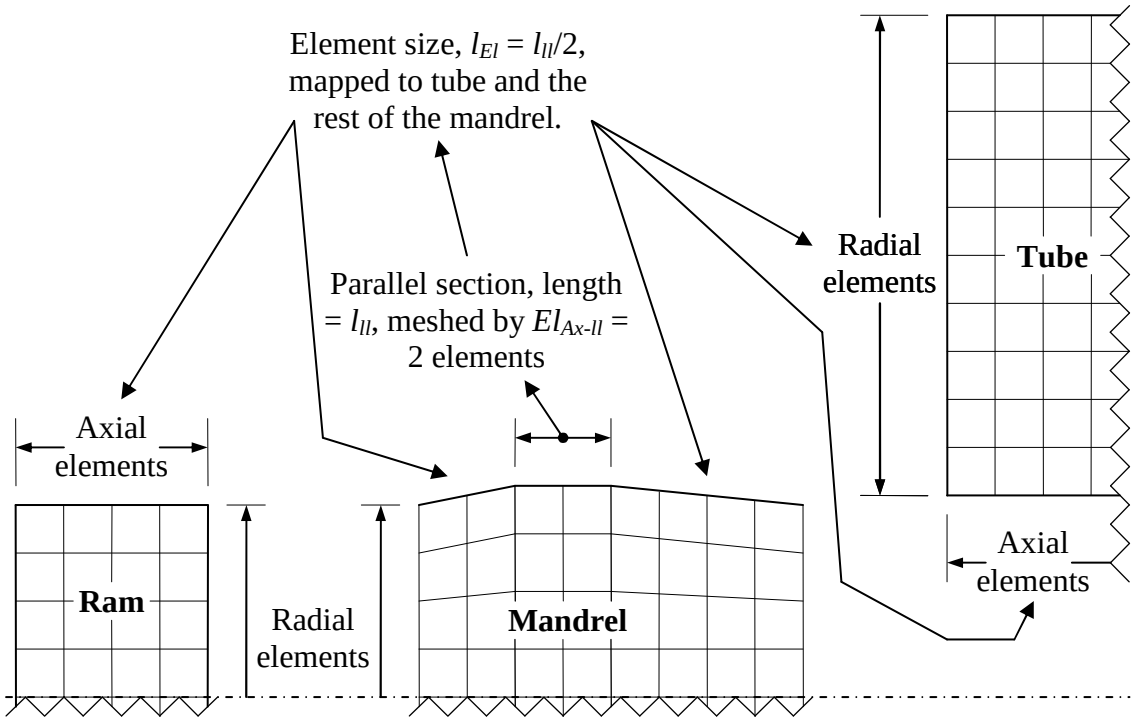

Figure 8.6: Mesh Sizing Diagram

8.3.3.3. Constraint

The tube was constrained axially in a similar manner to O'Hara's model, via a node on the OD 1/32nd of l_z from the entry end. However it was found that when finer meshes were used, large deformation of the tube resulted around the constrained node. To avoid this, the nodes along 1/32nd of the OD were constrained – a length equal to the edge of an element at the OD of O'Hara's model. This prevented large deformation while still localising the constraint force to a similar area.

8.3.3.4. Material

The tube material was specified to match that used by O'Hara as closely as possible (as stated in sub-section 8.3.2, he does not specify the elastic properties of the material), as was that of the mandrel. The ram material was specified as steel (again, E_r = 209 GPa, v_r = 0.3) with a yield stress of 600 MPa and a plastic modulus equal to 5% of it is Young's Modulus (H_r = 10.45 GPa). These values are summarised in Table 8.2.

The analysis was specified as a single load step broken down into a number of "sub-steps", which are synonymous with the time steps described in O'Hara's report. Dynamic effects are not implied, and such steps merely serve to ensure that the progression of the mandrel through the ID of the tube is analysed sufficiently frequently enough to capture the plastic response of the tube accurately. To achieve

this, the analysis is initially set to use 5,000 sub-steps; automatic time-stepping is employed to dynamically vary this throughout the solution between 1,000 and 10,000 according to the state of the model at a given time in the solution. The number of sub-steps effectively sets bounds on the size of the time increments applied; in this case the size is bounded between $1/1{,}000^{th}$ and $1/10{,}000^{th}$ of the applied time span. ANSYS also employs equilibrium iterations between these sub-steps to achieve a converged solution, but sub-steps are the primary mechanism of ensuring the solution is analysed at an appropriate granularity.

The analysis of mesh fineness sensitivity was conducted by varying the number of elements along the parallel section of the mandrel from one to seven, and scaling the meshes for each component using the resultant element edge length.

8.3.3.5. Summary

The following tables summarise the various properties used in O'Hara's analysis:

1. Table 8.2 contains the tube, mandrel and ram material properties,
2. Table 8.3 contains the geometrical properties,
3. Table 8.4 contains the contact parameters.

Property	Value	Property	Value	Property	Value
E_t	209 GPa	E_m	500 GPa	E_r	209 GPa
ν_t	0.3	ν_m	0.24	ν_r	0.3
σ_{Y0t}	1195 MPa	σ_{Y0m}	n/a	σ_{Y0r}	600 MPa
H_t	3.723 GPa	H_m	n/a	H_r	10.45 GPa

Table 8.2: O'Hara Comparison Material Properties

Property	Value
K	2.257
l_z	$7.714r_a$
Interference	2.5%
θ_{MF}	1.5°
θ_{MR}	3.0°
l_{ll}	$0.12r_a$

Table 8.3: O'Hara Comparison Geometric Properties

Property	Value	Property	Value
Friction	0.015	Friction	0.05
Normal Contact Stiffness, FKN	0.5	Normal Contact Stiffness, FKN	0.1
Normal Penetration Tolerance, FTOLN	0.1	Normal Penetration Tolerance, FTOLN	0.1
Tube-Mandrel Contact		Ram-Mandrel Contact	

Table 8.4: O'Hara Comparison Contact Properties

8.3.4. Results

Below are plotted the residual radial (Figure 8.7), hoop (Figure 8.8), axial (Figure 8.9) and equivalent (Figure 8.10) stresses; seven sets of results (from meshes of increasing fineness) are plotted against those calculated by O'Hara.

O'Hara's results are reproduced from Figure 2 in his paper. While this was done as accurately as possible, it is a source of potential error. In addition, it appears that the original graph was slightly mis-plotted as the radial positions of some near-OD results seem too small. This is most noticeable in the radial stress case (Figure 8.7).

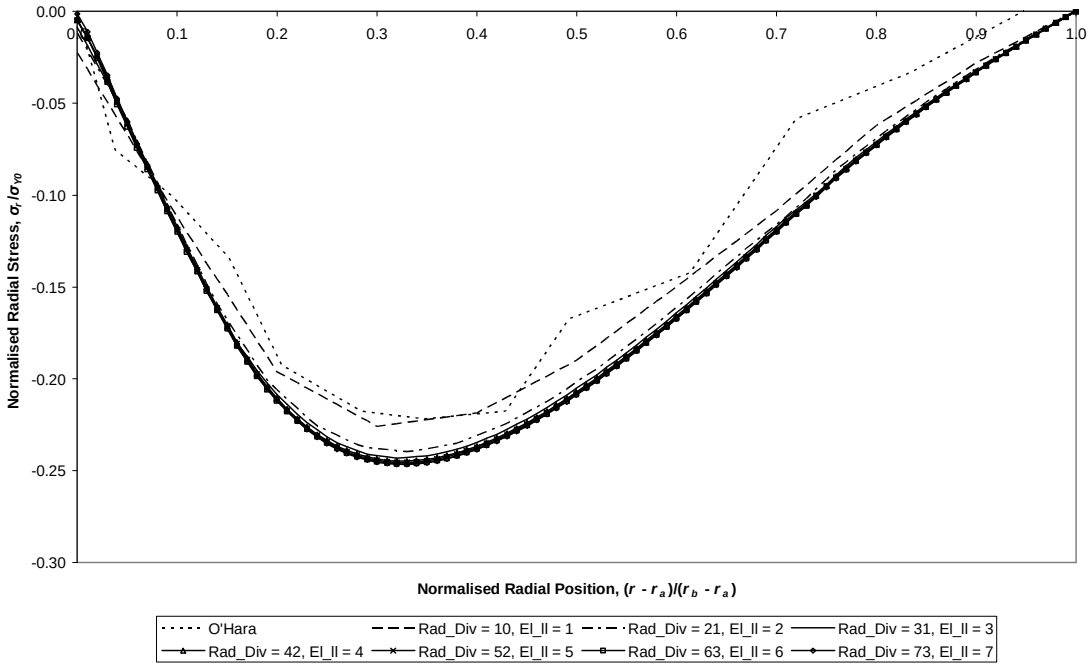

Figure 8.7: Residual Radial Stresses at mid-length resulting from Swage Autofrettage, as mesh fineness varies, compared with O'Hara's results

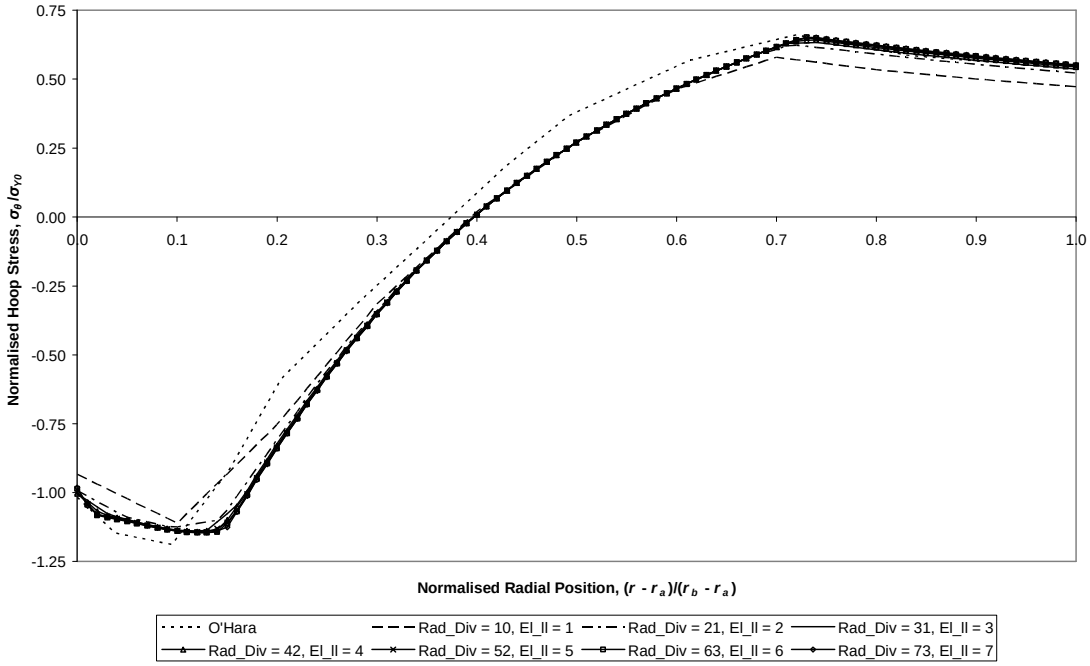

Figure 8.8: Residual Hoop Stresses at mid-length resulting from Swage Autofrettage, as mesh fineness varies, compared with O'Hara's results

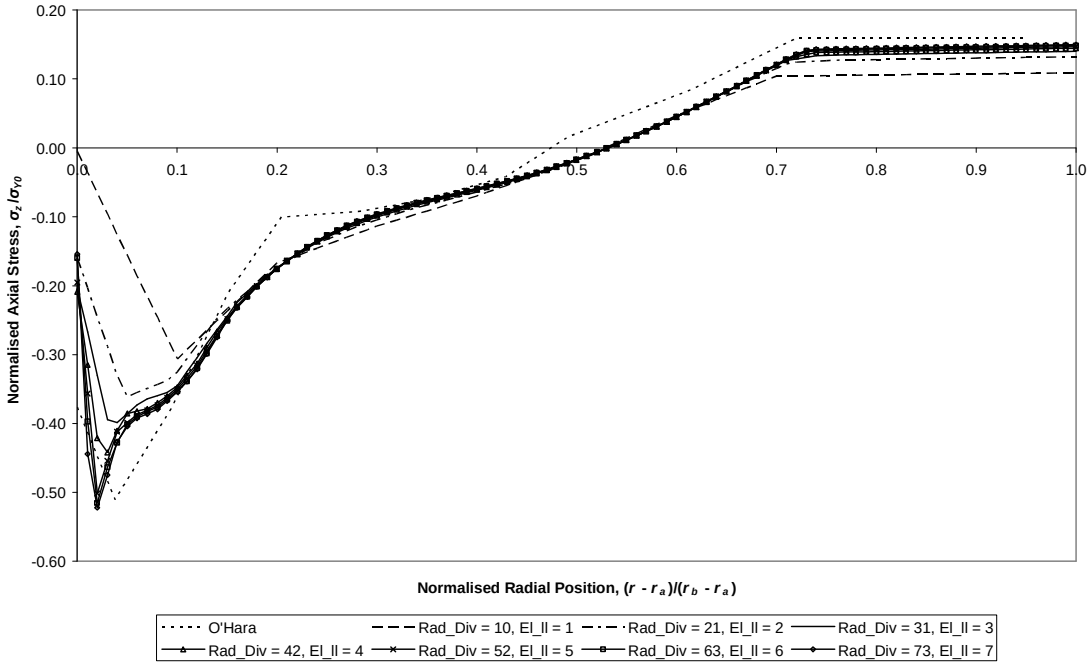

Figure 8.9: Residual Axial Stresses at mid-length resulting from Swage Autofrettage, as mesh fineness varies, compared with O'Hara's results

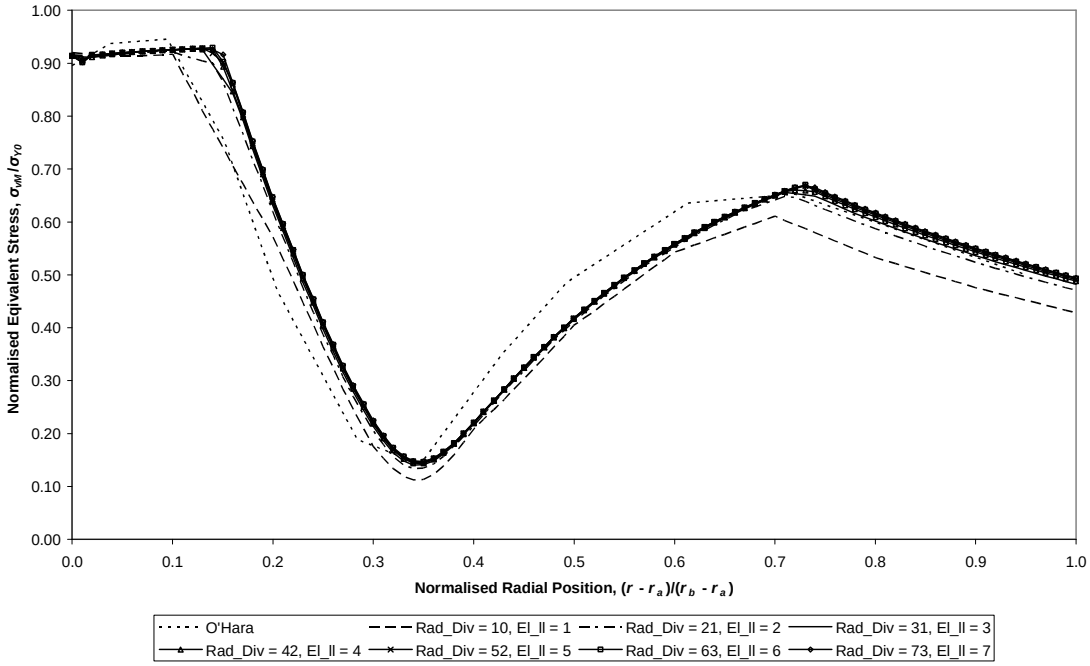

Figure 8.10: Residual Equivalent Stresses at mid-length resulting from Swage Autofrettage, as mesh fineness varies, compared with O'Hara's results

8.3.5. Discussion

Inspection of the solution monitoring output from ANSYS revealed that the progression was consistent and achieved within an acceptable number (typically between one and three for $El_{Ax\text{-}ll}$ = 1, rising to between seven and nine for $El_{Ax\text{-}ll}$ = 7) of equilibrium iterations per sub-step. This indicates that the model is generally specified well, in particular the contact parameters and number of sub-steps specified. As would seem logical, the number of equilibrium iterations is to some degree proportional to the number of axial elements in the tube (El_{Ax}); the motion of the mandrel must be simulated at enough locations to allow each element to accurately experience the applied deflection. The exact number of equilibrium iterations will depend on the number of sub-steps specified.

Additionally, the fact that the number of equilibrium iterations is fairly consistent suggests that the solution proceeds smoothly without intermittent difficulties, such as excessive penetration.

During processing, ANSYS set the Newton-Raphson to "Full" (which uses a symmetric matrix) at solution time, indicating frictional effects did not alter the displacement field sufficiently to require an unsymmetrical matrix. As the coefficient of friction for the tube-mandrel contact was low (0.015), the Newton-Raphson options were left as "Auto"; future cases may involve higher coefficient values, which may then affect the displacement field sufficiently to make an unsymmetrical matrix necessary.

In terms of mesh sensitivity, the lowest mesh fineness ($El_{Ax\text{-}ll}$ = 1) set of results appear quite similar to those calculated by O'Hara; as the number of elements along the parallel section of the mandrel was increased, the four sets of residual stress data converge relatively quickly. The relative error of residual hoop stress at mid-length on the ID, a key indicator of the degree of pre-stressing applied, is plotted in Figure 8.11.

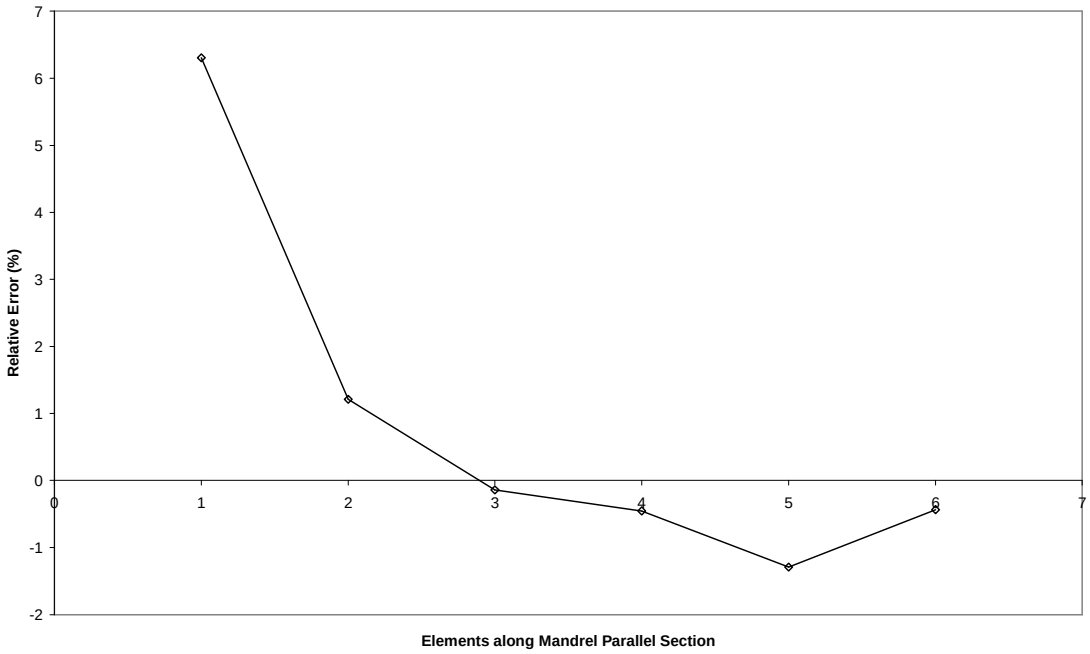

Figure 8.11: Relative Error of Residual Hoop Stresses at mid-length on the ID

Although relative error does not appear to decrease asymptotically to zero, when the residual hoop stresses for values of $El_{Ax\text{-}ll} \geq 4$ are replotted (Figure 8.12) for clarity, the sets show very close agreement.

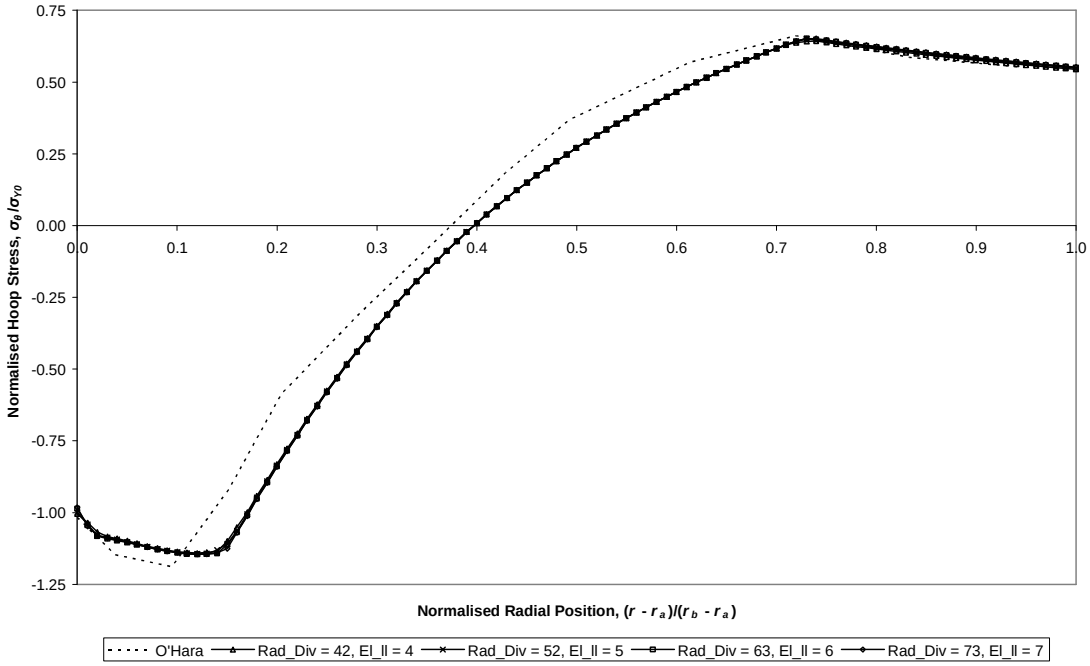

Figure 8.12: Residual Hoop Stresses at mid-length resulting from Swage Autofrettage, as mesh fineness varies, compared with O'Hara's results, $El_{Ax\text{-}ll} \geq 4$

On this basis, $El_{Ax\text{-}ll} = 4$ was selected as a suitable initial value to use for the sensitivity analyses that would follow. This would be subject to re-evaluation if element sizing did subsequently appear to be non-optimal.

Using $El_{Ax\text{-}ll} = 4$, residual hoop stresses were compared for the cases with and without the driving ram. As may be seen from Figure 8.13, the results are almost identical, but the solution time increased by approximately 10% when the ram was present (11.75 hours to 13 hours). For this reason, the ram was omitted from future models. While the ram could potentially be added in a less computationally demanding manner, it was felt that the possible extra precision would be meaningless without full knowledge of the exact mandrel dimensions. For example, not knowing the precise lengths of the mandrel for which the slopes decrease in radius below r_a would have a potentially greater effect on mandrel deformation given the greater stiffness of the mandrel material.

If the ANSYS swage model were used to investigate a real world example where all geometrical details were known, it would then be appropriate to model the ram and all such features.

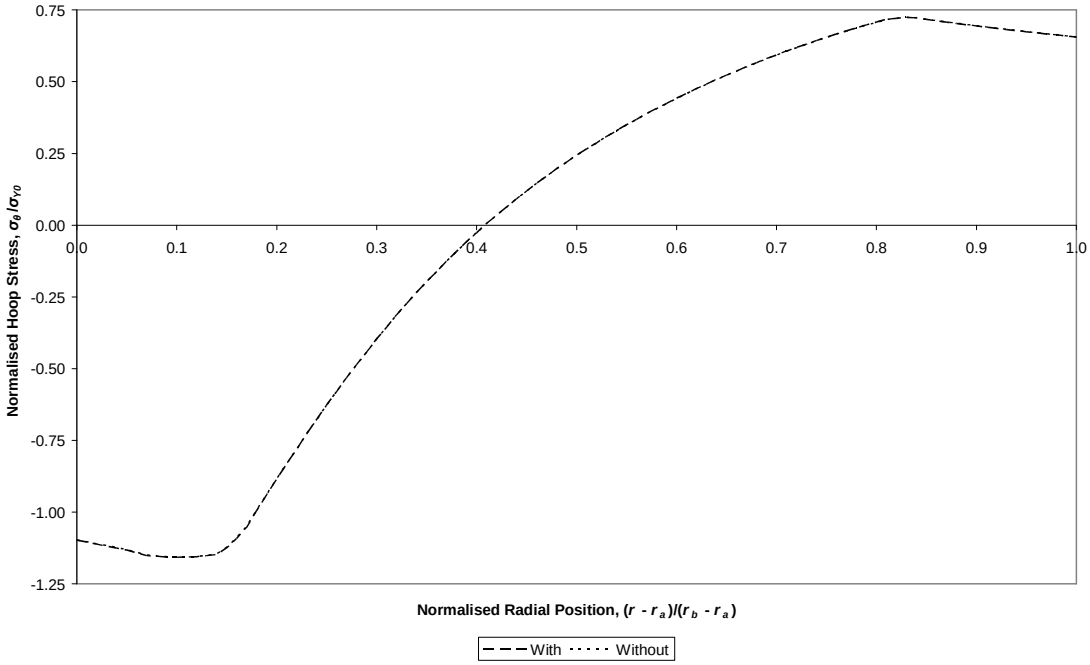

Figure 8.13: Residual Hoop Stresses at mid-length resulting from Swage Autofrettage, with and without ram, from ANSYS model with $El_{Ax\text{-}II} = 4$

As with any numerical analysis, it is always desirable to increase the number of sub-divisions employed; however, due to the large number elements required to mesh the long length of tube, the progressive solution and contact analysis, swage autofrettage takes considerably longer to solve than hydraulic autofrettage.

8.4. SENSITIVITY ANALYSIS

8.4.1. Introduction

After completing the initial comparison with O'Hara's results, and the behaviour of the model had been demonstrated to be representative of swage autofrettage, it was then necessary to ensure that results obtained during the parametric analysis were representative of those expected to be found in a real swaged tube. Specifically, this meant checking that the section length was sufficient to allow consistent results to be gathered in the mid-section zone, and that enough sub-steps were being used to prevent axial irregularity of the calculated properties.

Two sets of sensitivity analyses were conducted to investigate these issues, each of which are described below.

8.4.2. Model Parameters

The dimensions were largely as used in the comparison with O'Hara's results, with the exception of wall ratio and tube length. To be more consistent with previous results, wall ratio, K, of 2.5 was selected, and the length of the tube was normalised with respect to its inner radius, r_a. Both the sensitivity analyses described below, utilised a swage geometry identical to that used in the O'Hara comparison.

Whilst it was expected all stress and strain components would show axial variation, it was felt that axial components would show the most variation. This would be caused mainly by two factors:

1. Axial stresses must become zero at the tube ends, as no force acts upon them,
2. Hoop and radial properties are strongly linked, as demonstrated for plane sections by the equilibrium equations (2.1) and (7.3).

For this reason, as well as assessing the residual properties at mid-length, axial stresses were recorded along four axial paths to allow their axial variation to be investigated. The locations of the axial paths are shown in Figure 8.14.

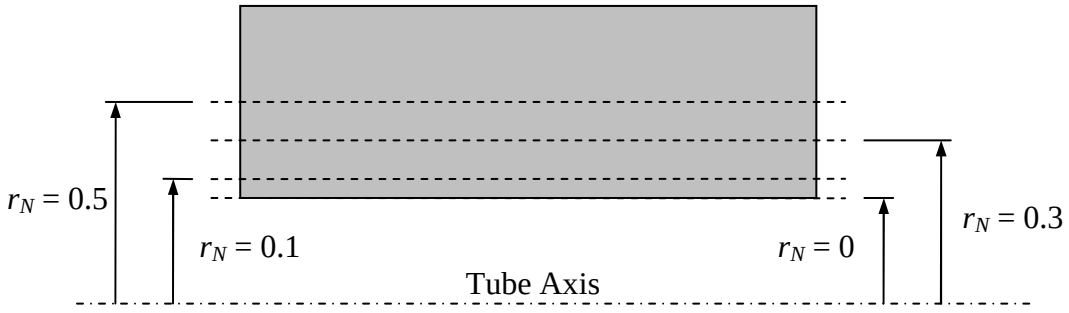

Figure 8.14: Axial Data Path locations within tube

8.4.3. Stage 1 – Tube Length Analysis

To determine what length of tube was required to generate suitable mid-length values of residual stress, required during a parametric analysis of the swage autofrettage process, the tube section length was systematically altered and residual stresses were compared. This way, the results of a parametric analysis could be confidently deemed free of "end effects" that are observed at and near the ends of a swage autofrettaged tube.

Tube lengths, l_z, of $5r_a$, $10r_a$, $15r_a$, $20r_a$, $25r_a$ and $30r_a$ were used.

8.4.4. Results 1 – Tube Length Analysis

Residual hoop and axial stresses from the tube length analysis are plotted below in Figure 8.15 and Figure 8.16, respectively.

Residual axial stresses, in the region $0 \leq l \leq l_z$, for the tube length analysis are shown below for the r_N = 0 path (Figure 8.17), r_N = 0.1 path (Figure 8.18), r_N = 0.3 path (Figure 8.19) and r_N = 0.5 path (Figure 8.20),

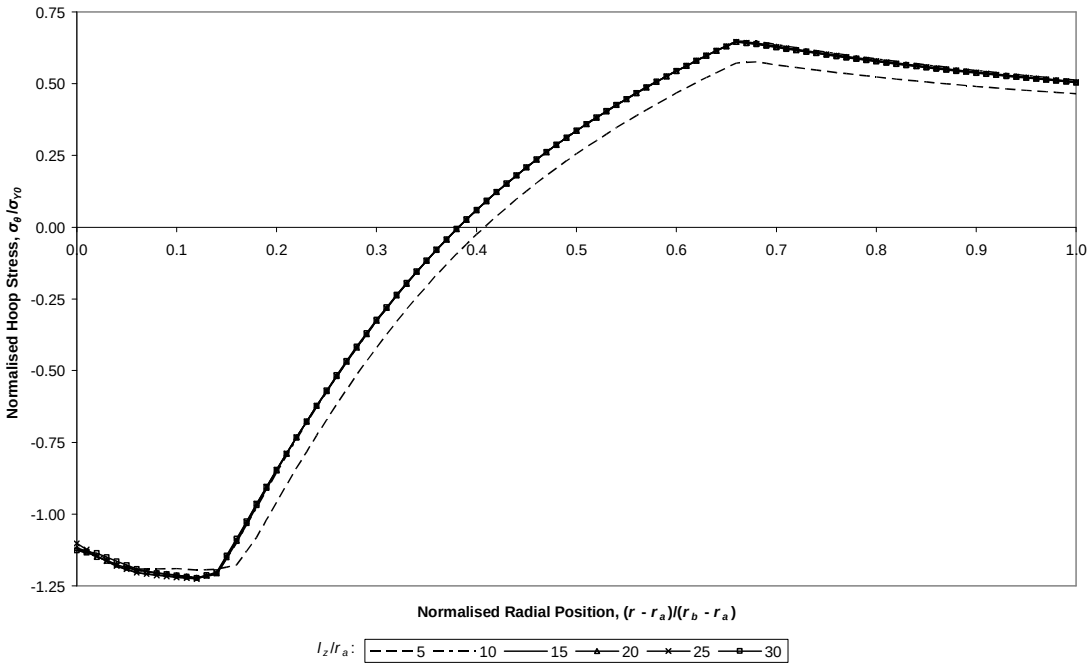

Figure 8.15: Residual Hoop Stresses at mid-length resulting from Swage Autofrettage, as tube section length varies

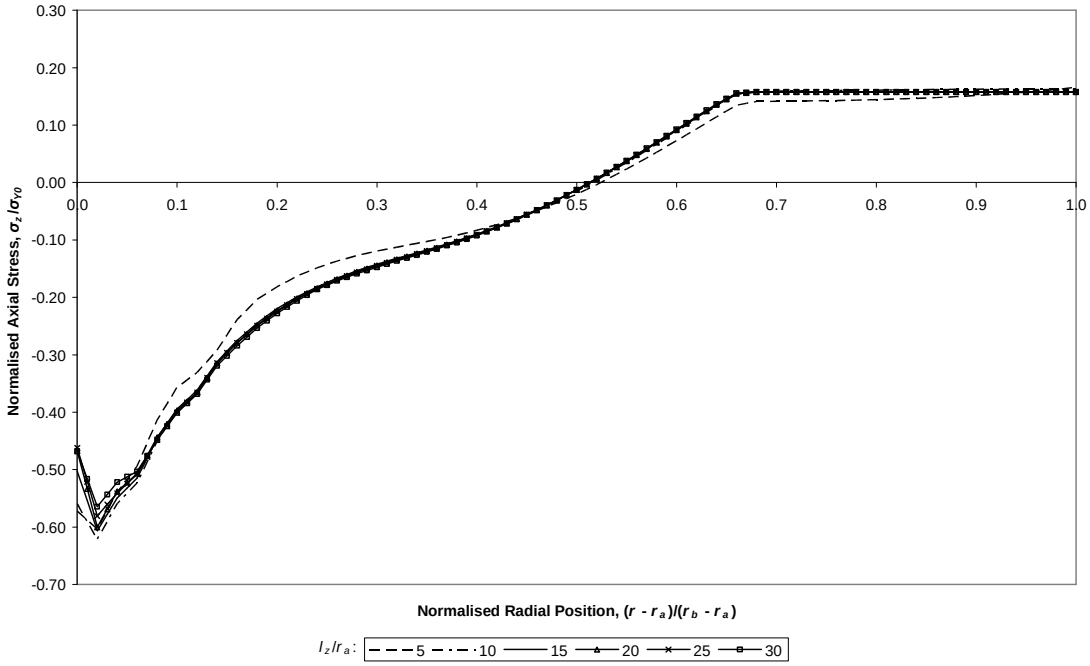

Figure 8.16: Residual Axial Stresses at mid-length resulting from Swage Autofrettage, as tube section length varies

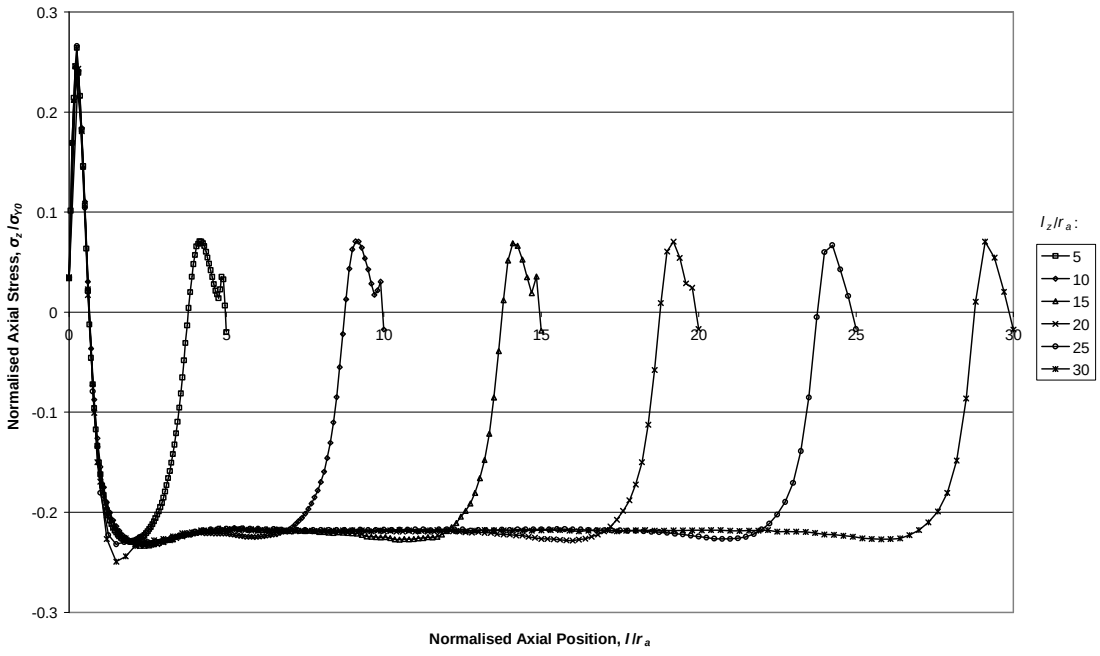

Figure 8.17: Residual Axial Stresses along axial path at $r_N = 0$, resulting from Swage Autofrettage, as tube section length varies

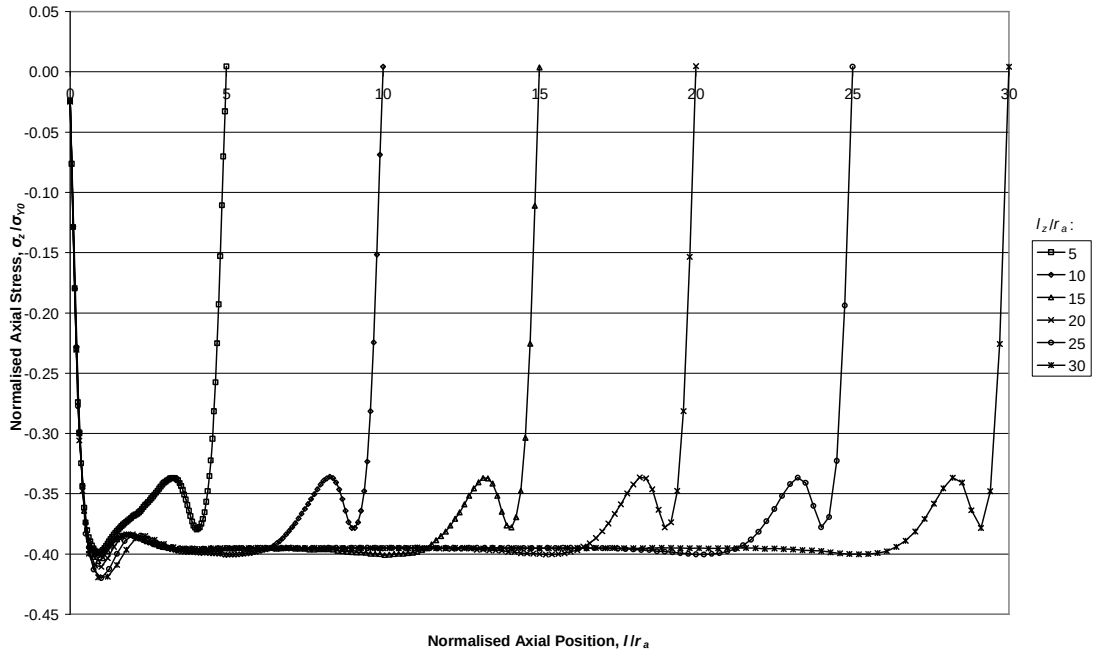

Figure 8.18: Residual Axial Stresses along axial path at r_N = 0.1, resulting from Swage Autofrettage, as tube section length varies

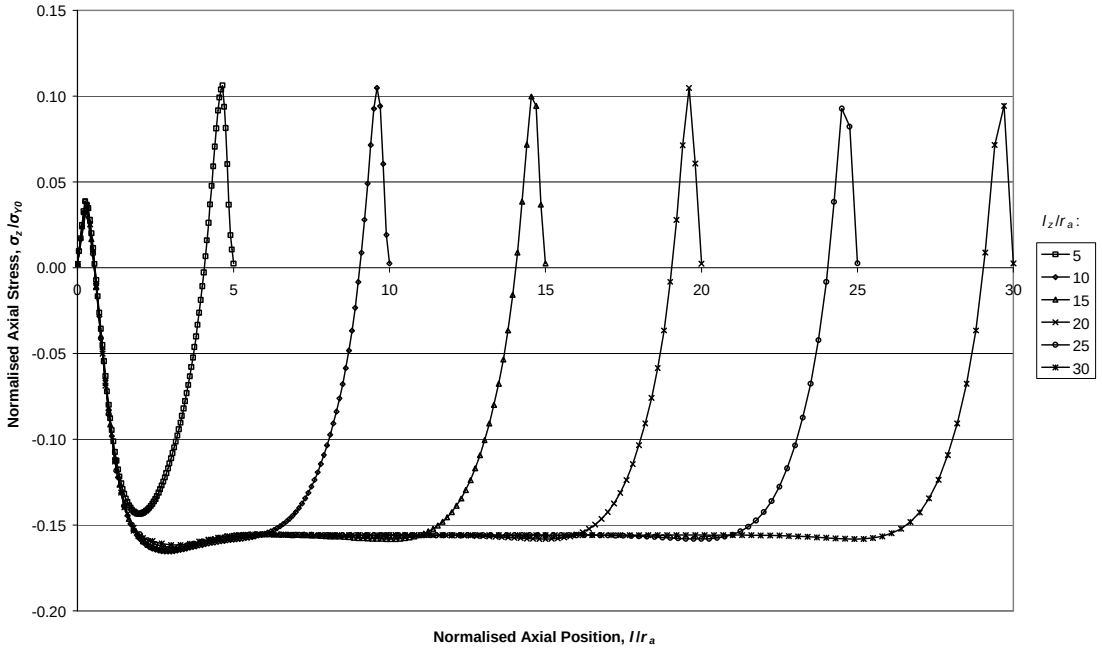

Figure 8.19: Residual Axial Stresses along axial path at r_N = 0.3, resulting from Swage Autofrettage, as tube section length varies

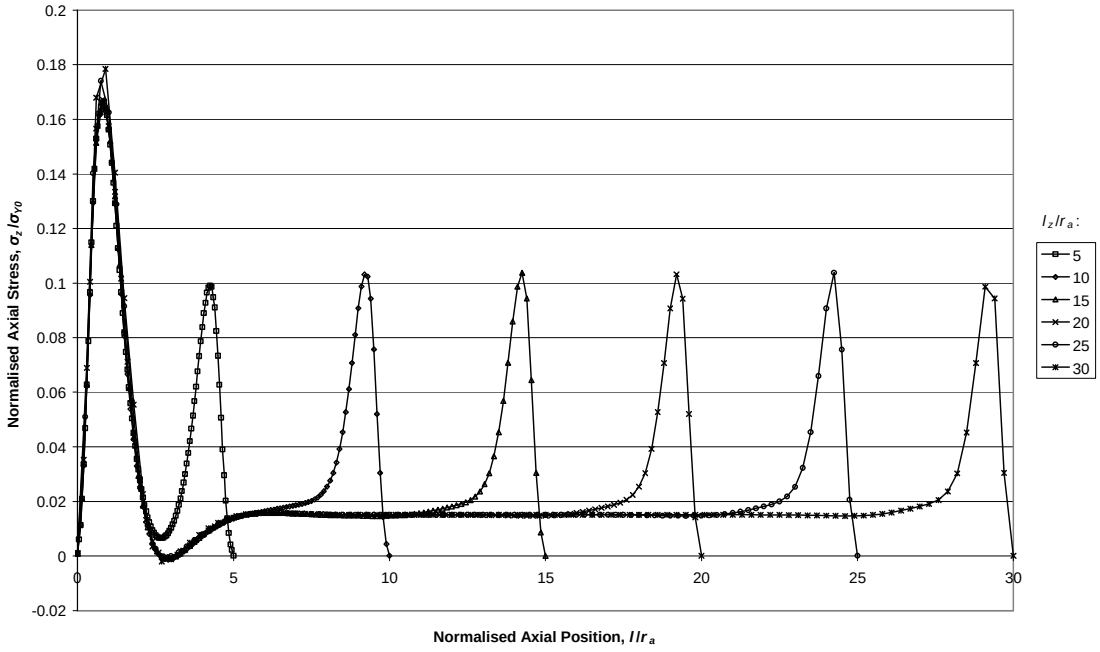

Figure 8.20: Residual Axial Stresses along axial path at r_N = 0.5, resulting from Swage Autofrettage, as tube section length varies

8.4.5. Discussion 1 – Tube Length Analysis

Inspection of the mid-length residual stresses (Figure 8.15 and Figure 8.16) reveals a visible difference between results from tube lengths of $5r_a$ and $10r_a$, and only very slight differences between those from tube lengths of $10r_a$ and $15r_a$.

The residual axial stresses (Figure 8.17 to Figure 8.20), taken along axial paths, show a similar pattern; a tube length of $5r_a$ shows no stable central region where consistent values prevail for a certain length. Results from a tube length of $10r_a$ also do not show a consistent central band, but the rates of change of axial stress are decreased. Results from a tube length of $15r_a$ do show a consistent central band.

For this reason, a tube length of $15r_a$ was selected as suitable for generation of results that may confidently be assumed to be representative of mid-length properties. This value was used for all subsequent analyses, including the sub-step optimisation that is presented below.

In all cases (Figure 8.17 to Figure 8.20) residual axial stresses are observed to become zero at the free ends; a useful check that the applied constraints behaved as was intended. Figure 8.17 shows negative (compressive) residual axial stresses over much of the length of the ID (for all tube lengths), but small regions around the end show positive (tensile) stresses. This may be explained by Figure 7.20; as the ends of the tube are not constrained in the same way the mid-length section is, tensile axial deformation of the near ID region does not occur at the tube ends.

8.4.6. Stage 2 – Sub-Step Analysis

The influence of the number of sub-steps specified was investigated by varying the minimum, maximum and initial number of sub-steps. The number of sub-steps the load step is divided into, which is potentially of importance in a progressive analysis such as in this swage model. The number of sub-steps specified is based on the number of element lengths moved by the mandrel as it passes through the tube undergoing swage autofrettage (a distance of l_z + l_m). This number is then scaled using a parameter (termed *PS* below), which was iterated through the values of 0.2, 0.4, 2 and 4.

The number of element lengths moved by the mandrel is given by the following:

$$N_{El-Ax} = \frac{El_{Ax} \cdot (l_z + l_m)}{l_z}$$

The number of sub-steps specified is then given by the following:

Minimum sub-steps = $El_{N\text{-}Ax}$ * *PS*
Maximum sub-steps = $El_{N\text{-}Ax}$ * 10 * *PS*
Initial sub-steps = $El_{N\text{-}Ax}$ * 5 * *PS*

These numbers of sub-steps were applied to the swage autofrettage of a tube of section length equal to $15r_a$.

8.4.7. Results 2 – Sub-Step Analysis

Residual hoop (Figure 8.21), axial (Figure 8.22) and equivalent (Figure 8.23) stresses are plotted below for the values of *PS* specified. Residual radial stresses were considered similar enough not to warrant plotting.

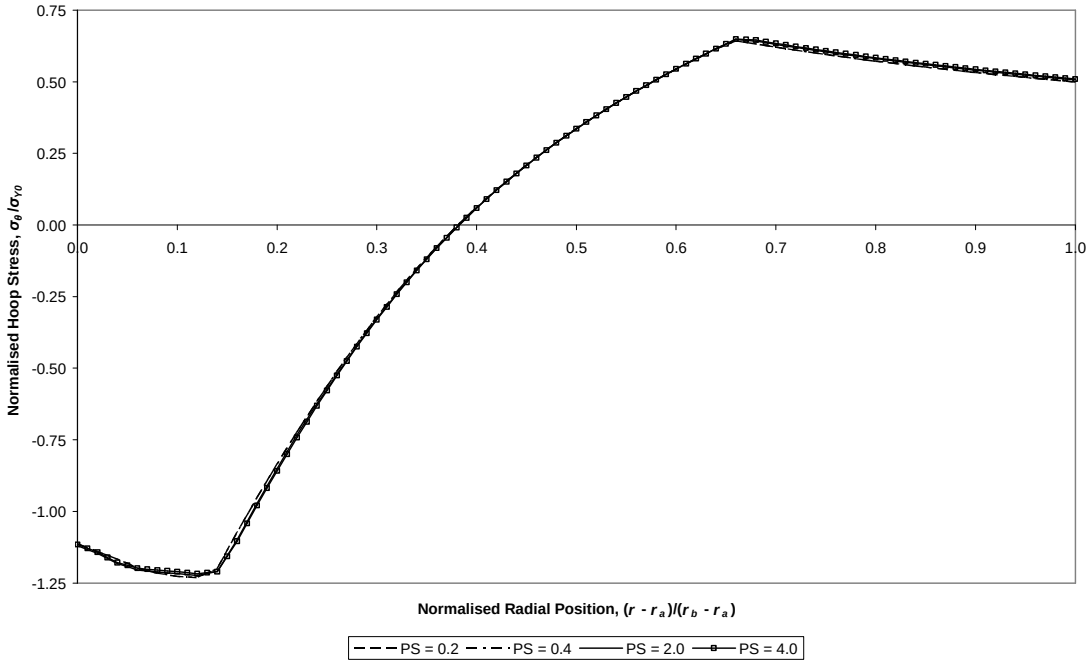

Figure 8.21: Residual Hoop Stresses at mid-length resulting from Swage Autofrettage, as time steps vary

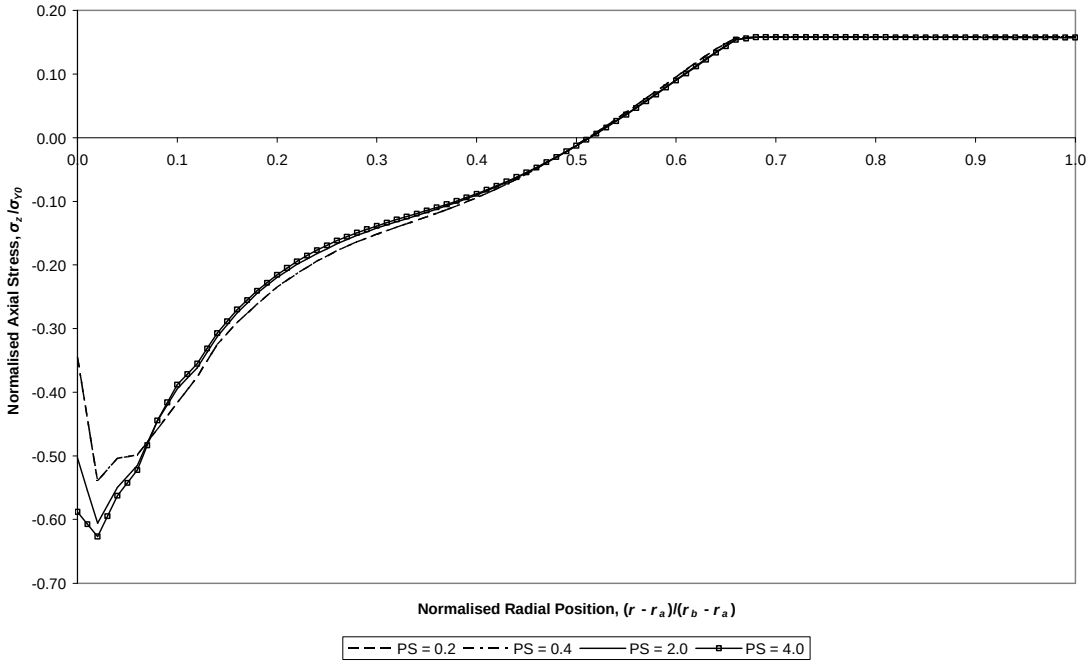

Figure 8.22: Residual Axial Stresses at mid-length resulting from Swage Autofrettage, as time steps vary

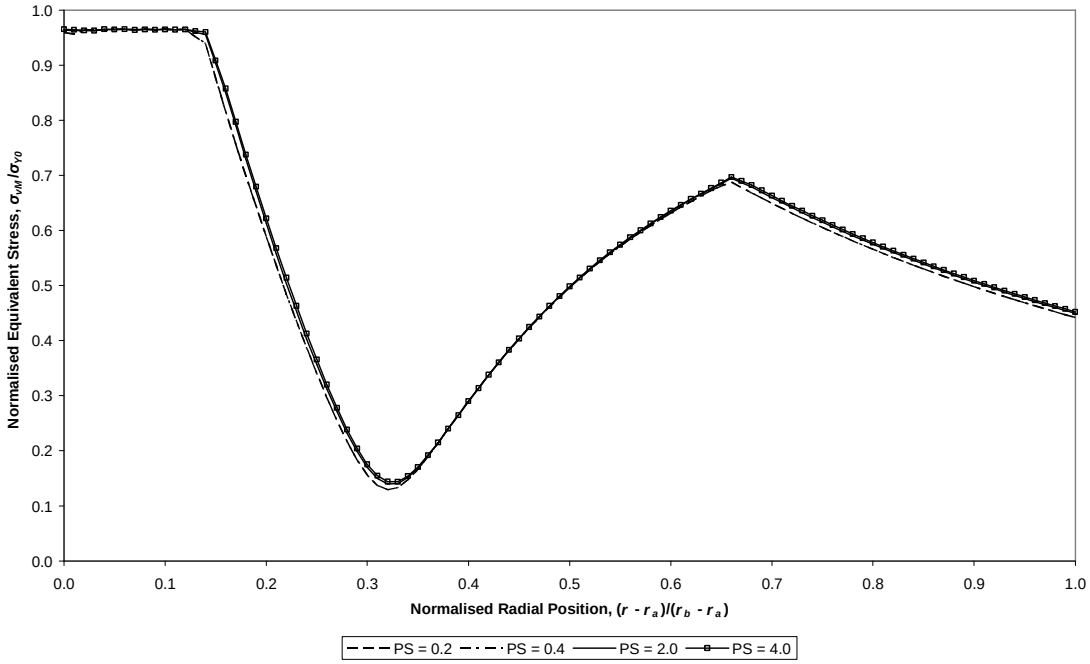

Figure 8.23: Residual Equivalent Stresses at mid-length resulting from Swage Autofrettage, as time steps vary

8.4.8. Discussion 2 – Sub-Step Analysis

Both residual hoop and equivalent stresses at the mid-length position (Figure 8.21 and Figure 8.23) show almost no variation with the number of sub-steps used, and hence are not a useful measure of their effect.

Residual axial stresses at the mid-length position (Figure 8.22) do show some variation at the ID between *PS* = 4 and the other values; it is logical that differences are most apparent at the ID as this region is adjacent to the localised loading from the mandrel.

It was observed that the number of sub-steps used by ANSYS during the solution procedure was constant at approximately 445 for the *PS* = 0.2 and 0.4 cases, which explains the similarity between the two sets of results. However, for the *PS* = 2 and 4 cases the number of sub-steps was only slightly higher than the specified minimum; this explains why the solution time for the *PS* = 4 case was approximately twice that for the *PS* = 2 case.

Ideally, *PS* = 4 would be used in future solutions, meaning that incremental movements of the mandrel would be 0.25 element lengths (l_{El}), hence its parallel section would take $El_{Ax\text{-}ll}$ * 4, or 16 sub-steps to pass. However, the computer used to solve the cases presented in this chapter was a shared resource; for this reason, it was necessary to select *PS* = 2 to ensure the required results could be obtained within the time available. It is felt that the resultant loss of accuracy was acceptable, as variation was effectively only present in the residual axial stresses calculated.

Based on these findings, it was decided to specify $10El_{N\text{-}Ax}$ sub-steps initially, with $2El_{N\text{-}Ax}$ sub-steps as the minimum allowable and $20El_{N\text{-}Ax}$ as the maximum allowable. While this would alter the exact values of results, it was felt that the change would be small enough such that trends could be meaningfully identified during parametric analyses.

8.5. PARAMETRIC STUDY 1 – PARALLEL SECTION LENGTH INVESTIGATION

8.5.1. Overview

The first parameter to be investigated was the length of the parallel section of the mandrel, l_{ll}; intuitively a longer section would increase the depth of deformation resulting from the swaging operation, but it was not clear what other effects would manifest.

To achieve this, a series of swaging simulations were run between which l_{ll} was varied whilst all other parameters remained static and as determined by section 8.4. The following values of l_{ll} were used: $0.25l_{ll\text{-}0}$, $0.5l_{ll\text{-}0}$, $0.75l_{ll\text{-}0}$, $1l_{ll\text{-}0}$, $1.5l_{ll\text{-}0}$, $3l_{ll\text{-}0}$ and $4.5l_{ll\text{-}0}$, where $l_{ll\text{-}0}$ is the value of l_{ll} used previously, equal to $0.12r_a$.

8.5.2. Results

Figure 8.24 plots the depth of overstrain (plastic deformation) achieved against the parallel section length, l_{ll}, of the mandrel used.

Autofrettage (i.e. values taken from the mid-length position of the tube, when the centre of the parallel surface of the mandrel is coincident) values are shown in Figure 8.25, Figure 8.26, Figure 8.27 and Figure 8.28, which respectively show radial, hoop and axial stresses and plastic hoop strains through the tube wall.

Residual values are shown in Figure 8.30, Figure 8.31 and Figure 8.32, which respectively show hoop and axial stresses and plastic hoop strains through the tube wall.

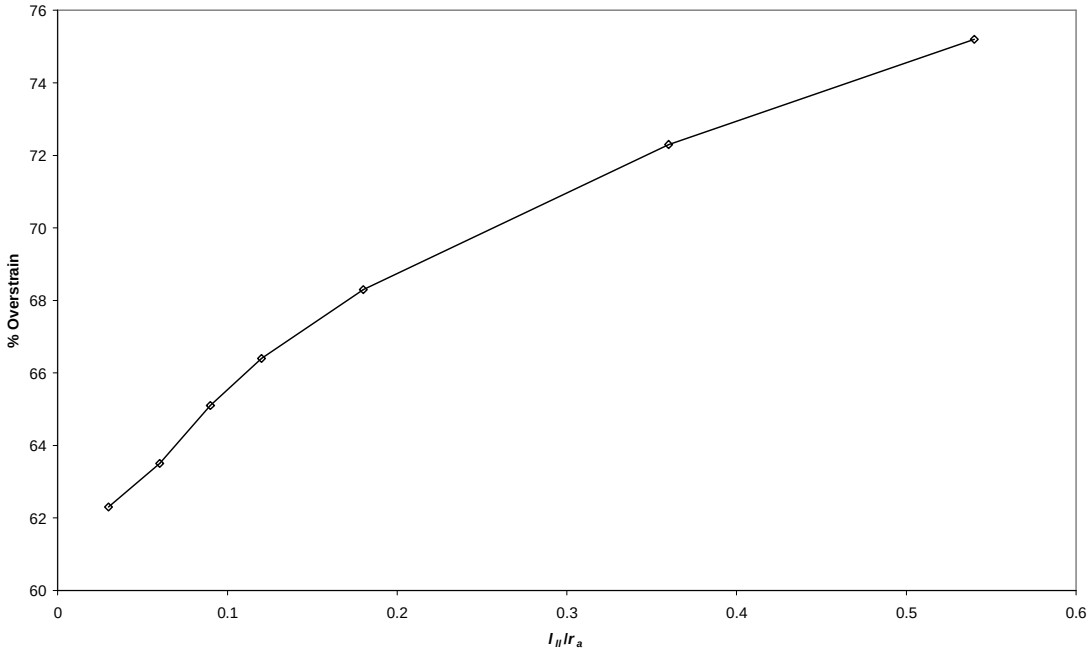

Figure 8.24: Overstrain Depth, at mid-length, as Parallel Section Length, l_{ll}, varies

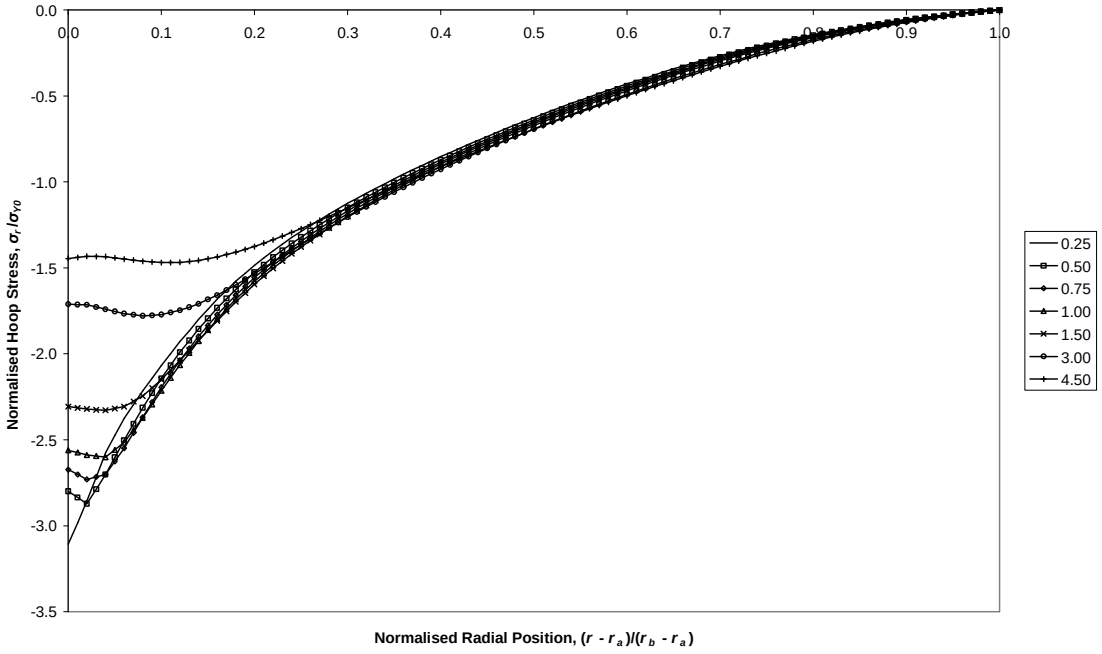

Figure 8.25: Autofrettage Radial Stresses, at mid-length, as Parallel Section Length, l_{ll}, varies

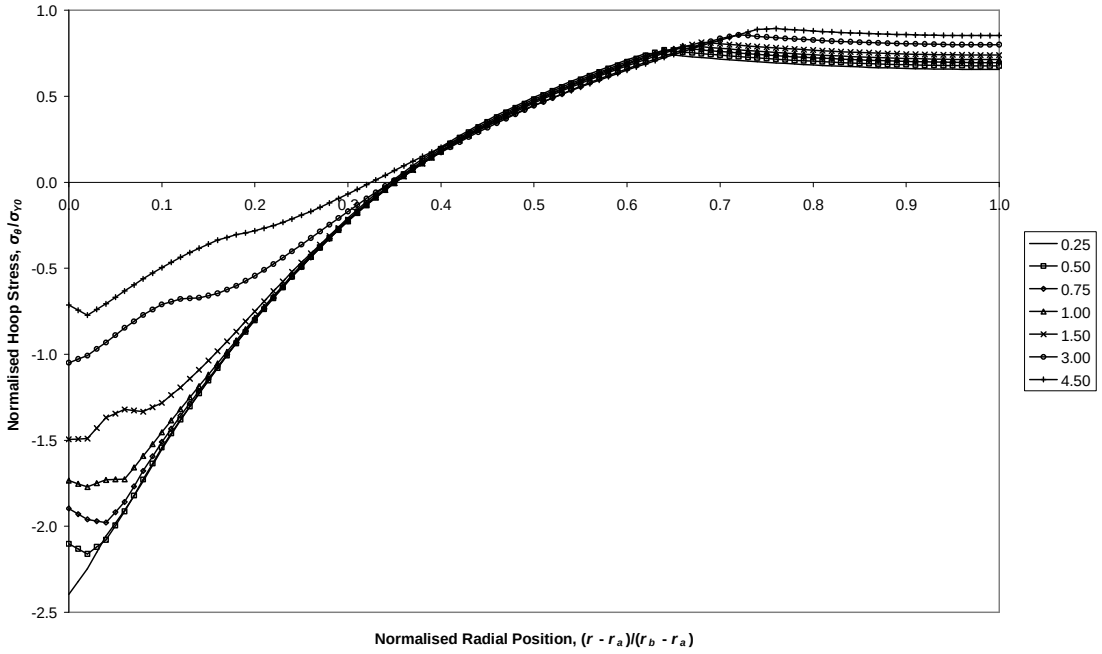

Figure 8.26: Autofrettage Hoop Stresses, at mid-length, as Parallel Section Length, l_{ll}, varies

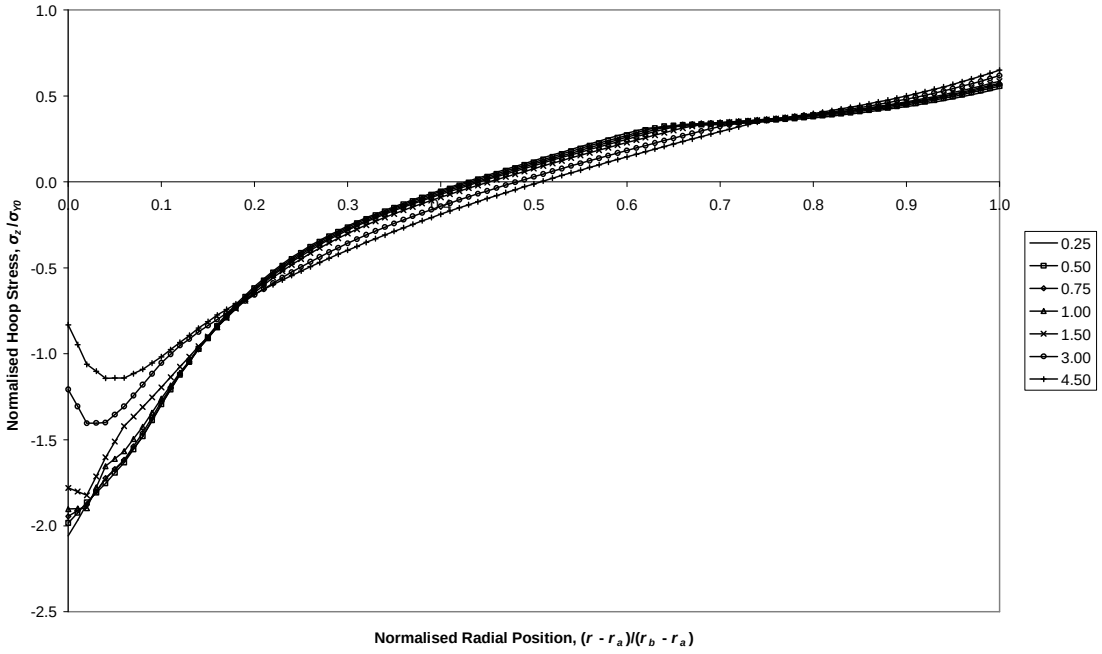

Figure 8.27: Autofrettage Axial Stresses, at mid-length, as Parallel Section Length, l_{ll}, varies

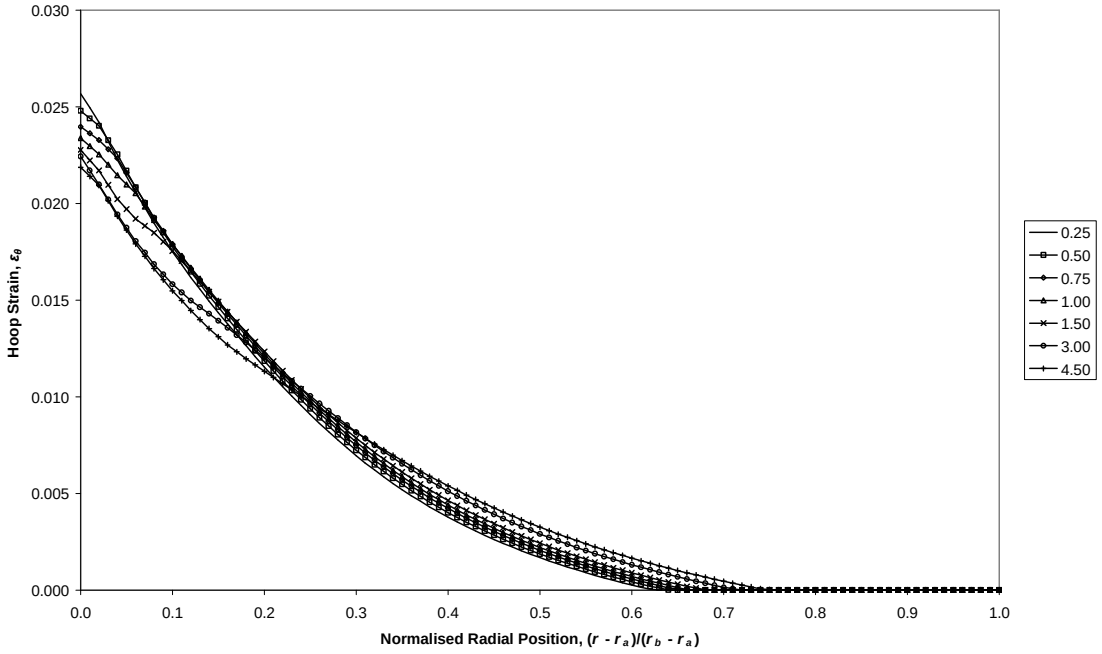

Figure 8.28: Autofrettage Plastic Hoop Strains, at mid-length, as Parallel Section Length, l_{ll}, varies

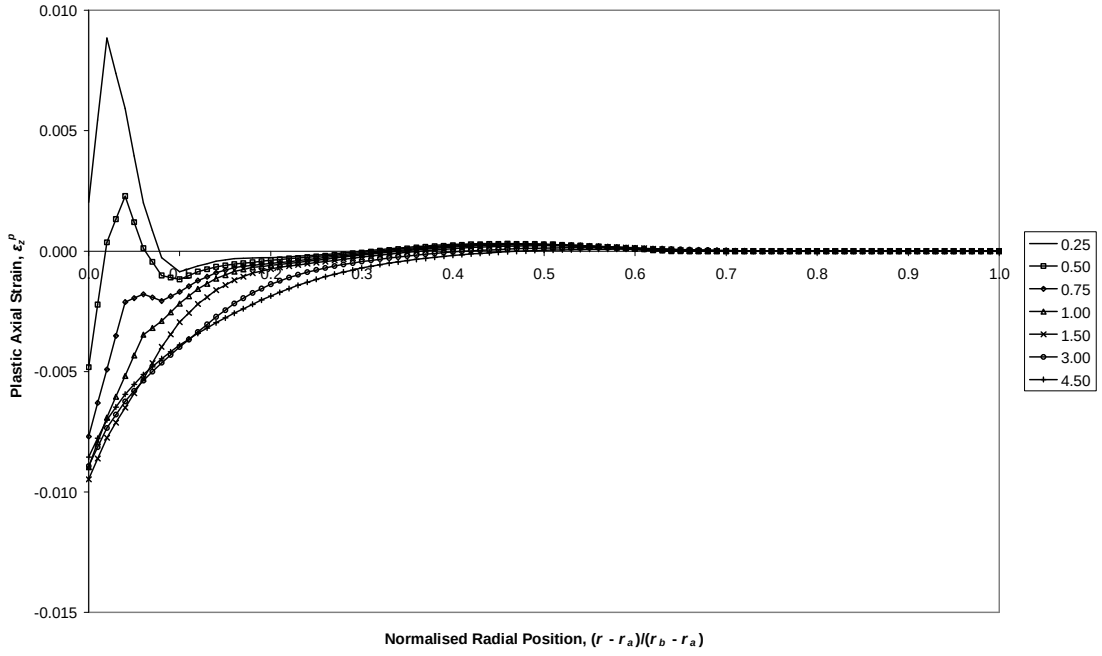

Figure 8.29: Autofrettage Plastic Axial Strains, at mid-length, as Parallel Section Length, l_{ll}, varies

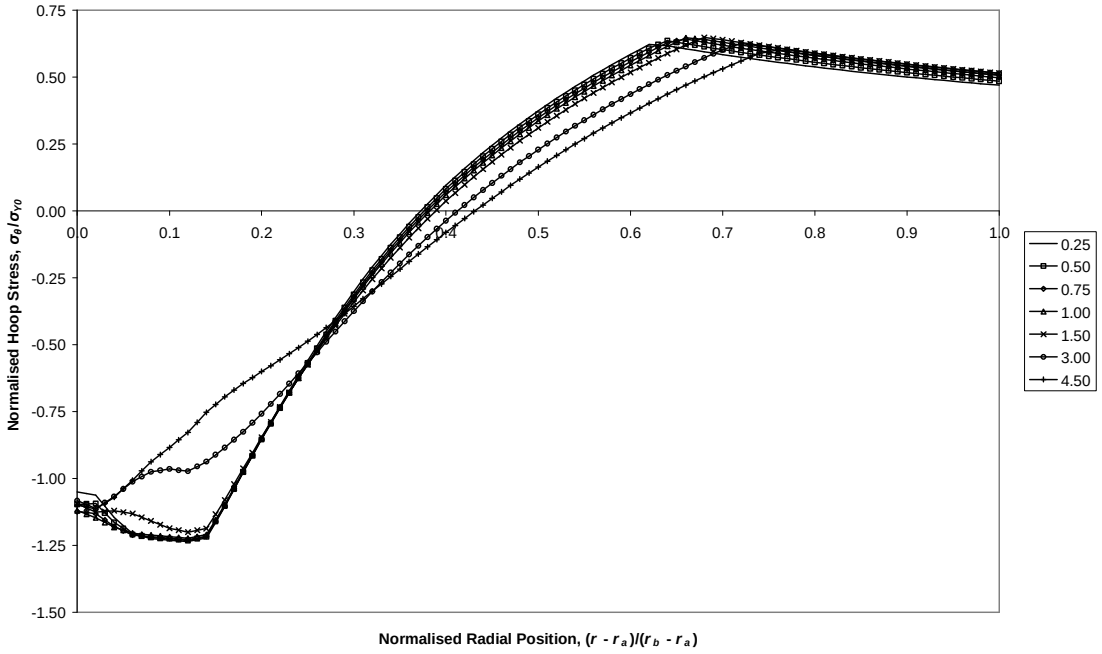

Figure 8.30: Residual Hoop Stresses, at mid-length, as Parallel Section Length, l_{ll}, varies

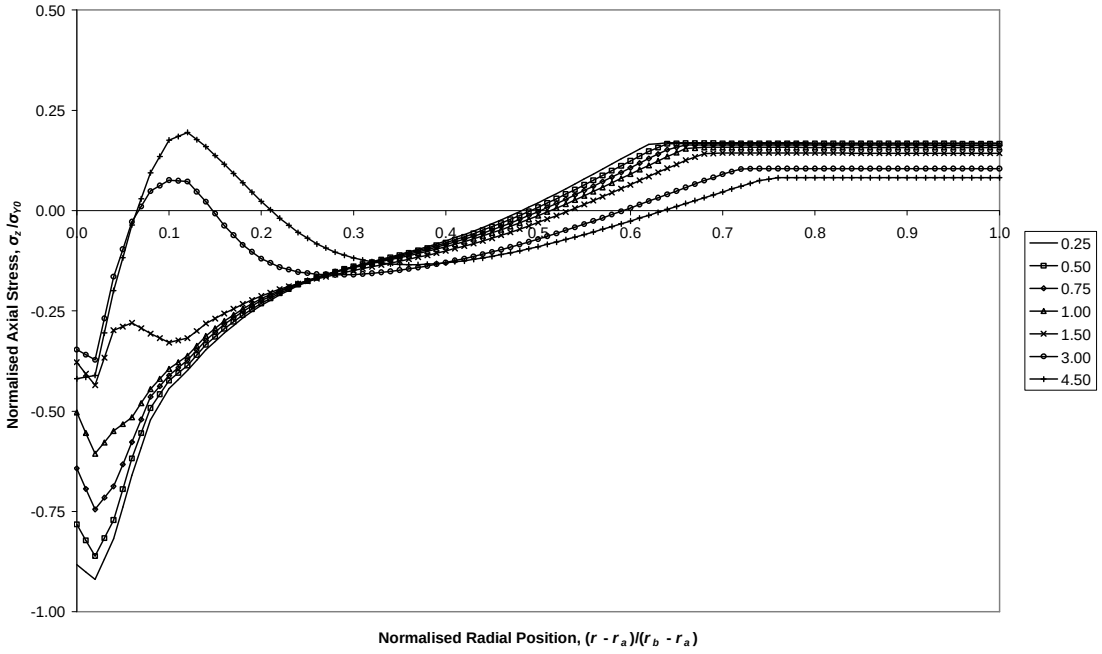

Figure 8.31: Residual Axial Stresses, at mid-length, as Parallel Section Length, l_{ll}, varies

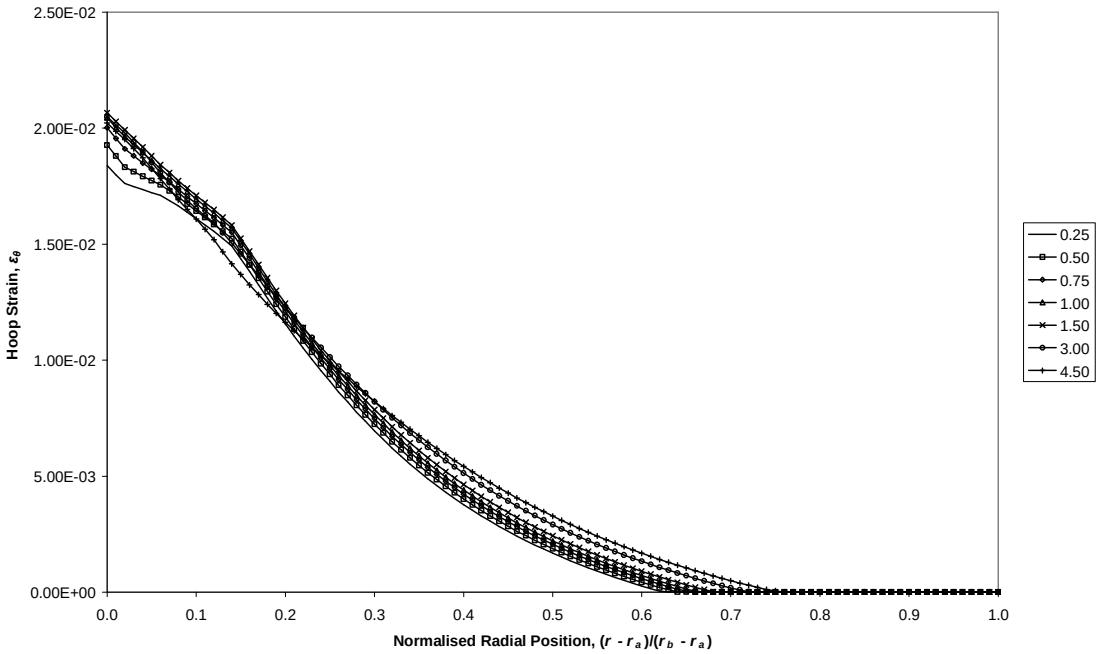

Figure 8.32: Residual Plastic Hoop Strains, at mid-length, as Parallel Section Length, l_{ll}, varies

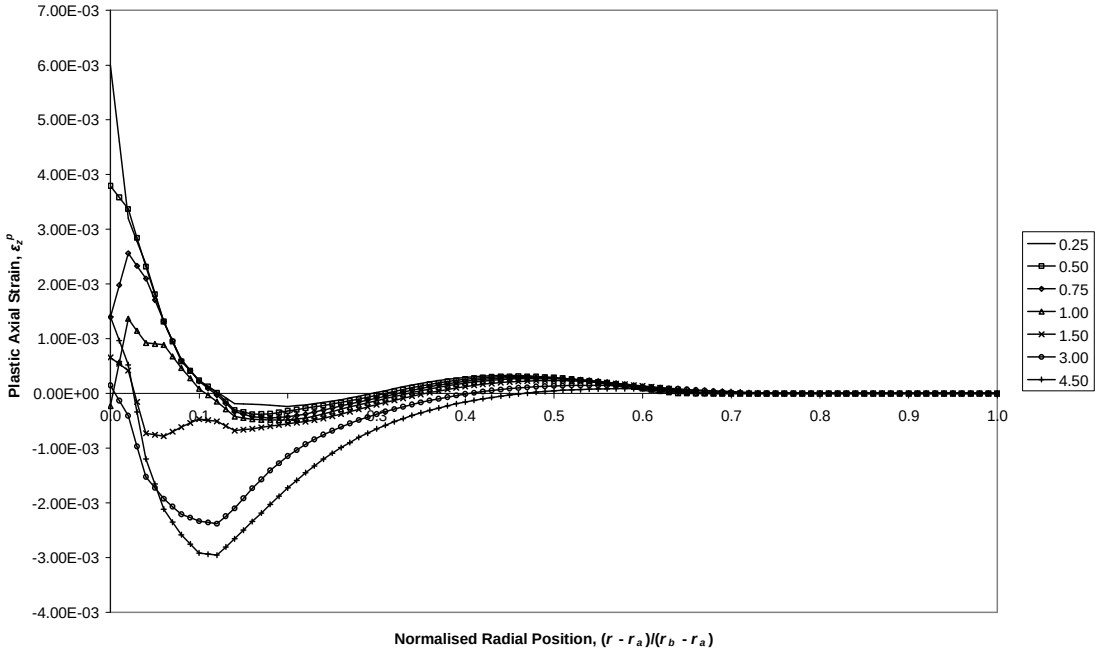

Figure 8.33: Residual Plastic Axial Strains, at mid-length, as Parallel Section Length, l_{ll}, varies

8.5.3. Discussion

As was expected, the longer the parallel section length, the greater the depth of overstrain (Figure 8.24).

Contact pressure (equal to $-\sigma_r$) was observed to decrease (Figure 8.25) as l_{ll} increased, due to the resultant widening of the yielded band. This decreases the relative stiffness of the portions of tube that immediately border the section of tube over the centre of the parallel section, reducing the radial support transferred by shear stress from these neighbouring portions.

Autofrettage hoop stresses (Figure 8.26) near the ID indicate greater shear loading for shorter values l_{ll} as the region generates a greater net outwards force. This may be compared with the observations made when the pressure band width was varied (sub-section 7.5.3). As observed for the contact pressures, the reduced relative stiffness of the neighbouring portions of the tube for longer values of l_{ll} reduce the transferral of radial force through shear stresses.

Autofrettage axial stresses (Figure 8.27) near the ID become more negative for short values of l_{ll}. This occurs because smaller radii of curvature arise (due to the outward deflection of the tube around the mandrel) for shorter l_{ll} causing greater compressive axial stresses at the ID.

Very similar residual hoop stresses are observed at the ID, apart from the shorter values of l_{ll} – indeed, the value of $l_{ll\text{-}0}$ seems optimum (that used in [9]). This appears to be due to the values of residual axial stress (σ_z) at the ID; from the von Mises yield criterion, the maximum residual hoop stress for a given residual equivalent stress is achieved when σ_z is the mean of σ_r and σ_θ. Table 8.5 compares the measured values of σ_z with the mean of σ_r and σ_θ; the closest match is observed when $l_{ll}/l_{ll\text{-}0} = 1$.

$l_{ll}/ll_{l\text{-}0}$	Residual Axial Stress, σ_z	Mean Residual Radial and Hoop Stress, $(\sigma_r + \sigma_\theta)/2$	% Difference, w.r.t. $(\sigma_r + \sigma_\theta)/2$
0.25	-0.8823	-0.5303	-66.38
0.50	-0.7826	-0.5542	-41.21
0.75	-0.6426	-0.5671	-13.32
1.00	-0.5028	-0.5649	10.99
1.50	-0.3781	-0.5485	31.06
3.00	-0.3464	-0.5413	36.00
4.50	-0.4193	-0.5524	24.09

Table 8.5: Residual Axial Stress Comparisons (stress values are normalised w.r.t. σ_{Y0})

The optimum value of l_{ll} is likely to depend on several factors such as tube wall ratio (K), mandrel slopes, mandrel-tube interference and material used.

The magnitude of residual hoop stresses (Figure 8.30), for the cases $l_{ll} = 3l_{ll\text{-}0}$ and $4.5l_{ll\text{-}0}$, in the region $0 \leq r_N \leq 0.3$ drop due to an increasingly positive peak in residual axial

stresses (Figure 8.31), resulting from compressive plastic axial strain. The plastic axial deformation occurs, for these cases, on the rear surface of the mandrel, due to the greater shear stresses that exist there for larger values of l_{ll}. The changes in residual hoop stresses decrease the summed residual compressive hoop force, lessening the efficacy of autofrettage.

8.6. PARAMETRIC STUDY 2 – FRICTION COEFFICIENT INVESTIGATION

8.6.1. Overview

The second parameter to be investigated was the coefficient of friction, μ, between the mandrel and the tube, for which a value of 0.015 had been used until this stage. According to the Coulomb model of friction used, the shear stress (σ_{rz}) at the surface when sliding occurs is given by Equation (8.1). This constitutes a boundary value for the shear stress field within the tube during the swaging procedure, hence the shear stress field will vary as friction coefficient is changed, in turn influencing the other stress components.

To achieve this, a series of swaging simulations were run between which μ was varied whilst all other parameters remained static and as determined by section 8.4. The following values of μ were used: 0, 0.015, 0.03, 0.045, 0.06, 0.12, 0.18 and 0.24.

8.6.2. Results

Autofrettage stresses are shown in Figure 8.34, Figure 8.35 and Figure 8.36, which respectively plot radial, axial and shear components through the tube wall.

Residual hoop and axial stress components are plotted in Figure 8.37 and Figure 8.38, respectively.

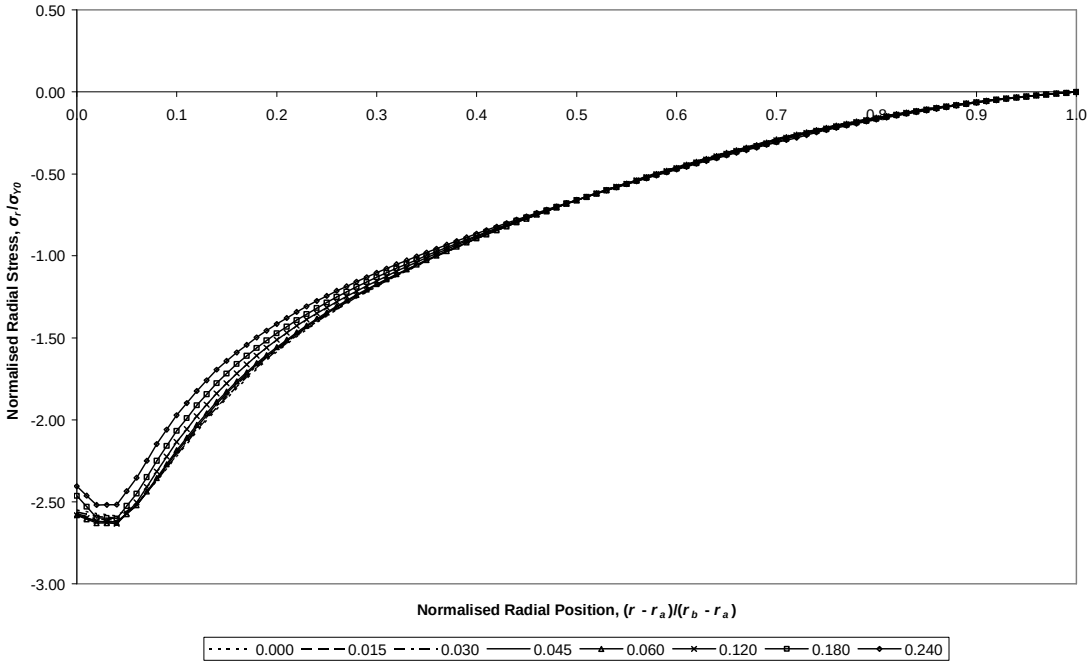

Figure 8.34: Autofrettage Radial Stresses, at mid-length, as Coefficient of Friction varies

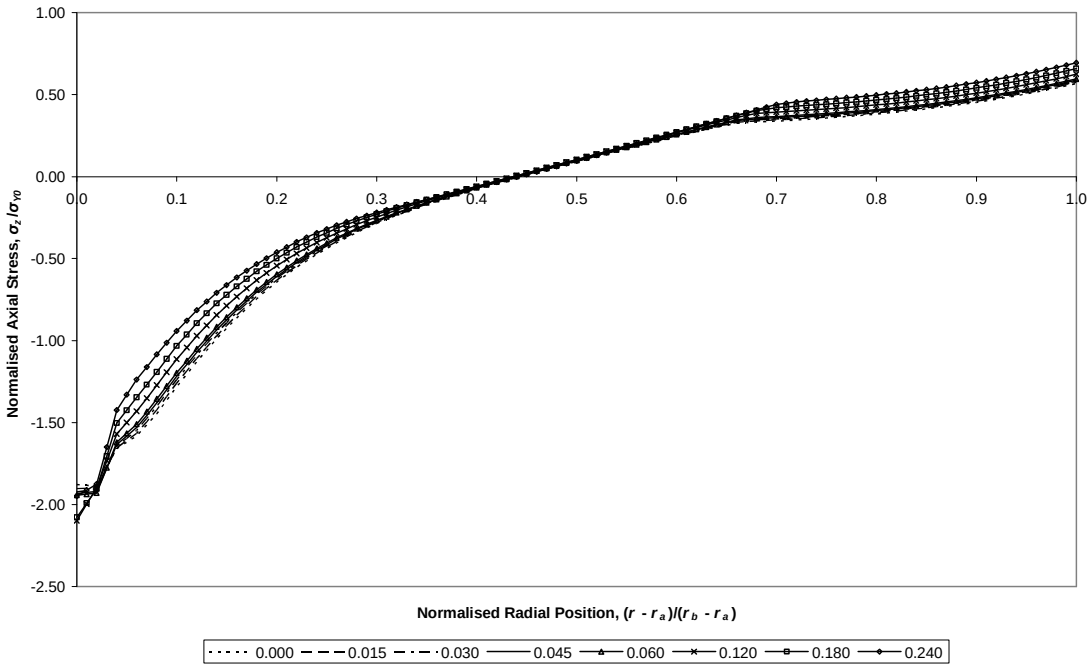

Figure 8.35: Autofrettage Axial Stresses, at mid-length, as Coefficient of Friction varies

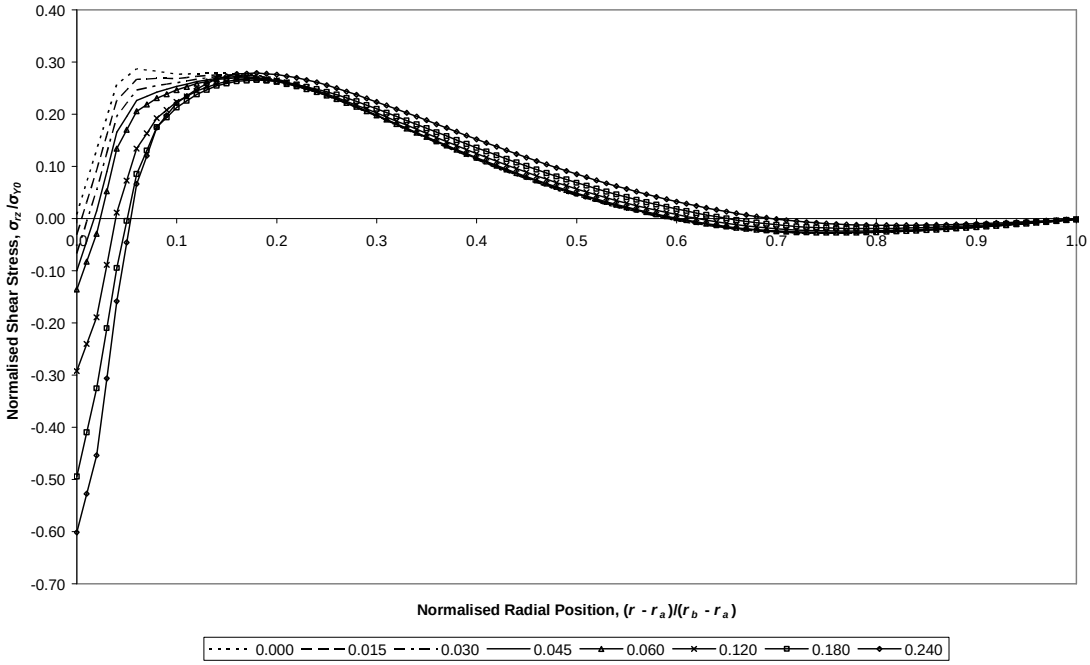

Figure 8.36: Autofrettage Shear Stresses, at mid-length, as Coefficient of Friction varies

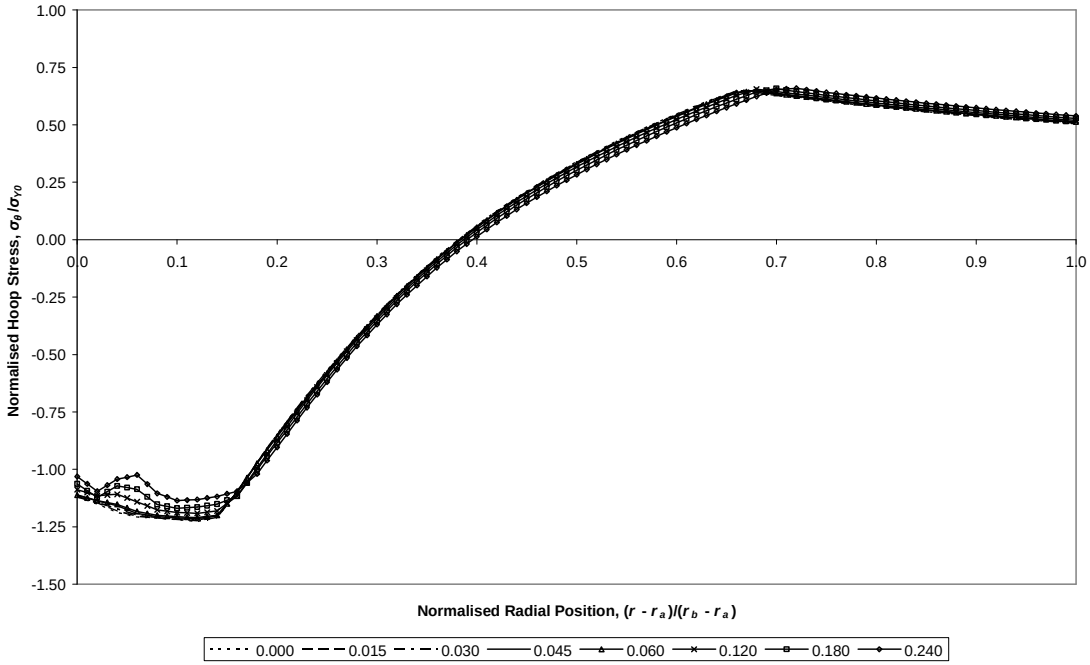

Figure 8.37: Residual Hoop Stresses, at mid-length, as Coefficient of Friction varies

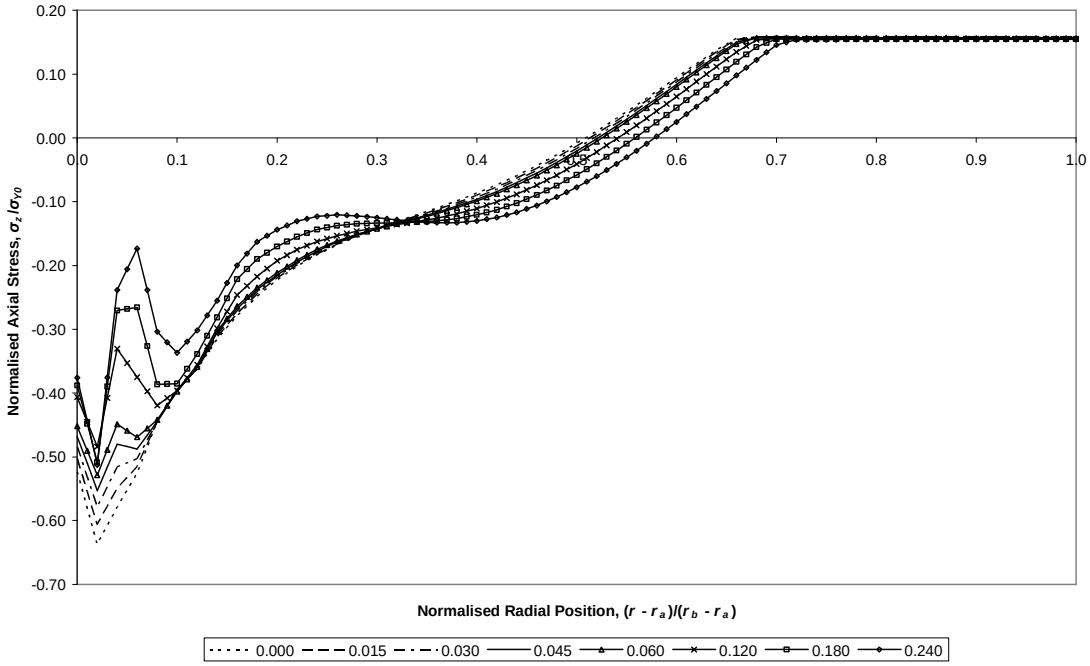

Figure 8.38: Residual Axial Stresses, at mid-length, as Coefficient of Friction varies

8.6.3. Discussion

The depth of overstrain increases slightly when friction coefficient is increased, most clearly seen as the radial position of the onset of constant axial stress in Figure 8.38, in the region $0.6 \leq r_N \leq 0.7$. This occurs because shear stresses do not directly cause outward deflection of the tube (the strongest influence on the depth of autofrettage), and only significantly vary near the ID; Figure 8.36 shows such variation effectively limited to $0 \leq r_N \leq 0.2$.

Radial (Figure 8.34) and axial (Figure 8.35) stresses during autofrettage show only small variation with change in the friction coefficient. Particularly, contact pressure (σ_r at r_a) remains relatively stable while friction coefficient varies. Axial stresses generally become more positive/less negative as friction coefficient increases, but follow a similar trend. This reflects the increased tensile axial load resulting from a greater frictional force.

The shear component of stress during autofrettage shows the greatest variation with change in friction coefficient. The magnitudes of shear stresses at the ID conform to the frictional stress between the mandrel and tube, which applies a boundary condition of $\mu\sigma_r$.

For the cases μ = 0.12, 0.18 and 0.24, a drop in magnitude of residual hoop stress is observed for $0.02 < r_N < 0.17$. This is caused by a similar pattern observed in the residual axial stress distribution in the same region; to maintain a similar equivalent stress, the differences between stress components must also remain similar. Hence, for

a largely static radial stress, when axial stress increases, so must hoop stress. The fluctuation in axial stress in the tube is likely due to the step change in contact friction that occurs when the mandrel breaks contact with a given point on the tube.

8.7. PARAMETRIC STUDY 3 – MANDREL SLOPE INVESTIGATION

8.7.1. Overview

The third set of parameters to be investigated was the forward and rear slopes of the mandrel, for which initial values of 1.5° and 3.0°, respectively, had been used until this stage. The slopes of the mandrel determine the rate of change of deflection w.r.t. axial position which directly affects shear stresses in the deflected region. Shear stresses in turn influence the other stress components.

To achieve this, a series of swaging simulations were run between which a scaling parameter *PFR* was varied whilst all other parameters remained static and as determined by section 8.4. The original slope values of 1.5° and 3.0° (forward and rear) were multiplied by *PFR*, for which the following values were used: 1/3, 2/3, 1.0, 1.5, 2.0 and 2.5.

PFR	**Forward Slope (°)**	**Rear Slope (°)**
1/3	0.5	1.0
2/3	1.0	2.0
1.0	1.5	3.0
1.5	2.25	4.5
2.0	3.0	6.0
2.5	3.75	7.5

Table 8.6: Mandrel Slopes for the range of Scaling Factors (*PFR*) used

8.7.2. Results

Autofrettage stresses are shown in Figure 8.39, Figure 8.40, Figure 8.41 and Figure 8.42, which respectively plot radial, hoop, axial and shear components through the tube wall.

Residual hoop and axial stress components are plotted in Figure 8.45 and Figure 8.46, respectively.

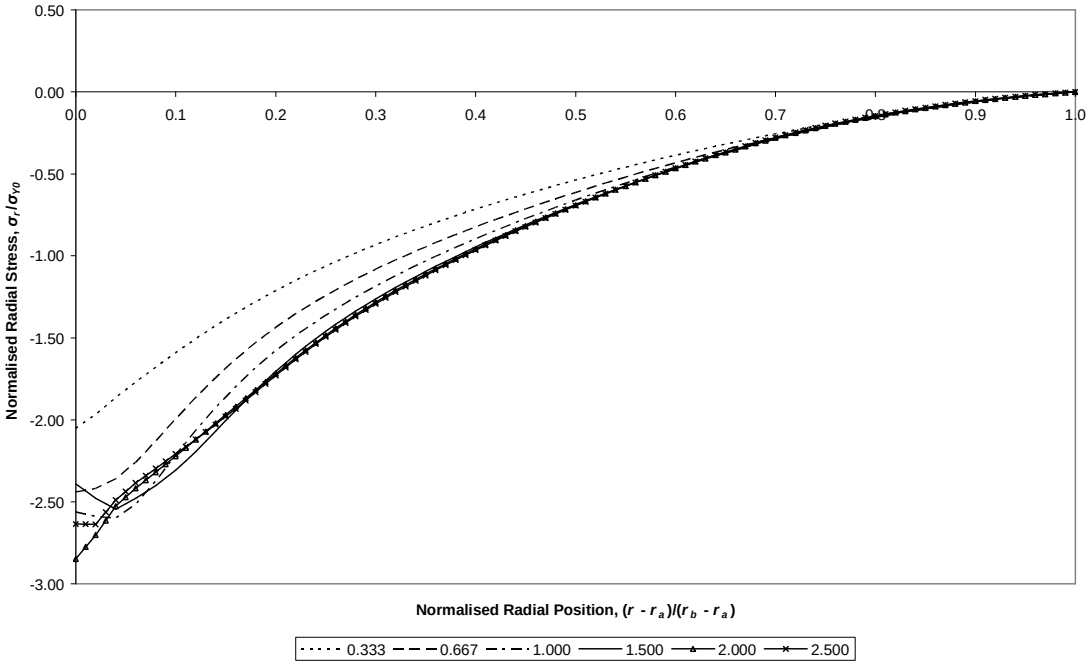

Figure 8.39: Autofrettage Radial Stresses, at mid-length, as Slope Scaling Factor varies

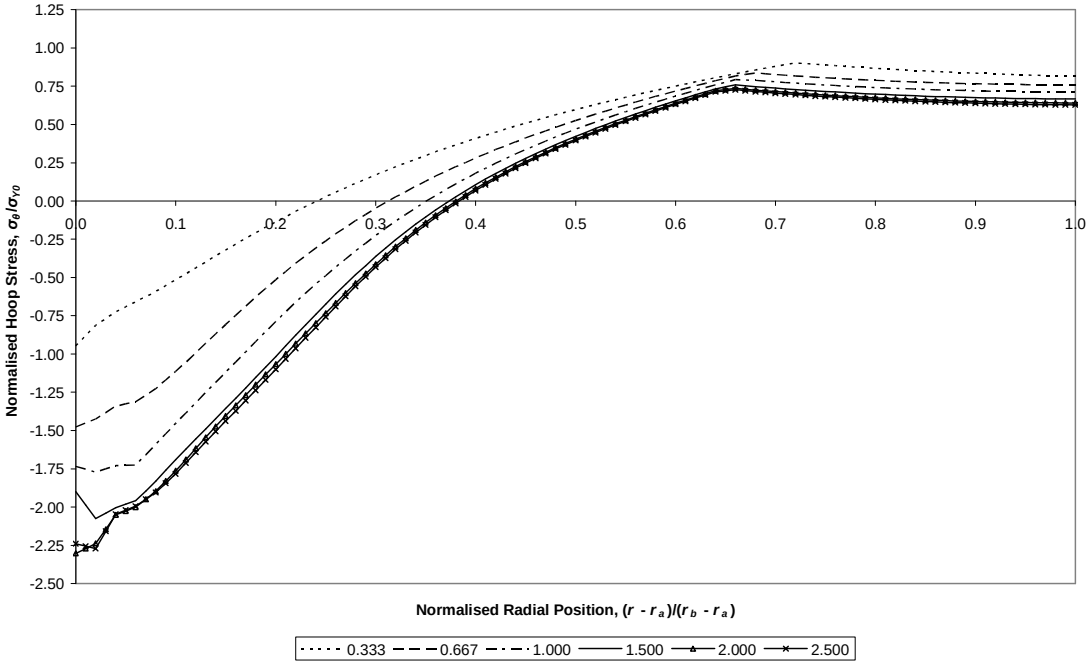

Figure 8.40: Autofrettage Hoop Stresses, at mid-length, as Slope Scaling Factor varies

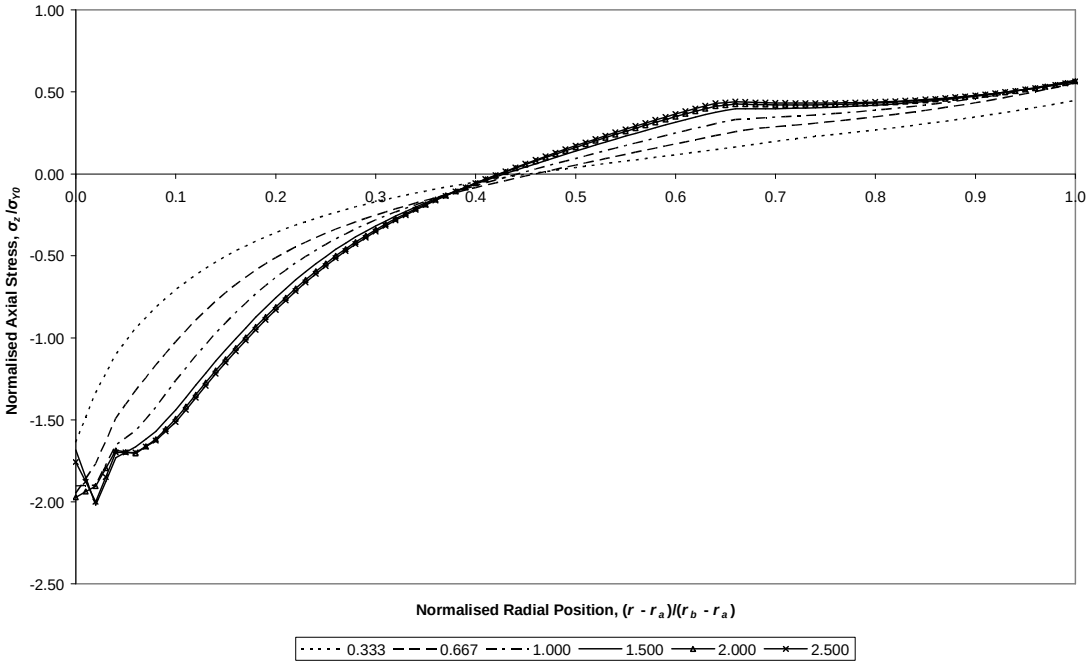

Figure 8.41: Autofrettage Axial Stresses, at mid-length, as Slope Scaling Factor varies

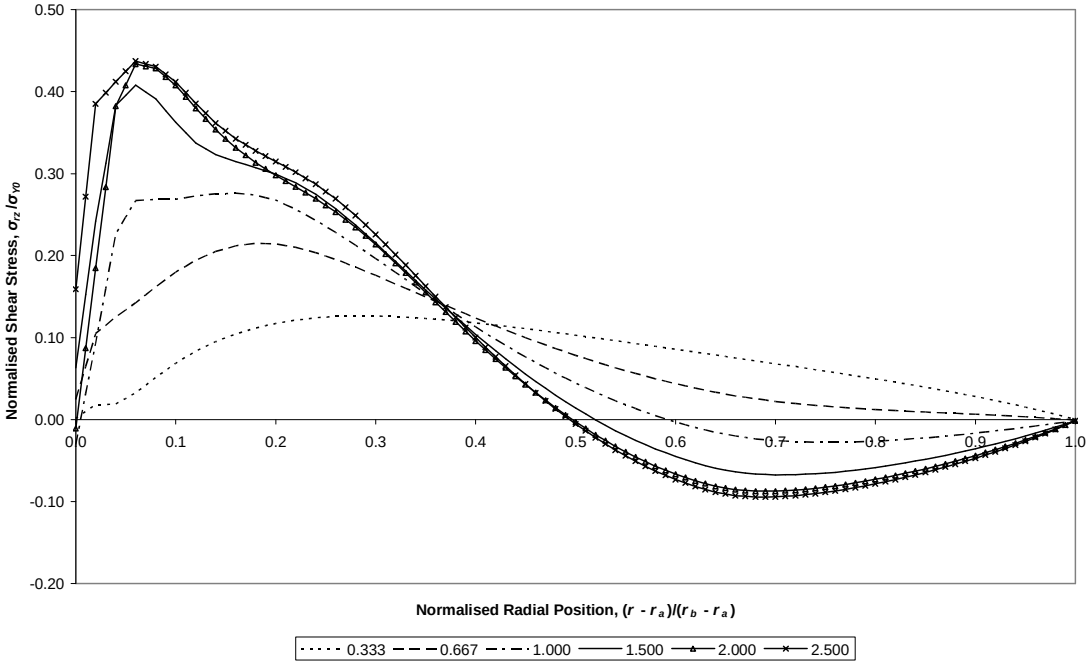

Figure 8.42: Autofrettage Shear Stresses, at mid-length, as Slope Scaling Factor varies

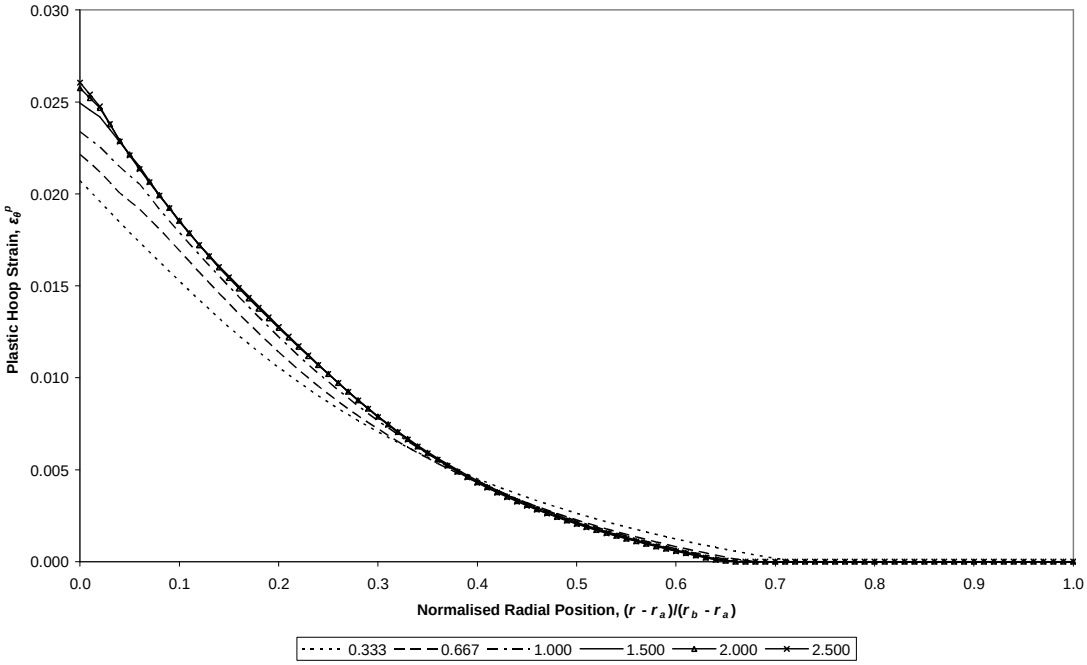

Figure 8.43: Autofrettage Plastic Hoop Strains, at mid-length, as Slope Scaling Factor varies

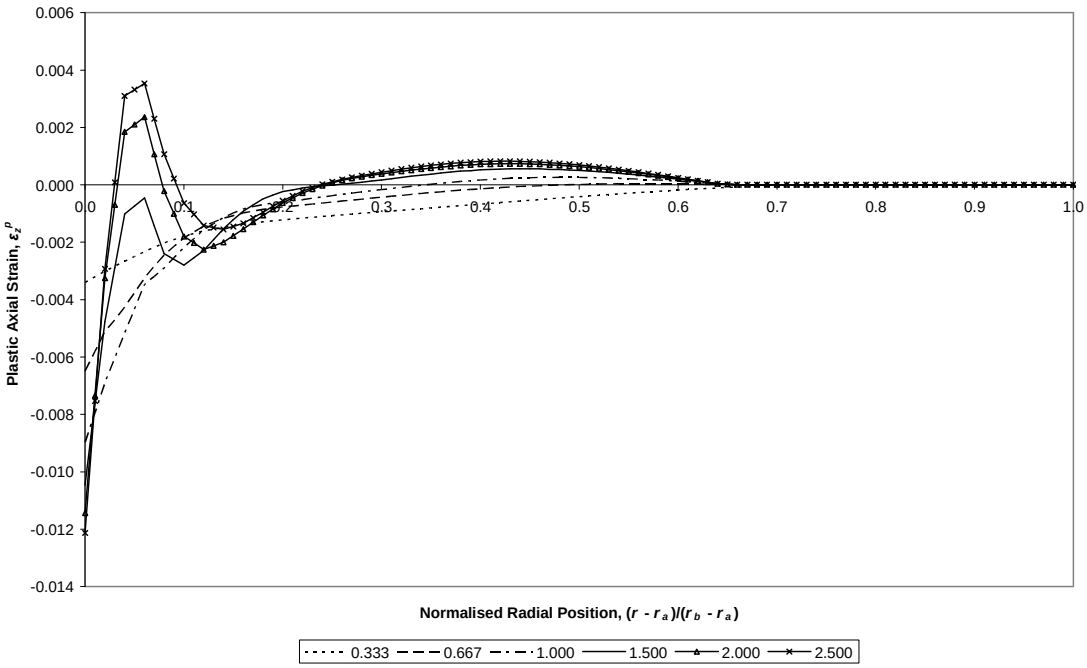

Figure 8.44: Autofrettage Plastic Axial Strains, at mid-length, as Slope Scaling Factor varies

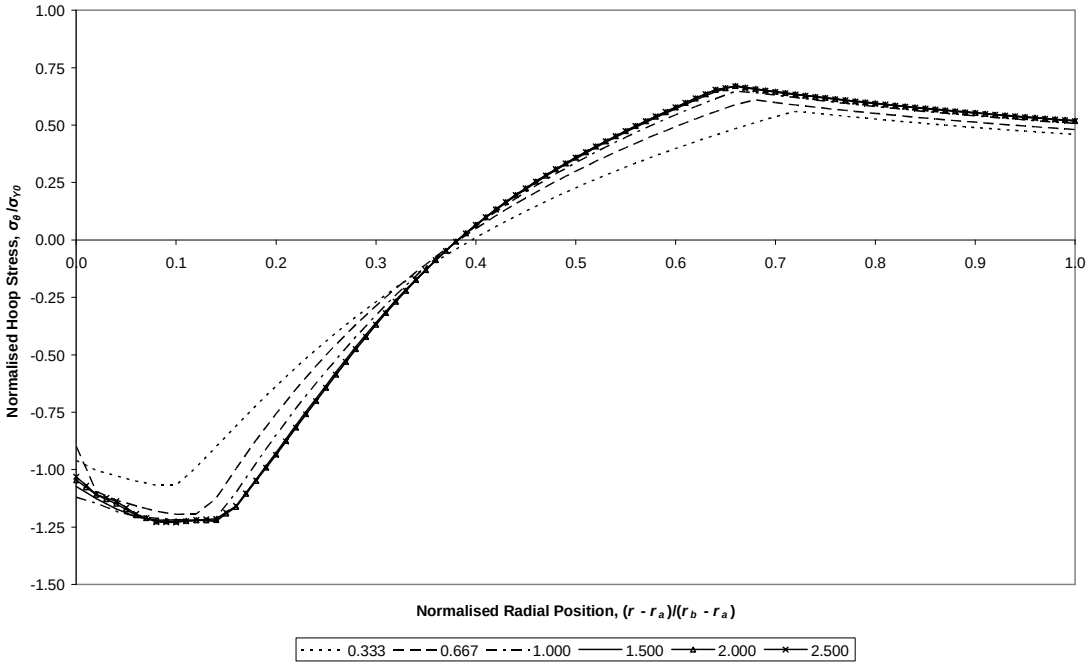

Figure 8.45: Residual Hoop Stresses, at mid-length, as Slope Scaling Factor varies

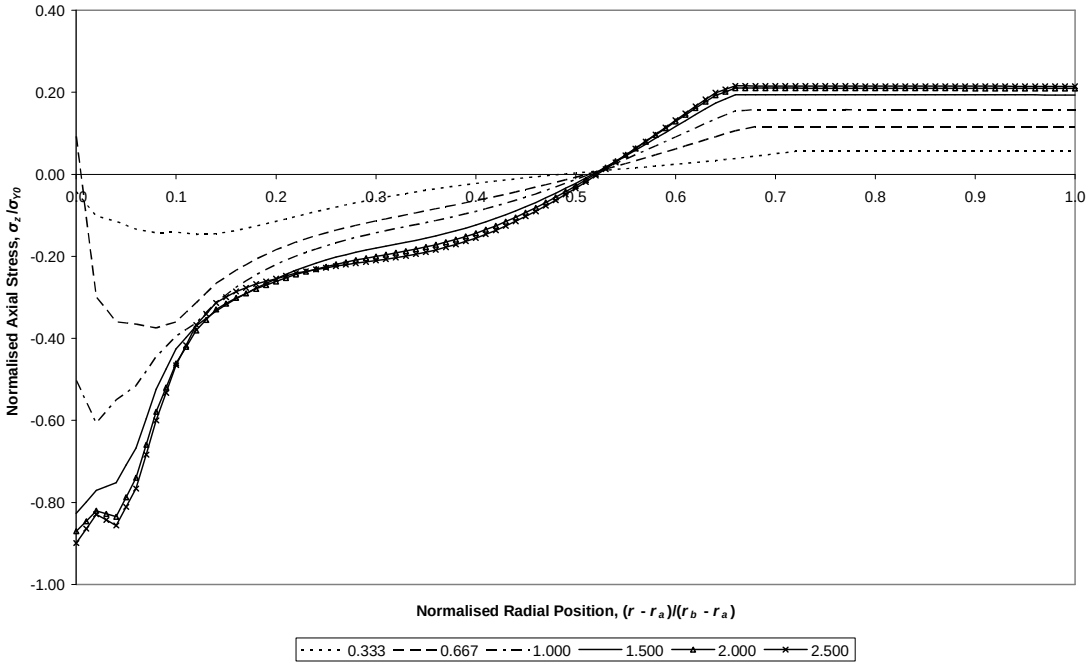

Figure 8.46: Residual Axial Stresses, at mid-length, as Slope Scaling Factor varies

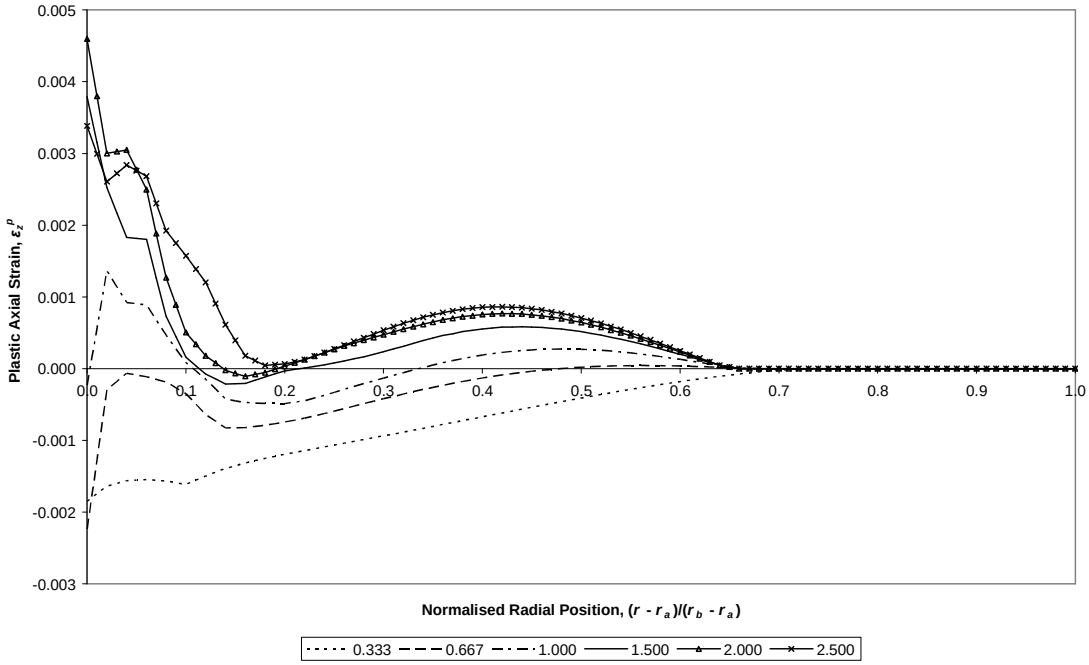

Figure 8.47: Residual Plastic Axial Strains, at mid-length, as Slope Scaling Factor varies

8.7.3. Discussion

Figure 8.39 shows the contact pressure (radial stress at r_a) increases as the mandrel slopes increase. This is due to the greater length of tube that is deflected by mandrels whose slopes are shallower, which in turn reduces the inward loading of the tube over the parallel section of the mandrel by the neighbouring regions (via shear stresses). Figure 8.42 shows the intensity of shear stresses decrease with mandrel slope angle.

Figure 8.40 shows that the degree of overstrain (given by the radial location of the peak hoop stress in the upper-right quadrant) increases as mandrel slopes decrease, and Figure 8.43 also shows the plastic hoop strains increase towards the ID as mandrel slopes increase; both result from the more intense shear stresses present, exerting an inwards force on the tube around the mandrel parallel section, when greater mandrel slopes are used.

In addition, hoop stresses (Figure 8.40) become more negative around the ID as the mandrel slopes increase, another indication of the inwards loading by shear stresses (compare with discussion of hoop and shear stresses for the Band of Pressure model, in sub-section 7.5.3).

Shear stresses, shown in Figure 8.42, show a marked difference compared to those observed during the friction coefficient investigation (Figure 8.36). This highlights the difference between those shear stresses arising mostly due to friction, and those largely developed due to axial variation of radial deflection.

Residual hoop stresses (Figure 8.45) were observed to be static except in the PFR = 1/3 and 2/3 cases, when the magnitude decreased. This coincided with residual axial stresses becoming less negative (Figure 8.46), limiting the residual hoop stress that may be developed for a given equivalent stress.

Figure 8.46 shows significant variation of residual axial stresses near the ID, especially for shallower slope values, resulting from different degrees of plastic axial strain (Figure 8.47) that had previously occurred in the region. Comparison with plastic axial strains developed during the initial loading of the tube (Figure 8.44) reveals that the variation of axial stresses is largely due to the axial deformation that occurs as the tube unloads from its loaded state.

8.8. SUMMARY

Generally, a good match was achieved with O'Hara's results; for the case of the most similar mesh to that used in O'Hara's analysis, strong likeness was observed between the stress distributions calculated by the two models. This indicates the relevant aspects of the swage model developed by O'Hara were incorporated into the ANSYS model. The finer meshes generate results that follow the trends displayed by O'Hara's, and converge relatively quickly; a mesh of effectively four times the linear density of that used by O'Hara was judged to produce suitably accurate results.

A tube length of $15r_a$ was found to allow stable mid-length results to be obtained; an initial number of $10El_{N\text{-}Ax}$ sub-steps, with upper and lower limits of $20El_{N\text{-}Ax}$ and $2El_{N\text{-}Ax}$, respectively, was found to give suitably consistent results while remaining computationally feasible.

The length of the parallel section specified for the mandrel had a significant impact on axial stress and plastic strain profiles within the tube, both during and following the swaging procedure. It was found that the initial value of $l_{ll\text{-}0} = 0.12r_a$ used by O'Hara gave the best degree of pre-stressing (compressive residual hoop stresses near the ID), although pre-stressing values are relatively consistent apart from the longer parallel section cases ($l_{ll} = 3.0l_{ll\text{-}0}$ and $4.5l_{ll\text{-}0}$). The optimum value for a given mandrel-tube system is likely to depend on several factors such as tube wall ratio (K), mandrel slopes, mandrel-tube interference and material used.

Mandrel slopes were also found to have a large influence on the developed stresses. Both effect the initial deformation of the tube (the forward slope has the greatest influence, as its shallower slope deforms a greater length of tube), but the rear slope more directly influences residual stresses due to its creation of residual compressive axial stresses near the ID. Investigation of the effect of the forward and rear mandrel slopes independently would reveal more details of these relationships.

No investigation was made of the effects of mandrel-tube interference on the development of residual stresses, as analysis of the influence of other properties was felt to be more beneficial for the understanding of the swage autofrettage process. Investigation of the precise effects of varying interference would be a suitable topic for future study, especially with the addition of an accurate material model.

9. DISCUSSION

9.1. OVERVIEW

When this study commenced, the process of autofrettage was relatively unexplored in terms of finite element analysis. The two distinct phases of hydraulic autofrettage allow it to be more easily tackled (via super-positioning) than the single continuous process of swage autofrettage, which is reflected by the distribution of models developed for the two methods.

A number of analytical models of hydraulic autofrettage existed, although each was limited by the simplifying assumptions which had been incorporated into it. Crucially, accurate material representation was often not possible, which was of particular importance when calculating residual stresses; the materials often used for high pressure vessels typically display significant non-linearity when unloading from prior plastic strain.

Several numerical models of hydraulic autofrettage had also been developed, mostly more general in their application than analytical methods. In addition, adoption of numerical means of solution made it possible to introduce accurate material behaviour into models.

Despite this, swage autofrettage had not been modelled with accurate material behaviour, particularly non-linear unloading (Bauschinger effect); the progressive nature and axial variation of the swaging process, the inherent shear stresses that result and the contact between the mandrel and tube all conspire to make the process non-trivial to model. The only openly published investigation of swage autofrettage, modelling only a single case, was that by O'Hara [9], which modelled the material as subject only to simplistic bi-linear kinematic hardening.

Once an initial review of existing methods had been made, early work (Chapter 3) centred on the implementation and adaptation of the Tresca elastic-plastic solution, and assessment of existing models of hydraulic autofrettage that would be suitable for comparison with FE-based models of the same that would subsequently be developed. Once this was accomplished, research efforts shifted to the development of a series of FE models.

Throughout the different stages of development, an FEA package (ANSYS) was progressively applied and verified for a series of hydraulic autofrettage scenarios. In the first (Chapter 4), the structural models for a set of tube sections under a range of end conditions were developed, using a simplistic bi-linear kinematic hardening material. This allowed the constraint sets to be developed, and the relative error due to mesh fineness to be investigated.

Two methods of modelling accurate material behaviour were then investigated, to replicate the significant non-linearity exhibited by relevant steels when unloading from

prior plastic strain. The first model (Chapter 5) was quasi-elastic, which allowed the desired stress-strain response to be obtained by iterative alteration of elastic properties; this worked well in the context of hydraulic autofrettage due to the discrete loading/unloading cycle. However it was recognised that due to its elastic nature the material representation could not calculate residual stresses resulting from swage autofrettage.

Instead a material routine (USERMAT) was customised (Chapter 6), allowing direct control over the stress-strain state and plasticity. This is applicable in both hydraulic and swage autofrettage, and was verified against both spreadsheet data in a uni-axial test, and against an existing numerical method in hydraulic autofrettage comparisons.

A swage-like model was then developed (Chapter 7), in which a band of pressure (both static and moving) caused the plastic deformation required for autofrettage. This allowed the effect of a shear component on the stress field to be investigated, in the absence of frictional effects and without the complexity of a contact analysis. The understanding gained would then be useful when interpreting the results generated during simulations of swage autofrettage.

Finally a full model of swage autofrettage was developed (Chapter 8), which included a deformable mandrel. After sensitivity analyses were completed, it was used in a series of parametric analyses to investigate the effects of several properties on the resultant autofrettage and residual stress field.

9.2. CONFIDENCE LEVELS

For any analysis that is made, it is of crucial importance to assess the different sources of imprecision so that an objective judgement may be made as to the level of confidence in which conclusions drawn from the results should be held. The principle sources are addressed below.

9.2.1. Suitability of Analysis Tools

It is felt that the case for the use of numerical methods was clearly made in the opening chapters of this thesis, so only the suitability of the selected tools is addressed here. Aside from initial implementation of the Tresca elastic-plastic hydraulic autofrettage case within Matlab, all numerical analysis presented within this thesis was conducted within ANSYS and a spreadsheet application (Microsoft Excel). Both Matlab and Microsoft Excel were readily available, which is the primary reason for their initial selection for use.

The conditional operators present within the Matlab programming language provide all the features required, for example to detect yield; coupled with the graphing

capabilities also present, it makes Matlab a rational choice. Use of a spreadsheet application allows for rapid and interactive manipulation of output values, as well as the implementation of some hydraulic autofrettage models.

The choice of the finite element method, as opposed to other numerical methods, is still thought to be appropriate. The presence of non-plane deflection during swage autofrettage would make the use of a finite difference model arduous at best, especially given the progressive nature of the process. The boundary element method could have been employed, with the possibility of reduced solution time. However, the requirement for non-linear material behaviour would probably have eliminated this potential advantage, and it is not known what the effect of the mandrel-tube contact would have had on model preparation. Finally, relatively few BEM tools are available, which would have likely required manual preparation of structural equations – time consuming and potentially error prone. Compare this with finite element tools, of which several well-developed examples are readily available. This makes choice of the finite element method sensible, as it allows low level structural modelling to be conducted by the software package; this in turn reduces the development cost of modelling different geometries.

After extensive use of ANSYS, it is the author's opinion that it was a suitable FEA package for the prosecution of the goals of this research. The combination of both GUI operation and scripted batch running allow for rapid model development and refinement, and the internal post-processing tools allow results to be extracted with reasonable convenience. The ability to create UPFs added the crucial flexibility that was required to simulate general non-linear material behaviour. While other FEA packages may all offer some, or maybe all, of these features, it is felt that they would not have been more suitable for this research than ANSYS.

9.2.2. Applicability of Models and Boundary Conditions

More fundamental than concerns of precision, it must be ensured that the modelled case accurately reflects the true conditions of the physical case that is considered. In addition, it is essential to assess whether the physical case is useful.

The three sets of autofrettage models which were created are enumerated and addressed below, based on the above.

9.2.2.1. Hydraulic Autofrettage Models

The four hydraulic autofrettage models consist of three general plane strain cases (Plane Strain, Open- and Closed-Ends) and the Plane Stress case. The Plane stress represents a thin sheet, and as such the modelled geometry is close to that in which the considered conditions would apply. The general plane strain cases instead model the mid-length position of the tube, but only the Open-Ends case would experience any

significant axial variation during autofrettage, due to the short portions at each end of the tube not subjected to the applied pressure. Even then these end sections would be removed from the finished tube, practically eliminating any axial variation.

As such, all four cases are felt to represent their respective end conditions. Of the four, it is considered that the Open- and Closed-Ends conditions most closely reflect actual conditions generated during hydraulic autofrettage process, as they would be most practically sealed.

9.2.2.2. Band of Pressure Model

As described in Chapter 7, the Band of Pressure model was not intended to be truly representative of a real autofrettage. Instead, it was developed to allow swage-like loading to be investigated prior to the creation of a swage model. In this role, it was fit for purpose.

9.2.2.3. Swage Model

Conceptually, the swage model may simulate the swage autofrettage of any axi-symmetric tube, and if so needed it could be expanded into a three-dimensional model to allow a non-axi-symmetric tube to be modelled. The mandrel profile used was that described by O'Hara [9], but may be easily adjusted to whatever shape is desired. Two features of O'Hara's model were omitted: the tapers at the ends of the ID, and the ram that was used to drive the mandrel. The reasons for their omission are explained in Chapter 8, and the author still deems this to be a suitable decision as they had negligible impact on mid-length stresses and strains.

As noted in the description of swage autofrettage in Chapter 2, it differs substantially from hydraulic autofrettage due to the large amount of axial variation present, in addition to shear stresses and friction. This required the length optimisation documented in Chapter 8, to ensure the mid-length properties recorded were representative of the conditions found along the central band that would be retained following post-autofrettage machining.

Although every effort has been made to ensure the materials data used were accurate, they are often proprietary in nature and hence are not necessarily fully accurate. However, the parametric nature of the model means that it can be rapidly adjusted to reflect new parameter values so this is not a major problem. Overall, it was felt that the model is reasonably representative of real world swaging conditions.

9.2.2.4. Overview

The hydraulic and swage autofrettage models, and their boundary conditions, are both felt to be suitably representative of their respective processes, although it is recognised

that in each case the models could be refined with process-specific information. Such refinement could be accomplished rapidly, given the nature of the models, once precise conditions are known.

In particular, post-autofrettage material removal from the ID has not been addressed in these studies; hence residual stresses presented here are not fully representative of those in finished vessels. Generally only a small amount of material is removed, so large changes in residual stresses are unlikely unless a substantial change of reverse yield stress occurs over the removed region. The cases presented in this thesis utilise either a bi-linear kinematic hardening material or the A723 fit, both of which feature a consistent reverse yield stress near the ID; as such, it is thought that material removal would cause only a small change in the presented residual stresses.

9.2.3. Precision

Although defects exist in all pieces of software, the author is aware of no errors in ANSYS, Matlab or Microsoft Excel that would compromise the accuracy of results generated by them, aside from the limits of numerical precision. It is impractical to fully assess the effects of numerical precision (or to alter them), but it is felt that they would remain very small even after many stages of calculation.

However, several aspects of the way the different software packages are used do affect the precision of results generated; these all affect only the use of ANSYS. Neither Matlab nor Excel were used in iterative processes, which could allow errors to accumulate, so the accuracy of the CPU is likely the limit of precision (typically 80 bits for floating point calculations for modern CPUs).

9.2.3.1. Meshing

For both autofrettage models, mesh sensitivity tests were conducted to ensure sufficient accuracy while minimising solution times. Were computing resources unlimited, a near infinite number of elements would have been used which would have allowed near perfectly accurate solutions of the posed problems to be gained. This is not the case, however, hence the requirement for the sensitivity tests.

For the hydraulic case, a mesh of 100 radial elements was selected for the general plane strain cases, and a mesh of 1500 radial elements for the Plane Stress case. This keeps relative errors of hoop stresses at the ID (both at peak pressure and residual) well within 0.5% for the general plane strain cases, and approximately an order of magnitude smaller for the Plane Stress case. For the comparisons specific to the Plane Stress case, summed axial stresses become a tiny portion of σ_{Y0} at the selected mesh size (relative error is exaggerated as axial stresses are converging to zero).

The relative error of residual hoop stresses in the swage case (Figure 8.11) shows a similar trend to that observed for the hydraulic case but the magnitude of the errors is larger. In part this is due to the comparatively lower number of radial elements present; the highest number used in the swage model was 73, meaning the stress field is not sampled as accurately. It is felt, based on the error trend observed, that the error of the selected case (42 radial elements) is within 1-2% of a high accuracy mesh (for example, using 200 radial elements). While higher than the hydraulic case, it was felt that this was acceptable as the plots of residual stresses through the wall at mid-length rapidly converge when plotted (Figure 8.7 to Figure 8.10).

9.2.3.2. Material Modelling

It is considered that the translation of the material-fit into the necessary Fortran code would not have caused noticeable error, since the same stages of calculation would be required whatever the method used. In addition, double precision functions were used throughout.

As the calculated stresses depend on the strain increments that are supplied as inputs to the material sub-routine by ANSYS, for the correct stresses to be calculated the correct strains must first be supplied. As this may only be indirectly controlled (via the Jacobian matrix that is returned to ANSYS by the material sub-routine), all that can be ensured is that the stresses returned are correct for the given strain input. This is demonstrated by the uni-axial test presented in Chapter 6, so this is not thought to be a meaningful source of error.

9.2.3.3. Reliance on Results

The hydraulic autofrettage results presented in this thesis are compared with equivalent data from independently validated models, providing appropriate validation of the FE-based hydraulic autofrettage model described in Chapters 4-6.

However, the only means of comparison for the swage model was the single set of data produced by O'Hara, and, indirectly, the Band of Pressure model. Although this is not desirable, the use of the bi-linear kinematic material within the swage model allowed it to be compared with O'Hara's results; strong similarity was observed, particularly in the notable differences between axial stress values obtained for swage autofrettage compared to those resulting from hydraulic autofrettage.

Both sets of swage results were obtained using FEA, but different packages were used (ANSYS and ABAQUS) on very different computer platforms, and the two models were developed independently, separated by more than a decade. For this reason, it is felt reasonable to consider the swage model with some level of confidence. A more thorough validation will be possible once the USERMAT is correctly adapted to the latest ANSYS and Fortran compiler pairing, allowing accurate material behaviour to be

modelled; these results would then be suitable for comparison with empirical data of measured residual stresses.

9.3. COMPUTING ISSUES

While the issues listed below only indirectly affect the research presented in this thesis, they are considered relevant to its review.

9.3.1. ANSYS

While ANSYS will run on most modern PCs, the solution time is heavily dependent on CPU speed, size of physical memory and hard disc speed. Aside from raw processing capability, it is crucial to store the structural matrices within the PCs physical memory (termed "in core" by ANSYS) to ensure calculations proceed at the maximum rate. Beyond this, it is highly beneficial if the PC possesses sufficient physical memory to cache the results file(s) to minimise the amount of data that must be read from the hard disc. In addition, a fast hard disc (or array thereof) will allow all disc writes and any non-cached reads to be more rapidly accomplished. It was found that the results files placed the greatest restriction on the mesh fineness that could be used in the swage case; when they became too large to be satisfactorily cached within physical memory, solution time became prohibitively long.

The author found great benefit, especially when running the swage model, from increases in physical memory. The desktop machine, used initially, possessed 1 gigabyte (GB) and ran the hydraulic cases easily, but the band of pressure and swage models placed great demands on physical memory making it impractical to use the machine for other tasks. Instead, workstations with 2 GB of physical memory, and a server machine with 16 GB of physical memory greatly expedited solution.

9.3.2. Principles of modelling in ANSYS

The models presented in this thesis were initially developed using the ANSYS graphical user interface (GUI). The "log" files (containing sequences of APDL commands) generated by these operations were then revised and adapted (crucially, to introduce variable substitution.) such that they could subsequently be read by ANSYS to repeat the simulation. This allows parametric models to be interactively developed, modified and run.

9.3.3. Efficiency of computing

At all stages, efforts were made to make the developed models most efficient computationally, so that they could be run rapidly, parameters could be iterated, and to allow maximum scalability. Primarily this was achieved by the use of axi-symmetric sections, reduction of section lengths while maintaining mid-length properties with appropriate boundary conditions, and mesh sensitivity analyses.

9.3.4. Customisation of material model

The apparent simplicity of the customised USERMAT model presented in Chapter 6 belies the complications that were encountered during its development. The development was conducted incrementally, as the process of developing a UPF is sparsely documented and many aspects had to be explored and deciphered. When the material did not behave as expected (which occurred many times), debugging was a lengthy task as it was often not apparent whether an error had been made or a variable had been mis-specified or wrongly configured.

Once completed, however, the benefits of the customised USERMAT relative to the EMPRAP were plain: not only was it possible to use a custom material in an analysis other than hydraulic autofrettage, but solution was achieved far more rapidly as one level of iteration was removed.

9.4. SIGNIFICANCE OF FINDINGS

As was discussed in Chapter 2, hydraulic autofrettage has already been well investigated; in light of this, the main significance of the findings from this study relate to swage autofrettage. The swage model developed during this study has the ability to predict residual stresses for any combination of mandrel and tube geometries, and contact parameters. Following a small amount of additional work, it will also be possible, via the customised USERMAT model, to include realistic material behaviour for any stress-strain profile.

The “band of pressure” model, although not directly reflecting a real world process, provided some significant insights. It was interesting to note that for the narrowest pressure band, compressive residual axial stresses were developed on the ID at the mid-length position, as was observed in the swage cases modelled. This happened because of the tensile axial deformation that occurred at the edges of the narrowest band of pressure; normally the compressive axial deformation that takes place mid-band prevails, leaving tensile residual axial stresses.

During swage autofrettage, an analogous process to this takes places over the rear surface of the mandrel. Large compressive axial stresses are observed at the ID of the

tube as the centre of the parallel surface of the mandrel passes (which would otherwise cause a tensile residual axial stress). Compressive residual axial stresses are favourable as they reduce the magnitude of tensile axial stresses seen in use, helping to prevent circumferential cracks opening around the ID, thereby increasing fatigue lifetime.

In addition, a compressive residual axial stress half the magnitude of the (compressive) residual hoop stress allows for a greater residual hoop stresses by reducing the magnitude of the difference between stress components, which in turn determine the von Mises equivalent stress.

This suggests that the rear surface of the mandrel is of critical importance in the development of favourable residual stresses.

A parallel section length of $0.12r_a$ does indeed seem to generate an optimum distribution of residual hoop stresses; the value at the ID possesses the equal highest magnitude, and that value is retained through the inner ~15% of the tube wall.

It appears that minimising the coefficient of friction between the mandrel and tube is generally beneficial; residual hoop stresses are predicted to be slightly degraded when a large coefficient is used, and increasing the friction coefficient would only increase the required driving force.

The magnitude of the slopes on the mandrel were observed to have a greater effect on the stress field developed; increasing the slopes (both front and rear) caused an increase in mandrel-tube contact pressure, and a decrease in the depth of overstrain. Residual hoop stress experienced a slight drop in magnitude when the slope scaling factor decreased below one; conversely, residual axial stresses near the ID became significantly more negative as the slope scaling factor increased.

9.5. FUTURE WORK

This programme of work has achieved its primary goals of developing a method for determining the residual stress distribution resulting from swage autofrettage. Below are listed a number of areas of future work which would usefully expand the scope of this study.

9.5.1. Develop USERMAT

Despite the author's best effort, it was not possible to combine the USERMAT with the swage model, as the swage investigations were conducted following the upgrade to ANSYS v11 and the required Intel Visual Fortran compiler. Continued development of the USERMAT is hence the first piece of suggested future work; it is the author's opinion that the material model is viable, but some unforeseen change in behaviour of the UPF scheme has occurred between versions.

Although impossible to predict, given the awkward environment in which debugging must be conducted, it is felt that a working USERMAT could be achieved relatively rapidly building on the work done so far.

A further feature that could be added is temperature dependence, which would allow thermal treatments of autofrettaged vessels to be investigated.

9.5.2. Model further Materials in USERMAT

Once the USERMAT is altered to work with the current ANSYS version, altering the material profile modelled by it would be the author's next recommendation. This would demonstrate the ability of the USERMAT to be adapted to reflect arbitrary material behaviour, and hence the ability of ANSYS to accurately model both the swage process and candidate materials.

9.5.3. Optimisation of swage parameters

With the two above items accomplished, it would then be possible to make a detailed assessment of the precise influence of various parameters on the residual stresses developed during swage autofrettage. These could include mandrel shape, friction coefficient and autofrettage sequence (i.e. multiple passes of the mandrel).

9.5.4. Effect of machining

Finally, the effect of machining and material removal could be investigated, allowing the residual stresses within finished articles to be assessed. This has not been previously modelled.

10. CONCLUSION

The following are the key conclusions arising from the work presented in this thesis.

10.1. CONCLUSIONS FROM CHAPTER 3

A review of material models was made, with emphasis on response to plastic strain. The Tresca elastic-plastic solution was then implemented and subsequently adapted to reflect some of the plastic strain responses previously identified. Finally, the solution was extended to include an interference fit with a solid, elastic, cylinder within the tube's ID.

A review of analytical and numerical models suitable for comparison with future models of hydraulic autofrettage was then made.

10.2. CONCLUSIONS FROM CHAPTER 4

Models of hydraulic autofrettage under four end conditions (three general plane strain, and a Plane Stress model) were developed; sensitivity tests were conducted to demonstrate their response to variations in mesh density. The observed trends were used to optimise the meshes for accuracy and solution time/computational resources.

10.2.1. Comparison Tests

During comparison tests, good agreement was observed between the results generated by the ANSYS FE model, the Hencky numerical programme and Huang's analytical model. This demonstrates that given a correctly calculated degree of plastic strain at the bore, an accurate value of residual stress may be predicted by the ANSYS model for a number of end conditions. The bi-linear stress-strain profile used is an approximation; a more accurate material model is required to obtain more realistic values of residual stress.

10.2.2. Mesh Sizing

Mesh Sensitivity tests conducted on the general plane strain models indicated that 100 radial elements (El_{Rad} = 100) would provide suitable accuracy (the results suggested that more than 70-80 were needed). Likewise, to attain a sufficient short section such that $\sigma_z \rightarrow 0$, El_{Rad} =1500 was selected for the Plane Stress model. Achieving the desired levels of summed residual axial stress largely determined this value; it was the measure most sensitive to section length. In both cases, two axial elements are used.

10.3. CONCLUSIONS FROM CHAPTER 5

An existing mesh and constraint set, optimised and developed in Chapter 4, was utilised to provide the basis for a model in which the Jahed and Dubey EMPRAP could be implemented. The EMPRAP was used to represent the gun steel A723-1130, which exhibits non-linear unloading from plastic strain, within the ANSYS model. The combined model was then used to simulate the hydraulic autofrettage of a series of thick-walled tubes. With the exception of a small discrepancy in the unloading stresses near the ID, the calculated stresses matched very well against equivalent results from the Hencky programme. This supports its use in comparisons with future material models developed.

In summary, an FEA procedure for simulating non-linear stress-strain behaviour during hydraulic autofrettage was implemented and investigated.

10.4. CONCLUSIONS FROM CHAPTER 6

A one-dimensional material (*usermat1d*) model was created to gain familiarity with the ANSYS solution procedure, and determine how to programme the desired material within it. A close match between the results generated using it and data from the material-fit equations, indicating that the sub-routine calculates stress states accurately, and in a manner that allows ANSYS to reach solution normally.

A three-dimensional material model (*usermat3d*) was created to be used in all autofrettage simulations (hydraulic and swage), hence confirmation of its accuracy was vital. Uni-axial tests demonstrated a generally close match between results from the material model and the material-fit equations. Agreement is less complete where off-axis (direct) stresses increase in magnitude, altering the relationship between equivalent and axial stress. These off-axis stresses arise from the circular relationship between the Jacobian matrix output to ANSYS from the sub-routine, and the resultant strain increments that ANSYS supplies in return.

The three-dimensional material model was then used in a series of hydraulic autofrettage simulations, under a range of end conditions. The results showed good agreement; disparities are in line with the variations expected from the different numerical methods. Apart from the plastic strains calculated for the Plane Stress case, all residual stress and strain values showed very close agreement. Differences between constant-strain end condition cases may be explained by variations in the axial stress which is the intermediate principal stress.

In summary, a custom material model of a real world gun steel (A723-1130) was programmed utilising the USERMAT feature within ANSYS. USERMAT behaves as a standard material and, crucially, retains plastic strains; this makes the customised material suitable for use in more general load cases than allowed by the EMPRAP method – in particular, simulating swage autofrettage of a pressure vessel.

10.5. CONCLUSIONS FROM CHAPTER 7

A band of pressure model was developed to represent some of the key characteristics of the swage autofrettage process. Two variants of the model were developed: a static, expanding band model and a moving band model. Although neither model is a true representation of swage autofrettage, they both provided valuable insights into the difference between swage and hydraulic autofrettage.

As would be expected, the results from the static band model supported the observation that the required pressure for a constant depth of autofrettage increases as the width of the pressure band decreases.

The relationship between band width and pressure was observed to follow a pattern similar to an offset inverse ratio; based on this a representative relationship was created, the results from which showed reasonable agreement with the data.

The results from the moving band model showed the same trend; the narrower the fringe width, the greater the pressure needed to obtain a given depth of overstrain. As would also be expected, shear stress magnitude near the band was seen to increase as fringe width decreased, due to the greater step size between the applied pressure and zero pressure in the non-loaded section.

Shear stresses switched sign appropriately between the front and rear edges of the pressure band.

Through wall hoop stresses at peak pressure were found to be markedly different from those observed at peak pressure during hydraulic autofrettage; indeed, at and around the ID, they were seen to be strongly negative (compressive) – creating a net outwards force for that section. This is due to the propagation, via shear stresses, of the applied load to more than just the directly loaded section.

Residual hoop stresses at the ID were seen to increase in magnitude as the pressure at the band edge increased (found with lower fringe widths and pressure gradients); the increasing curvature resulting from the more sudden change in pressure causes decreasingly tensile residual axial stresses at the ID, allowing more compressive residual hoop stresses to be developed.

While compressive axial stresses are found at the ID at the centre of the pressure band, towards the edges of the band stresses become increasingly tensile. If the band is narrow enough, this can cause sufficient tensile axial plastic strains to result in significant compressive residual axial stresses at the ID, as was the case when fringe width equalled two.

10.6. CONCLUSIONS FROM CHAPTER 8

A model of swage autofrettage was developed to simulate the deformation of a tube by contact with a mandrel moving through its inner void. It was initially dimensioned to match an existing analysis of swage autofrettage, developed by O'Hara, against which it was also assessed. Generally, a good match was achieved; for the case of the most similar mesh to that used in O'Hara's analysis, strong likeness was observed between the stress distributions calculated by the two models. This indicates the relevant aspects of the swage model developed by O'Hara were incorporated into the ANSYS model. The finer meshes generate results that follow the trends displayed by O'Hara's, and converge relatively quickly; a mesh of effectively four times the linear density of that used by O'Hara was judged to produce suitably accurate results.

Two sensitivity analyses were conducted to determine both the minimum length of tube section and number of sub-steps required. It was determined that a tube length of $15r_a$ was needed for stable mid-length results to be obtained; an initial number of $10El_{N\text{-}Ax}$ sub-steps, with upper and lower limits of $2El_{N\text{-}Ax}$ and $20El_{N\text{-}Ax}$, respectively, was found to give suitably consistent results while remaining computationally feasible. If more computational resources were available, these numbers would be doubled.

The length of the parallel section specified for the mandrel had a significant impact on axial stress and plastic strain profiles within the tube, both during and following the swaging procedure. It was found that the initial value of $0.12r_a$ used by O'Hara gave the best degree of pre-stressing (compressive residual hoop stresses near the ID), although pre-stressing values are relatively consistent apart from the longer parallel section cases ($l_{ll} = 3.0l_{ll\text{-}0}$ and $4.5l_{ll\text{-}0}$). The optimum value for a given mandrel-tube system is likely to depend on several factors such as tube wall ratio (K), mandrel slopes, mandrel-tube interference and material used.

Observations made while mandrel-tube friction coefficient was varied confirmed what would be expected; during autofrettage, shear stresses increased in magnitude with friction coefficient, and axial stresses became less negative/more positive (in response to greater axial load) while retaining a relatively similar distribution.

Mandrel slope angles were also found to have a large influence on the developed stresses. Both effect the initial deformation of the tube (the forward slope has the greatest influence, as its shallower slope deforms a greater length of tube), but the rear slope more directly influences residual stresses due to its creation of residual compressive axial stresses near the ID. Investigation of the effect of the forward and rear mandrel slopes independently would reveal more details of these relationships.

11. APPENDICES

11.1. A1 – LAMÉ'S SOLUTION

The Equilibrium Equation (2.1) is statically indeterminate – σ_r and σ_θ cannot be separated and solved for without further relationships. To the axial constitutive relation, Equation (2.6), Lamé applied the compatibility requirement that initially plane transverse sections remain so after loading (ε_z is constant w.r.t. r).

Substituting the deflection-based definition of hoop strain from (2.3) for that in the constitutive Equation (2.5), manipulating, applying the plane strain criterion, and conducting further manipulation, yields:

$$\sigma_r + \sigma_\theta = 2A \tag{11.1}$$

Where A is a constant. Substituting for σ_θ in the Equilibrium Equation (2.1) and rearranging, the following is obtained:

$$\frac{d\sigma_r}{(\sigma_r - A)} = -2\frac{dr}{r}$$

Integrating yields:

$$\sigma_r = A - \frac{B}{r^2} \tag{11.2}$$

Substituting the above into Equation 11.1 gives:

$$\sigma_\theta = A + \frac{B}{r^2} \tag{11.3}$$

A and B may be solved for, given suitable boundary conditions; applying an internal pressure, p_i, and setting the external pressure, p_o, to zero is achieved by the following:

$$\sigma_r\big|_{r=r_a} = -p_i \quad \sigma_r\big|_{r=r_b} = -p_o = 0$$

For a fully elastic tube, this gives:

$$\sigma_r = -p_i\left(\frac{r_b^2/r^2 - 1}{r_b^2/r_a^2 - 1}\right)$$
$$\sigma_\theta = p_i\left(\frac{r_b^2/r^2 + 1}{r_b^2/r_a^2 - 1}\right) \qquad (11.4)$$
$$\sigma_z = p_i\left(\frac{2\nu_t}{r_b^2/r_a^2 - 1}\right)$$

(Axial stresses are calculated from the radial and hoop values using the constitutive relation, Equation (2.6)).

11.2. A2 – TRESCA ELASTIC-PLASTIC SOLUTION

11.2.1. Autofrettage

Whether autofrettage is achieved hydraulically or through swaging, the process involves expansion and plastic deformation of the tube, followed by relaxation and the development of compressive stresses around the ID.

Consider a tube loaded by an internal pressure, p_i, which increases from zero to the final autofrettage pressure, p_{AF}. Once the pressure is high enough (p_e) tensile yielding initiates at the ID ($r = r_a$), propagating outwards as the pressure increases. Lamé's solution clearly shows that the Tresca equivalent stress is highest at the ID. When the applied pressure reaches p_{AF}, the maximum radius of plasticity is termed the *Primary Yield Radius*, r_p ($r_a \leq r_p \leq r_b$).

Upon removal of the autofrettage pressure compressive stresses are developed within the expanded material found within the primary yield region ($r_a \leq r \leq r_p$), partnered by tensile stresses in the elastic region ($r_p \leq r \leq r_b$). As in the pressure application phase, these compressive stresses are greatest around the ID. If these stresses become large enough, compressive yielding initiates at the ID and propagates outwards – the limit of this reyielding is termed the *Secondary Yield Radius*, r_s. As will be demonstrated, unless the tube material $r_a \leq r \leq r_p$ loses all strength ($\sigma_Y = 0$) following the plastic strain experienced during autofrettage, $r_s < r_p$. Figure 11.1 illustrates these radii.

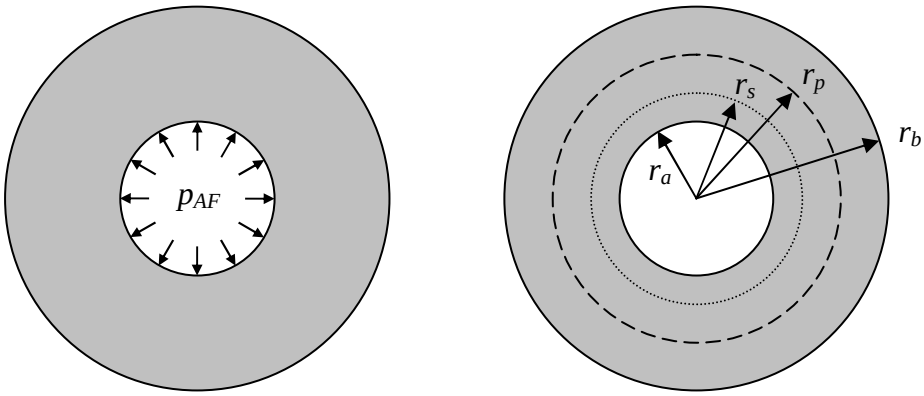

Figure 11.1: Yield Diagram

As noted towards the end of sub-section 2.4.2.2, the first elastic-plastic solution investigated was that based on Tresca's yield criterion, which allows for explicit solution of the stress field (within a hydraulically autofrettaged tube). An elastic, perfectly plastic material was used which is the most simple stress-strain response that includes plasticity (see Figure 3.2).

11.2.2. Autofrettage Stresses

First the stresses in the elastic region, $r_p \leq r \leq r_b$, are established. Introducing the Lamé stresses (11.2, 11.3) at $r = r_p$ into the yield criterion (2.10), the following value is obtained for B:

$$A + \frac{B}{r_p^2} - \left(A - \frac{B}{r_p^2} \right) = \sigma_{Y0}$$

$$B = \frac{\sigma_{Y0} r_p^2}{2}$$

Re-inserting this value into the Lamé radial stress Equation (11.2) at $r = r_b$, gives the following value for A:

$$\sigma_r = 0 = A - \frac{B}{r_b^2}$$

$$A = \frac{\sigma_{Y0} r_p^2}{2 r_b^2}$$

Substituting these values back into the Lamé stress Equations (11.2, 11.3) gives:

$$\sigma_r = -\frac{\sigma_{Y0} r_p^2}{2 r_b^2} \left(\frac{r_b^2}{r^2} - 1 \right) \qquad \sigma_\theta = \frac{\sigma_{Y0} r_p^2}{2 r_b^2} \left(\frac{r_b^2}{r^2} + 1 \right)$$

Given conditions at $r = r_p$ it is now possible to solve for stresses within the plastic region. Substituting from the Tresca yield criterion (2.10) into the equilibrium Equation (2.1):

$$\frac{d\sigma_r}{dr} = \frac{\sigma_{Y0}}{r} \tag{11.5}$$

Separating the variables and integrating gives:

$$\sigma_r = \frac{\sigma_{Y0}}{2} \ln\left(r^2\right) + C$$

As σ_r is continuous across the elastic-plastic interface (at $r = r_p$), its value from the above formula will be equal to that given by Lamé's Equations.

$$\frac{\sigma_{Y0}}{2}\ln\left(r_p^2\right)+C=-\frac{\sigma_{Y0}r_p^2}{2r_b^2}\left(\frac{r_b^2}{r_p^2}-1\right)$$

$$C=-\frac{\sigma_{Y0}}{2}\left(1-\frac{r_p^2}{r_b^2}+\ln\left(r_p^2\right)\right)$$

Hence the following expression for σ_r is found:

$$\sigma_r=-\frac{\sigma_{Y0}}{2}\left(1-\frac{r_p^2}{r_b^2}+\ln\left(\frac{r_p^2}{r^2}\right)\right)$$

It is now possible to substitute the above value for σ_r and its derivative into the equilibrium equation, to find σ_θ.

$$\frac{\sigma_{Y0}}{r}=\frac{\sigma_\theta+\frac{\sigma_{Y0}}{2}\left(1-\frac{r_p^2}{r_b^2}+\ln\left(\frac{r_p^2}{r^2}\right)\right)}{r}$$

$$\sigma_\theta=\frac{\sigma_{Y0}}{2}\left(1+\frac{r_b^2}{r_p^2}-\ln\left(\frac{r_p^2}{r^2}\right)\right)$$

These equations are summarised below, along with those for axial stress found from the constitutive law (Equation (2.6)).

Plastic Region

$$\sigma_r=-\frac{\sigma_{Y0}}{2}\left[1-\frac{r_p^2}{r_b^2}+\ln\left(\frac{r_p^2}{r^2}\right)\right]$$

$$\sigma_\theta=\frac{\sigma_{Y0}}{2}\left[1+\frac{r_p^2}{r_b^2}-\ln\left(\frac{r_p^2}{r^2}\right)\right] \qquad r_a\le r\le r_p \qquad (11.6)$$

$$\sigma_z=E_t\varepsilon_z+\upsilon_t\sigma_{Y0}\left[\frac{r_p^2}{r_b^2}-\ln\left(\frac{r_p^2}{r^2}\right)\right]$$

Elastic Region

$$\sigma_r=-\frac{\sigma_{Y0}r_p^2}{2r_b^2}\left(\frac{r_b^2}{r^2}-1\right)$$

$$\sigma_\theta=\frac{\sigma_{Y0}r_p^2}{2r_b^2}\left(\frac{r_b^2}{r^2}+1\right) \qquad r_p\le r\le r_b \qquad (11.7)$$

$$\sigma_z=E_t\varepsilon_z+\upsilon_t\sigma_{Y0}\left(\frac{r_p^2}{r_b^2}\right)$$

The primary yield radius, r_p, cannot be determined through rearrangement or other direct means; instead, it must be found through a short iteration using the boundary condition $\sigma_r = p_{AF}$ at the ID ($r = r_a$) applied to the radial stress expression from Equation (11.6). This was achieved (using Matlab, but any other suitable numerical method would quickly achieve a converged answer) by incrementing r from an initial value of r_a.

A special case of the radial stress from Equation (11.6) can be formed to give an expression for the minimum pressure required for yielding (or limiting elastic pressure) at the inner face, p_e. Setting r and r_p to r_a:

$$p_e = \frac{\sigma_{Y0}}{2}\left[1-\frac{r_a^2}{r_b^2}\right] = \frac{\sigma_{Y0}}{2}\left[1-\frac{1}{K^2}\right] \tag{11.8}$$

If the autofrettage load is hydraulic, a simple comparison of the applied pressure to the limiting elastic pressure, from Equation (11.8), will determine the presence of yielding.

11.2.3. Unloading

Once the autofrettage stresses within the tube have been determined, the unloading stresses must then be assessed so that the residual values may be calculated. Depending on the magnitude of the compressive residual stresses developed, unloading may follow one of two paths – elastic or elastic-plastic. Accordingly, a check must first be made.

To determine whether secondary yielding occurs, Tresca's yield criterion (2.10) is again employed.

Assessing the value of σ_θ - σ_r using Equations (11.6), (11.7) and (11.4), yields:

$$\sigma_\theta - \sigma_r = \sigma_{Y0}\left(1-\frac{pr_a^2}{p_e r^2}\right) \qquad r_a \le r \le r_p \tag{11.9}$$

$$\sigma_\theta - \sigma_r = \sigma_{Y0}\frac{r_a^2}{r^2}\left(\frac{r_p^2}{r_a^2}-\frac{p}{p_e}\right) \qquad r_p \le r \le r_b \tag{11.10}$$

It is found that σ_θ - σ_r has its most positive value when $r = r_b$; however, it is of greatest magnitude when $r = r_a$, i.e. when r_a^2/r^2 reaches its maximum value of 1. Here, the contents of the brackets of Equation (11.9) evaluate as –1 or greater (in magnitude) if $p \ge 2p_e$. This means that σ_θ - σ_r exceeds the magnitude of σ_{Y0} – the Tresca yield criterion (2.10) at which point secondary yielding is considered to occur. This can more easily be seen by rearranging Equation (11.9), and making the substitution $r = r_a$:

$$\frac{\sigma_\theta - \sigma_r}{\left(1 - \frac{p}{p_e}\right)} = \sigma_{Y0} \tag{11.11}$$

If the left hand side of Equation (11.11) exceeds the right hand side, secondary yielding is assumed to take place; if less that the RHS, unloading proceed elastically. It can be shown [26] that even with maximum autofrettage (i.e. $r_p = r_b$) secondary yielding will not occur unless $r_b/r_a \geq 2.22$.

11.2.4. Residual Stresses – Elastic Unloading

If the residual stresses are insufficient to cause compressive reverse yielding, residual stresses are calculated by superposing standard Lamé elastic stresses, caused by the application of $-p_{AF}$, from Equations (11.4) upon those created during pressurisation.

11.2.5. Residual Stresses – Plastic Unloading

If residual stresses are sufficient to cause reverse yielding, a secondary yield radius, r_s, must designated. It is then possible to form two further sets of equations to describe secondary yielding of the tube, equivalent to Equations (11.6) and (11.7) (from the primary yielding stage). They take the place of the elastic stresses from Equations (11.4), and are subtracted from the autofrettage stresses in the same way. As shown in Figure 3.2, as an autofrettaged tube is depressurised, the tube material must unload from a peak stress of $+\sigma_y$ to $-\sigma_y$ before reverse yielding occurs. Therefore the unloading stresses achieve double the magnitude of the autofrettage before reverse yielding occurs; this is reflected in Equations (11.12) and (11.13) as their apparent magnitude is twice that of Equations (11.6) and (11.7). For example, hoop stress is tensile at the bore during autofrettage – after load removal, it becomes compressive.

Plastic Region

$$\begin{aligned}
\sigma_r &= -\sigma_{Y0}\left[1 - \frac{r_s^2}{r_b^2} + \ln\left(\frac{r_s^2}{r^2}\right)\right] \\
\sigma_\theta &= \sigma_{Y0}\left[1 + \frac{r_s^2}{r_b^2} - \ln\left(\frac{r_s^2}{r^2}\right)\right] \qquad r_a \leq r \leq r_s \\
\sigma_z &= E_t \varepsilon_z + \nu_t\left(\sigma_r + \sigma_\theta\right)
\end{aligned} \tag{11.12}$$

Elastic Region

$$\sigma_r = -\frac{\sigma_{Y0} r_s^2}{r_b^2}\left(\frac{r_b^2}{r^2} - 1\right)$$

$$\sigma_\theta = \frac{\sigma_{Y0} r_s^2}{r_b^2}\left(\frac{r_b^2}{r^2} + 1\right) \qquad r_s \le r \le r_b \qquad (11.13)$$

$$\sigma_z = E_t \varepsilon_z + \nu_t(\sigma_r + \sigma_\theta)$$

The secondary yield radius, r_s, is found using the zero internal pressure after relaxation criterion. This means that the residual radial stress (from Equation (11.12)) summed with the radial stress during Autofrettage (from Equation (11.6)) must give an answer of zero (at $r = r_a$), as seen below.

$$-\frac{\sigma_{Y0}}{2}\left[1 - \frac{r_p^2}{r_b^2} + \ln\left(\frac{r_p^2}{r_a^2}\right)\right] + \sigma_{Y0}\left[1 - \frac{r_s^2}{r_b^2} + \ln\left(\frac{r_s^2}{r_a^2}\right)\right] = 0 \qquad (11.14)$$

As with r_p from Equation (11.6), r_s may be found by a short iteration. The secondary yield radius, r_s, will be found to be smaller than r_p.

It can be seen from Equation (11.9) that as p/p_e increases from 2, secondary yielding occurs for radii progressively greater than r_a.

Plots of residual hoop and axial stresses within a tube with Wall Ratio 3.0 can be seen in Figure 11.2. The ratio of autofrettage pressure to yield strength, p_i/σ_{Y0}, is equal to 1.0909; the normalised primary and secondary yield radii are 0.8703 and 0.0612 respectively (they are indicated by the peak magnitudes of hoop stress).

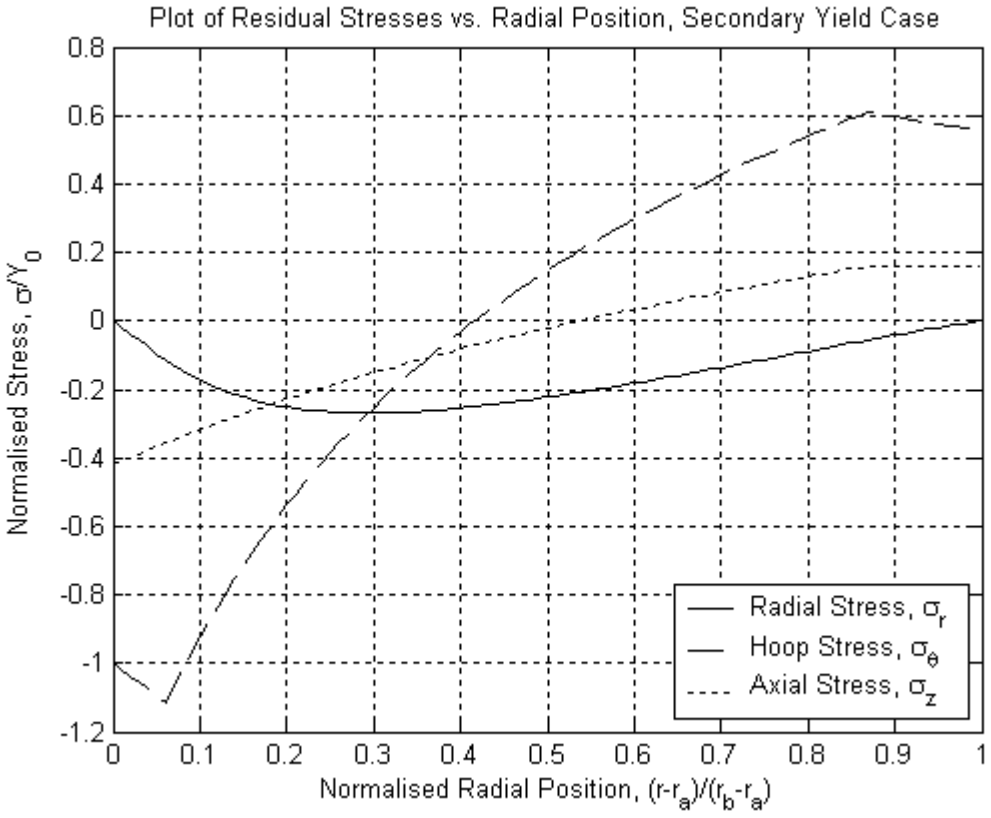

Figure 11.2: Residual Stresses from the Tresca Solution, for *K* = 3.0

11.2.6. Strains

While Equations (2.4) – (2.6) provide a means for assessing component elastic strains, they are not capable of calculating plastic strains; this will now be addressed, by subtracting elastic strain components from the total values. As axial strain is assumed to be entirely elastic, Equation (2.6) is true throughout the tube. Plane strain conditions ($\varepsilon_z = 0$) are then applied to Equation (2.6):

$$\sigma_z = \nu(\sigma_r + \sigma_\theta)$$

Substituting this value back into Equations (2.4) and (2.5), equating each with Equations (2.2) and (2.3) respectively, the following are obtained.

$$\varepsilon_r = \frac{du}{dr} = -\nu\varepsilon_z + \frac{1+\nu}{E}\left[(1-\nu)\sigma_r - \nu\sigma_\theta\right] \tag{11.15}$$

$$\varepsilon_\theta = \frac{u}{r} = -\nu\varepsilon_z + \frac{1+\nu}{E}\left[(1-\nu)\sigma_\theta - \nu\sigma_r\right] \tag{11.16}$$

This means that at a given radius, deflections can be found if the circumferential strains are known.

It then remains to assess the total strains within the deformed region, $r_a \leq r \leq r_p$. First, the Equilibrium Equation (2.1) is integrated by parts, the following is obtained:

$$r(\sigma_r + \sigma_\theta) = \frac{\partial}{\partial r}\left(r^2 \sigma_r\right) \tag{11.17}$$

While plastic strains remain small – as is the case when wall ratios remain less than ~5, and less than total yielding has occurred – positional changes may be ignored. Summing Equations (11.15) and (11.16) yields:

$$\varepsilon_r + \varepsilon_\theta = \frac{\left[(1-\nu)(\sigma_r + \sigma_\theta) - 2\nu\sigma_z\right]}{E} \tag{11.18}$$

In terms of the associated integrated flow rule we have $\varepsilon_r^p + \varepsilon_\theta^p = 0$ – this gives:

$$\varepsilon_r + \varepsilon_\theta = \varepsilon_r^e + \varepsilon_\theta^e = \frac{\partial u}{\partial r} + \frac{u}{r} \tag{11.19}$$

Substituting Equations (11.19) and (2.6), and the relationship $G = E/2(1 + \nu)$ into Equation (11.18):

$$\frac{\partial u}{\partial r} + \frac{u}{r} = -2\nu_t \varepsilon_z + \frac{1-2\nu_t}{2Gr} \cdot \frac{\partial}{\partial r}\left(r^2 \sigma_r\right) \tag{11.20}$$

This is valid throughout both elastic and plastic regions of the tube. Integrating Equation (11.20) w.r.t. r, using the boundary condition $\sigma_r = 0$ when $r = r_b$, the following is obtained:

$$\frac{u_t}{r} = \underbrace{-\nu_t \varepsilon_z}_{Elastic} + \underbrace{(1-\nu_t)\frac{\sigma_{Y0} r_p^2}{2G_t r^2}}_{Plastic} + \underbrace{(1-2\nu_t)\frac{(\sigma_r)_t}{2G_t}}_{Elastic} \qquad r_a \leq r \leq r_p \tag{11.21}$$

Plastic hoop strains may then be found by subtracting elastic hoop strains, calculated by Equation (11.16), from the total value, Equation (11.21).

$$\varepsilon_\theta^p = (1-\nu^2)\left(\frac{\sigma_{Y0} r_p^2}{E r^2} - \frac{\sigma}{E}\right) \tag{11.22}$$

Where σ represents the yield strength *during loading* of the material *at that position*. Hence when modelling the Bauschinger effect if there is no strain hardening present (i.e. $H = 0$) it equals σ_Y, and when modelling strain hardening it increases according to the hardening relationship defined.

Also, given the associated integrated flow rule, plastic radial strain is given by:

$$\varepsilon_r^p = -\varepsilon_\theta^p \tag{11.23}$$

11.3. A3 – JAHED AND DUBEY'S METHOD

Jahed, Sethuraman and Dubey [20] proposed a method, subsequently termed an EMPRAP; it describes how an iterative, numerical linear elastic analysis can be transformed into a complex non-linear stress-strain analysis, through manipulation of E and v. Jahed and Dubey [19] employed the procedure to implement a single, non-linear loading behaviour and a single, non-linear unloading behaviour for plane stress and plane strain conditions. Their method was extended by Parker [22] to incorporate unloading behaviour that varies with radius as a function of loading plastic strain. Designated the *Hencky Programme,* it was subsequently further extended to solve any plane condition, including the crucial open-ends case. The theoretical basis of the EMPRAP method is explained below, together with the routine used for solution of E_{eff} and v_{eff} in an FE environment.

A body, Ω, is defined, enclosed within a surface Γ. The boundary value problem is formulated on the following conditions:

1. Traction and displacements applied to Γ,
2. Stress equilibrium within Ω.

The stress equilibrium condition specifies that, in the absence of body forces:

$$\sigma_{ij} = 0\big|_{\Omega} \qquad i, j = 1, 2 \,\&\, 3$$

Traction (a vector of the surface density of cohesive forces), t_i^*, over the boundary, Γ_1:

$$\sigma_{ij} n_j = t_i^*\big|_{\Gamma_1}$$

Displacements, u_i^*, over the boundary Γ_2:

$$u_i = u_i^*\big|_{\Gamma_2}$$

The full boundary, Γ, is summed from the other part boundaries:

$$\Gamma = \Gamma_1 + \Gamma_2$$

The total strain tensor is the sum of the elastic and plastic strain tensors:

$$\varepsilon_{ij} = \varepsilon_{ij}^e + \varepsilon_{ij}^p \tag{11.24}$$

The elastic strain is given by Hooke's Law:

$$\varepsilon_{ij}^{e} = \frac{1+\nu}{E}\sigma_{ij} - \frac{\nu}{E}\sigma_{kk}\delta_{ij} \tag{11.25}$$

The plastic strain is given by Hencky's total deformation equation:

$$\varepsilon_{ij}^{p} = \phi s_{ij} \tag{11.26}$$

From the above expression, s_{ij} is the deviatoric stress tensor:

$$s_{ij} = \sigma_{ij} - \tfrac{1}{3}\sigma_{kk}\delta_{ij} \tag{11.27}$$

The uni-axial relationship, ϕ, between equivalent stress and equivalent plastic strain is defined as:

$$\phi = \frac{3}{2}\frac{\varepsilon_{eq}^{p}}{\sigma_{eq}} \tag{11.28}$$

In turn the equivalent plastic strain, ε_{eq}^{p}, and equivalent (total) stress, σ_{eq}, are defined as:

$$\varepsilon_{eq}^{p} = \sqrt{\tfrac{2}{3}}\left|\varepsilon_{ij}^{p}\right|, \qquad \sigma_{eq} = \sqrt{\tfrac{3}{2}}\left|s_{ij}\right|$$

The total strain tensor, Equation (11.24), can then be rewritten, using Equations (11.25), (11.26) and (11.27):

$$\varepsilon_{ij} = \left(\frac{1+\nu}{E} + \phi\right)\sigma_{ij} - \left(\frac{\nu}{E} + \tfrac{1}{3}\phi\right)\sigma_{kk}\delta_{ij} \tag{11.29}$$

Substituting to alter Equation (11.29) to the same form as (11.25), i.e. to reduce it to elastic form:

$$\varepsilon_{ij} = \frac{1+\nu}{E_{eff}}\sigma_{ij} - \frac{\nu_{eff}}{E_{eff}}\sigma_{kk}\delta_{ij} \tag{11.30}$$

Where E_{eff} and ν_{eff} are the effective Young's modulus and Poisson's ratio, representing plastic behaviour:

$$E_{eff} = \frac{3E}{3+2E\phi}, \qquad \nu_{eff} = \frac{3\nu + E\phi}{3+2E\phi}$$

E_{eff} may be determined from the material stress-strain relationship, from which ν_{eff} may then be determined using Equation (11.31):

$$\nu_{eff} = E_{eff}\frac{3\nu + E\phi}{3E} \tag{11.31}$$

To be used within a model, the model must simulate the geometry and loads present; the stress-strain state is then calculated using the initial, elastic properties of the material. If any parts of the model are assessed to have exceeded the yield stress (or the limit of linearity, according to the material-fit), the EMPRAP is invoked. The EMPRAP accepts (equivalent) strain as its input; this value is entered into the material-fit σ-ε expression, which calculates the stress magnitude that would result. A new, effective, elastic modulus is calculated using Equation (11.32):

$$E_{eff}^{n} = \frac{\sigma^{n}}{\varepsilon^{n}} \tag{11.32}$$

Figure 11.3 shows how E_{eff}^{n} is calculated iteratively, until σ^{n} tends to the stress value generated by the material-fit, given ε^{n}. When the non-linear section of the material σ-ε fit has a positive gradient, σ^{n} monotonically approaches the final value.

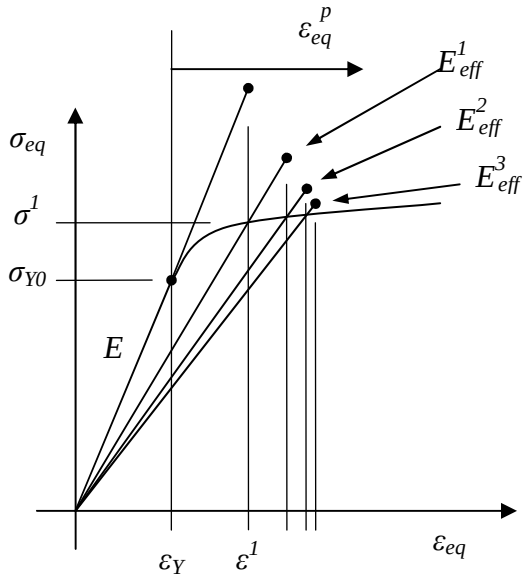

Figure 11.3: E_{eff} convergence diagram, when material is loaded beyond Yield Stress

In addition, ϕ must be calculated (Equation (11.28)), using:

$$\varepsilon_{eq}^{p} = \varepsilon^{n} - \varepsilon^{Y}$$
$$\sigma_{eq} = \sigma^{n}$$

This is achieved by:

1. Solving the initial system using a linear elastic analysis
2. Equivalent stresses in elements are evaluated against σ_{Y0} – if the yield stress is exceeded, E and v are calculated (using Equations (11.32) and (11.31)) on a per-element basis, depending on the degree by which the yield stress is exceeded.
3. Solve using modified values.
4. Check for convergence – if error is greater than that desired, return to step 2.

11.4. A4 – ADDITIONAL EMPRAP RESULTS FROM CHAPTER 5

11.4.1. Autofrettage Stresses

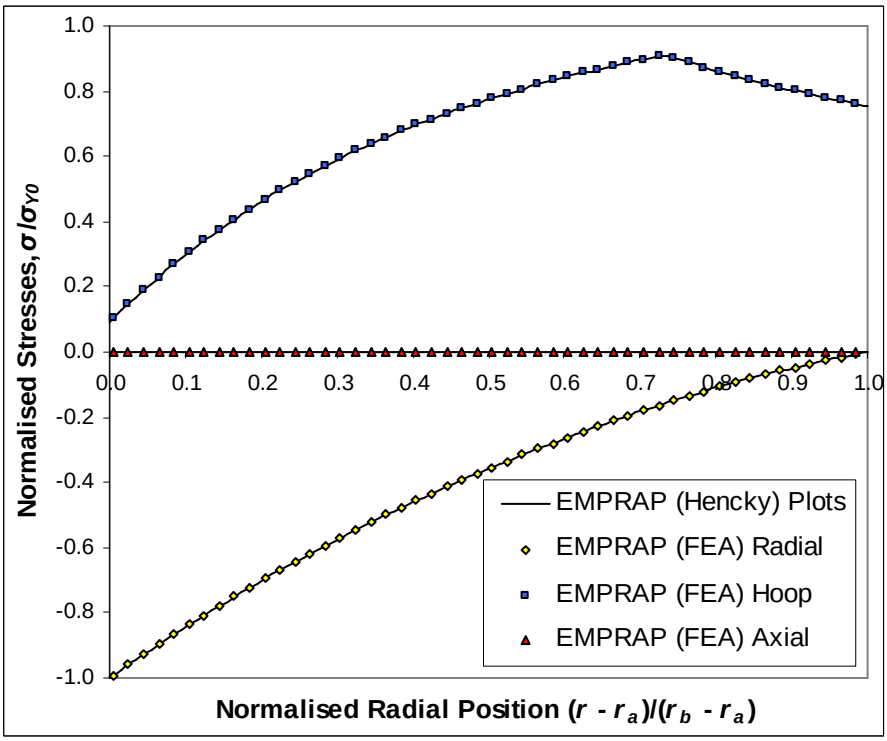

Figure 11.4: Plane Stress

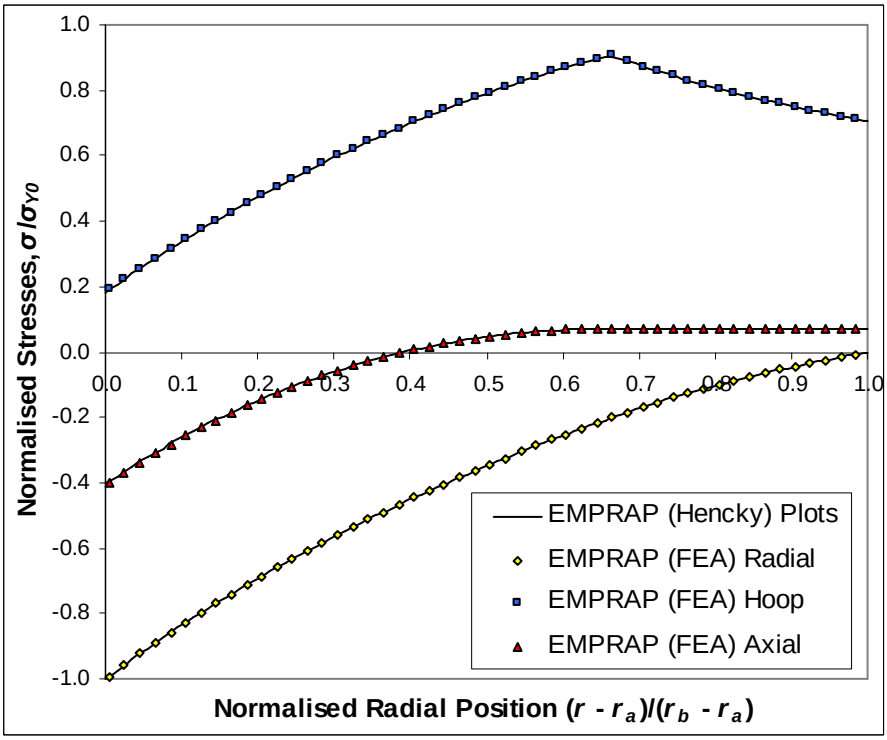

Figure 11.5: Open Ends

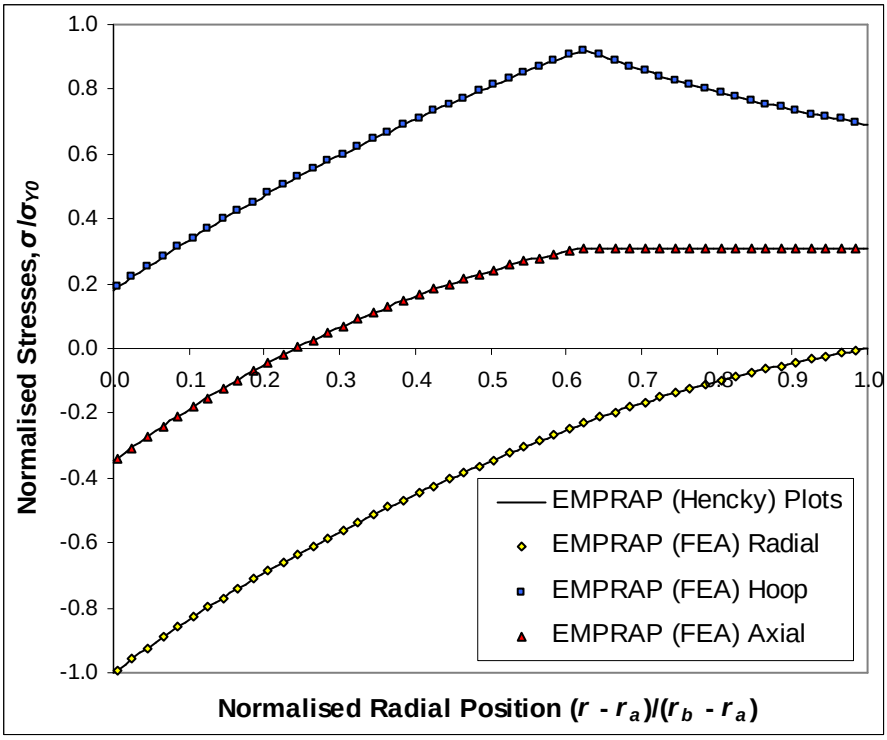

Figure 11.6: Closed Ends

11.4.2. Unloading Stresses

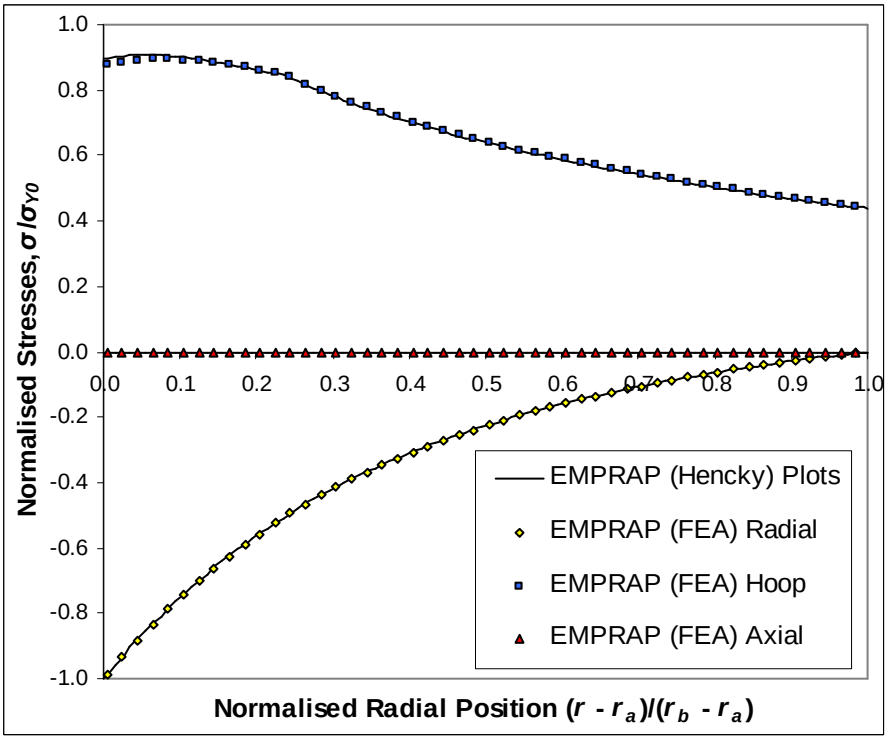

Figure 11.7: Plane Stress

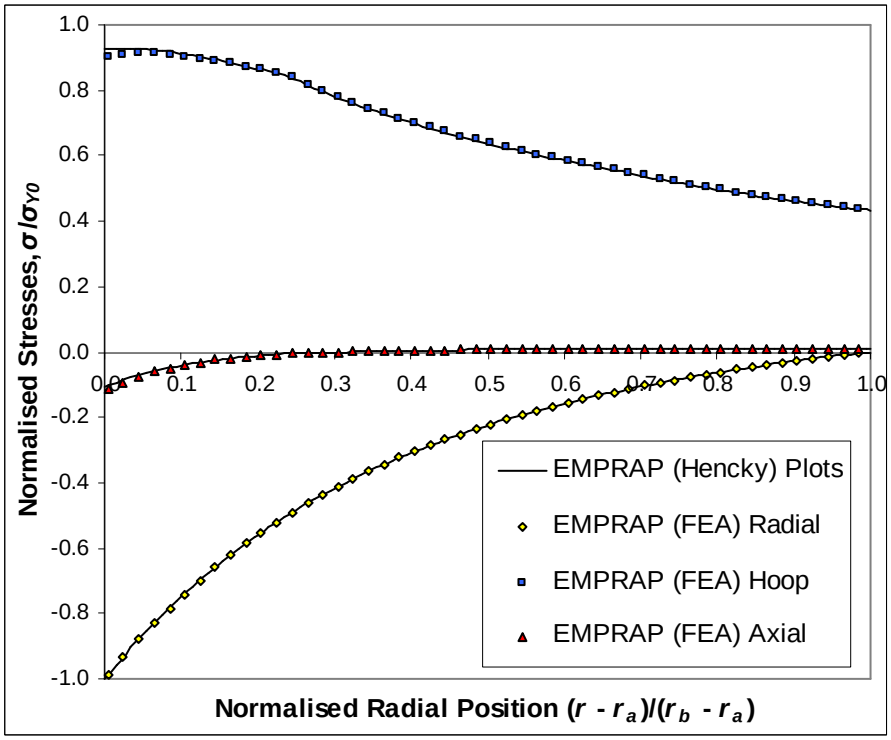

Figure 11.8: Open Ends

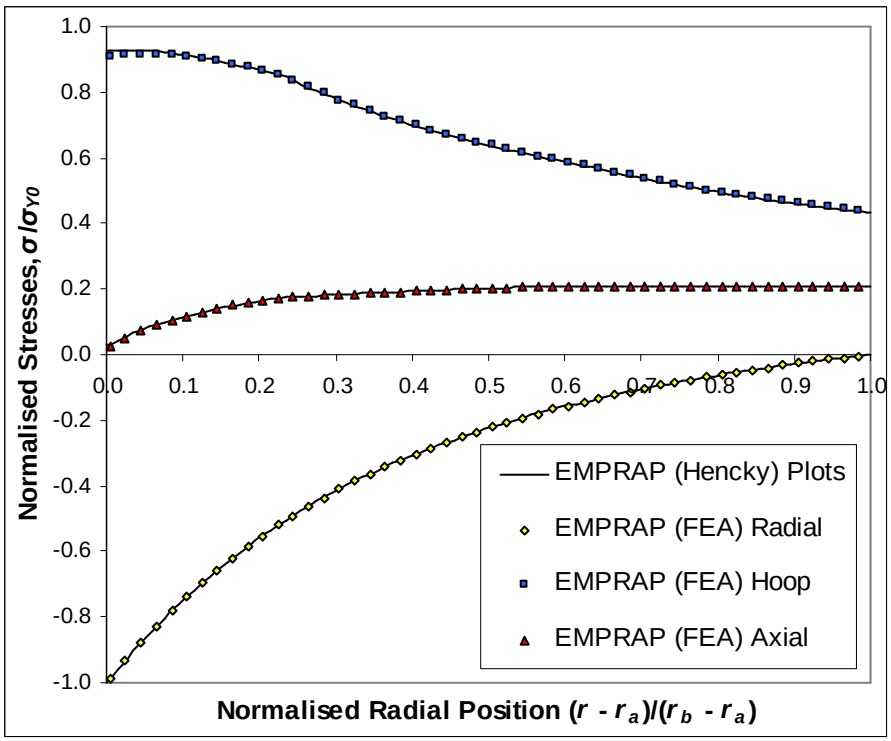

Figure 11.9: Closed Ends

11.4.3. Residual Stresses

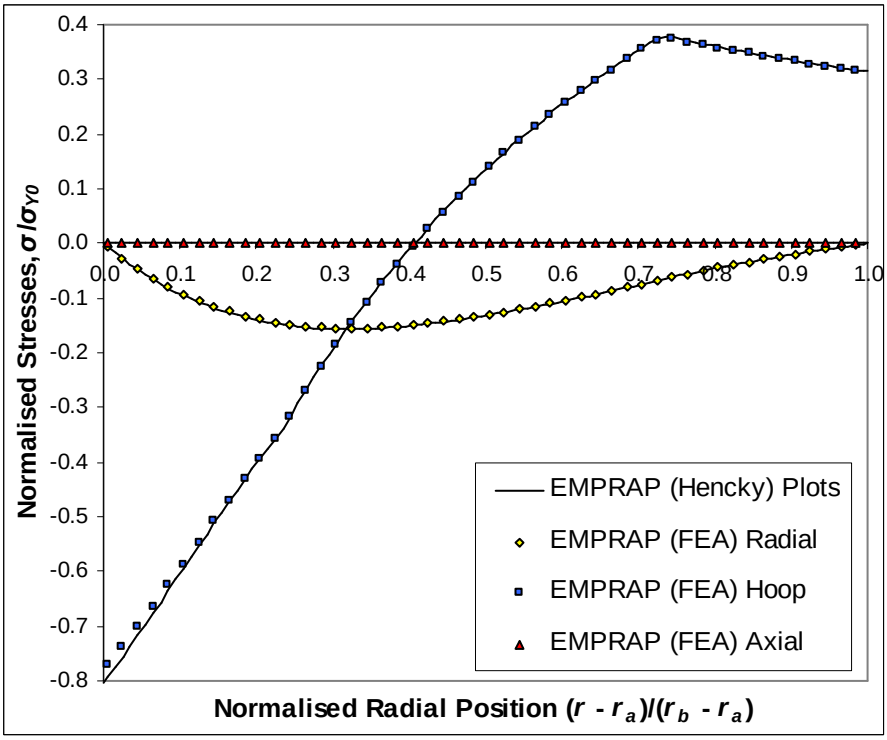

Figure 11.10: Plane Stress

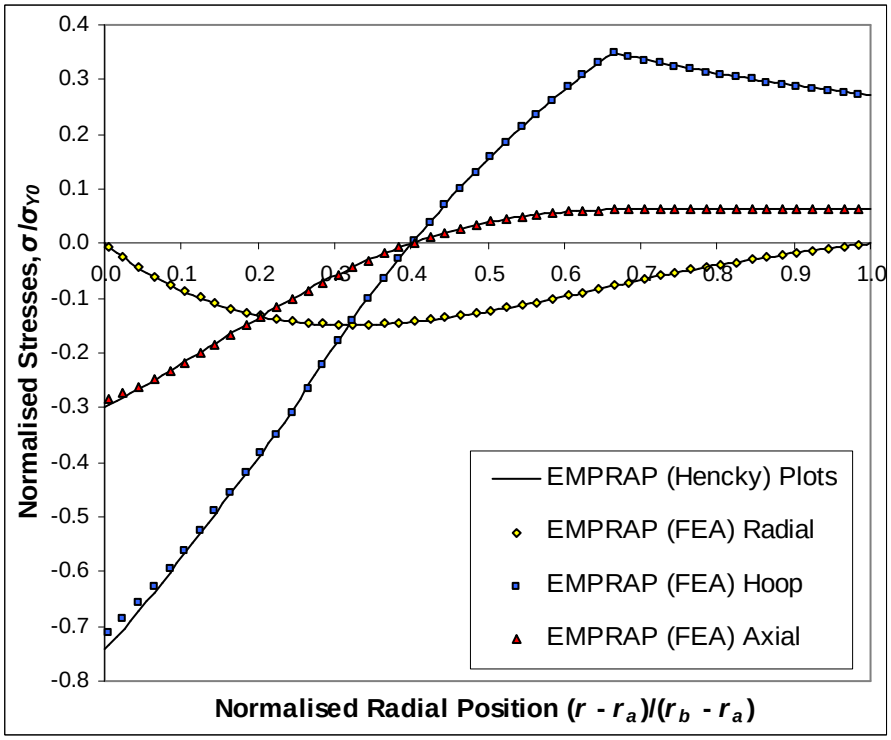

Figure 11.11: Open Ends

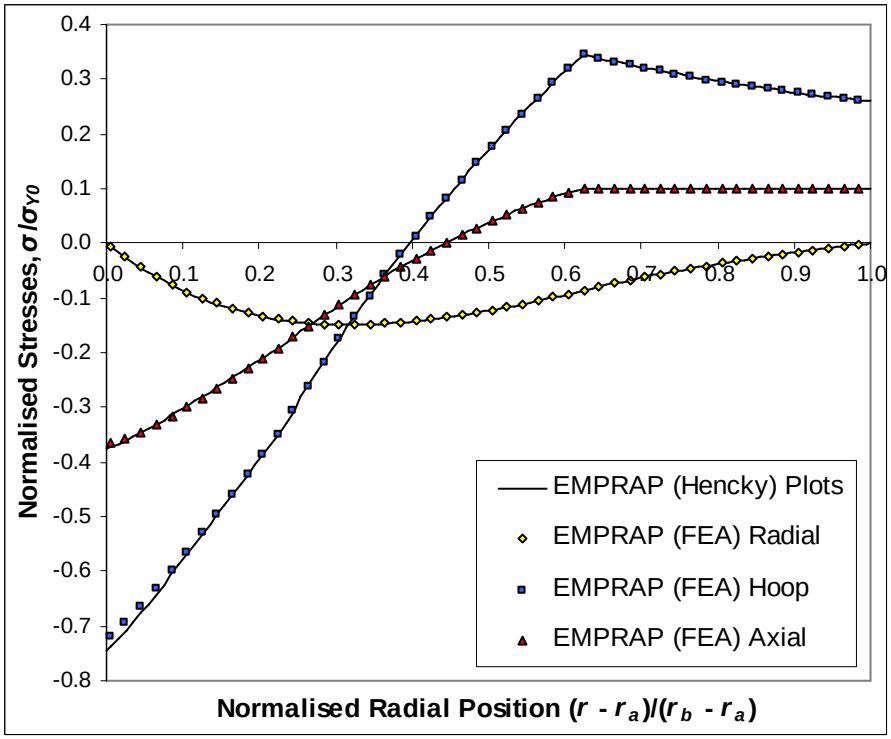

Figure 11.12: Closed Ends

References

[1] "Modern Weapons and Weapon Systems," Technology of War article, Encyclopædia Britannica, Volume 29, 1992.

[2] Rodman, T J, "Improvement in Casting Ordnance," US Patent No. 5236, August 14, 1847.

[3] Lamé, G, "Leçons sur la Théorie Mathématique de l'Élasticité des Corps Solides," Gauthier-Villars, Paris, 1852.

[4] Macrae, A E, "Overstrain in Metals," HM Stationery Office, London, 1930.

[5] Manning, W R D, "High Pressure Engineering, Bulleid Memorial Lectures," University of Nottingham, Volume II, 1963.

[6] Dirmoser, O, "Design of High Strength Gun Tubes (Built up and Cold Worked) having Normal and Artificially Raised Elastic Limit," Vienna Technical College, Vienna, Austria, 1931.

[7] Faupel, J H, "Residual Stresses in Heavy-Wall Cylinders," Journal of the Franklin Institute, Volume 259, Issue 5, pp. 405-420, 1955.

[8] Davidson, T E, Kendall, D P and Rainer, A N, "Residual Stresses in Thick-walled Cylinders Resulting from Mechanically Induced Overstrain," Experimental Mechanics, Vol 3, pp 253-262, 1963.

[9] O'Hara, G P, "Analysis of the Swage Autofrettage Process," US Army ARDEC Technical Report ARCCB-TR-92016, Benét Laboratories, Watervliet Arsenal, NY 12189, USA, 1992.

[10] Iremonger, M J I and Kalsi, G S, "A Numerical Study of Swage Autofrettage," Journal of Pressure Vessel Technology, Volume 125, Issue 3, pp. 347-351, 2003.

[11] Timoshenko, S P and Goodier, J N, "Theory of Elasticity (Third Edition)," New York: MacGraw Hill Book Company, 1970.

[12] Lancaster, P R and Mitchell, D, "Advanced Solid Mechanics," The Macmillan Press Ltd, 1980.

[13] Hill, R, Lee, E H and Tupper, S J, "The Theory of Combined Plastic and Elastic Deformation with Particular Reference to a Thick Tube under Internal Pressure," Proceedings of the Royal Society of London, Series A, Mathematical and Physical Sciences, Volume 191, Number 1026, pp. 278-303, 1957.

[14] Avitzur, B, "Determination of Residual Stress Distributions in Autofrettaged Tubing: A Discussion," Benét Laboratories Technical Report ARCCB-MR-88034, Benét Laboratories, Watervliet Arsenal, NY 12189, USA, 1988.

[15] Avitzur, B, "Autofrettage - Stress Distribution under Load and Retained Stresses after Depressurization," Benét Laboratories Technical Report ARCCB-TR-89019, Benét Laboratories, Watervliet Arsenal, NY 12189, USA, 1989.

[16] Huang, X P and Cui, W, "Effect of Bauschinger Effect and Yield Criterion on Residual Stress Distribution of Autofrettaged Tube," ASME *Journal Pressure Vessel Technology*, Volume 128, Issue 2, pp. 212-216, May 2006.

[17] Chu, S-C, "A More Rational Approach to the Problem of an Elastoplastic Thick-walled Cylinder," Journal of the Franklin Institute, Volume 294, pp. 57-65, 1972.

[18] Hodge, P C and White, G N, "A Quantitative Comparison of Flow and Deformation theories of Plasticity," Journal of Applied Mechanics, Volume 72, pp. 180-184, 1950.

[19] Jahed, H. and Dubey, R. N., 1997, "An Axisymmetric Method of Elastic-Plastic Analysis Capable of Predicting Residual Stress Field," Trans ASME, Journal of Pressure Vessel Technology, 119, pp. 264-273.

[20] Jahed, H, Sethuraman, R and Dubey, R N, "Variable Material Properties approach in Elastic-Plastic Solution of Thick-Walled Cylinders," Mechanics in Design, Ed. Meguid, S A , CSME Forum, Toronto, Volume 1, pp. 187-197, 1996.

[21] Milligan, R V, Koo, W H and Davidson, T E, "The Bauschinger Effect in a High-Strength Steel," ASME Journal of Basic Engineering, Vol 88, pp. 480-488, 1966.

[22] Parker, A P, 2001, "Autofrettage of Open End Tubes – Pressures, Stresses, Strains and Code Comparisons," ASME Journal of Pressure Vessel Technology, Vol 123, pp. 271–281.

[23] Hill, R, "The Mathematical Theory of Plasticity," Oxford University Press, 1967.

[24] Parker, A P, Gibson, M C, Hameed, A, Troiano, E, Hetherington and J G, "Material Modeling for Autofrettage Stress Analysis including the 'Single Effective Material," accepted for conference, to be published in the proceedings of PVP2008, Chicago, 27-31 July, 2008.

[25] Bauschinger, J, "Über die Veranderung der Elasticitatagrenze und dea Elasticitatamoduls verschiadener Metalle," Zivilingenieur, Vol 27, 1881, columns 289-348.

[26] Chakrabarty, J, "Theory of Plasticity (Third Edition)," Elsevier Press, 2006.

[27] Bland, D R, “Elastoplastic thick-walled tubes of work-hardening material subject to internal and external pressures and temperature gradients,” Journal of the Mechanics and Physics of Solids, Volume 4, pp. 209–229, 1956.

[28] ANSYS Finite Element Program, ANSYS Inc, Southpointe, 275 Technology Drive, Canonsburg, PA 15317.

[29] Gibson, M C, Hameed, A, Parker, A P, Hetherington, J G, 2006, “A Comparison of Methods for Predicting Residual Stresses in Strain-Hardening, Autofrettage Thick Cylinders, Including the Bauschinger Effect,” ASME Journal of Pressure Vessel Technology, Vol 128(2), pp. 217-222.

[30] Parker, A P, Troiano, E, Underwood, J H and Mossey, C, “Characterization of Steels Using a Revised Kinematic Hardening Model (NLKH) Incorporating Bauschinger Effect,” GT2002 - Gun Tubes Conference, Keble College Oxford, September 2002, paper S2P8, published in ASME Journal of Pressure Vessel Technology, Vol 125, pp. 277-281, 2003.

[31] ANSYS Theory Manual, Section 4.2. Rate-Independent Plasticity, ANSYS Release 11.0 Documentation, ANSYS Inc.

[32] Lemaitre, J, and Chaboche, J-L, “Mechanics of Solid Materials,” section 5.3.3.4, English Edition.

[33] Gibson, M C, Hameed, A, Hetherington, J G, Parker, A, “Custom Material Modeling within FEA for use in Autofrettage Simulation,” PVP2007-26341, Proceedings of PVP2007, San Antonio, Texas, USA, July 22-26, 2007.

[34] de Matos, P F P, Moreira, P M G P, Camanho, P P and de Castro, P M S T, “Numerical simulation of cold working of rivet holes,” Finite Elements in Analysis and Design, Volume 41, Issue 9-10 (May 2005), pp. 989-1007, 2005.

[35] de Matos, P F P, Moreira, P M G P, Pina, J, Dias, A M, and de Castro, P M S T, “Residual Stresses Around an Expanded Hole in an Aluminum Clad Sheet,” Proceedings of the 7th International Conference on Residual Stress (ICRS7) CD ROM, Xi'an, China, 14-16 June, 2004.

[36] ANSYS Contact Technology Guide, ANSYS Release 11.0 Documentation, ANSYS Inc.

[37] Madenci, E and Guven, I, “The Finite Element Method and Applications in Engineering Using ANSYS” (specifically section 10.3), Springer Science and Business Media, Inc, New York, 2006.

[38] Bihamta R, Movahhedy M R and Mashreghi A R, “A numerical study of swage autofrettage of thick-walled tubes,” Materials and Design, Volume 28, pp. 804–815, 2007.

[39] Tribology article, Encyclopædia Britannica, Volume 11, 1974.